



TECHNISCHE
UNIVERSITÄT
WIEN

A Quantum Cascade Laser-Based Sensor For Ambient Air Monitoring

A thesis submitted for the degree of

Doctor of Technical Sciences (Dr. techn.)

at

Technische Universität Wien

Faculty of Technical Chemistry

Institute of Chemical Technologies and Analytics

under supervision of

Univ. Prof. Dr. Bernhard Lendl

defended by

DI Andreas Genner

Mat. Nr. 0625135

Vienna, December 2020



Die approbierte gedruckte Originalversion dieser Dissertation ist an der TU Wien Bibliothek verfügbar.
The approved original version of this doctoral thesis is available in print at TU Wien Bibliothek.

Zusammenfassung

Das Bestimmen und Messen von Schadstoffen in der Luft liefert einen wesentlichen Beitrag, um den Menschen sichere und gesunde Lebensbedingungen zu garantieren. Die erlaubten Grenzwerte der jeweiligen Stoffe sind in nationalen Gesetzen geregelt und orientieren sich an den Richtlinien der Weltgesundheitsorganisation. Es ist die Aufgabe nationaler Luftmessnetzwerke und den zuständigen Behörden, repräsentative Standorte auszuwählen und Immissionsmessungen durchzuführen. Die dazu verwendeten Geräte sind meistens für einen einzelnen Analyten optimiert, und deren nicht zu unterschätzenden Abmessungen erfordern eine Installation in umgebauten Kastenwägen, Transport-Containern oder dedizierten Labors in Amtsgebäuden.

Obwohl es für sämtliche Schadstoffe bereits hochpräzise Referenzmessgeräte gibt, verhindern vor allem deren Anschaffungskosten und Abmessungen den Aufbau dichter Messnetzwerke. Dieses Problem könnte in Zukunft mit dem Einsatz von Infrarotspektroskopie gelöst werden, da alle zu erfassenden gasförmigen Schadstoffe charakteristische Absorptionslinien in diesem Wellenlängenbereich aufweisen. Folglich könnten mehrere Gase mit einem einzigen Messgerät quantifiziert und so die Installations- und Betriebskosten gesenkt werden. Um die Technologie für kompakte Multi-Gas-Analysatoren weiter voranzutreiben, wurde in dieser Arbeit ein Prototyp, mit dem die Schadstoffe CO, NO, NO₂ und SO₂ in der Umgebungsluft gemessen werden können, entwickelt. Dieser besteht aus vier Quantenkaskadenlaser, einer Gasmesszelle mit 76 m optischer Weglänge und zwei Quecksilber-Cadmium-Tellurid-Detektoren, wobei bei der Wahl der einzelnen Komponenten auf deren kommerzielle Verfügbarkeit geachtet wurde. Damit die Schadstoffe auch im niedrigen ppbv-Bereich gemessen werden können, basiert der Prototyp auf der 2f-Wellenlängenmodulationsspektroskopie.

Weil die CO-Konzentration aber auch sehr leicht Werte den einstelligen ppmv-Bereich erreichen kann, wurde zusätzlich eine Technik mit deutlich höheren linearen Bereich installiert. Die heterodyne phasen-sensitive Dispersionsspektroskopie kann sehr einfach in einem für 2f-Wellenlängenspektroskopie gedachten Versuchsaufbau mit Standardkomponenten integriert werden. Während direkte auf Absorption basierende Techniken durch die starke Signalabschwächung des Analyten

limitiert sind, wird bei dieser die wellenlängenabhängige Phasenverschiebung zur Konzentrationsbestimmung herangezogen. Dazu wird der Laser im Megahertz-Bereich moduliert, um zwei weitere Wellenlängen zu erzeugen (optische Seitenbänder). Diese interagieren anschließend mit dem Analyten und ergeben am Detektor ein charakteristisches Schwebungssignal. Obwohl dessen Amplitude durch die starke Absorption verrauscht ist, lässt sich die Phasenlage, und somit die Konzentration, präzise messen.

Die Anwendbarkeit des Prototyps wurde während zweier Messkampagnen gezeigt, wobei die erste in Szombatheley (Ungarn), in der Nähe einer Holzverarbeitenden Fabrik durchgeführt wurde und zehn Tage dauerte. Aufgrund des damaligen Entwicklungsstandes konnten nur die Analyten CO, NO und NO₂ mit der 2f-Wellenlängenmodulationsspektroskopie gemessen werden. Für die zweite Feldmessung wurde der Prototyp nahe einer stark befahrenen Straße in Wien aufgestellt und erneut die Schadstoffe CO, NO und NO₂ quantifiziert. Zusätzlich wurde die CO-Konzentration für 42 Stunden mit der Dispersions-basierten Messtechnik bestimmt und dessen Tauglichkeit für Umweltmessungen gezeigt.

Abstract

Measuring the ambient air quality is essential to guarantee a safe and healthy environment for the people living there. The pollutants and their maximum allowed concentration levels are regulated by the national governments and they are usually in accordance with the guidelines published by the World Health Organization. It is the task of local air quality networks and national departments to install suitable sensors at representative locations and to monitor the pollution caused by traffic, power plants and other anthropogenic sources. The equipment is often placed in mobile laboratories, cargo containers or local governmental buildings and each target analyte requires its dedicated hardware.

With the demand to reduce the size and operating costs, novel measurement concepts are evaluated to replace the highly optimized and specialized reference hardware. A promising technology is infrared spectroscopy, as all gaseous pollutants and greenhouse gases absorb within this spectral range of the electromagnetic spectrum. Subsequently, it is possible to combine the quantification of multiple gases in a single multi-analyzer unit and reduce the overall dimensions of the analytical devices. The aim of this thesis was to build a prototype that is capable to quantify the pollutants CO, NO, NO₂ and SO₂ in the ambient air. This has been achieved by combining commercially available Quantum Cascade Lasers, a multi-pass gas cell with 76 m optical path length and off-the-shelf infrared-detectors. To ensure optimum performance in the single-digit ppbv-range, the 2f-Wavelength Modulation Spectroscopy has been employed to quantify the analytes of interest.

As CO can easily reach concentrations in the single-digit ppmv-region, a technique that can cover a significantly higher linear range has been installed in the prototype as well. Heterodyne Phase Sensitive Dispersion Spectroscopy can easily be integrated into an existing 2f-Wavelength Modulation Spectroscopy-based setup and, again, only off-the-shelf components were used. While direct absorption based techniques rely on sensing the amplitude of the transmitted light, this one quantifies the concentration with a dispersion based technique. In particular, an optical three-tone-signal, emitted by the laser, is used to probe the dispersion, induced by the absorption

line of the analyte. The consequence is a more robust signal generation, especially at higher concentration levels.

Finally, the applicability of this prototype has been evaluated in the field during two measurement campaigns. The first one was located in Szombathely (HU), in vicinity to a wood-processing factory, and the performance has been investigated for ten days. Due to the development progress of the prototype, only CO, NO and NO₂ have been investigated with 2f-Wavelength Modulation Spectroscopy. The second campaign took place in Vienna (AT), next to a busy road, and the same analytes have been monitored for five weeks. In addition, CO has been quantified with a dispersion-based technique for 42 hours to prove its application in ambient air monitoring.

Acknowledgements

After spending years in the research group of Bernhard Lendl, it is time to say "Thank You" to the project partners, co-workers and friends for their contributions to my research topics at the TU Wien.

First of all, I would like to thank Bernhard for giving me the opportunity to investigate the various topics of Infrared Spectroscopy. Although it has been dominated by Quantum Cascade Lasers, different side projects required to work with Raman-Spectroscopy, classical Fourier-Transform-Infrared-Spectroscopy and filter-based techniques as well. His contacts to other research groups and the chemical industry made it possible to gain experience in fundamental research, to develop novel IR-based sensors and even to test and deploy them in real applications.

Special thanks go to J. Jeney and K. Gaal, the representatives of *Green Lab Hungary Engineering*, for initiating and financing this research project, and to K. Ronaszeghi, for the discussions about laser drivers, lock-in-amplifiers and infrared spectroscopy in general.

For the technical advises in the field of Wavelength Modulation Spectroscopy and Dispersion Spectroscopy, I would like to thank H. Moser and P. Martín-Mateos. Their help in the lab, the technical discussions and their skills in their research areas have been of significance for this project.

The work on the different setups and prototypes has often been interrupted by coffee-breaks, especially together with C. Gasser, G. Ramer, S. Tauber and K. Wieland. However, these breaks ended usually with technical discussions and led to useful ideas for the work in the lab.

Moreover, I would like to thank

- ... the numerous colleagues I have been working with in the group of B. Lendl:
K. Akhgar, A. Balbekova, B. Baumgartner, M. Brandstetter, E. Chrysostom, E. Gonzalez García, A. Dabrowska, F. Frank, S. Freitag, J. Hayden, D. Hermann, C. Koch,

J. Kuligowski, C. Kristament, P. Lendl, S. Lindner, L. Lux, D. Pinto, S. Radel, C. Reidl-Leuthner, W. Ritter, C. Santos, Z. Kubus-Schaden, A. Schwaighofer, D. Wacht, P. Wacławek, C. Wagner, B. Zachhuber and M. El-Zahry,

... the other researchers, technicians and co-workers at the TU Wien, I had to work with and learn from:

P. Ecker, J. Frank, M. Harasek, A. Huber, A. Kasper-Giebl, B. Kirchsteiger, M. Kistler, J. Lohninger, B. Lukitsch, A. Satzinger, C. Schwarzer, G. Strasser and W. Tomischko,

... and the employees of the *Municipal Department for Environmental Protection* (MA22) of Vienna for giving me access to the air quality measurement station at the Hietzinger Kai: R. Bacher, J. Ofner and H. Tizek.

Finally, I would like to thank my family, especially my parents Christa and Günter, for supporting my studies and my research activity at the TU Wien.

”Clean air is considered to be a basic requirement of human health and well-being. However, air pollution continues to pose a significant threat to health worldwide.”

World Health Organization

WHO Air quality guidelines for particulate matter, ozone, nitrogen dioxide and sulfur dioxide. 2005.



Die approbierte gedruckte Originalversion dieser Dissertation ist an der TU Wien Bibliothek verfügbar.
The approved original version of this doctoral thesis is available in print at TU Wien Bibliothek.

Contents

1. The Motivation for Ambient Air Monitoring	1
1.1. Reference Methods Used in Ambient Air Monitoring	2
1.2. Possibilities for New Air Quality Measurement Systems	5
2. Infrared Spectroscopy as an Alternative to Quantify Gases	9
2.1. Ro-Vibrational Spectroscopy of Gases	11
2.1.1. Rotation of Diatomic Molecules	11
2.1.2. Vibration of Diatomic Molecules	13
2.1.3. Improving the Models	13
2.1.4. Combining Rotation and Vibration	14
2.1.5. Polyatomic Molecules	17
2.1.6. Linewidth Broadening	18
2.2. Fourier Transform Infrared Spectroscopy	20
2.3. Semiconductor Lasers for the Mid Infrared	23
2.3.1. Quantum Cascade Lasers	24
2.3.2. Resonator and Wavelength Selection	25
2.4. Measurement Techniques and Quantification	29
2.4.1. The Beer-Lambert-Bouguer Law	29
2.4.2. Tunable Diode Laser Absorption Spectroscopy	30
2.4.3. Wavelength Modulation Spectroscopy	32
2.4.4. Heterodyne Phase Sensitive Dispersion Spectroscopy	37
2.4.5. Other Mid-IR based Techniques	41
3. Development of a Multi-Gas-Analyzer for Ambient Air Monitoring	45
3.1. Building Prototypes in General	45
3.2. Requirements and Target Analytes of the Gas Sensor	46
3.2.1. Spectral Ranges	47

Contents

3.3. Optical Setup	48
3.3.1. Lasers	49
3.3.2. Multipass Gas Cell	51
3.3.3. Detector	54
3.4. Electronics and Additional Components	55
3.4.1. Laser Driver and Demultiplexer	55
3.4.2. Temperature Control	57
3.4.3. Pressure Control	58
3.4.4. Modifications for HPSDS	59
3.5. Software	60
3.6. Mechanical Layout	65
4. Experiments and Results	69
4.1. Identifying the Optimum Laser Parameters	69
4.1.1. FTIR Spectra	69
4.1.2. Fine-Tuning the Laser Parameters and Modulation Depth	70
4.2. 2f-WMS Performance Under Laboratory Conditions	71
4.2.1. Calibration Curves	71
4.2.2. Allan-Werle Plot	75
4.3. Calibration Curves Recorded With HPSDS	75
4.4. Field Experiments	77
4.4.1. Szombathely - January 2019	79
4.4.2. Vienna - October and November 2019	80
5. Conclusion, Outlook	87
5.1. Achievements	88
5.2. Future Improvements	89
Bibliography	91
A. Simulated Gas Spectra	111
B. 1f-, 2f- and 3f-WMS-Spectra	115
C. Demultiplexer	117
D. Mechanical Parts, CAD Drawings	121

E. Results Vienna, October 22 - November 29, 2019	127
F. Scientific Publications on Infrared-Based Gas Sensing	131
G. Curriculum Vitae	195



Die approbierte gedruckte Originalversion dieser Dissertation ist an der TU Wien Bibliothek verfügbar.
The approved original version of this doctoral thesis is available in print at TU Wien Bibliothek.

1. The Motivation for Ambient Air Monitoring

Investigating the isotope ratios of elements or analyzing antarctic glacier ice that was formed millions of years ago, allows scientists to reconstruct the composition of the Earth's atmosphere back to 4 billion years ago. It reveals, that its composition has always been changing [1, 2] and had a significant impact on the evolution of all living things and the way how the earth looks like now.

With the first human settlements and getting stationary, mankind began to influence the environment. First the early Egyptians and later the Romans and Greeks had a heavy demand on fire wood, releasing significant amounts of CO, CO₂ and soot in the air. This pollution of the air has already been described by the Roman philosopher Seneca in AD 61 [3]:

As soon as I had gotten out of the heavy air of Rome and from the stink of the smoky chimneys thereof, which, being stirred, poured forth whatever pestilential vapors and soot they had enclosed in them, I felt an alteration of my disposition.

This famous quote is an important evidence of the long history of air pollution caused by humans. At the same time, also the first laws addressing the air quality were enacted, although their main focus was reducing the smell of decaying organic waste [4, 5].

Several hundreds of years later - to be accurate, in 1306 - another notable law/regulation addressing the air quality has been passed: King Edward I has prohibited burning coal while Parliament was in session [6, 7]. During the following centuries, the demand on refined metals and coal increased, and reached its next peak with the industrialization in the 18th century. The development of the steam engine was responsible for further increasing demand on mineral coal and industrialized cities were soon covered in smog.

With the development of the Otto- and the Diesel-engines and the mass production of cars in the early 20th century, the emission of NO and NO₂ (known as NO_x), and SO₂ began to

1. The Motivation for Ambient Air Monitoring

increase. The release of SO₂, which resulted from the oxidation of sulfur in fossil fuels, was the main reason for acid rain in central Europe. The changing pH of rain had severe effects on the vegetation and soil. Desulfurization of fossil fuels and the emitted flue gas improved the situation significantly and the SO₂ pollution is nowadays a minor issue.

Reducing the fuel consumption and optimizing the engines caused, as a consequence, higher combustion temperatures. Together with an increased oxygen content, not only the fuel gets oxidized but also the N₂ as well. Subsequently, NO_x are produced as well and an additional catalyst is required to limit its release into the ambient air. Compared to the emission of SO₂, NO_x causes less visible problems in the environment, but they are an important precursor for particulate matter and are supposed to cause respiratory diseases [8].

Although measuring and monitoring the ambient air quality is a global issue, it is regulated in local laws. In the European Union, the *Directive 2008/50/EC of the European Parliament and of the Council* ("Ambient Air Quality and Cleaner Air for Europe") [9] has to be implemented by each member state. It regulates, for example, the sampling points, the reporting, the data quality objectives and, most important, the limit values to ensure the protection of human health. The maximum allowed concentrations of the pollutants, averaging periods and tolerated number of exceedances are listed in Table 1.1.

Similar to this directive in the EU, the *Clean Air Act of 1963* is the pendant in the USA, the *National Clean Air Program, 2019* in India and the *Air Pollution Prevention and Control Law* (2000) is applied in China. Although individual numbers can differ, many of them are based on the *Air Quality Guidelines*, released by the World Health Organization [10].

1.1. Reference Methods Used in Ambient Air Monitoring

To guarantee Europe-wide comparable results, the directive defines reference methods for the ambient monitoring as well. They are European Standards and each pollutant has to be quantified with an optimized measurement technique, as listed in Table 1.2. The methods for gaseous pollutants, like CO, NO_x, O₃ and SO₂, are of special interest and are discussed further below.

1.1. Reference Methods Used in Ambient Air Monitoring

Pollutant	Limit Value	Averaging Period	Not to be exceeded more than
SO ₂	350 µg m ⁻³	One hour	... 24 times a calendar year
	125 µg m ⁻³	One day	... 3 times a calendar year
NO ₂	200 µg m ⁻³	One hour	... 18 times a calendar year
	40 µg m ⁻³	One calendar year	
Benzene	5 µg m ⁻³	One calendar year	
CO	10 mg m ⁻³	Maximum daily eight hour mean	
Pb	0.5 µg m ⁻³	One calendar year	
PM ₁₀	50 µg m ⁻³	One day	... 35 times a calendar year
	40 µg m ⁻³	One year	

Table 1.1.: Limit values for pollutants in the *Directive 2008/50/EC, Annex XI*

Pollutant	European Standard	Analytical method
SO ₂	EN 14212:2012	Ultraviolet fluorescence
NO and NO ₂	EN 14211:2012	Chemiluminescence
Pb	EN 14902:2005	Atomic absorption spectrometry, mass spectrometry
PM ₁₀	EN 12341:2014	Gravimetric
PM _{2.5}	EN 12341:2014	Gravimetric
Benzene	EN 14662:2005	Gas chromatography
CO	EN 14626:2012	Non-dispersive infrared spectroscopy
O ₃	EN 14625:2012	Ultraviolet photometry

Table 1.2.: Reference methods listed in the *Directive 2008/50/EC, Annex VI* (latest consolidated version: 18/09/2015).

1. The Motivation for Ambient Air Monitoring

Quantifying NO and NO₂

The quantification of NO and NO₂ in the ambient air is specified in the European Standard EN 14211:2012 [11] and is based on chemiluminescence, caused by the chemical reaction of NO and O₃. The ambient air passes a particle filter and enters a reaction chamber where O₃ is added. The O₃ is produced in a separate reactor either by ultraviolet radiation or by a high-voltage electric discharge and can oxidize the NO according to the following reactions:



The emitted photon ($h\nu$) is detected with a photo multiplier or a photodiode and the output signal is direct proportional to the NO concentration. To avoid additional pollution by releasing excessive O₃, a filter (e.g. activated carbon) is installed between the reaction chamber and the sampling pump.

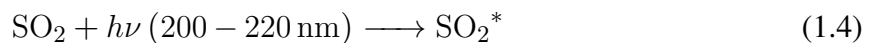
The NO₂ can be quantified with the same technique but requires an additional processing step. A converter is installed in the sample stream before the reaction chamber and reduces the NO₂ to NO, according to:



Typically, these converters are either heated furnaces made out of molybdenum, copper or stainless steel, or use photolysis to decompose the NO₂. The additionally produced NO is then measured together with the already present NO and the concentration is proportional to the difference of the signals measured with and without the converter.

Measuring SO₂ in the Ambient Air

The reference method for quantifying SO₂ in the ambient air is found in the European Standard EN 14212:2012 [12] and uses ultraviolet fluorescence to quantify the analyte. Particles and interfering substances (e.g. aromatic hydrocarbons) are removed from the sample stream with appropriate filters and the gas to be analysed is transported into the measurement cell. Light from an UV lamp passes an optical filter and is absorbed by the SO₂ molecules in the gas cell. After a certain lifetime, the excited molecules relax again and emit a photon at longer wavelength:



The fluorescence is measured with a photomultiplier and an additional detector can be used to compensate for intensity fluctuations of the UV lamp.

1.2. Possibilities for New Air Quality Measurement Systems

Quantification of CO

Another important parameter for evaluating the ambient air quality is the CO concentration. The reference method uses non-dispersive infrared spectroscopy and it is described in the European Standard EN 14626:2012 [13]. It relies on the wavelength dependent absorption of infrared radiation by diatomic hetero-atomic molecules and three different optical designs are suggested. They all have in common to suppress the cross-sensitivity with other gases such as H₂O, CO₂, N₂O and hydrocarbons.

Measuring O₃

According the European Union, O₃ has to be measured with an optical method and the specifications can be found in the European Standard EN 14625:2012 [14]. Here, UV light with 253.7 nm from a mercury discharge lamp passes an absorption cell and the attenuation caused by the presence of the analyte is detected with a photomultiplier detector or a photodiode.

1.2. Possibilities for New Air Quality Measurement Systems

The reference methods, that are recommended by the EU, are mechanically robust, easy to repair and ensure a high selectivity to other substances that occur in the ambient air. As neither the directive nor the European Standards define maximum mechanical dimensions of such equipment, many commercial sensors are designed to fit in 19" racks (48 cm width) for easier installation. Subsequently, device manufacturer can optimize their hardware to fulfill the previously listed requirements and are not required to miniaturize the dimensions of the hardware.

So far, equipment has been installed in dedicated measurement stations like 20ft-shipping containers, small trucks/transporters or in dedicated buildings. They are equipped with air conditioning, a calibration module and a computer system for data reporting and remote control. Considering the ongoing trend to investigate the air pollution and the emission of greenhouse gases in more detail, the number of measurement stations will increase and could benefit from smaller and cheaper hardware.

The regulation to use non-reference methods is given by the section B of the Annex VI of the directive 2008/50/EC. It says that a new method must produce results that are equivalent to the

1. The Motivation for Ambient Air Monitoring

reference methods and the Commission may require a report on the demonstration of equivalence. This means that the device performance should achieve similar detection limits and robustness to other substances in the ambient air.

With the possibility to develop hardware on other analytical techniques, one can identify two chances to optimize the costs:

- Employ cheaper sensors.
- Combine and simplify the hardware.

Sensors based on metal oxides are typical low cost devices and they are often combined to detect and quantify numerous substances. Different manufacturers are on the market and their cross-sensitivity depends on the individual metal oxides and their surface modifications [15–19]. Due to their low price, the small package and low power consumption, they are often combined with a data communication module and build a compact measurement node [20–31].

Although their small mechanical dimensions and the low price allow a dense monitoring network, these sensors are not perfectly suited for official measurements as they still show a significant cross sensitivity to other substances and do not comply with the air quality directive [32, 33]. Nevertheless, they can be used to identify general trends and fit perfectly in the topics Internet of Things and Citizen Science.

A more expensive, but more precise and robust technique, is infrared spectroscopy with laser sources. It allows to quantify gaseous, heteroatomic molecules with comparable detection limits as the reference methods and is subsequently a good candidate for being an equivalent measurement method according the directive *2008/50/EC*. Selecting the correct wavelength and reducing the pressure in the measurement cell makes interference-free measurements possible and one can even quantify multiple analytes with the same equipment by simply adding an additional laser source.

Within this thesis, the basics of ro-vibrational spectroscopy and the applied laser-based measurement techniques will be discussed. The implementation of these concepts is shown in a prototype that is capable to quantify the pollutants CO, NO, NO₂ and SO₂ and the green house gas N₂O. The requirements of the individual hardware components will be discussed and a fully assembled prototype will be presented. Its performance and applicability for ambient air measurements will be evaluated and the results of two measurement campaigns in Szombathely and Vienna will be shown.

1.2. Possibilities for New Air Quality Measurement Systems

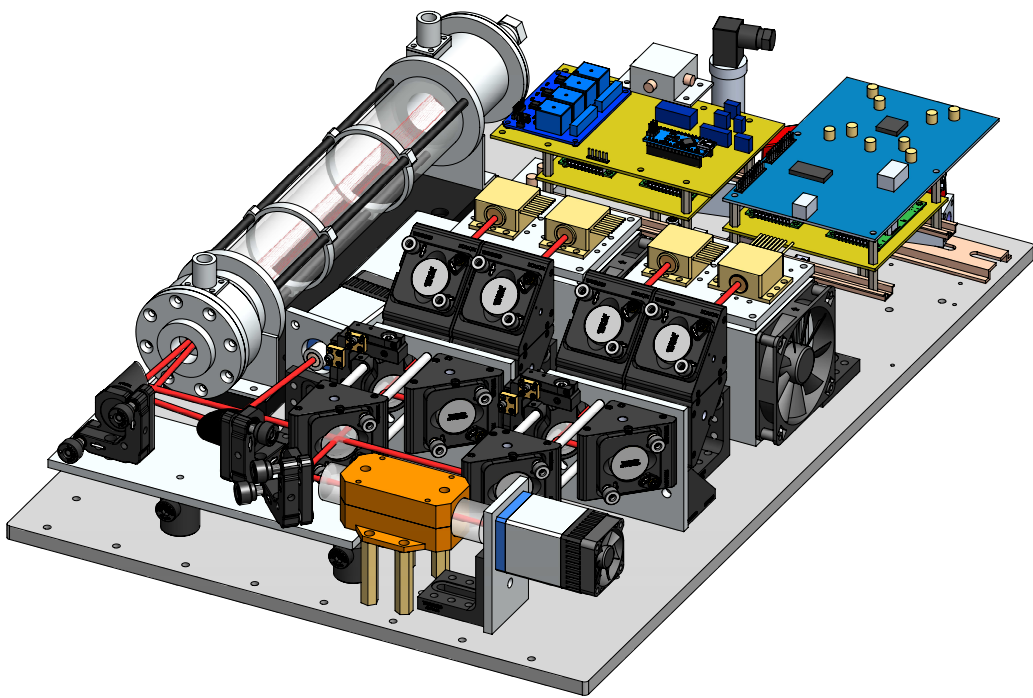


Figure 1.1.: Drawing of the optics rack of the prototype developed within this thesis.



Die approbierte gedruckte Originalversion dieser Dissertation ist an der TU Wien Bibliothek verfügbar.
The approved original version of this doctoral thesis is available in print at TU Wien Bibliothek.

2. Infrared Spectroscopy as an Alternative to Quantify Gases

A general view on science and technology reveals that many research fields, from astronomy, physics, chemistry and even medicine, rely nowadays on the interactions between matter and electromagnetic waves/photons. Investigating and having knowledge on how molecules, atoms and other particles interact with these waves allows, for example, to analyze the atmosphere of exoplanets [34–36], to observe chemical reactions in the femto-second-range [37, 38], or detect cancer [39, 40]. While these applications require an interaction between the wave and matter, other technologies, such as telecommunication [41–46] or certain physical experiments [47–49], try to avoid them to maximize the distance between repeaters or to minimize other signal disturbances.

It was Maxwell, who described the electromagnetic waves mathematically in 1865 [50], and these formulas belong to the most important ones in science. Originally, they consisted of twenty equations which have later been reduced to a group of four by Heaviside, Gibbs and Hertz. This set is nowadays known as the "Maxwell's equations" [51] and one can derive from these, in short, that electromagnetic waves consists of an electric and a magnetic field which oscillate and are also synchronized.

In practical terms for developing scientific equipment, the most important property of such an electromagnetic wave is the wavelength. As it travels through space, the wavelength is the spatial period of the wave and it defines the interaction with matter. In numbers, this practical range is ~ 15 orders of magnitude. Depending on the application and field of research, the wavelength is often expressed in other units, such as the frequency (Hz), energy (eV) or wavenumbers (cm^{-1}). The conversion is described with the Einstein-Planck relation:

$$E = h\nu = hc\tilde{\nu} = \frac{hc}{\lambda} \quad (2.1)$$

2. Infrared Spectroscopy as an Alternative to Quantify Gases

whereas E is the energy of the wave/photon, h the Planck constant, c the speed of light, ν the frequency, $\tilde{\nu}$ the wavenumber and λ the wavelength of the wave. This relation is visualized in Figure 2.1 whereas the different spectral ranges are labeled.

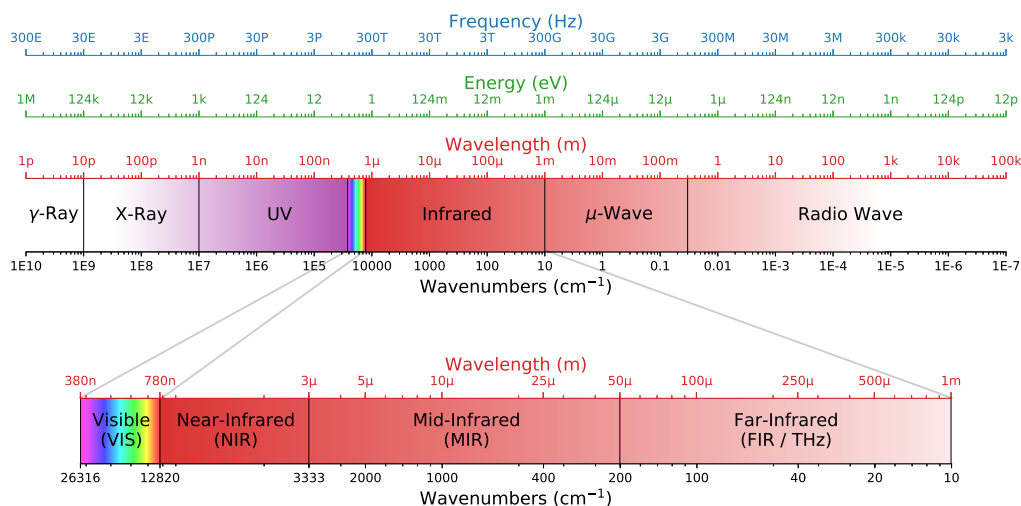


Figure 2.1.: An overview of the electromagnetic spectrum and different scales to express the energy of the resulting wave/photon. The labeled sections correspond to the type of interaction between an electromagnetic wave and atoms/molecules [52].

The individual ranges have different effects on atoms and molecules and, subsequently, other applications. Radio waves, for example, are mainly used for telecommunication, and require antennas to detect and emit them. In contrast, microwaves have a shorter wavelength which allows significant higher data rates. They already have sufficient energy to induce rotation in molecules with an electric dipole and can be used for heating. The following frequency region is the infrared and three important sub-ranges can be identified:

- The far-infrared is defined as the range between 50 μm and 1 mm, according to ISO 20473 [52], and is also known as THz region. The electromagnetic waves can cause the rotation of molecules or lattice vibrations.
- The mid-infrared lies between 50 μm and 3 μm . The fundamental vibration modes of molecular bonds and rotational-vibrational transitions are within this range and it can be seen as the most important one in infrared spectroscopy.
- The near-infrared, which closes the gap to the visible, spans from 3000 to 780 nm and excites overtones of vibrations.

The next higher energy range is the visible. Its frequency is high enough to excite electronic states in atoms and molecules and it corresponds to the human visual capacity. For the sake of

completeness, it is followed by the three ionizing radiation types ultraviolet, x-ray and γ -ray. Their energies are already sufficient high to remove electrons from the atomic shell which can cause severe damage to organic tissue at high doses.

2.1. Ro-Vibrational Spectroscopy of Gases

Quantifying the gaseous pollutants in the ambient air requires a technique that allows to measure molecule-specific properties. A reliable way is to probe the gas-sample with electromagnetic waves in the infrared and microwave regions. The mid-IR is perfectly suited as it can interact with the covalent bonds of molecules. Radiation is attenuated if the wavelength corresponds to the energy of certain molecular rotation or vibration. The main properties - the geometry, their distance, masses, charges and the forces between the involved atoms - define at which wavelength absorption can occur and where the radiation is transmitted. The basic concepts and their mathematical description for small molecules is summed up in the following subsections and is derived from literature [53–58].

2.1.1. Rotation of Diatomic Molecules

Heteronuclear diatomic molecules, such as CO and NO, show a dipole moment which is caused by the different particle charges (electrons, protons) of the individual atoms. In the case of CO, the carbon atom has a positive net charge, while the oxygen atom is negatively charged. This electrical dipole $\vec{\mu}$ is the sum of each charge q_i multiplied with its location in the coordinate system (\vec{r}_i):

$$\vec{\mu} = \sum_i q_i \vec{r}_i \quad (2.2)$$

If the condition $\vec{\mu} \neq 0$ is fulfilled, electromagnetic waves can interact with the molecule. For energies in the far infrared and micrometer range, the interaction will cause rotation of the molecule.

In classical mechanics, as shown in Figure 2.2, one would calculate the moment of inertia I for this rotation according the equation:

$$I = \sum_i m_i r_i^2 = \mu r_e^2, \quad \text{with} \quad \mu = \frac{m_1 m_2}{m_1 + m_2} \quad \text{and} \quad r_e = r_1 + r_2. \quad (2.3)$$

2. Infrared Spectroscopy as an Alternative to Quantify Gases

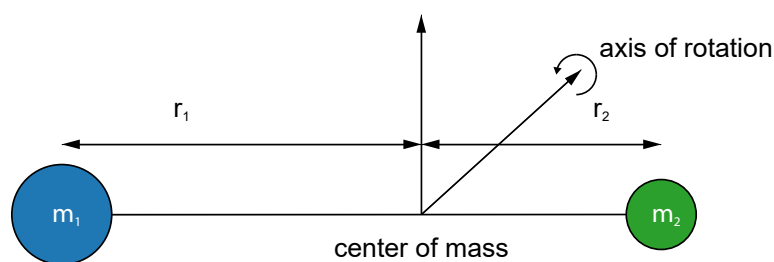


Figure 2.2.: Visualization of two different masses (m_1, m_2) rotating at constant distance ($r_e = r_1 + r_2$).

It is possible to describe the two-body problem of the masses m_1, m_2 with a single (reduced) mass μ rotating at the distance r_e . The corresponding angular momentum L is calculated by multiplying the moment of inertia I with the angular frequency ω_{rot} . Moreover, the rotational energy is calculated according:

$$E_{rot} = \frac{1}{2} I \omega_{rot}^2. \quad (2.4)$$

In quantum mechanics, however, the allowed values and directions for the angular momentum are quantized:

$$|I\omega_{rot}| = \frac{h}{2\pi} \sqrt{J(J+1)} \quad \text{and} \quad J = 0, 1, 2, 3, \dots \quad (2.5)$$

The quantum number J describes the total angular momentum and its values are integers. Similar to classical mechanics, the rotational energy is:

$$E_{rot} = \frac{1}{2} I \omega_{rot}^2 = J(J+1) \frac{h^2}{8\pi^2 I} = E_J \quad (2.6)$$

By expressing the energy in units of cm^{-1} and introducing the rotational constant $B = h/(8\pi^2 I c)$, one can simplify the equation:

$$F(J) = BJ(J+1) \quad (2.7)$$

So far, the only limitation is given by the quantized angular momentum. By introducing the Schrödinger equation to describe the phenomena of absorption/emission as transition probability, one yields another selection rule for rotational transitions:

$$\Delta J = J_{final} - J_{initial} = \pm 1 \quad (2.8)$$

The consequence is that the rotational quantum number must change by 1 when a pure rotational transitions takes place. Still assuming that the molecule behaves like a rigid rotor (RR), this leads to an evenly spaced absorption spectrum where the individual lines correspond to the quantized rotational transitions.

2.1.2. Vibration of Diatomic Molecules

A basic model for understanding the vibration of a chemical bond is given by the simple harmonic oscillator (SHO). Here, two atoms are connected with a spring and they oscillate around the equilibrium distance, as illustrated in Figure 2.3.

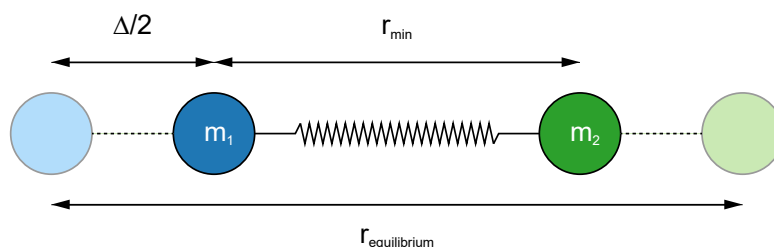


Figure 2.3.: The simple harmonic oscillator (SHO) consists of two masses that are connected with a spring and oscillate.

The force F between the atoms depends on the spring constant k_s , the distance r and the equilibrium distance r_e according to:

$$F = k_s(r - r_e). \quad (2.9)$$

The corresponding fundamental resonance frequency ν_{vib} is a function of the spring constant and the reduced mass μ :

$$\nu_{\text{vib}} = \frac{1}{2\pi} \sqrt{k_s/\mu} \quad \text{with} \quad \mu = \frac{m_1 m_2}{m_1 + m_2} \quad (2.10)$$

For practical reasons, the frequency ν_{vib} can be written in wavenumbers, according to $\omega_e = \nu_{\text{vib}}/c$. By introducing the vibrational quantum number $\nu = 0, 1, 2, 3, \dots$, one can then describe the energy of a vibrating diatomic molecule with:

$$G(\nu) = \omega_e(\nu + 1/2) \quad (2.11)$$

2.1.3. Improving the Models

Rotation

The rigid rotor is a very basic idea derived from classical and quantum mechanics but it does neither compensate the vibrational stretching nor the centrifugal distortion. To take those into account, the formula $F(J) = BJ(J + 1)$ is extended as follows:

$$F_\nu(J) = B_\nu J(J + 1) - D_\nu J^2(J + 1)^2 \quad (2.12)$$

2. Infrared Spectroscopy as an Alternative to Quantify Gases

Here, B_ν is the vibrationally dependent rotational constant (indicated with the index ν) and D_ν is the centrifugal distortion constant. They depend on the vibrational quantum number according:

$$B_\nu = B_e - \alpha_e(\nu + 1/2) \quad (2.13)$$

$$D_\nu = D_e + \beta_e(\nu + 1/2) \quad (2.14)$$

Vibration

The presence of anharmonic oscillations in a vibration can be compensated by improving the primitive model of the SHO with a Taylor series:

$$G(\nu) = \omega_e(\nu + 1/2) - \underbrace{\omega_e x_e(\nu + 1/2)^2}_{\text{anharmonicity corr.}} + \dots + H.O.T. \quad (2.15)$$

The quadratic term is also known as the anharmonicity correction with its corresponding constant x_e . This adjustment has two consequences: First, the energy differences between two energy levels is no longer constant and it decreases for higher values of ν . Second, the selection rule for vibrational quantum numbers allows additional values for $\Delta\nu$, namely integers ≥ 2 . This means that not only fundamental vibrations can be excited, but overtones as well. However, their transition probabilities are ten to hundred times smaller and the required energies lie in the NIR range.

Instead of describing the potential energy with a quadratic function, it is recommended to replace it with the Morse function:

$$U = D_{eq} \left[1 - e^{-\alpha(r-r_e)} \right]^2 \quad (2.16)$$

The potential energy U depends on the bond-dissociation energy D_{eq} , the displacement $r - r_e$ from the equilibrium distance r_e between the atoms and the constant α . The improved model describes the propulsion of the atoms at lower distances significantly better and allows the dissociation of the bond (Figure 2.4).

2.1.4. Combining Rotation and Vibration

So far, the concepts of rotation and vibration have been discussed separately. However, these two models have to be combined to understand the absorption spectra of molecules and the simplest model can be derived from the Born-Oppenheimer approximation. Assuming, that both

2.1. Ro-Vibrational Spectroscopy of Gases

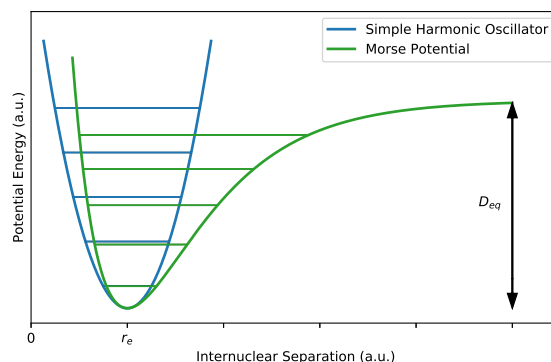


Figure 2.4.: Illustration of the potential energy of an SHO (without anharmonicity correction) and the more precise Morse potential (with the correction term). One can clearly see the constant (SHO) and decreasing differences (Morse potential) of the energy levels, caused by the additional correction term.

phenomena are independent and the total energy is the sum of the energy for the rigid rotor and the SHO, allows to denote the following equation:

$$T(\nu, J) = E_{RR} + E_{SHO} = F(J) + G(\nu) = BJ(J + 1) + \omega_e(\nu + 1/2) \quad (2.17)$$

Together with the selection rules for $\Delta\nu$ and ΔJ , one can calculate the rovibrational transitions in a diatomic heteronuclear molecule. Figure 2.5a shows the Morse potential with the rovibrational energy levels in the ground state and an excited electronic state. The possible transitions for ($\nu = 0 \rightarrow \nu = 1, J_{initial} = 0, 1, \dots, 5$) of the ground state are illustrated in Figure 2.5b. The vectors are grouped by the value of ΔJ and the forbidden transition $\Delta J = 0$ is plotted too, but indicated by the dashed lines.

A more precise way to describe the rovibrational energy levels is to compensate for the anharmonicity and the non-rigid rotation:

$$T(\nu, J) = G(\nu) + F(\nu, J) \quad (2.18)$$

$$= \underbrace{\omega_e(\nu + 1/2)}_{\text{SHO}} - \underbrace{\omega_e x_e(\nu + 1/2)^2}_{\text{anharmon. corr.}} + \underbrace{B_\nu J(J + 1)}_{\text{RR}(\nu)} - \underbrace{D_\nu J^2(J + 1)^2}_{\text{centrifugal dist.}} \quad (2.19)$$

An exemplary section of the rovibrational spectrum of CO is shown in Figure 2.6 where the line strengths of the absorption lines of the fundamental vibration $\Delta\nu = 1$ are plotted. One can clearly identify the two regions of the transitions with $\Delta J = -1$ and $\Delta J = +1$. Moreover, the space between individual lines is increasing towards smaller wavenumbers, which is caused by the non-rigid rotation of the molecule.

2. Infrared Spectroscopy as an Alternative to Quantify Gases

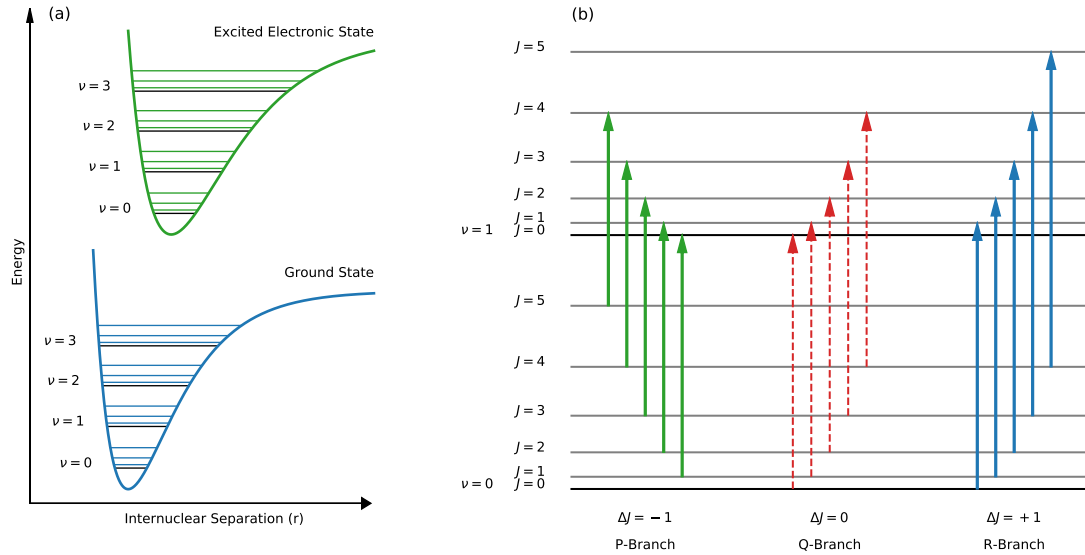


Figure 2.5.: (a): Illustration of the Morse potential and the corresponding ro-vibrational energy levels in the ground and excited electronic states. (b): For a diatomic molecule, such as CO, only transitions with $j = \pm 1$ are allowed. The forbidden Q-Branch is indicated with dashed arrows.

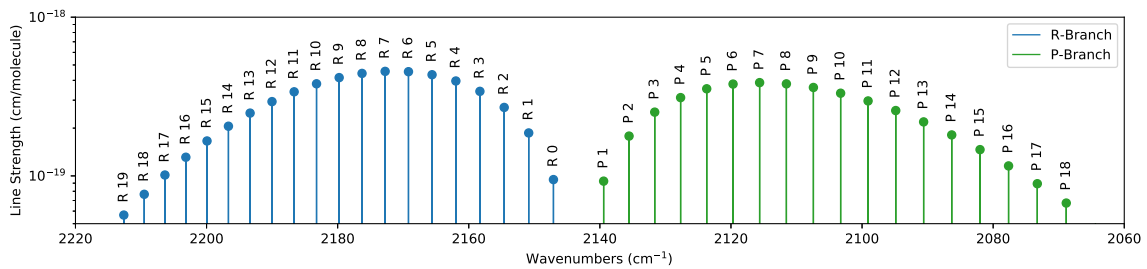


Figure 2.6.: Visualization of the characteristic P and R branch of the fundamental vibration of CO. The numerous absorption lines are caused by the rotational transitions of the molecule. The corresponding values are derived from the database *HITRAN2016* [59, 60].

2.1.5. Polyatomic Molecules

The concept to describe rovibrational spectra of polyatomic molecules is similar to the diatomic model. As the number of atoms, and subsequently the complexity of the system increases, it is necessary to adjust or extend the selection rules for most molecules. In short, the consequence is that additional vibrations are allowed and the space between rotational energy levels decreases. An example for these vibrations is illustrated in Figure 2.7 where the different vibrations for CO_2 are shown. While the asymmetric stretching and the symmetric bending are IR active, the electric dipole moment is $\vec{\mu} = 0$ for the symmetric stretching and therefore not present in IR spectra.

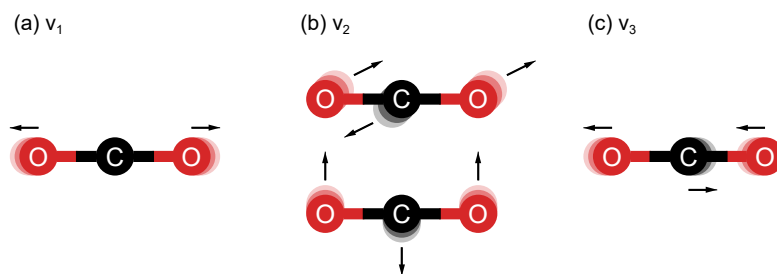


Figure 2.7.: Visualization of the vibrational modes of CO_2 . (a): symmetric stretching mode that is not IR-active ($\nu_1 = 1330 \text{ cm}^{-1}$), (b): the degenerate symmetric bending ($\nu_2 = 667 \text{ cm}^{-1}$) and (c): the asymmetric stretching ($\nu_3 = 2349 \text{ cm}^{-1}$), adopted from [53].

Under certain conditions, the Q branch of a vibration can also be present. This leads, together with the narrow line spacing, to a more complex infrared spectrum which is also illustrated in Figure 2.8. It shows the vibration ν_3 of the molecule CH_3Cl (stretching of $\text{C}-\text{Cl}$) and one can clearly identify the additional lines between the P and R branches. [54, 57]

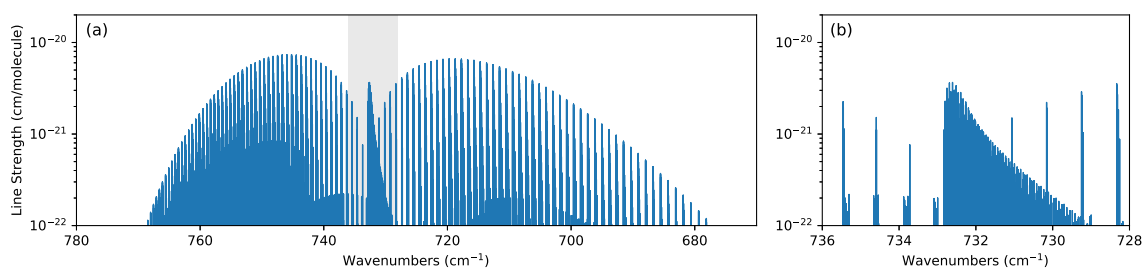


Figure 2.8.: (a): Visualization of the rovibrational lines of CH_3Cl of ν_3 . The grey area indicates the Q branch which is plotted in detail in (b).

2. Infrared Spectroscopy as an Alternative to Quantify Gases

2.1.6. Linewidth Broadening

The theoretical discussion of rovibrational spectra lets assume that absorption occurs only if the electromagnetic wave has exact the required energy to excite a certain transition. In reality, however, this is not the case and three important phenomena are responsible that IR spectra of gases do not consist of perfect lines and are rather be described with line functions.

Natural Broadening

The first broadening effect arises from the Heisenberg Uncertainty Principle. It allows to relate the uncertainty in energy (ΔE_i) of a specific state i with its lifetime τ_i , according:

$$\Delta E_i \tau_i \geq \frac{h}{2\pi} \quad (2.20)$$

The consequence is, that the energy difference, which corresponds to the transition, is also not exact and therefore broadened. The Full Width at Half Maximum (FWHM) of natural broadening can be calculated from the lifetimes of the two states τ' and τ'' :

$$\Delta\nu_N = \frac{1}{2\pi} \left(\frac{1}{\tau'} + \frac{1}{\tau''} \right) \quad (2.21)$$

Assuming that the atomic system behaves like a damped oscillator, one can use the Lorentzian function, centered at ν_0 , to describe the resulting line shape $\Phi_L(\nu)$:

$$\Phi_L(\nu) = \frac{1}{2\pi} \frac{\Delta\nu}{(\nu - \nu_0)^2 + \left(\frac{\Delta\nu}{2}\right)^2} \quad (2.22)$$

Collision Broadening

While the natural broadening can be explained with a single molecule, this effect is caused by the collision with other molecules. Energy can be transferred between the involved species, reducing the lifetime of a specific energy state and leads, subsequently, to a broadened absorption line. From the optical collision diameters σ_A and σ_B of two gases, the temperature T and the Boltzmann constant k , one can derive the number of collisions (Z_{AB}) per second for a single molecule B with all (n_A) molecules of A , according:

$$Z_{AB} = n_A \pi \sigma_{AB} \bar{c} \quad \text{with} \quad \sigma_{AB} = \frac{1}{2}(\sigma_A + \sigma_B) \quad \text{and} \quad \bar{c} = \left(\frac{8kT}{\pi\mu_{AB}} \right)^{1/2} \quad (2.23)$$

2.1. Ro-Vibrational Spectroscopy of Gases

For a gas mixture with more than two components, one can introduce the ideal gas law $P = nkT$ with the mole fraction X_A and build the sum of all components:

$$Z_B = P \sum_A X_A \pi \sigma_{AB}^2 \left(\frac{8}{\pi \mu_{AB} kT} \right)^{1/2} \quad (2.24)$$

From the relation $\Delta\nu = \frac{1}{2\pi} (1/\tau' + 1/\tau'')$ and $Z_B = 1/\tau' = 1/\tau''$, the FWHM caused by the collisional broadening is written as:

$$\Delta\nu_C = Z_B/\pi = P \sum_A X_A 2\gamma_{AB} \quad \text{with} \quad 2\gamma_{AB} = 1.013 \times 10^6 \sigma_{AB}^2 \left(\frac{8}{\pi \mu_{AB} kT} \right)^{1/2} \quad (2.25)$$

Here, $2\gamma_{AB}$ is the broadening coefficient of the gas B interacting with another gas A . Depending on the application, this complex system can be simplified and only the collisions of the species B itself (also known as self-broadening) and the dilutant (e.g. N_2) are taken into account. To compensate the temperature, one can extrapolate the value of γ from a reference value (γ_{T_0} at temperature T_0), according the following equation:

$$2\gamma(T) = 2\gamma_{T_0} \left(\frac{T_0}{T} \right)^n \quad (2.26)$$

Typical values for 2γ are $\approx 0.1 \text{ cm}^{-1}$ at room temperature and 1 atm, and $n = 0.5$ can be used for temperature compensation.

Doppler Broadening

This type of line broadening arises when atoms or molecules have a velocity component in the same direction as the electromagnetic wave. It is caused by the Doppler effect and shifts the frequency where absorption will occur to either higher or lower wavelength. The velocities of molecules in a gas are described with the Maxwell velocity distribution and the resulting line shape $\Phi_D(\nu)$ can be written with a Gaussian function:

$$\Phi_G(\nu) = \frac{2}{\Delta\nu_D} \left(\frac{\ln 2}{\pi} \right)^{1/2} \exp \left[-4 \ln 2 \left(\frac{\nu - \nu_0}{\Delta\nu_D} \right)^2 \right] \quad (2.27)$$

Again, the curve is centered at ν_0 and the FWHM $\Delta\nu_D$ follows the equation:

$$\Delta\nu_D = \nu_0 \left(\frac{8kT \ln 2}{mc^2} \right)^{1/2} = \nu_0 (7.1623 \times 10^{-7}) \left(\frac{T}{M} \right)^{1/2} \quad (2.28)$$

whereas M is the molar mass, in the unit g/mol.

2. Infrared Spectroscopy as an Alternative to Quantify Gases

Voigt Profile - Combination of Doppler and Collisional Broadening

In many cases it is sufficient to approximate the line shape of an absorption line with either a Lorentzian or a Gaussian line shape, depending which FWHM is dominating. For the situation that the Doppler and the collisional broadening contribute similar ($\Delta\nu_D \sim \Delta\nu_C$), one can use the convolution of the Lorentz and the Gaussian function, that is also known as Voigt profile:

$$\Phi_V(\nu) = \Phi_D(\nu) * \Phi_C(\nu) = \int_{-\infty}^{+\infty} \Phi_D(u)\Phi_C(\nu - u)du \quad (2.29)$$

The basic idea behind the Voigt profile is that each velocity, defined by the Gaussian function, has its own Lorentz line shape, indicated with the integration over the shift from the line center u . With the parameters a , w and y , according

$$a = \frac{\sqrt{\ln 2}\Delta\nu_C}{\Delta\nu_D}, \quad w = \frac{2\sqrt{\ln 2}(\nu - \nu_0)}{\Delta\nu_D}, \quad y = \frac{2u\sqrt{\ln 2}}{\Delta\nu_D} \quad (2.30)$$

one can mathematically describe the Voigt profile with the equation

$$\Phi_V(\nu) = \Phi_D(\nu_0) \frac{a}{\pi} \int_{-\infty}^{+\infty} \frac{\exp(-y^2)dy}{a^2 + (w - y)^2} = \Phi_D(\nu_0)V(a, w) \quad (2.31)$$

whereas $V(a, w)$ is the famous Voigt function.

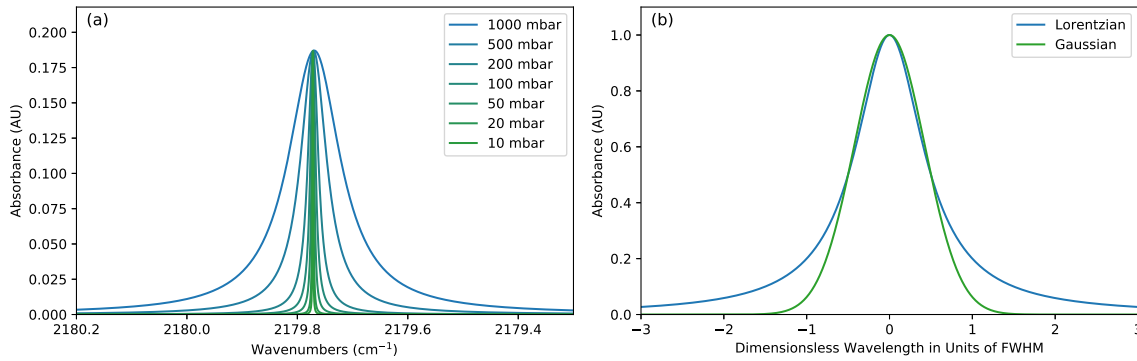


Figure 2.9.: (a): Simulation of an absorption line of CO at different pressures ($c = 1$ ppmv, $L = 76$ m, $T = 23$ °C and Lorentzian line shape). (b): Comparison of the Lorentzian and Gaussian line shape with FWHM = 1.

2.2. Fourier Transform Infrared Spectroscopy

Investigating the composition of an unknown sample (gaseous, liquid or solid) with an infrared based technique requires equipment that is capable to measure the wavelength dependent absorption with sufficient precision. While spectrometers for the UV, VIS and NIR region employ

2.2. Fourier Transform Infrared Spectroscopy

an optical grating to resolve the spectral components of a broadband light source, most infrared spectrometers are based on an interferometer. Typically, they use a scanning Michelson interferometer, as visualized in Figure 2.10a.

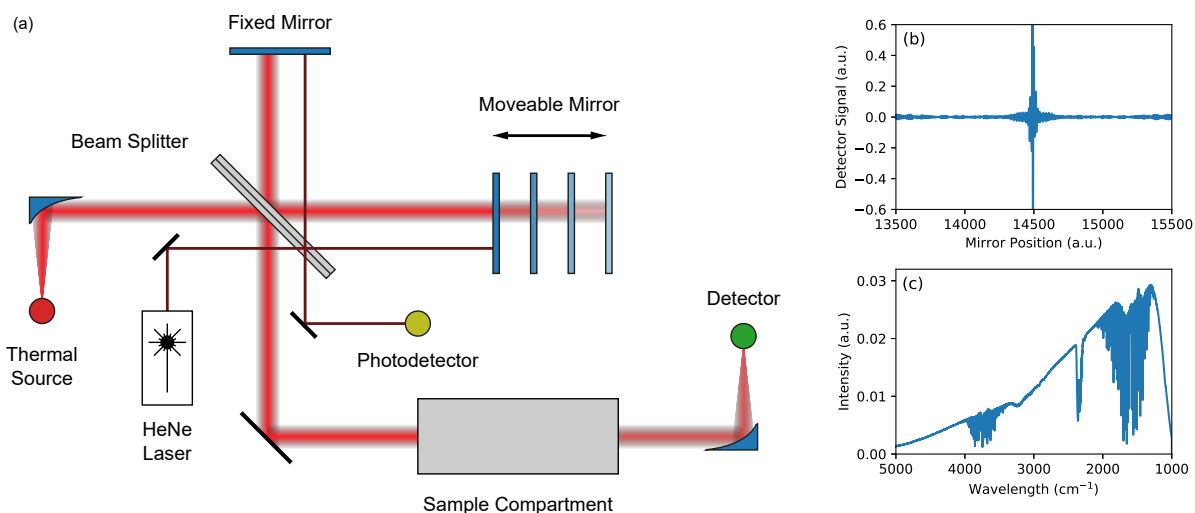


Figure 2.10.: Illustration of a Michelson Interferometer (a). The interferogram (b) is recorded by measuring the detector intensity at different mirror positions. Applying the Fourier Transformation on the interferogram leads to the single channel spectrum, as shown in (c).

Instead of measuring the intensity for each wavelength consecutively, Fourier Transform Infrared (FTIR) spectrometers detect all optical frequencies simultaneously and reconstruct the desired spectrum. To do so, the blackbody radiation of a broadband IR source is collimated and a beam splitter diverts it into two beams with same intensity. One beam is reflected at a fixed, the other one at a movable mirror. Both waves are combined again at the beam splitter, redirected to the sample to be analyzed and finally focused towards an IR detector, like a liquid N₂ cooled Mercury-Cadmium-Telluride (MCT) detector.

The principle of the Michelson interferometer is explained best with a collimated, monochromatic light source with the wavelength λ : one beam from the beam splitter travels to the fixed mirror, gets reflected and can interfere with the second beam. If the path length to the second mirror is identical to the first one, the phase difference will be 0° and the beams interfere constructively and cause maximum signal at the detector. The same intensity will be detected if the mirror position is changed by $\lambda/2$, as the phase difference is $360^\circ = 0^\circ$. Destructive interference will occur if the recombining waves show a phase shift of 180° and result in zero intensity at the detector. In reality, the light source emits a continuous spectrum, and constructive/destructive interference will occur simultaneously. Measuring the detector signal at different mirror positions results in an interferogram that contains the spectral information. Applying the Fourier Transformation on

2. Infrared Spectroscopy as an Alternative to Quantify Gases

this signal leads to the infrared spectrum, as shown in Figure 2.10b and c . It should be noted here, that the maximum optical path difference d_{MOPD} of the two interferometer arms is often the resolution limiting parameter of an FTIR spectrometer [61]. The relation is derived from the finite length of the interferogram and, if other optical effects like the aperture, are ignored, the spectral resolution $\Delta\tilde{\nu}_{FWHM}$ is calculated according:

$$\Delta\tilde{\nu}_{FWHM} = \frac{1.207}{2d_{MOPD}} \quad (2.32)$$

Although such an interferometer based spectrometer is significant more complex than a simple grating or prism based one, it has several advantages too [62]. First of all, the signal to noise ratio (SNR) is better than in dispersive spectrometers, which analyze one wavelength after another (or pixel by pixel). The Michelson interferometer, in contrast, detects the information of all wavelengths simultaneously but encoded in the interferogram. This effect is also known as **Fellgett advantage** [63].

The **Jacquinot advantage** [64] arises from the fact that Michelson interferometers no longer require an input slit before the monochromator. Subsequently, the energy throughput is higher and improves the SNR.

The third one, also known as **Connes advantage** [65], is traced back to installing an additional laser in the interferometer. Usually, this is a HeNe laser and acts as the wavelength reference for recording the interferogram. Originally, the zero crossings of this reference interferogram were used to trigger the data acquisition of the IR detector signal. With improved analog to digital converters (ADCs), both, the photodiode for the HeNe laser and the IR detector, are digitized simultaneously at much higher sampling rate and allow precise extrapolation for the correct retardation values.

The FTIR spectrometer is the workhorse in IR spectroscopy and can be found in various applications such as process analytics, quality control or research [66–69]. Depending on the analyte to be measured and its state, one has to find a trade-off between its price, robustness, physical dimensions and the spectral resolution. Liquids or solids, for example, show rather broad absorption lines in the mid-IR and a spectral resolution of $1\text{--}4\text{ cm}^{-1}$ is often sufficient. Subsequently, a physically smaller interferometer can be chosen and installed in a compact or extra-rugged case. If, in contrast, the desired application is to investigate and measure the ro-vibrational absorption lines of gases, a resolution $\leq 0.1\text{ cm}^{-1}$ is required. To achieve this, the maximum optical path difference of the interferometer must be increased and the quality and precision of the other optical elements have to support this as well. Due to the physical

dimensions, state-of-the-art FTIR spectrometers are typically installed in research facilities and barely found in industrial environments.

2.3. Semiconductor Lasers for the Mid Infrared

The classical concept to combine a thermal/broadband light source, such as a tungsten lamp or a Globar, and a spectrometer/interferometer is a very flexible one but it comes with disadvantages like limited spectral resolution, insufficient signal to noise ratio or mechanically complex designs. If the measurement equipment is intended to be used for a specific and defined application, one can try to optimize the setup by replacing the light source and simplifying the optical components. One could profit from a reduced maintenance time as less mechanical parts are required, a higher precision could be achieved, and compact dimensions would also help to optimize the hardware costs.

The development of innovative light sources during the last decades provides the technology to develop new instruments for process analytics and environmental monitoring. The most important one is the diode laser and the first devices were published in 1962 [70–72]. They emitted in the NIR and VIS and were made out of GaAs-diodes. Compared to already developed gas (HeNe) and solid state lasers (ruby), the photons for pumping the laser are generated in the gain element and a flashlamp for pumping the laser is no longer required. An electrical current allows the electrons and holes in the diode to recombine and the energy of the photon corresponds to the band gap. Subsequently, the emitted wavelength can be slightly tuned by varying the semiconductor material.

Very soon after the first demonstration of electrically pumped semiconductor laser diodes, infrared lasers based on InAs and InSb [73, 74] have been presented. The devices emitted at 3.1 μm and 5.2 μm , required cooling with liquid helium and a pump current of several amperes. One year later, in 1964, the wavelength region was extended to 8.5 μm by switching to the material systems PbTe and PbSe. In the following years, this laser type, also known as lead-salt laser, emerged to useful light sources in infrared spectroscopy and has also been implemented in numerous gas sensors [75–80]. Although room temperature operation at reasonable optical output powers [81] and continuous wave (cw) mode has been achieved [82], they have been superseded by a significantly more flexible laser technology - the Quantum Cascade Laser.

2. Infrared Spectroscopy as an Alternative to Quantify Gases

2.3.1. Quantum Cascade Lasers

A different approach for building infrared lasers was proposed by Kazarinov and Suris in 1971 [83] and is nowadays known as Quantum Cascade Laser (QCL). As the band gaps of typical semiconductor materials is higher than the energy of infrared photons, the idea was to modify the conduction band. This should be realized with alternating nm-thick layers where the electrons could tunnel through the created barriers and, as the following quantum well is of lower energy, a photon would be emitted (*active region*). A basic illustration of modified conduction band is shown in Figure 2.11b and the calculated energy levels of a real QCL can be seen in Figure 2.12. Generating the photon with the correct wavelength/energy is one challenge in developing such a laser. Another requirement is to achieve the population inversion, which occurs when more members of a system are in a higher/excited state than members in the lower energy state. In the case of QCLs, this means that more electrons must be in the upper lasing level than in the lower lasing level. To solve this, the active region is followed by a miniband which depopulates the lower lasing level. In the same way, this zone fills the upper lasing level of the following active region and it is therefore known as *injector*. Another unique property results from the fact that the photons are produced in the conduction band: As the electrons do not recombine with the corresponding holes, the charge carriers can be reused and emit multiple photons, by repeating the growth sequence of the injector and the active region multiple times. Subsequently, the optical output is increased and enables a higher efficiency.

It took more than 20 years, until the first working Quantum Cascade Laser (QCL) was demonstrated in 1994 [84] and it was achieved by growing alternating layers of InGaAs/InAlAs on an InP wafer. Like the first NIR and lead salt laser, it had to be operated in pulsed mode and required liquid N₂ for cooling. Since then, numerous improvements, such as cw operation [85, 86], or extra wide gain ranges have been presented [87–89]. It should be noted here, that growing the quantum cascade on a suitable substrate wafer is still a challenge. Two processes, namely the Molecular Beam Epitaxy (MBE) [90, 91] and the Metal Organic Vapor Phase Deposition (MOVPE) [92, 93], are suited to deposit the nm-thick layers with the required precision. Additional cladding layers, encapsulating the typically 25–30 periods of the active region, and growing calibration samples in the reaction chamber decreases the possible output of the wafer production. Further improvements in the field of QCLs are the topics of book chapters and extended review papers, such as [88, 94–101].

2.3. Semiconductor Lasers for the Mid Infrared

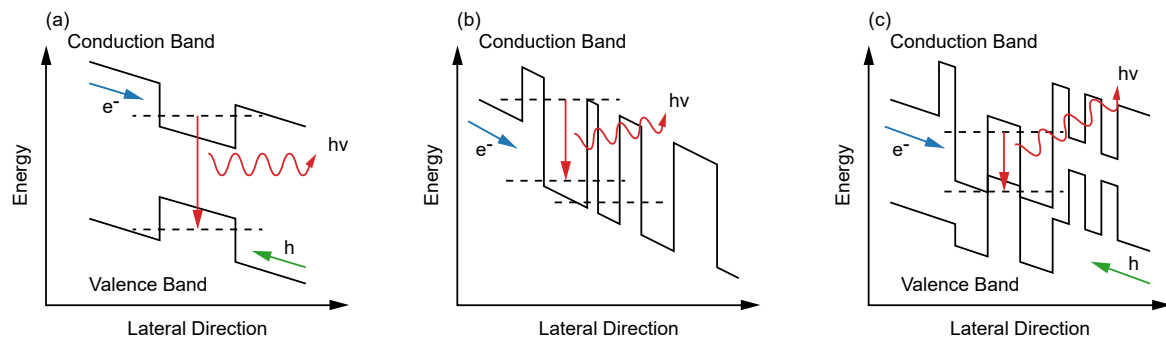


Figure 2.11.: Comparison of three different semiconductor lasers: conventional diode lasers (a) produce photons in the VIS and NIR by recombining electrons with holes. Quantum Cascade Lasers (b), in contrast, emit photons in the mid-IR by modifying the conduction band. Interband Cascade Lasers (c) combine both techniques and allow a lower threshold current.

2.3.2. Resonator and Wavelength Selection

Producing photons in the mid-IR and achieving population inversion are two requirements for a working QCL. Another one is amplifying the light in a cavity. In the case of a gas laser, such as a HeNe-laser, the dimensions of the resonator are clearly defined by the gas cell and the highly reflective mirrors. Semiconductor lasers require such a confinement as well and this is typically realized by etching a waveguide structure into the wafer. Different geometries are available, and most QCLs are based on linear ridge-type waveguides.

Depending on the spectral requirements and the later application of the QCL, additional processing steps or mechanical parts can be used to meet the specifications. These modifications have a significant impact on the spectral emission of the laser and are discussed in detail.

2.3.2.1. Fabry-Pérot Cavity

Manufacturing a Fabry-Pérot (FP) QCL from a suitable substrate wafer requires etching of a ridge waveguide, depositing an insulation layer, such as Si_3N_4 , and evaporating/sputtering a contact layer (e.g. gold). The front and backside of the ridge can either be cleaved or milled with Focused-Ion-Bombardment (FIB) [108] and act as highly reflective mirrors. If emission from only one facet is required, one can deposit a highly-reflective coating on the back, and an anti-reflective coating on the front side [109–112]. A schematic illustration of an FP-QCL is shown in Figure 2.13.

2. Infrared Spectroscopy as an Alternative to Quantify Gases

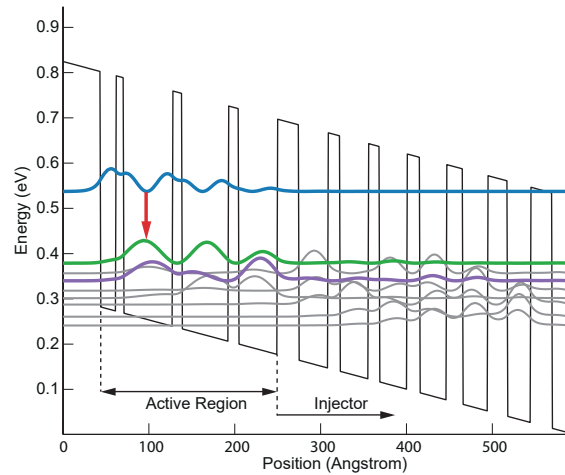


Figure 2.12.: Energy levels of a quantum cascade calculated with the software tool *ErwinJR* [106, 107]. The blue and green levels are the upper and lower lasing state. The purple curve represents the first level of the injector (other levels in gray).

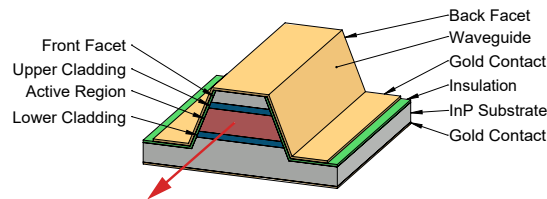


Figure 2.13.: The waveguide of an FP-QCL is achieved by etching the wafer with common semiconductor processes. The facets at the front and at the back correspond to the highly reflective mirrors in a conventional gas laser. The red arrow indicates the direction of the laser beam.

Although this laser type is simple to manufacture, it is rather unsuited for developing precise sensors. Devices emit at several frequencies simultaneously which is caused by the Fabry-Pérot cavity [113]. It amplifies all wavelengths (λ) that are a fraction (m) of the cavity length (L), according $\lambda = 2n_{\text{eff}}/mL$. The refractive index of the waveguide has to be considered in the equation as well, which is typically $n_{\text{eff}} \sim 3.1$. As this property depends on the temperature, the emitted wavelength range can be adjusted a few wavenumbers by changing the temperature of the gain chip. They have been successfully integrated in liquid [114–118] and gas phase sensors [119, 120], but their multi-mode emission makes them rather unsuited for precise ambient air sensors.

2.3.2.2. External Cavity

The External-Cavity (EC) design is based on an FP-QCL and employs an external optical grating to reduce the number of emitted wavelengths, as shown in Figure 2.14. One distinguishes the *Littrow* [121, 122] and *Littman-Metcalf* [123, 124] configuration which have different approaches to create a feedback to the gain element and to amplify a certain wavelength. Tuning is achieved by either rotating the grating with a motor (piezo [125], stepper [126], micro-opto-electro-mechanical systems [127]), alternating its periodicity [128] or adjusting the angle of the feedback mirror [129]. Mode-hop-free operation and cw emission have been demonstrated as well [130] and the tunable range has been increased over the years significantly. While the first devices could cover $\approx 33 \text{ cm}^{-1}$ [131], a few years later a tuning range $\geq 430 \text{ cm}^{-1}$ has been achieved [87]. Their application in various research fields has been shown, ranging from the gas phase [126, 132, 133], to sensing liquids [134, 135] up to solid phase measurements [136].

Despite their outstanding properties, EC-QCLs are barely found in gas sensors. Several reasons can be identified, such as the limited number of manufacturers, the presence of mechanical components for the wavelength selection, difficulties in mode-hop stability and the mechanical dimensions in general.

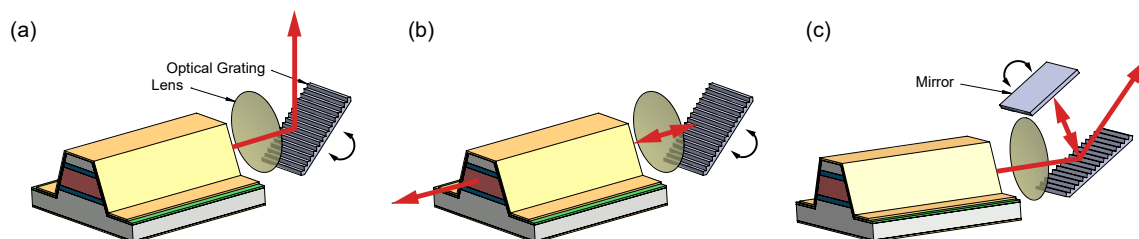


Figure 2.14.: Three typical configurations of an EC-QCL. (a): Littrow, (b): Rear-Littrow, (c): Littman-Metcalf configuration. The red arrow indicates the beam path.

2.3.2.3. Distributed Feedback Cavity

A different approach to achieve single-mode emission of a QCL is etching the optical grating into the waveguide. This has been presented for the first time in 1997 [137] and the manufacturing process is similar to a conventional FP-QCL. The grating, however, can either be etched at the top (illustrated in Figure 2.15a) or into the side walls [138] of the waveguide or buried within [139–142]. The desired emitted wavelength must be, of course, within the gain range of the laser

2. Infrared Spectroscopy as an Alternative to Quantify Gases

material, and the required grating period Λ for a specific wavelength λ is calculated according:

$$\lambda = 2n_{\text{eff}}\Lambda m \quad (2.33)$$

Again, the effective refractive index n_{eff} of the gain material must be taken into account and m represents the numeric order of the grating.

Commercially available DFB-QCLs typically employ a 1st order grating, causing emission at the facets of the waveguide. Similar to FP-QCLs, reflection coatings on the front and back allow to favor an output direction. Another property they share with the simplest type of QCLs is the wavelength tunability, which is achieved by influencing the refractive index of the waveguide. One can either change the temperature directly by heating/cooling the device with e.g. a Peltier cooler, or by modifying the laser current, which heats the gain element through the electrical resistance. Together with cw operation, compact packaging and devices available over the whole mid-IR makes them a perfect tool for developing gas sensors.

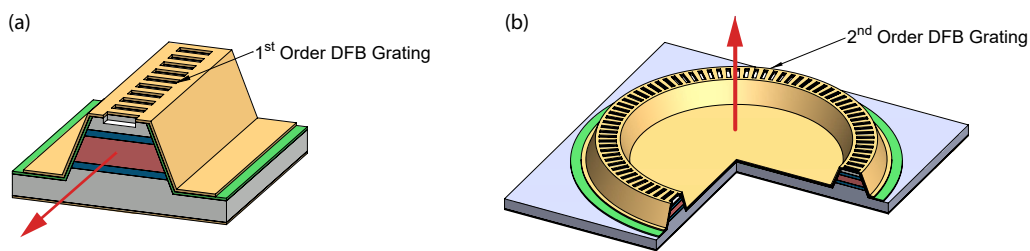


Figure 2.15.: Most DFB-QCLs are manufactured by etching a 1st order grating into the top layer of the waveguide and emit at the facets, indicated with the red arrow (a). DFB-QCLs with a 2nd order grating emit perpendicular to the wafer (b, section view) and the facets of the FP-cavity are no longer required.

DFB-QCLs with a 2nd order grating have also been reported in literature [143]. In contrast, they emit perpendicular instead of parallel to the wafer. As the facets of the ridge waveguide are no longer required for light extraction, circular waveguides, as shown in Figure 2.15b, are also possible [144–149]. They emit at a significantly narrower angle, allow two dimensional arrays [150] and make, due to the absent facets, wider mode-hop-free operation possible (up to 12 cm^{-1} , [151, 152]).

2.3.2.4. Other Designs

Closely related to 1st order DFB-QCLs are lasers with Bragg reflectors [153]. Different versions have been presented, such as a Bragg grating at one end of the waveguide [154], two different

2.4. Measurement Techniques and Quantification

grating periods with independent electrical contacts (*Sampled-Grating Distributed Bragg Reflector* (SGDBR)-QCL, [155–158]) or deeply etched Bragg reflectors, separated from the actual waveguide [159].

An even further modification is the digital grating design that is achieved by mixing the period length of two frequencies. Subsequently, the structure can be applied on the full length of the waveguide. The individual wavelength is selected by heating a section of the waveguide and adjusting the refractive index, so that only one wavelength can be emitted [160]. Implementing this technique with a suitable gain material allows to manufacture a laser device that can be switched between two different wavelengths, separated up to 300 cm^{-1} , in a single ridge QCL.

Many other waveguide designs and techniques to select a certain wavelength, single mode emission or higher optical power have been presented [149, 161–167]. They demonstrate the various possibilities to process QCLs and are building tools for future light sources. From a technical point of view however, conventional 1st order ridge-type DFB-QCLs and EC-QCLs are still the "workhorses" in laser-based IR spectroscopy.

2.4. Measurement Techniques and Quantification

With having the wavelength-selective element defined, the possibilities for measuring the concentration of an gaseous analyte should be discussed in detail. Numerous techniques and modifications thereof have been presented in literature, but the focus here is on robust techniques, that are fit for purpose and could indeed be integrated in a commercial sensor.

2.4.1. The Beer-Lambert-Bouguer Law

One of the most important or even *the equation* for optical quantification has been discovered by Pierre Bouguer, Johann H. Lambert and August Beer. In the 18th century, Bouguer and Lambert found out that the loss of light intensity is proportional to the initial intensity and the path length [168]. Almost a century later, in 1852, Beer discovered that the transmittance of a liquid is constant, if the product of the optical path length and the concentration is constant [169]. Nowadays, the two relations are often written as

$$T_\nu = \frac{I(\nu)}{I_0(\nu)} = \exp(-k_\nu L) = \exp(-S(T)\Phi_\nu P_i L). \quad (2.34)$$

2. Infrared Spectroscopy as an Alternative to Quantify Gases

The wavelength dependent transmittance T_ν is the fraction of the detected and the initial intensity (I and I_0) and depends on the interaction length L and the spectral absorption coefficient k_ν (sometimes also written as $\alpha(\nu)$). It can also be described as a function of the line strength S , the line shape function Φ_ν and the partial pressure P_i .

Closely related with the transmittance is the absorbance A , according:

$$A_\nu = \log \frac{1}{T_\nu} = \log \frac{I_0}{I} = \epsilon_\nu c L \quad (2.35)$$

Here, the absorbance depends on the molar absorptivity ϵ , the concentration c and, again, on the interaction length L .

From the technological aspect, it is versatile and applied for all states of matter. To record an absorption spectrum, a background- and a sample-measurement have to be performed. By applying the Beer–Lambert–Bouguer law, one can calculate the absorbance for every measured wavelength, resulting in the spectrum.

2.4.2. Tunable Diode Laser Absorption Spectroscopy

If the analyte to be measured is gaseous, absorbs in the mid-IR and has ro-vibrational absorption lines with a FWHM of $<1 \text{ cm}^{-1}$ under measurement conditions, one can employ a DFB-QCL as light source and perform Tunable Diode Laser Absorption Spectroscopy (TDLAS). Here, the emitted wavelength of the laser diode is typically tuned across an absorption feature by either pulsing the semiconductor or operating it in cw and applying a current ramp. The electric current induces heating of the gain material and leads to a shift in the emitted wavelength. The laser beam passes the gas cell and the transmitted intensity during the tuning process is recorded with a fast-enough detector and data acquisition system, as shown in Figure 2.16.

Applying the Beer-Lambert-Bouguer law to get an absorption spectrum requires usually a sample and a background spectrum. For gaseous analytes with clearly separated absorption lines in a non-absorbing matrix (e.g. measuring low concentrations of CO in N₂) it is possible to perform background-free measurements. It requires a stable tuning behavior of the QCL and is achieved by interpolating the measured signal, as illustrated in Figure 2.17. Depending on the laser properties and the detector response, it can be sufficient to perform a linear or 2nd order polynomial fit to interpolate the background signal. This approach is a powerful tool, especially if it is technically not possible to replace the sample in the laser beam with the non-absorbing

2.4. Measurement Techniques and Quantification

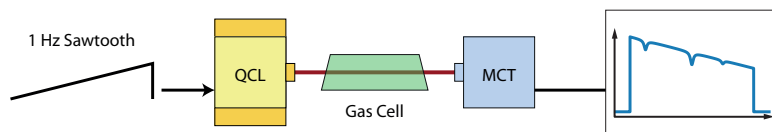


Figure 2.16.: Components required for Tunable Diode Laser Absorption Spectroscopy. The spectral tuning of the QCL is realized by either pulsing it or applying a current ramp on the constant laser current. The detector signal is recorded with a fast enough data acquisition card or an oscilloscope.

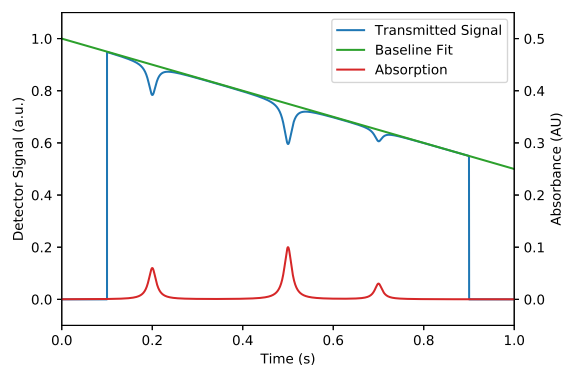


Figure 2.17.: Simulated detector signal of a laser tuning across three individual absorption lines with Lorentzian line shape and the absorbances 60 mAU, 100 mAU and 30 mAU. The background spectrum is retrieved by interpolating across the absorption features and by applying the Beer-Lambert-Bouguer law, the absorption spectrum can be calculated.

matrix. Prominent examples, where this technique is applied, are open path measurements in the ambient air [170–176] or inline process monitoring [177, 178].

A major advantage of this technique is the relatively simple access to calibration-free measurements. Considering that the optical path length is known and the target analyte has sufficiently separated ro-vibrational absorption lines, one can derive its concentration from the well known line-strength values. As the peak height of the absorption spectrum is mainly influenced by the pressure and the temperature, these parameters have to be estimated by fitting a Lorentzian or Voigt function. In addition, the tuning behavior of the QCL must be known and is often monitored with an etalon and an additional detector.

Another useful feature is the pulsed operation of the QCL with a typical pulse length of several hundred nanoseconds. Together with a sufficient fast detector and electronics, this allows to record $>100\,000$ intra-pulse spectra per second. The high data rate enables to investigate either fast processes or to improve the signal-to-noise ratio by averaging.

However, disadvantages are also associated with this technique. Depending on the application, it might not be sensitive enough, especially, if extremely small concentrations of a gas have to be

2. Infrared Spectroscopy as an Alternative to Quantify Gases

measured. Another difficulty are changes in the sample matrix that can influence the algorithm for simulating the background for the Beer-Lambert-Bouguer law.

2.4.3. Wavelength Modulation Spectroscopy

This technique is closely related to the TDLAS but it is specially optimized to quantify small optical absorbance. As the signal noise decreases often at higher frequencies, the idea is to shift the detection process to higher frequencies and demodulate the signal afterwards. Wavelength Modulation Spectroscopy (WMS) has been introduced to mid-IR spectroscopy in the late 1970s with lead salt diode lasers [179–186].

The experimental setup is similar to TDLAS, as illustrated in Figure 2.18, and requires an additional signal source for the modulation and a lock-in amplifier for demodulating the signal.

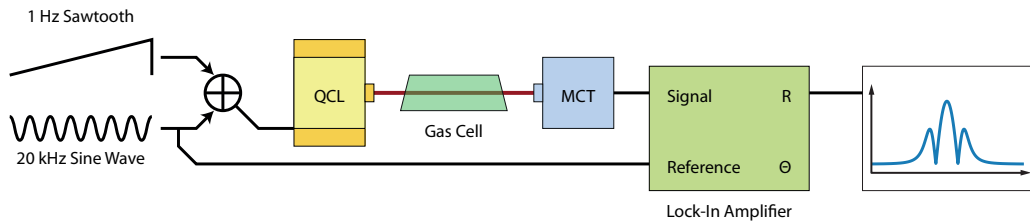


Figure 2.18.: Illustration of the required components to record a WMS spectrum. The laser is modulated in the kHz-range and slowly tuned across the absorption feature. The $2f$ -WMS spectrum is recorded by demodulating the detector signal at the 2^{nd} harmonic of the modulation frequency.

The main application of WMS is to retrieve the concentrations from extremely weak signals, which are caused by ro-vibrational absorption lines. Therefore, a few simplifications are useful for discussing the signal path [184, 187, 188]. First, the spectral absorbance $\alpha(\nu) = k_\nu L$ should be <0.1 . This allows to substitute the Beer-Lambert-Bouguer law and approximate the transmitted intensity $I(\nu)$, with I_0 as incident intensity, according:

$$I(\nu) \simeq I_0(\nu) [1 - \alpha(\nu)]. \quad (2.36)$$

Second, the investigated absorption feature is dominated by pressure broadening and Doppler broadening can be neglected. Subsequently, the wavelength dependent absorbance $\alpha(\nu)$ in vicinity of the line center ν_0 can be described with the Lorentzian line shape:

$$\alpha(\nu) = \alpha(\nu_0) \frac{1}{1 + \left[\frac{\nu - \nu_0}{\Delta\nu} \right]^2} \quad (2.37)$$

2.4. Measurement Techniques and Quantification

In this definition of the Lorentzian line shape, $\Delta\nu$ is the Half Width Full Maximum (HWHM) of the absorption line and $\alpha(\nu_0)$ the spectral absorbance of the feature. Shifting to higher detection frequency is done by modulating the laser current i_0 with a cosine wave of the amplitude k and the frequency ω (~ 10 kHz). The resulting time-dependent laser current is described as:

$$i(t) = i_0 + k \cos \omega t. \quad (2.38)$$

As the emitted wavelength of the laser is a function of the injected laser current, one can introduce the modulation depth a and describe the emitted wavelength $\nu(t)$ as follows:

$$\nu(t) = \nu_0 + a \cos(\omega t). \quad (2.39)$$

Similar to the Direct Absorption Spectroscopy, WMS requires to tune the emitted wavelength across the absorption line to be investigated. This is typically done by increasing the laser injection current periodically ($\bar{i} = i_0 + i_{\text{ramp}}$, frequency: ~ 1 Hz) and indicated as $\bar{\nu}$. Subsequently, the emitted wavelength $\nu(t)$ is now:

$$\nu(t) = \bar{\nu} + a \cos(\omega t). \quad (2.40)$$

The detected signal $I(t)$ is a periodic even function and can be expanded in a Fourier cosine series [187, 189]:

$$I(t) = I_0 [1 - \alpha(\bar{\nu} + a \cos(\omega t))] = I_0 \left[1 - \sum_{k=0}^{\infty} H_k(\bar{\nu}, a) \cos(k\omega t) \right] \quad (2.41)$$

$$\text{with } H_0(\bar{\nu}, a) = \frac{1}{2\pi} \int_{-\pi}^{+\pi} \alpha(\bar{\nu} + a \cos \theta) d\theta \quad (2.42)$$

$$H_k(\bar{\nu}, a) = \frac{1}{\pi} \int_{-\pi}^{+\pi} \alpha(\bar{\nu} + a \cos \theta) \cos k\theta d\theta. \quad (2.43)$$

Here, H_k is the k^{th} order Fourier coefficient, which depends on the modulation depth, the wavelength and the line shape of the absorption feature. These coefficients have been intensively studied and calculated for different line shapes functions in literature [184, 187, 188, 190–193] and enable to use either a lock-in amplifier or an FFT-approach to demodulate the signal and retrieve a value that is proportional to the concentration of the analyte.

The modulation depth a is a crucial property in WMS as it influences the the shape of the WMS spectrum and also affects recovered signal intensities. Still assuming that the investigated absorption feature has a Lorentzian line shape, it is useful to introduce the modulation index $m = a/\Delta\nu$ [184]. A detailed characterization of the influence of the modulation index on the line shape was done by Arndt [190]. The main consequence for WMS is, that the maximum signal for the 1st harmonic is achieved with $m = 2$ and for the 2nd at $m \approx 2.2$. WMS spectra of different harmonics are plotted in Figure 2.19b and the peak maximum as function of the modulation index m is shown in Figure 2.19c.

2. Infrared Spectroscopy as an Alternative to Quantify Gases

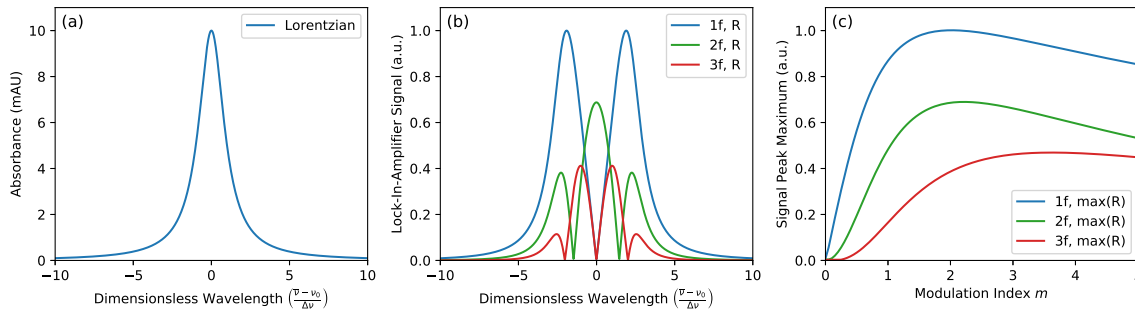


Figure 2.19.: An absorption feature with Lorentzian line shape (a) and the recovered 1f-, 2f- and 3f-WMS spectra (b). The peak maxima of the WMS spectra depend on the modulation depth and on the order of the harmonic (c).

2.4.3.1. Lock-In Amplifier

One option to isolate the harmonics of the detector signal is employing a lock-in amplifier [194, 195]. Its underlying principle is the trigonometric identity, which describes the multiplication of two sine functions:

$$\sin(\alpha) \sin(\beta) = \frac{1}{2} \cos(\alpha - \beta) - \frac{1}{2} \cos(\alpha + \beta) \quad (2.44)$$

The result is the difference of two cosine functions, whereas one is the sum frequency ($\alpha + \beta$) and the other one is the difference ($\alpha - \beta$).

In the case of WMS, the detector signal is multiplied with the laser modulation frequency (reference signal, f_{mod}). Assuming that the 1st harmonic is the desired one, the output signal of the multiplication will consist of the difference frequency $f = 0$ (=DC) and their sum frequency $2f_{\text{mod}}$. At this point it should be pointed out, that only the amplitude of the frequency f_{mod} contributes to the DC component and all other signal components from the detector with $f \neq f_{\text{mod}}$ (also noise), can be filtered with a suitable low-pass filter. Higher harmonics, such as the 2nd or 3rd, are accessible by multiplying the reference frequency to achieve the desired harmonic at the input. The filtered signal is also known as *X-component* (or *in-phase component*, *I*) and contains the desired WMS-signal, if the phase θ between the signal and the reference is zero.

For the more common case, that electronic components, the laser diode or the detector introduce phase shifts $\theta \neq 0$, one can extend the signal processing by multiplying the input signal with a 90° shifted reference. Again, a low-pass filter with identical filter parameters isolates the DC-component, producing to the *Y-component* (or *quadrature component*, *Q*).

2.4. Measurement Techniques and Quantification

With this dual-phase or phase-insensitive lock-in amplifier, one can calculate the magnitude R and the phase shift θ from the X - and Y -component, according:

$$R = \sqrt{X^2 + Y^2} \quad \text{and} \quad \theta = \arctan\left(\frac{Y}{X}\right) \quad (2.45)$$

The basic concept of such a dual-phase lock-in amplifier is visualized in Figure 2.20.

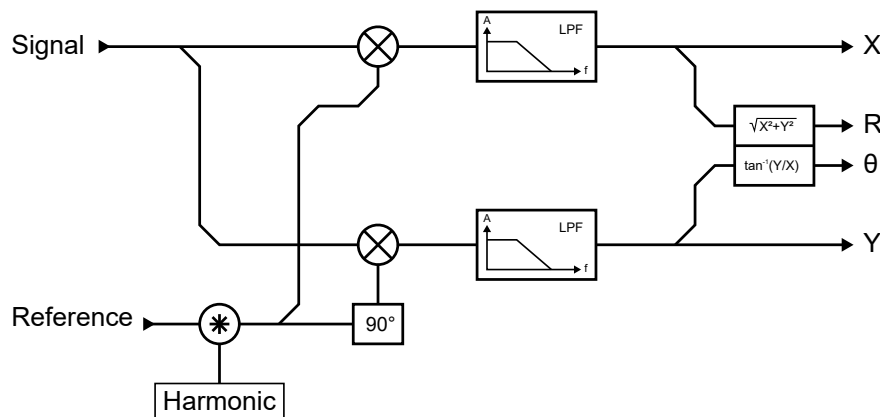


Figure 2.20.: Lock-in amplifiers are designed to extract the amplitude of the same frequency as the reference signal (or its harmonic). The magnitude R and the phase θ is calculated from the in-phase and quadrature signals X and Y .

Different approaches are nowadays available to build a lock-in amplifier [196]. Depending on the experiment, the simplest one requires only an analog switch that is triggered by a square wave reference signal, an RC-filter and an operational amplifier [197]. More advanced analog ones are based on multiplying amplifiers for the input stage, a frequency multiplier to generate the harmonic and a differentiator for the 90° phase shift [194, 198]. Additional operational amplifiers can be used to extract the magnitude of the X - and Y -component.

With the development of fast ADCs, it is also possible to digitize the analog signals and perform the multiplication, the filtering and the calculation of R and θ on a micro-processor [199], or even faster, on a Field Programmable Gate Array (FPGA) [200–203]. Similar, the lock-in amplifier can be programmed as a software on a Personal Computer (PC) [204], which simplifies the following data processing (storing, additional filtering, ...) even further.

2.4.3.2. Fourier Transform Based Demodulation

While the lock-in amplifier selects the n^{th} harmonic by multiplying the measured signal with a reference and converting it to a DC-component, the signal processing can also be performed in

2. Infrared Spectroscopy as an Alternative to Quantify Gases

the frequency domain. To do so, the signal is digitized and a Fourier Transformation algorithm is applied. In the next step, a band-pass filter passes only the frequencies in vicinity of the demodulation-frequency whereas the bandwidth defines the desired filter range.

The selected frequency range is transformed back to the time-domain and an envelope function, e.g. the absolute of the Hilbert-transformation $|\mathcal{H}|$, is applied. The resulting line shape is identical to the magnitudes recovered with a lock-in amplifier. The required steps for processing the detector signal in the frequency domain are illustrated in Figure 2.21.

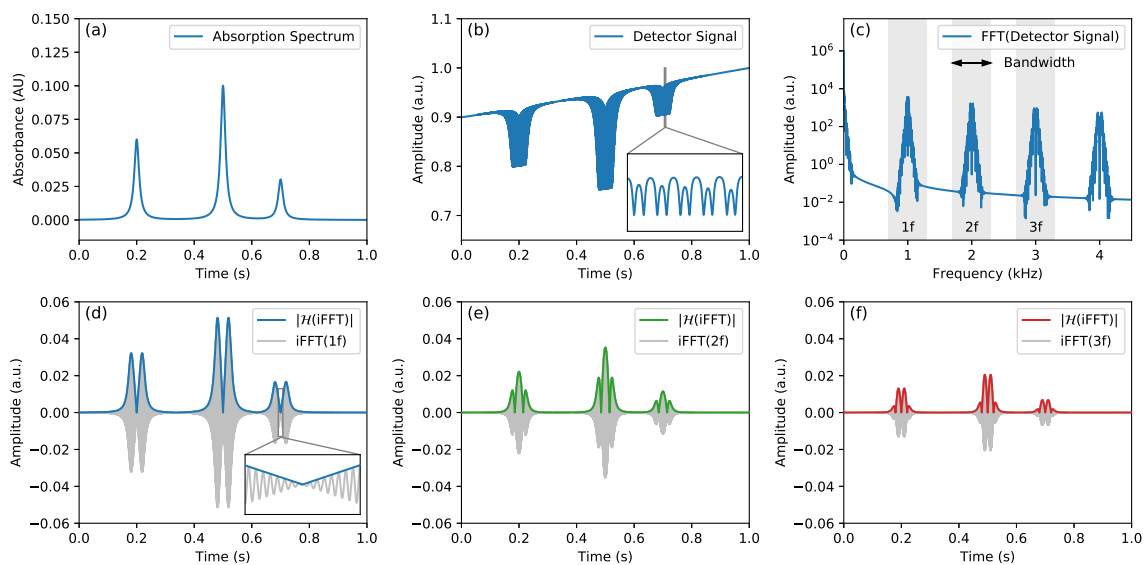


Figure 2.21.: WMS spectra can also be extracted from the detector signal by filtering in the frequency-domain and applying an envelope-function. Absorption features ((a), parameters as in Figure 2.17) probed with a modulated, ideal laser (here: sine-wave, 1 kHz) lead to the characteristic signal pattern in the detector signal (b). The desired harmonic and bandwidth is selected in the frequency domain (c) and transformed back to the time-domain. The positive part of an applied envelope function leads to the 1f-, 2f- and 3f-WMS spectrum (d-f).

Regarding measuring the concentration of a gas species with WMS, it is a common reliable way to evaluate the 2nd harmonic of the detector signal. Its shape is closely related to the 2nd derivative of the absorption line [190] and the peak maximum is proportional to the concentration. While others have investigated the reconstruction of the original line shape, the influence of laser properties or other innovative approaches [188, 205–214], this work is focused on the technical implementation in a field-deployable prototype. Subsequently, the concentrations of the target analytes are derived from the maximum of the magnitude of the 2nd harmonic, which delivers a sufficient precision for real world application, as later discussed in the results section. From a technical point of view, calibration-free measurements are possible as well, but require precise

2.4. Measurement Techniques and Quantification

knowledge of the laser tuning properties. As the shape of the recorded spectrum depends not only on the temperature and the pressure, but on the modulation depth too, advanced models are necessary and rather topic for scientific purpose [215–219].

2.4.4. Heterodyne Phase Sensitive Dispersion Spectroscopy

In general, most of the experiments in IR spectroscopy rely on measuring the wavelength-dependent attenuation of light, caused by the presence of an absorbing analyte. It is described by the Beer-Lambert-Bouguer law, whereas the absorbance of a sample at a certain wavelength is proportional to the concentration of the analyte. Although this model fits for many applications in optical spectroscopy, it is useful to understand the underlying, more general, concept of the complex refractive index, as well. This relation allows to develop innovative experimental setups that quantify an analyte by measuring other properties of the transmitted light than the intensity itself.

2.4.4.1. Relation between Absorption and Dispersion

The well-known refractive index n of a sample, defined as the ratio of the speed of light in vacuum and the speed of light in the sample, can be extended by an imaginary part κ which is proportional to the absorption coefficient α and also depends on the vacuum wavelength λ_0 , according [55]:

$$n = n' - i\kappa \quad \text{and} \quad \kappa = \frac{\alpha\lambda_0}{4\pi}. \quad (2.46)$$

The real part n' depends, like the absorption coefficient, on the optical frequency ω and represents the dispersion of the wave. To stay in consistency with the literature, it is recommended to express the wavelength in units of frequency. For an absorption feature with a Lorentzian line shape, one can also write:

$$n'(\omega) = 1 + s \frac{\omega_0 - \omega}{(\omega_0 - \omega)^2 + (\gamma/2)^2} \quad (2.47)$$

Here, s is a spectral line dependent coefficient, ω_0 the frequency of the line center, and γ the FWHM of the spectral feature. In addition, the refractive index $n(\omega)$ and the absorption

2. Infrared Spectroscopy as an Alternative to Quantify Gases

coefficient α are related via the Kramers-Kronig relation [220, 221], which is also illustrated in Figure 2.22:

$$n(\omega) = 1 + \frac{c}{\pi} \int_0^{+\infty} \frac{\alpha(\omega')}{\omega'^2 - \omega^2} d\omega' \quad (2.48)$$

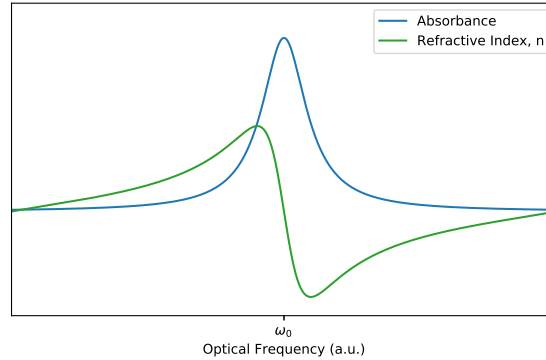


Figure 2.22.: The relation between the absorbance and the refractive index in vicinity of an absorption line is described with the Kramers-Kronig relation.

The consequence is that light, traveling through an absorbing medium, is attenuated and the phase will be, due to the dispersion, shifted. This phase shift can be measured and correlates with the concentration of the analyte. One approach is to employ a monochromatic, coherent light source and detect the constructive/destructive interference in a Mach-Zehnder-Interferometer, as presented in [222, 223]. In the gas phase, however, the absorption features are significantly narrower and the interferometer can be substituted with an electronics based approach.

2.4.4.2. Signal Generation

Two effects can be observed when a laser diode is current modulated: At lower frequencies, typically <MHz, the changing laser current influences the refractive index of the active region/waveguide due to joule heating. Subsequently, the emitted wavelength can be controlled and this behavior is the basis of TDLAS and WMS. At higher frequencies, however, the joule heating is limited due to the thermal mass of the semiconductor and the electronic tuning caused by carrier dynamics dominates [224]. The time-dependent optical field $E(t)$ can be written as [225, 226]:

$$E(t) = E_0 [1 + M \sin(\omega_{rf}t + \psi)] \exp [i(\omega_0t + \beta \sin \Omega t)], \quad (2.49)$$

2.4. Measurement Techniques and Quantification

whereas E_0 is the electric field amplitude of the original laser beam, M and β are the amplitude- and frequency-modulation (AM, FM) indices, ψ the phase difference between AM and FM, ω_0 the center frequency and Ω the modulation frequency. Assuming that $M \ll 1$ and $\beta \ll 1$ leads to an optical signal which consists of the carrier signal ω_0 and two side bands located at $(\omega_0 - \Omega)$ and $(\omega_0 + \Omega)$. The same effect can be realized with electro- and acousto-optical modulators but, due to the availability of these components, this approach is typically applied in combination with NIR lasers.

One way to use this spectral narrow-spaced beam for spectroscopic applications was described by Bjorklung [227, 228] and is known as Frequency Modulation Spectroscopy (FMS). Here, an absorption feature is probed with one of the optical side bands and the measured beat signal depends on attenuation due to absorption and the phase shift, caused by the dispersion. The side band is tuned across the absorption line by either increasing the laser current (similar to WMS) or by chirping the modulation frequency ω_{rf} . Notable improvements and modifications are, to list a few, Two-Tone FMS [229], Noise-Immune Cavity-Enhanced Optical Heterodyne Molecular Spectroscopy (NICE-OHMS) [230–232] and Chirped-Laser Dispersion Spectroscopy (CLaDS) [233–236].

Also related to FMS is the Heterodyne Phase Sensitive Dispersion Spectroscopy (HPSDS) [237–239] which shall be discussed in detail. Compared to other FM based experimental setups, its design allows to integrate it in an existing WMS setup with minimum hardware modifications and its applicability for environmental measurements will also be shown in this work.

For HPSDS experiments with mid-IR QCLs [240, 241] and ICLs [242], the laser diode is directly modulated to emit the optical three tone. The modulation signal, generated from a suitable signal generator, is added to the laser current with a bias-tee circuit and lets the laser emit the optical three-tone signal. When the laser beam propagates through a medium with an absorption feature close to the center wavelength of the laser, each frequency will undergo a slightly different refractive index, due to the Kramers-Kronig relation. The consequence is that the phases will be shifted after the absorbing sample, as illustrated in Figure 2.23a.

Each phase depends on the optical length of the gas cell L and the wavelength-dependent refractive index of the sample. Subsequently, one can express the electromagnetic fields E_1, E_2

2. Infrared Spectroscopy as an Alternative to Quantify Gases

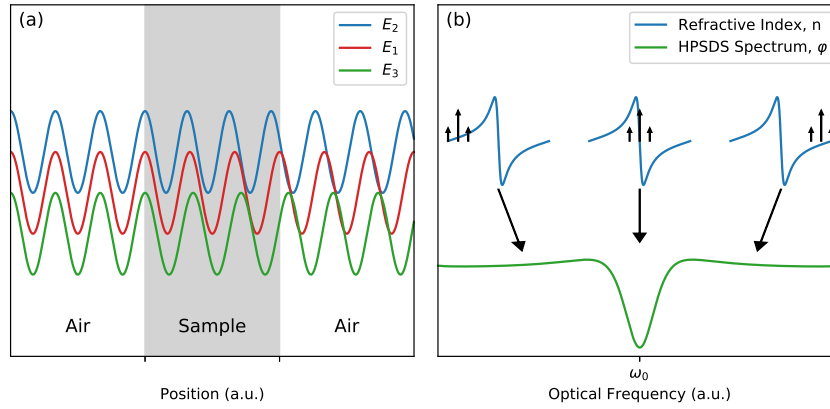


Figure 2.23.: (a): Illustration of the electric fields of the optical three-tone while passing an absorbing sample. The waves have been shifted along the y-axis for better visibility. (b): The HPSDS signal origins from the optical sidetones whereas each optical frequency undergoes different refractive indices. The corresponding spectrum is recorded by tuning the optical three-tone across the absorption feature.

and E_3 with the corresponding amplitudes (A_1, A_2, A_3) and phases ($\varphi_1, \varphi_2, \varphi_3$):

$$E_1 = A_1 \cos(\omega_0 t - \varphi_1) \quad \varphi_1 = \frac{\omega_0 L}{c} [n(\omega_0) - 1] \quad (2.50)$$

$$E_2 = A_2 \cos[(\omega_0 + \Omega)t - \varphi_2] \quad \varphi_2 = \frac{\omega_0 L}{c} [n(\omega_0 + \Omega) - 1] \quad (2.51)$$

$$E_3 = A_3 \cos[(\omega_0 - \Omega)t - \varphi_3] \quad \varphi_3 = \frac{\omega_0 L}{c} [n(\omega_0 - \Omega) - 1] \quad (2.52)$$

When the phase-shifted frequencies hit the square law detector, three beatnotes, originating from the three optical frequencies, will be detected and the resulting phase φ_0 is written as:

$$\varphi_0 = \arctan \frac{a \sin(\varphi_2 - \varphi_1) + b \sin(\varphi_1 - \varphi_3)}{a \cos(\varphi_2 - \varphi_1) + b \cos(\varphi_1 - \varphi_3)} \quad (2.53)$$

$$a = 10^{-(A(\omega_0) + A(\omega_0 - \Omega))/2} \quad (2.54)$$

$$b = 10^{-(A(\omega_0) + A(\omega_0 + \Omega))/2} \quad (2.55)$$

The coefficients a and b describe the absorption of the optical tones and can be neglected for small concentrations ($a = b = 1$) or if the precise line shape is not required [239]. Subsequently, the formula for φ_0 can be simplified to:

$$\varphi_0 = \arctan \left(\frac{\varphi_2 - \varphi_1 + (\varphi_1 - \varphi_3)}{2} \right) \approx \left(\frac{\varphi_2 - \varphi_3}{2} \right) \quad (2.56)$$

and finally:

$$\varphi_0 = \frac{\omega_0 L}{2c} (n(\omega_0 + \Omega) - n(\omega_0 - \Omega)). \quad (2.57)$$

2.4. Measurement Techniques and Quantification

To record the corresponding HPSDS spectrum, the center frequency ω_0 has to be shifted across the absorption feature, which is realized, like in WMS, by applying a slow current ramp. Regarding the data acquisition, it should be pointed out that the phase signal occurs at the modulation frequency. This is typically in the range of 100-500 MHz and exceeds the bandwidth of many laboratory lock-in-amplifiers. To circumvent this issue, the detector signal is down-mixed to the kHz-range by multiplying it with a sine-wave of slightly higher frequency than the modulation frequency ($\Omega + \delta$, e.g. $\delta = 10$ kHz). Now, the phase signal can be easily extracted by demodulating at the intermediate frequency δ .

A typical laboratory setup for HPSDS is illustrated in Figure 2.24 and one can see the similarity to the WMS setup, as shown in Figure 2.18. The additional components are a bias-tee to inject the high-frequency modulation signal, a two-channel signal generator and two mixers.

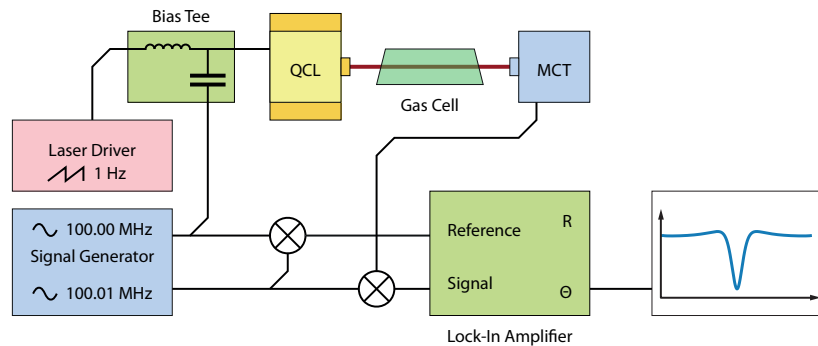


Figure 2.24.: Experimental setup to record a HPSDS spectrum. Assuming that the detector supports the required bandwidth, only two mixers, a bias-tee and a two-channel signal generator have to be added to an existing WMS setup.

Like for 2f-WMS and TDLAS experiments, calibration-free measurements are possible too [237], as the dispersion can be derived from simulated absorption spectra. With the focus on developing and testing a (mainly) 2f-WMS based multi-gas-analyzer, however, further scientific experiments shall be the topic of future projects. From a technical point of view, it is recommended to optimize the setup in terms of electrical and optical components first (bandwidth of detector and signal generator > 1 GHz, high-precision lock-in-amplifier, reducing number of optical elements in the beam path).

2.4.5. Other Mid-IR based Techniques

Mid-IR based sensors can be differentiated by the way how the light interacts with the sample and how it is quantified. For *direct* methods, the transmitted light is detected and its intensity

2. Infrared Spectroscopy as an Alternative to Quantify Gases

measured. This can be, for example, monitoring the intensity at the detector while tuning a diode laser across an absorption feature (TDLAS) [176, 243–245], or reconstructing a 2f-WMS signal with a lock-in-amplifier [246–248]. Similar, low-cost non-dispersive sensors, employing a thermal light source, an optical filter and a pyroelectric detector, can be built [249–255]. Many sensors in the liquid phase are based on this technique too, however, they often use broadly tunable EC-QCLs, tunable FP-filter detectors or commercially available FTIR spectrometers, as the absorption features are significantly broader than the ro-vibrational absorption lines in the gas phase [135, 256, 257]. They all have in common, that, if the analyte is present in a very small concentration, the measured signal is very close to the background signal and therefore difficult to quantify. Subsequently, stabilization of the light source and precise signal processing is crucial to achieve reasonable limits of detection (LOD). Depending on the matrix and the individual application, it can be improved by increasing the optical pathlength. This is relatively simple in the liquid phase, where flow cells with an optical path length of 10–500 μm are used. For trace gas measurements in ambient air or nitrogen, in contrast, an optical path length of several tens of meters are common and challenging to increase further.

The *indirect* methods, in contrast, measure a property that is influenced or generated by the absorption of light by the analyte. One of them is photoacoustic (PA) detection, which measures an acoustic wave with a microphone or comparable hardware [258–266]. A common application is the quantification of CO_2 whereas a blackbody emitter is employed as the light source. The emitted radiation is filtered so that only the spectral range around 4.5 μm enters the gas cell. The target analyte absorbs the radiation and, if the IR beam is modulated with e.g. a mechanical chopper, an acoustic wave with the modulation frequency will be produced. A low-cost microphone is sufficient to detect the sound wave and the signal can be further improved by installing an acoustic resonator. A lock-in amplifier extracts the signals that are in same phase as the chopper and improves the signal to noise ratio further. The most significant difference to the direct methods is the fact, that the property that is measured, is produced by the interaction of the radiation and the analyte. Subsequently, the signal to noise ratio can be improved by increasing the optical power of the incident beam and miniaturization helps as well.

Quartz Enhanced Photoacoustic Spectroscopy (QEPAS) is closely related whereas the microphone is replaced with a quartz tuning fork [267–273]. Due to its electro-mechanical properties, only certain mechanical vibrational modes can induce the piezoelectric effect and generate a signal. Experimental setups are typically based on precisely controllable laser sources, such as QCLs or ICLs, and the beam is focused in between the prongs of the fork. The target analyte absorbs the radiation and emits an acoustic wave during relaxation. The generated sound wave

2.4. Measurement Techniques and Quantification

pushes the prongs away from each other and a voltage signal can be measured at the electric contacts. To improve the signal further, resonator tubes can be installed at both sides of the tuning fork. This method benefits from the availability of low-cost tuning forks, their high Q-factor, the sharp resonance frequency at ≈ 32.76 kHz and the possibility to miniaturize the setup.

Another indirect method is Photothermal Spectroscopy (PTS) whereas the changing refractive index, induced by the absorption of light [274–278], is measured. The setup consists of two lasers, whereas one is matched to an absorption line of the analyte and the other one acts as probe laser. To detect the minimum changes of the refractive index caused by the absorption, the probe laser is installed in an interferometer geometry. Setups, based on the Mach-Zehnder-, Jamin- and Fabry-Perot-Interferometer have been realized and miniaturization is possible as well [279, 280].

Although these methods allow miniaturization of the gas measurement cell and rely on a relatively cheap detection equipment, one should mention the disadvantages as well. The photoacoustic and -thermal waves depend strongly on the water vapor content as shown in [268, 281]. Subsequently, either the humidity must be measured or humidified with additional equipment. Another one is that the acoustic wave or the change of the refractive index depends on the optical power of the excitation laser. Therefore, these setups depend on the availability of high-power cw-QCLs, which can be challenging as QCLs and ICLs are, in contrast to NIR laser diodes, still not mass products.

For the development of the multi-gas-analyzer, the direct method 2f-WMS has been identified as the best suited measurement technique. Numerous other prototypes and experimental setups based on this technique have been presented and successfully tested in the lab and in the field. The required components, such as the gas measurement cell, the laser driver, the detector and control electronics are all off-the-shelf parts and can be further optimized if commercialization of the sensor is requested.



Die approbierte gedruckte Originalversion dieser Dissertation ist an der TU Wien Bibliothek verfügbar.
The approved original version of this doctoral thesis is available in print at TU Wien Bibliothek.

3. Development of a Multi-Gas-Analyzer for Ambient Air Monitoring

Several reviews, book chapters and books have already addressed the applicability of infrared spectroscopy for ambient air monitoring, trace-gas sensing and other fields, extensively [249, 271, 282–288]. The demand to quantify pollutants in the air, monitor the composition of process streams and even measuring the atmosphere of other planets has led to numerous scientific publications in physics and chemistry and a coarse overview of the available techniques shall be topic of this chapter. Then, the requirements and the components for a 2f-WMS based prototype for ambient air measurements will be evaluated, beginning with the suitable wavelengths to quantify the analytes. The gas measurement cell, detector, mechanical assembly, electronics and the software will be discussed as well, and, finally, the modifications that are required to perform HPSDS measurements with the setup as well, will also be part of this chapter.

3.1. Building Prototypes in General

Before the target analytes and the individual components of the multi-gas-sensor are discussed in detail, one should clarify the term "prototype" to provide a better understanding of the desired aims of the here presented measurement device.

Taking a closer look in developing prototypes reveals different levels of the integration of the individual components and the effort it would take to bring a new product to the market. For example, it can occur that a researcher calls his/her experimental setup in the lab already a "prototype" when the setup is working and "transportable". This can also include that the optical components are mounted on a lab-breadboard, the required electronics (like signal generators and power supplies) are placed in a large box, made of aluminum profiles, and the software for

3. Development of a Multi-Gas-Analyzer for Ambient Air Monitoring

controlling the individual parts runs on an office PC. In contrast, a customer or sales representative might associate the word "prototype" with an already optimized and even field-tested device. The final steps before releasing it to the market could include minor adaptations on the user interface, the replacement/simplification of the power supplies, or last adjustments in the final specifications.

As the problem of different definitions of the term "prototype" is not new, NASA has introduced the *Technology readiness levels* (TRLs). In the mid-2000s, the European Space Agency adopted the TRL scale and soon it became an important definition in Horizon 2020-projects ([289], Framework Programmes for Research and Technological Development, European Commission). By applying this definition, the first example, showing the point of view of a researcher, corresponds to TRL 4 and the second case (sales representative) is described best with TRL 8.

Regarding the here discussed "prototype", the state of development is somewhere in between the previous examples and tries to satisfy both, the scientist and the customer (TRL 6). To achieve this within the given conditions, certain simplifications had been done. For example, the electronics have been chosen on the basis of already gained experience from earlier projects, instead of investing resources for developing or optimizing new electronics. Another one is the number of target analytes that could be quantified with the hardware. Although other greenhouse gases, such as CH₄, CO₂ or the pollutants O₃ and NH₃ could be measured with IR based techniques as well, the list of target analytes has been reduced to five.

The development process has been accompanied by computer-aided design (CAD) studies (e.g. Figure 3.18, also in the appendix) to stay within certain mechanical dimensions, which should make the prototype competitive to other manufacturers of ambient air monitors. In particular, the prototype must be transportable by car, should fit in widely used 19" racks for electronic equipment and achieve comparable detection limits.

3.2. Requirements and Target Analytes of the Gas Sensor

QCL-based gas sensors must fulfill certain expectations to be competitive with the established reference methods. Beside delivering the correct measurement values, the response time should be identical or better, the overall power consumption should be similar or lower and the mean time between failures must as long as possible. The physical dimension should be the same size

3.2. Requirements and Target Analytes of the Gas Sensor

Component	Concentration	
	... in the atmosphere according [291]	... typical values in an European city
H ₂ O	0.03 %	1.3 %
CO ₂	345 ppmv	410 ppmv
CH ₄	1720 ppbv	1900 ppbv
CO	150 ppbv	400 ppbv
N ₂ O	310 ppbv	310 ppbv
O ₃	65 ppbv	70 ppbv
NO	0.3 ppbv	40 ppbv
NO₂	0.023 ppbv	80 ppbv
SO₂	0.3 ppbv	3 ppbv

Table 3.1.: Typical concentrations of IR absorbing gases in the atmosphere and realistic values for an urban area. Gases written in bold are of special interest for ambient air monitoring, according the *Directive 2008/50/EC*.

or smaller than the existing measurement equipment and ideally fit in 19” racks [290], which is a defacto standard for these installations. Finally, a prototype should have at least one outstanding feature to be the definitive successor in a future discussion about reference methods.

In the case of the here discussed multi-gas sensor, most of these requirements are successfully fulfilled or could be easily adopted with minor modifications. The decisive factor for a possible commercialization, however, is the application of infrared spectroscopy, which allows to quantify multiple analytes with the same equipment. The only task is to identify an interference-free absorption line for each analyte and to combine the laser beam of the required light sources.

3.2.1. Spectral Ranges

Developing a trace gas sensor based on mid-IR laser spectroscopy requires a careful selection of the individual laser sources. Although the ro-vibrational absorption lines in the gas phase are relatively narrow and often nicely separated, it is necessary to know the composition of the matrix to avoid incorrect results, caused by overlapping absorption features. Therefore, Table 3.1 gives an overview of important IR active gases and their concentrations in the ambient air.

Normalized IR spectra of the four air-quality relevant analytes CO, NO, NO₂ and SO₂ and the greenhouse gas N₂O have been simulated with HAPI [59] and are plotted in Figure 3.1a.

3. Development of a Multi-Gas-Analyzer for Ambient Air Monitoring

Although some of the spectra are slightly overlapping, it would be possible to distinguish the target gases with low-cost bandpass-filters, if they were the only components mixed with N_2 . In practical terms, however, the analytes of interest have to be quantified in the low ppbv-region and in presence of water vapor, CO_2 and CH_4 . This situation is illustrated in Figure 3.1b, where the line strengths of the relevant gases are plotted.

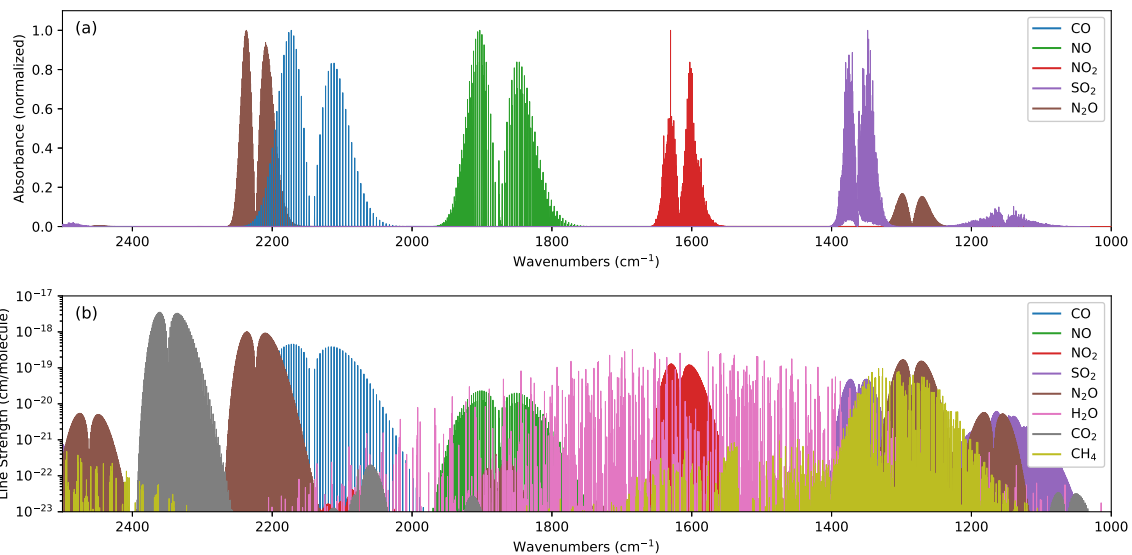


Figure 3.1.: (a): spectral ranges of the target analytes. (b): line strength of possible interferants in the ambient air

As a gas measurement cell defines the interaction of the laser beam and the gas sample, one can lower the pressure within it to reduce the FWHM of the absorption lines, as described earlier. Subsequently, it is possible to identify at least one wavelength for each analyte where the matrix does not influence the measurement. These wavelength regions are illustrated in Figure 3.2 whereas spectra of the target analyte and possible interferants are plotted. The concentration of each component is listed in the legend and are typical values for the ambient air. Moreover, a Lorentzian line shape, a pressure of 100 mbar and an optical path length of 76 m has been selected for the simulations. Additional calculated gas spectra of the ambient air at different pressures can be found in Appendix A.

3.3. Optical Setup

A schematic of the 2f-WMS based multi-gas-analyzer is shown in Figure 3.3 and gives an overview of the required components. Measuring the four pollutants and the greenhouse gas

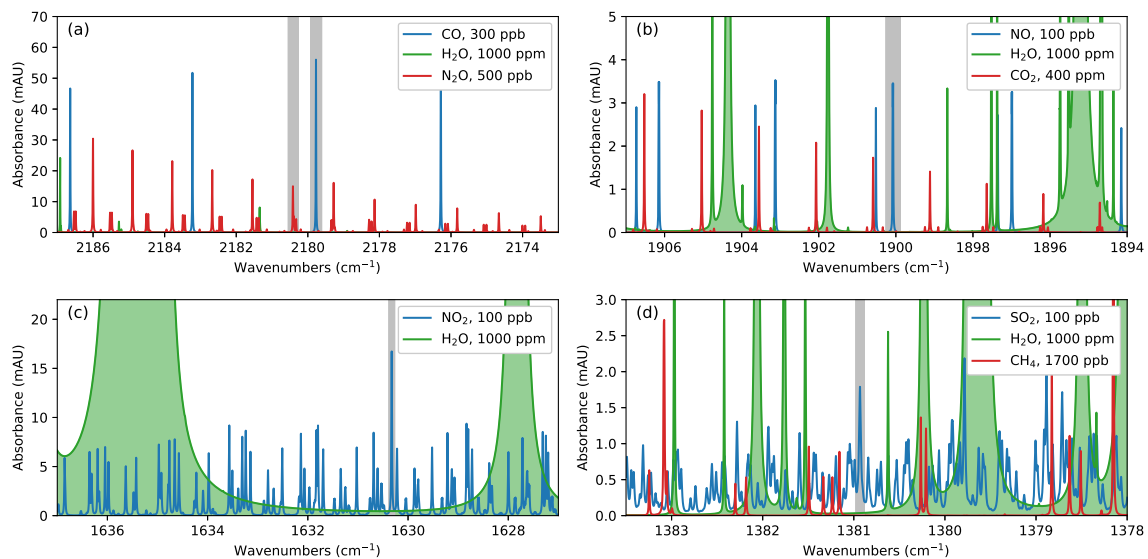


Figure 3.2.: Simulated spectra of the five analytes of interest: (a) CO and N₂O, (b) NO, (c) NO₂ and (d) SO₂. A pressure of 100 mbar, an optical path length of 76 m and Lorentzian line shape have been selected for the calculation. The grey section indicates the absorption line which is measured with the 2f-WMS setup.

is achieved with four DFB-QCLs which are mounted on aluminum heat-sinks and connected to the laser electronics. The emitted laser beams are redirected with gold mirrors (PF-10-M03, Thorlabs, Newton, NJ, USA) towards beam-splitters (PFE10-M01, Thorlabs, Newton, NJ, USA), which combines the individual beams. When the laser beam hits the first splitter, $\sim 45\%$ of the optical power will be lost and the other $\sim 45\%$ are redirected to a second splitter. The beam will be splitted again, whereas one half passes a set of reference gas cells (Wavelength References, Corvallis, OR, USA) and hits a Mercury-Cadmium-Telluride (MCT) detector (PCI-4TE-9, 20 MHz bandwidth, Vigo Systems, Ozarow Mazowiecki, PL). The other half is reflected into the gas measurement cell (AMAC 76, Aerodyne Research, Billerica, MA, USA) and the attenuated beam is focused with an off-axis parabolic mirror (MPD149-M01, Thorlabs, Newton, NJ, USA) towards a second detector (PCI-2TE-12, 200 MHz bandwidth, Vigo Systems, Ozarow Mazowiecki, PL).

3.3.1. Lasers

The QCLs installed in the prototype are DFB devices, can be operated in cw-mode and are already assembled in high-heat-load (HHL) packages. The laser package includes a Peltier-cooler, a temperature sensor (NTC 10k) and a collimation lens. Due to the availability of cw-DFB-QCLs,

3. Development of a Multi-Gas-Analyzer for Ambient Air Monitoring

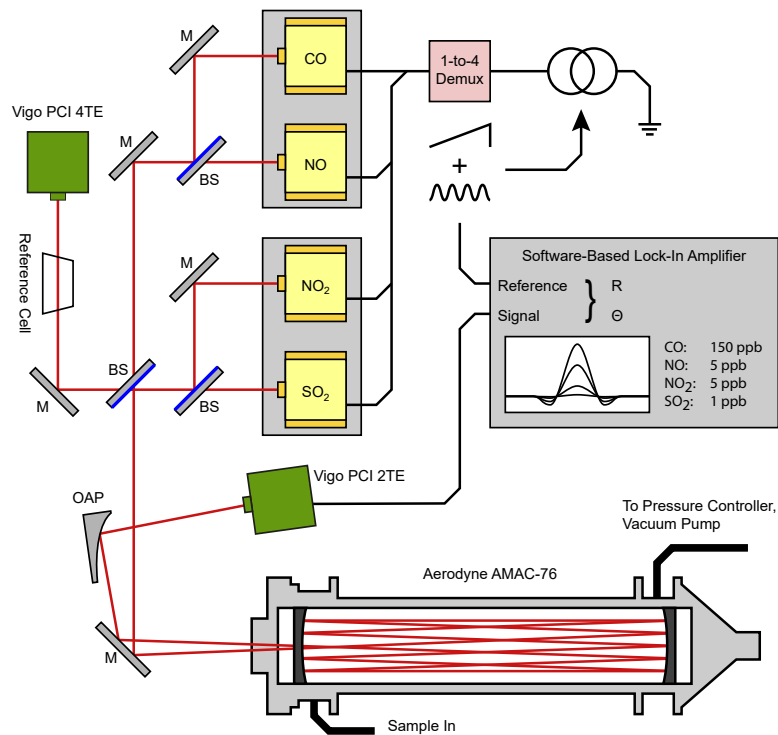


Figure 3.3.: Schematic of the setup.

three devices were from the company AdTech Optics (City of Industry, CA, USA) and one from Alpes Lasers (St. Blaise, CH). The most important laser parameters for a chip temperature of 25 °C are listed in Table 3.2 and are taken from the corresponding data sheets.

A picture and a section view of one of the packaged DFB-QCLs is shown in Figure 3.4. Each laser has been characterized with a laboratory FTIR-spectrometer (Vertex 80v, Bruker Optics, Ettlingen, DE) whereas the laser beam acted as the light source. Spectra were recorded at different gain-chip temperatures and laser currents (according the data sheets) to verify the single-mode operation and to identify possible mode-hops.

Target Analyte	Manufacturer	Device	Threshold Current (mA)	Max. Current (mA)	Wave-numbers (cm ⁻¹)	Max. Power (mW)
CO, N ₂ O	AdTech Optics	15-06	220	310	2179	50
NO	AdTech Optics	17-15	410	520	1900	40
NO ₂	AdTech Optics	17-17	490	670	1630	110
SO ₂	Alpes Lasers	507	630	650	1379	1

Table 3.2.: Laser parameters at 25 °C, according the corresponding data sheets.

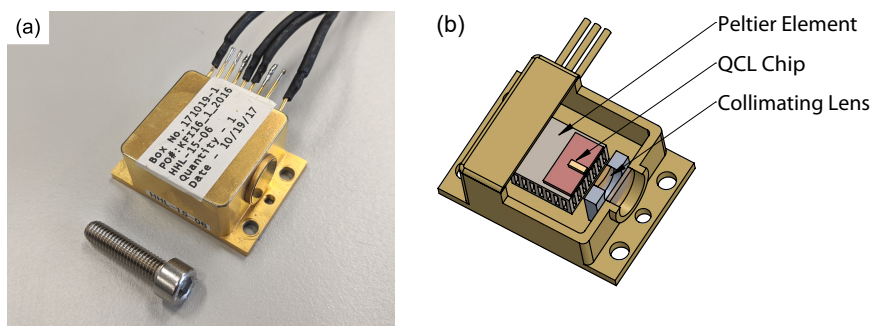


Figure 3.4.: (a): Picture of a high-heat-load (HHL) package and an M6x25-screw for scale. (b): section view of the HHL package, with the DFB-QCL, Peltier-cooler and the collimating lens inside.

3.3.2. Multipass Gas Cell

While measurement cells for the liquid phase have an optical path length between a few μm and up to several mm, gas cells are significantly longer. Depending on the application, they can be a few cm (e.g. quantifying the main components of a process stream) and exceed more than 200 m (e.g. for quantifying trace gases). Single-pass cells are usually a metal tube with IR transparent windows at the front and at the back and are limited by the dimensions of the experimental setup (typically <1 m). A longer optical path length can be realized with mirrors, reflecting the light multiple times.

Different cell designs have been developed over the time and the most prominent ones are the White cell [292], the circular multipass cell [293] and the Herriott cell [294]. The White cell consists of three spherical, concave mirrors with identical radius of curvature, and is illustrated in Figure 3.5a. The distance between the two objective mirrors (OM 1 and OM 2) and the field mirror (FM) is equal to the their focal length. It is a well established cell design and several improvements and applications have been reported over the time [295–297].

Circular multipass cells (Figure 3.5b) have the mirrors aligned in a circle and the recent improvements even employ the body itself as the reflecting mirror. This improves the robustness against vibrations and temperature changes and miniaturization is possible as well [298–301].

The Herriott cell, which is also installed in the prototype, is an improved version of a spherical mirror interferometer (Figure 3.5c) [302]. Here, two spherical mirrors with the focal length f are aligned coaxial at the distance d and match the condition $f \leq d \leq 4f$. An entering beam will be reflected multiple times in between, and the beam spots will either lie on a circle or an ellipse, depending on the input parameters. Under certain conditions, the beam will exit at the entry hole. In [294], Herriott and Schulte suggested to either insert a perturbing mirror or to replace

3. Development of a Multi-Gas-Analyzer for Ambient Air Monitoring

one or both of the spherical mirrors with astigmatic ones. The idea of the first modification is to slightly shift the last spot, lying on the previously mentioned ellipse, to enforce another round-trip between the spherical mirrors. The same effect can be realized with astigmatic mirrors, but it avoids the installation of another optical component.

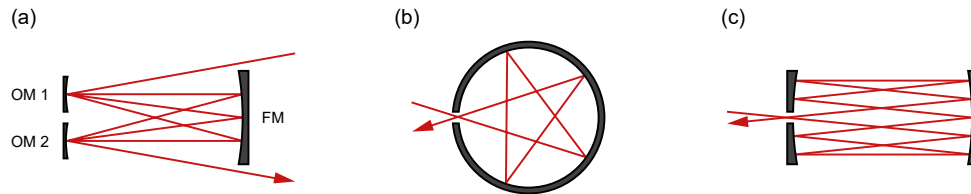


Figure 3.5.: Basic principle of three different types of multipass gas cells. (a): White cell, (b): circular multipass cell and (c): Herriott cell.

The coordinates x_i and y_i of the i -th beam spot on the astigmatic mirrors can be calculated according [303]:

$$x_i = X_0 \sin(i\Theta_x), \quad y_i = Y_0 \sin(i\Theta_y) \quad (3.1)$$

$$\Theta_x = \cos^{-1} \left(1 - \frac{d}{R_x} \right), \quad \Theta_y = \cos^{-1} \left(1 - \frac{d}{R_y} \right) \quad (3.2)$$

Here, the parameters X_0 and Y_0 define the overall dimension of the spot pattern on the mirror, d is the distance in between them, and R_x and R_y are the radii of the astigmatic mirror surface. The integer i counts the number of reflections whereas even values are spots on the entrance-mirror and odd values are spots on the back. The spot positions are sinusoidal with different frequencies and are similar to Lissajous curves. As the laser beam should exit the optical system at the same position as it enters, one can write the reentrance conditions

$$N\Theta_x = M_x\pi \quad \text{and} \quad N\Theta_y = M_y\pi. \quad (3.3)$$

Numerous combinations are possible for the integers N , M_x and M_y , but if the parameters M_x and M_y have common factors other than 2, the pattern will degenerate and the number of reflections will be reduced. In addition, N must be even, to place the exit- and entrance-spot on the same (front-) mirror. Another practical requirement is that spot positions next to the entrance should be avoided, to allow a larger input diameter.

Several useful values for N , M_x and M_y have been identified, tested in gas sensing prototypes and even commercialized. Two patterns of the input mirror are plotted in Figure 3.6 and the one shown in (b) corresponds to the beam pattern of the Herriott cell installed in the prototype (shown in Figure 3.7, parameters: $\{N, M_x, M_y = 238, 142, 134\}$ with a base path $d = 0.32$ m.

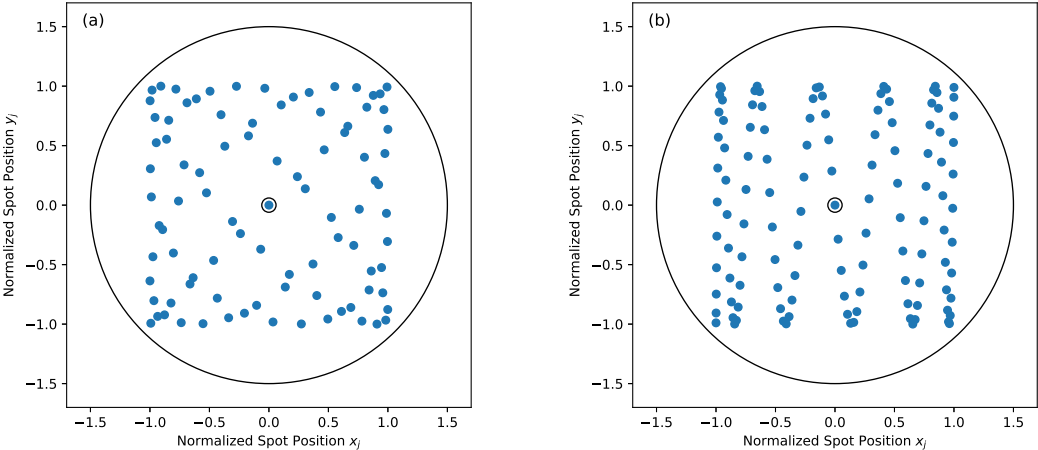


Figure 3.6.: Two beam pattern of the input mirrors of astigmatic Herriott gas cells. The following parameters were used: (a): $\{N, M_x, M_y = 182, 80, 76\}$, (b): $\{N, M_x, M_y = 238, 142, 134\}$. The spot at the coordinate $(0, 0)$ indicated with a black circle represents the input hole of the front mirror.

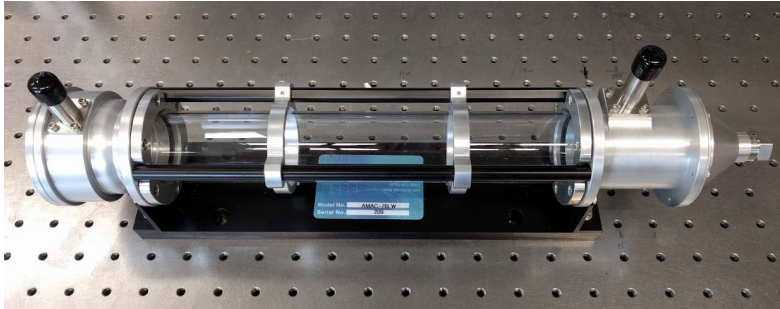


Figure 3.7.: Aerodyne AMAC 76 with 76 m optical path length.

3. Development of a Multi-Gas-Analyzer for Ambient Air Monitoring

This results in an optical path length of 76 m, which is sufficient to quantify the target analytes in the ambient air.

For practical applications, it is useful to set the distance between the mirrors close to their focal length (confocal spacing, $d \approx R_{x,y}$). This results in values of Θ_x and $\Theta_y \approx \pi/2$ and the first reflection on the back mirror will be close to the relative coordinate (1, 1), simplifying the alignment of the laser beam. In addition, it is common to rotate the axis of both mirrors by 45° . This lets the entering and output beams be parallel to the xy-plane (e.g. the optical table) and reduces the installation time further.

These multipass gas cells are commercially available in different lengths (e.g. classical Herriott cells: 3 m, 10 m, 15 m, 31 m; with astigmatic mirrors: 36 m, 76 m, 100 m, 210 m). The version with 76 m has been selected as it is a compromise of the outer mechanical dimensions and the achievable optical path length.

3.3.3. Detector

In general, two main types of IR detectors can be identified, namely thermal and photonic ones. The first one relies on thermal effects, such as changing the resistance or the thermoelectric effect. Due to their type of operation, they are relatively slow and their bandwidth is <10 kHz, depending on the detector material. As they are operated at room temperature, they are cost effective and often used in filter-based gas-sensors or maintenance-free FTIR spectrometers.

Photonic detectors, in contrast, are based on semiconductors with a bandgap, that is sufficient small, to be triggered by an infrared-photon. To limit the thermal noise, they have to be either cooled with liquid N_2 ($-196^\circ C$), or equipped with multi-stage Peltier coolers ($<-70^\circ C$). Depending on their preamplifier, the electrical bandwidth is in the MHz-range and goes up to 1 GHz.

The prototype is equipped with two MCT detectors, whereas one acts as a reference detector (the laser beam passes the gas reference cells) and the other one is used to measure the light passing the gas measurement cell. As the multi-gas-sensor was initially designed for 2f-WMS experiments only, the selected reference detector supports a bandwidth of 20 MHz (PCI-4TE-9, Vigo Systems, Ozarow Mazowiecki, PL, also shown in Figure 3.8). With the integration of HPSDS, the bandwidth of the measurement detector must be at least in the order of the laser modulation. Subsequently, an MCT detector with 200 MHz has been selected (PCI-2-TE-12, Vigo Systems, Ozarow Mazowiecki, PL).

3.4. Electronics and Additional Components

Recording 2f-spectra requires, beside the lasers, optics and detectors, several electronic components to operate and control these. The QCLs, for example, depend on a current supply with high precision (also known as laser driver) and accurate temperature control of the gain element. The detector signal must be digitized to be further processed with the measurement PC (software-based lock-in amplifier) and the pressure in the gas cell must be stabilized at 100 mbar.

Considering that the main priority of this prototype has been to demonstrate the applicability of 2f-WMS for ambient air monitoring, the optimization of the electronics was secondary. Building the prototype with off-the-shelf components reduces time-consuming hardware development and can still be done in a later stage of commercializing the prototype. One of the drawbacks of not optimizing the electronics is the number of individual power supplies. With components from different manufacturers, it is necessary to install a series of power supplies, as listed in Table 3.3.

With these power supplies and the measurement PC, it is possible to operate and control the electronic parts, which are discussed further in detail.

3.4.1. Laser Driver and Demultiplexer

From the electronic point of view, QCLs behave like diodes, operated in forward direction at relatively high voltages ($\sim 12-18$ V) and moderate currents ($\sim 100-1000$ mA). As the optical power



Figure 3.8.: Mercury-cadmium-telluride-based IR detector with an integrated Peltier-cooler and preamplifier (M6x25-screw for scale).

3. Development of a Multi-Gas-Analyzer for Ambient Air Monitoring

Device	Electrical Parameters	Purpose
Mean Well SP-480	24 V, 20 A, 480 W	Powers the TEC controllers, the pressure controller, the data acquisition card NI6366, the signal generator for HPSDS and the fans installed in the optics case.
Mean Well MDR-40	12 V, 3.3 A, 40 W	Connected to the MCT detectors.
2x TDK-Lambda HWS 50A-24/A	24 V, 2.2 A, 50 W	Low noise power supply for the laser driver.
HKC V-Power 450	450 W	ATX power supply for the measurement PC.

Table 3.3.: Several power supplies are required to operate the electronic components, such as the laser driver, the detectors and the TEC controller.

and the emitted wavelength depend strongly on the injected laser current and its temperature, it is of utmost importance to control these parameters as precise as possible.

While it is sufficient for a laser diode installed in a laser pen to connect a constant current circuit (Figure 3.9a), NIR diode lasers and QCLs used for spectroscopic applications require a more sophisticated control of the laser current. One approach to improve the current source is illustrated in Figure 3.9b, whereas a transistor is added in serial to the laser diode. A shunt resistor feeds a voltage, which is proportional to the laser current, to the inverting input of an operational amplifier. As its non-inverting input is connected to a signal source (e.g. a voltage divider), the output current will be adjusted so that the currents at its inputs are equal. This output current controls the base connector of an npn-transistor and regulates the current flowing from the emitter through the laser diode.

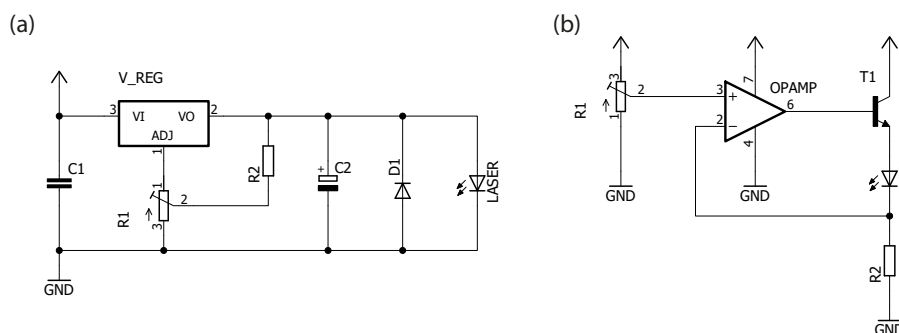


Figure 3.9.: Two basic concepts of laser drivers, based on (a): a voltage regulator and (b): a transistor, controlled with a shunt resistor and an operational amplifier.

The concept of this constant current source can be improved in several ways [247, 304–309]

3.4. Electronics and Additional Components

and low-noise laser drivers are nowadays based on high-precision voltage references and have several other features. The most important ones are a modulation input, a set-point input, a current-monitor output, a current-limitation circuit and additional laser protection. The laser driver installed in this prototype is the model QCL1000 OEM (Wavelength Electronics, Bozeman, MT, USA) and supports a maximum output current of 1 A.

As the installed data acquisition card NI6366 (8x 16 bit ADC, 2x 16 bit DAC, National Instruments, Austin, TX, USA) supports only two analog outputs (one for the lock-in amplifier reference signal, the other to control the laser driver), it has been decided to measure one analyte after another by redirecting the laser current to the desired QCL. This has been realized with a demultiplexer which consists of a commercial available relays module with four channels (SainSmart Technology, Lenexa, KS, USA). It disconnects the QCL from the laser driver and, as soon as the correct settings has been loaded in the software, it activates the corresponding QCL for measuring the next analyte.

The consequence is that the analytes can only be measured one after another, but taking into account that the *Directive 2008/50/EC* requires only one measurement value every 30 min, and assuming that the composition of the air (traffic in the area, exhaust gas of industrial plants) does not change tremendously within this time period, this simplification is acceptable for this prototype. It reduces the number of laser drivers, requires less components and saves space in the electronics rack. However, from the technical point of view, it would be possible to quantify all required gases at the same time. The underlying technique is known as frequency modulation multiplexing, whereas the lasers are operated simultaneously and modulated at different sine frequencies, as presented in [310]. The individual 2f-WMS spectra are then extracted with lock-in amplifiers, whereas the correct reference frequencies have to be used.

3.4.2. Temperature Control

DFB-QCLs can be typically tuned over $1\text{-}3\text{ cm}^{-1}$ by changing the injection current and keeping the temperature of the gain element constant. The joule heating caused by the electrical resistance influences the refractive index of the gain material and changes the emitted wavelength. Due to the relatively small thermal mass, the emitted wavelength can be influenced with the laser current up to the high kHz range and is actually the underlying property for 2f-WMS.

Changing the temperature of the gain element by heating/cooling its sub mount directly, gives access to a much wider tuning range (up to $\sim 10\text{ cm}^{-1}$). This depends strongly on the gain

3. Development of a Multi-Gas-Analyzer for Ambient Air Monitoring

material and the allowed operation range given by the laser manufacturer. The tunability by temperature helps, on the one hand, to find optimum laser parameters for a certain wavelength, but, on the other hand, requires a precise temperature control to avoid drifting from the desired wavelength. To address this, QCLs are usually installed in a HHL, TO-8 or similar package and equipped with a Peltier element and a temperature sensor. A temperature controller is then connected and regulates the current flowing through the Peltier and stabilizes the temperature of the gain element.

Each laser installed in the prototype is equipped with a dedicated thermoelectric cooler (TEC) controller (TEC-1091, Meerstetter Engineering, Rubigen, CH). As the heat from the Peltier element is spread via the HHL package, the aluminum plate where the lasers are mounted on, is temperature stabilized as well. Here, a two channel TEC controller is installed (TEC-1122, Meerstetter Engineering, Rubigen, CH).



Figure 3.10.: Temperature controller TEC-1091 with an M6x25-screw for scale.

3.4.3. Pressure Control

During the field experiments, the sample port is defined by the project partners and a PTFE-tubing connects the prototype to a glass-made manifold. A 5 μm particle filter protects the measurement cell from dust and aerosol in general. The gas stream to be analyzed (ambient air or calibration gas, depending on the experiment) passes a pressure controller (GSP-C5SA, Vögtlin Instruments, Aesch, CH) before entering the gas cell. It guarantees a stable and precise pressure which is mandatory for measuring ro-vibrational absorption lines in the mid-IR. For most measurements, the set point was 100 mbar, which guarantees a sufficient flow rate and reduction of the FWHM of the ro-vibrational absorption lines.

As shown in Figure 3.11, the outlet from the gas cell is connected to a laboratory vacuum pump (N860.3FT.40.18, KNF Neuberger, Freiburg, DE), which transports the gas to be analyzed

3.4. Electronics and Additional Components

through the gas cell. An additional needle valve keeps the volume flow through the the pressure controller within its flow limits, defined by the geometry/dimension of the regulating valve.

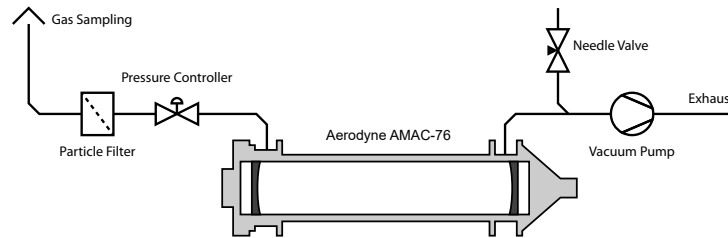


Figure 3.11.: Schematic of the piping. A pressure controller and a laboratory vacuum pump ensure a stable pressure of ≈ 100 mbar in the gas measurement cell.

3.4.4. Modifications for HPSDS

Implementing HPSDS in an existing 2f-WMS setup requires only minor modifications, which can be done with off-the-shelf parts. The optical three tone signal is realized by modulating the DFB-QCL and a bias tee circuit (ZFBT-6g+, Mini-Circuits, Brooklyn, NY, USA) combines the relatively constant laser current, generated by the laser driver, with the high-frequent modulation signal. This part is common for e.g. powering low noise amplifiers in antenna systems, and consists of a coil and a capacitor. While the coil passes the almost constant laser current to the output, it blocks the high-frequent modulation signal, connected at the capacitor. Vice versa, the capacitor transmits the radio signal (typically in the high MHz region) and blocks the laser current. Subsequently, the output of the bias tee is the sum of the laser current (also known as DC or direct current) and the modulation signal (RF, radio frequency). The DC-part lets the laser emit light and the RF-component enforces the amplitude modulation, generating the optical three tone signal.

Measuring the dispersion, caused by the presence of the analyte requires a detector that supports the electrical bandwidth of the modulation frequency. The output signal could be directly analyzed with a fast enough lock-in amplifier, but in order to employ the already installed software-based one (limited by the sample rate of the data acquisition card, 1 MSPS), the signal must be converted to a lower frequency. To do so, the signal is down-mixed by multiplying it with a slightly lower modulation frequency (ZAD-1-1+, Mini-Circuits, Brooklyn, NY, USA). Isolating the phase component with the software-based lock-in amplifier is achieved by demodulating at the difference frequency.

3. Development of a Multi-Gas-Analyzer for Ambient Air Monitoring

The first tests were performed with a laboratory signal generator (Rigol DG4162, RIGOL Technologies, Suzhou, CN) and the beat note was down-mixed to 10 kHz (ZAD-1-1+, Mini-Circuits, Brooklyn, NY, USA). A second mixer (ZLW-1-1+, Mini-Circuits, Brooklyn, NY, USA) produced the phase stable reference signal for the software-based lock-in amplifier, as presented in Figure 2.24.

The mechanical dimensions of the Rigol DG4162 are acceptable for lab experiments, but it does not fit in the electronics rack of the prototype. Therefore, it was replaced with a dedicated microchip for generating sine waves of different frequencies. In detail, the evaluation board with the chip AD9959 (Analog Devices, Norwood, MA, USA) was installed. It features four synchronized Direct Digital Synthesis (DDS) channels with up to 200 MHz. The frequency (32 bit), phase (14 bit) and amplitude (10 bit) can be controlled individually for each channel. The common clock generator guarantees a stable phase between the four outputs. With this chip it is possible to replace the lab-bench signal generator and one analog mixer too, as shown in Figure 3.12.

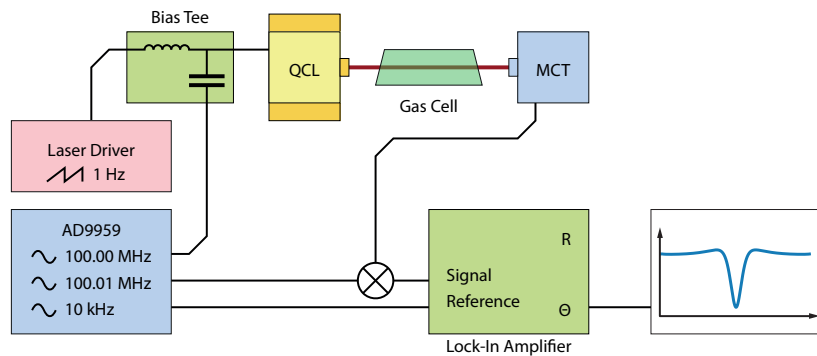


Figure 3.12.: Hardware modification required for HPSDS with AD9959 (four channel DDS).

3.5. Software

The prototype is controlled with a custom developed software, written in LabVIEW 2017 (National Instruments, Austin, TX, USA) which has several advantages, compared to other languages and development suites. For example, the graphical environment allows developers to understand programs faster than conventional text-based code. This is possible with the data-flow model whereas data/values are transported in wires and functions are realized with icons, that are connected with these wires. Numerous functions are implemented by default, ranging from basic input-/output-operations like saving and reading text-files up to advanced mathematics functions, like the FFT and matrix operations.

A special feature of LabVIEW 2017 is the perfect integration of the hardware components, sold by the company. This can be, for example, simple temperature sensors, low-cost ADCs with sample rates of several kS/s, or even high-speed digitizers based on FPGAs. Compared to other hardware manufacturers on the market, controlling the measurement equipment is straight-forward and numerous software examples and tutorials are available.

In addition, the software contains a large variety of user interface elements, such as tables and graphs. They are easy to integrate into the program and can be customized in different ways. With these it is possible to develop user friendly interfaces that are intuitive and flexible at the same time.

The software itself is based on the *Producer/Consumer*-architecture, which is a common way to write responsive programs in LabVIEW 2017 [311]. Here, the user interactions are separated from the tasks that are either time consuming or should run in the background continuously. An event handler is placed in a while loop and waits, for example, until the user presses a button to start the data acquisition. The corresponding event case contains only code that can be immediately executed, such as configuring the measurement channel or setting the data rate. The time-consuming code, in this example reading the data for several minutes, is located in an dedicated while loop and it should start as soon as the measurement channel is configured. The synchronization of these independent while loops is achieved with a queue, that can be interpreted as a First-In-First-Out (FIFO) buffer. The event handler, also known as the *producer*, inserts an element into this queue to trigger the waiting while loop. The second while loop removes the element for the queue (*consumer*) and records the signal. With this programming approach, it is possible to keep the user interface responsive, run multiple tasks in parallel and split the code into smaller sections.

The block diagram (LabVIEW code) for the multi-gas-analyzer is shown in Figure 3.13 and the tasks of the corresponding while loops are commented. The producer, located at the top, contains event cases for each button that can be pressed on the front panel (Figure 3.16). It is, for example, responsible to load the default settings when starting the software, lets the user adjust the laser parameters and starts/stops recording 2f-spectra. The consumer loops are below and each hardware component has its dedicated section. This allows to structure the code and makes it easier to adjust the code if certain hardware components are replaced or modified.

While the code for the TEC controller, the pressure controller, the laser demultiplexer and the data logging is relatively simple, the consumer loops for recording the spectra is more complex and should be explained in detail. The laser driver is controlled with an analog signal, that is

3. Development of a Multi-Gas-Analyzer for Ambient Air Monitoring

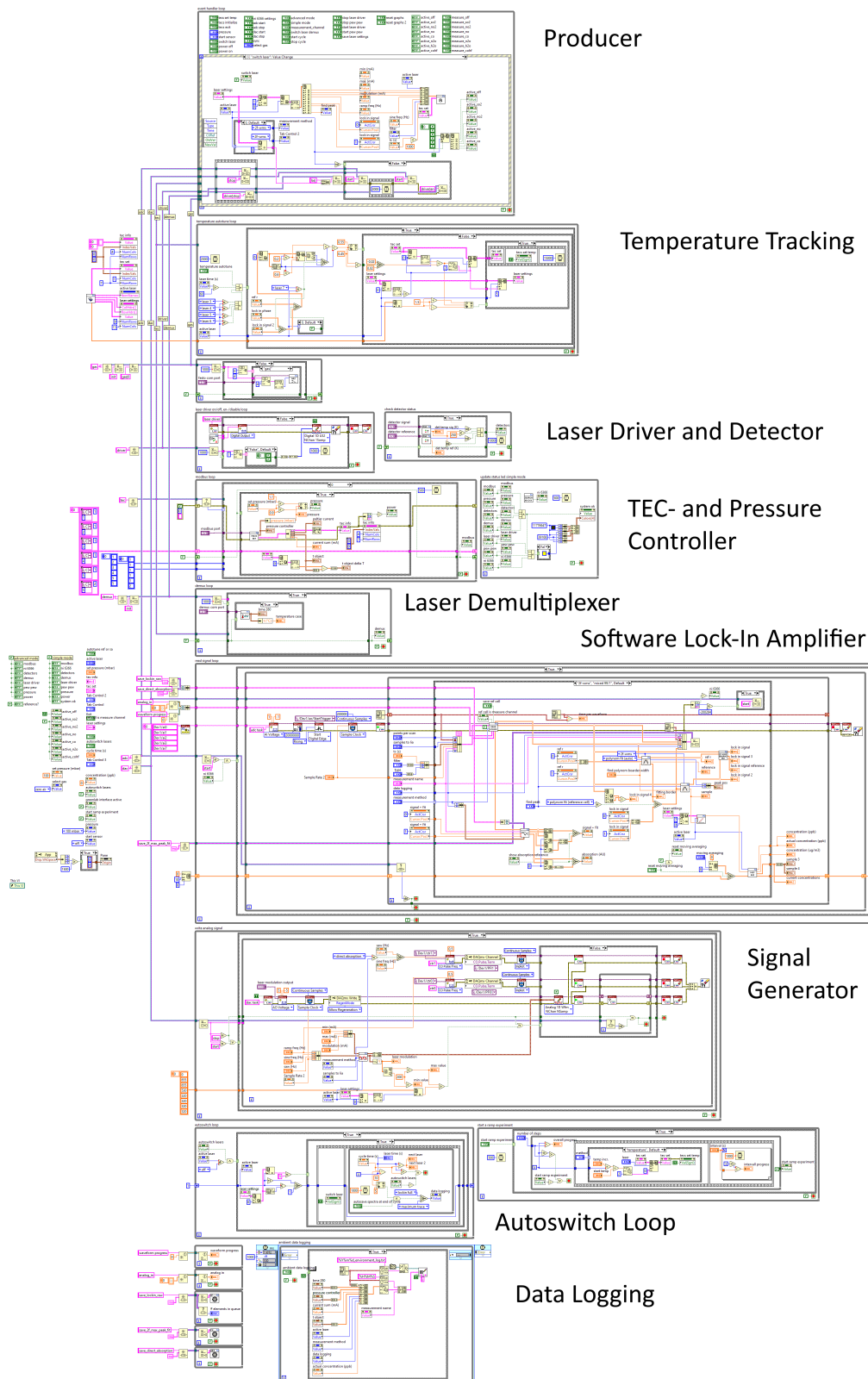


Figure 3.13.: Block diagram of the software for the prototype. The *producer* at the top handles all user interactions, the other while loops act as *consumer* and interact with the hardware components.

the sum of a slow sawtooth-like ramp (e.g. 1 Hz), for tuning across the absorption line, and a sine wave (e.g. 20 kHz), required to modulate the laser wavelength. The code in Figure 3.14 is responsible for this task. It reads the laser settings and creates a waveform that is fed into the laser driver. As the software lock-in amplifier requires a reference signal too, a second waveform with the sine wave only is generated. A digital trigger indicates the beginning of a new current ramp and synchronizes the spectrum acquisition.

The code for reading the detector signal is slightly more complex (Figure 3.15) as it calculates the gas concentration as well. Digitizing the analog signals of both detectors and the modulation-reference begins when a new current ramp is started (internal digital trigger). Smaller pieces of the signal (typically corresponding to 1 ms) are analyzed with the software-based lock-in amplifier and recorded while the laser tunes across the absorption feature. The result is the already discussed $2f$ -spectrum whereas the peak height at the center of the absorption line is proportional to the concentration of analyte (under certain conditions). As the peak maximum itself might be influenced by noise, one can fit a parabolic function at the center of the peak and get a more reliable value. Finally, the concentration of the target analyte is calculated with a linear calibration. It has been useful to apply a moving averaging filter over 10 s to reduce the noise further.

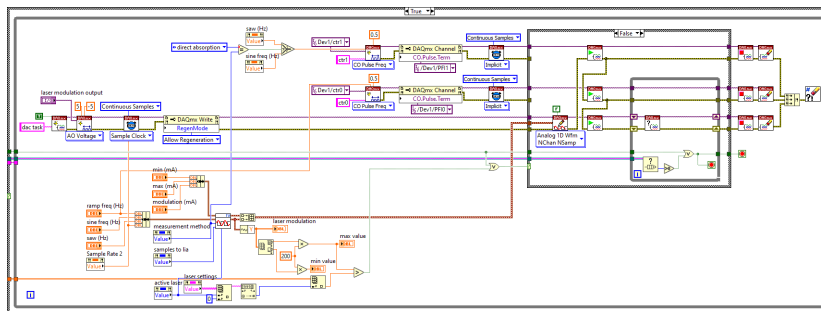


Figure 3.14.: LabVIEW-code for generating the waveform (sine wave plus sawtooth ramp) to control the laser driver. An internal trigger signal indicates the beginning of a spectrum.

The user interface contains two modes, which are shown in Figure 3.16. The advanced version (Figure 3.16, left) is designed for experiments in the lab and lets the user modify all parameters, ranging from the laser-temperatures over the modulation frequency up to the filter settings of the software-lock-in amplifier. The smaller one is optimized for a 7" LCD screen (1024 × 600 pixel), installed in the front of the electronics rack. It is intended for field experiments, where the operator should only be informed about the current device status and the measured concentrations.

3. Development of a Multi-Gas-Analyzer for Ambient Air Monitoring

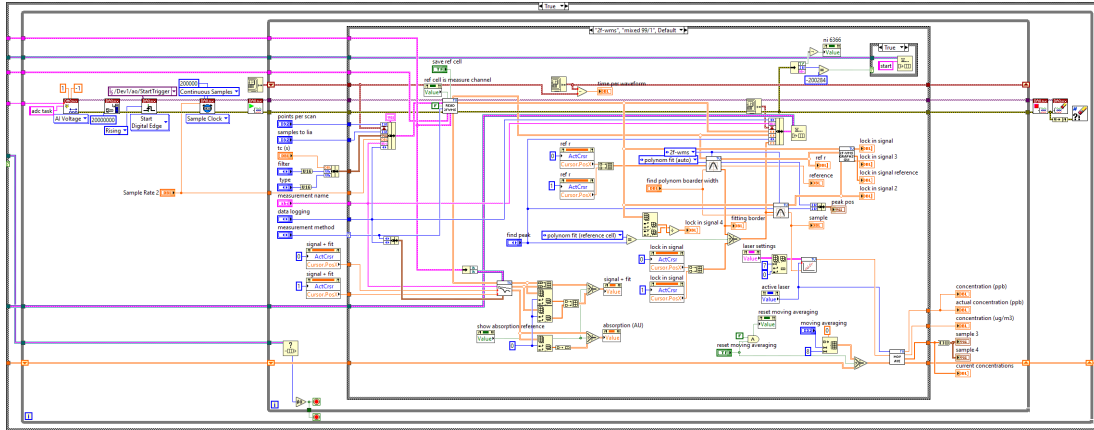


Figure 3.15.: LabVIEW-code to extract the 2f-spectrum from the detector signal. The peak at the center of the absorption feature is fitted with a parabolic function and its height is proportional to the concentration of the analyte.

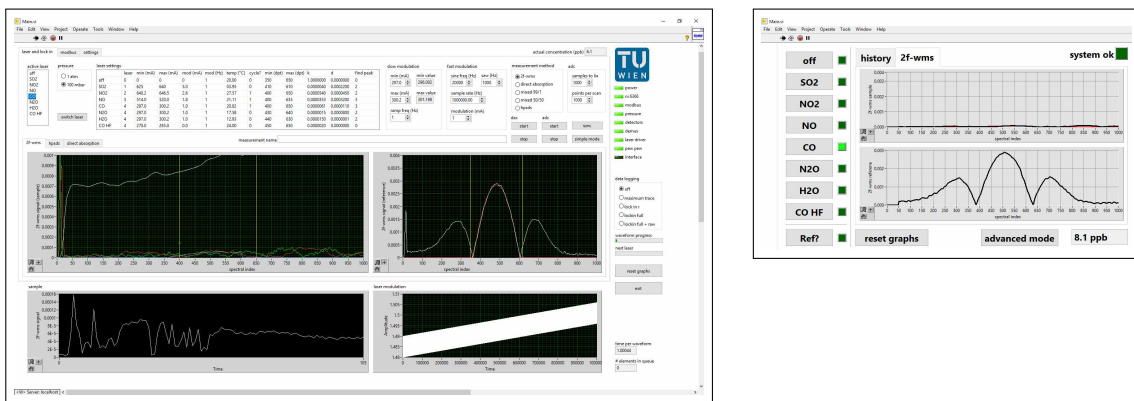


Figure 3.16.: User interface of the prototype - the *Advanced Mode* (left) is designed for experiments in the lab and allows access to all settings. The *Simple Mode* (right) is optimized for the LCD screen in the electronics rack and is intended for field campaigns.

3.6. Mechanical Layout

Several measures have been taken to make the multi-gas-analyzer transportable and ready for commercialization. First of all, the bulky electronic components (power supplies, measurement computer, laser driver, ADC/DAC module) are separated from the optics, lasers and the TEC-controllers. Therefore, the complex setup is split into two sub-assemblies, each installed in a 19" server rack (IPC 4U-4129-N, outer dimensions: $48 \times 18 \times 65$ cm, Inter-Tech Elektronik, Langenhagen, DE). Figure 3.17 shows both cases opened. The rather simple electronics rack contains the measurement PC and uses mountings according the ATX-standard to install DIN rails [312] for the 12 V and 24 V power supplies. The cases are connected with a set of cables, which allows to use the equipment with other experiments in the future (1x USB, 2x 12 V DC, 1x 24 V DC, 4x BNC cables).

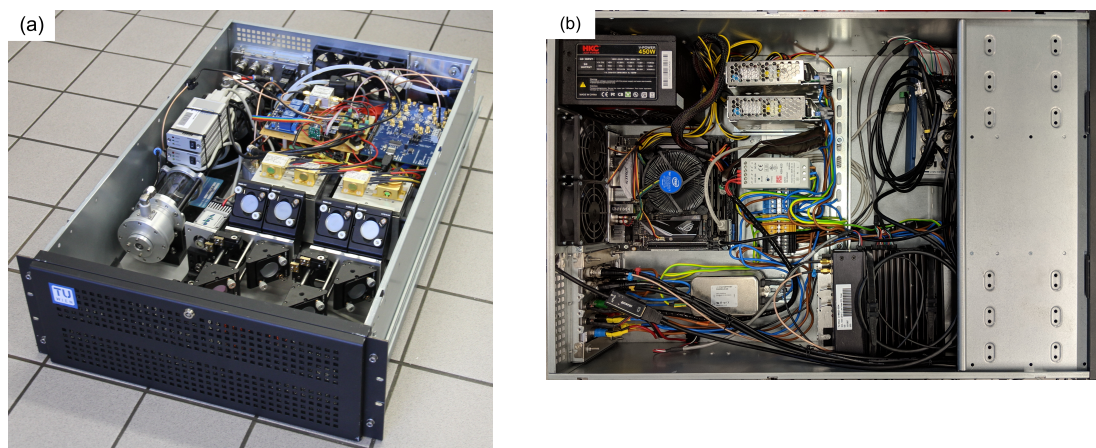


Figure 3.17.: Pictures of the optics (a) and electronics (b) of the prototype. The assembly fits in two 19" racks (height: ≈ 18 cm, depth: 65 cm).

Second, the number of different optical (mirrors, beam splitter) and opto-mechanical components (kinematic mounts, gimbals) has been kept as low as possible, to avoid mixing up parts during assembly. In addition, they are manufactured by a major supplier, guaranteeing quick delivery and long term availability.

Third, the breadboard and certain metal plates have been manufactured by a metal workshop (Schaeffer, Berlin, DE). This custom breadboard is not only thinner compared to commercial ones, it also fits perfectly into the 19" server rack and features threads for a TEC controller, the gas measurement cell and a DIN rail. The CAD drawings of these custom parts can be found in Appendix D.

3. Development of a Multi-Gas-Analyzer for Ambient Air Monitoring

Fourth, an LCD-screen with touch-functionality (7" Capacitive Touch Screen, Waveshare Electronics, Shenzhen, CN) has been installed on the front of the electronics rack (visible in Figure D.1). The customer can directly read the current status of the prototype and interact with the automated measurement software, without requiring an additional computer to log into the system.

Keeping the overall dimensions of the optical setup and the electronics within the initially defined limits has been achieved by intensive planning with CAD software (SolidWorks 2016, Dassault Systems, Velizy-Villacoublay, FR). The result is a digital model of the prototype that contains all optical components, mechanical parts and electronics. The sectional drawings, shown in Figure 3.18, gives a precise overview of the optical beam path and how the laser beams must be aligned to couple into the gas measurement cell.

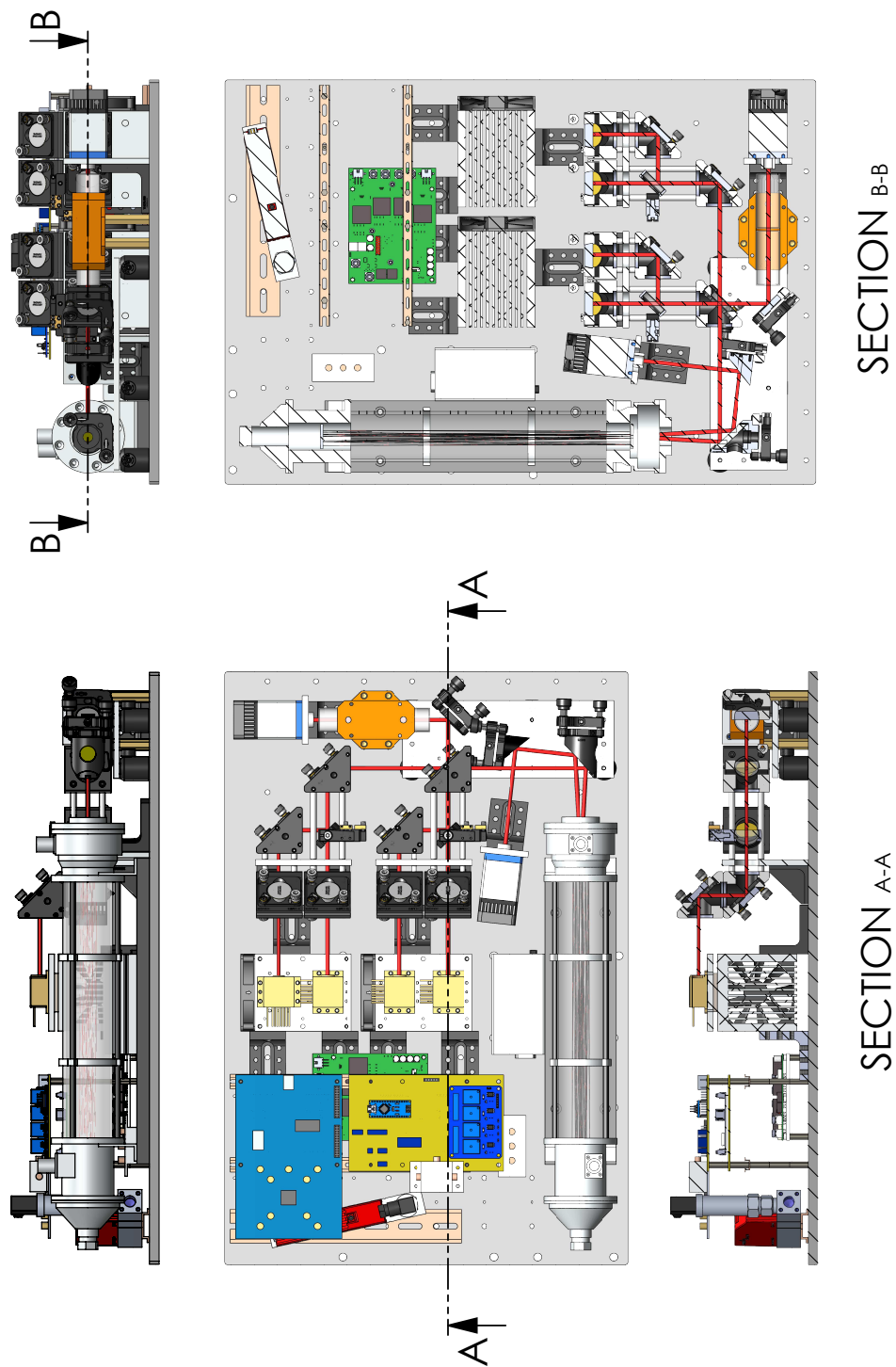


Figure 3.18.: Construction drawings of the multi-gas analyzer. The beam paths of the lasers are illustrated with red rods and is simplified in Figure 3.3. Sectional drawings allow a better understanding of the optical path.



Die approbierte gedruckte Originalversion dieser Dissertation ist an der TU Wien Bibliothek verfügbar.
The approved original version of this doctoral thesis is available in print at TU Wien Bibliothek.

4. Experiments and Results

Designing and assembling the prototype are the first steps in developing a new measurement device. Although QCLs are commercially available since two decades, their electrical and emission properties vary from device to device. While it is obvious that a different gain material requires completely different parameters, even devices, processed on the same wafer are not identical in terms of mode-hop-free emission and operation range. Subsequently, characterizing each QCL is of utmost importance before installing it in the prototype.

With the QCLs installed, the beams aligned to pass the gas measurement cell and hitting the detectors, one can optimize the laser parameters and evaluate the performance of the multi-gas-analyzer. To do so, 2f-spectra with different concentrations of the individual analytes have been recorded. These calibration experiments allow to verify the linearity of the sensor and to estimate the limit of detection (LOD).

While the experiments in the lab represent the performance under controlled conditions, measurement campaigns in the field show the robustness and stability of the prototype for the intended application in ambient air monitoring. Two successful measurement campaigns have been performed with the multi-gas-analyzer, whereas one was located in an industrial area (Szombathely, HU) and the other one next to a busy main road (Hietzinger Kai, Vienna, AT).

4.1. Identifying the Optimum Laser Parameters

4.1.1. FTIR Spectra

It is recommended, to characterize a new QCL before installing it in a prototype or experimental setup, as it allows to validate the properties stated by the manufacturer. In addition, one gains information on the tuning behavior, its spectral emission (single- vs. multi-mode) and the parameters where mode-hops occur. To evaluate the laser properties, the device is connected to

4. Experiments and Results

the TEC controller and laser driver, mounted next to an FTIR-spectrometer, and the beam points towards the input window for an external light source. Single-channel spectra are then recorded at different laser parameters (changing the temperature of the gain element and applying different laser currents) and interpreted.

Plotting the wavelength of the peak maxima against the laser current gives detailed information on the tuning behavior and helps selecting the laser settings to emit at the absorption line of the analyte to be measured. The ideal result of such a laser characterization is single-mode-emission within the defined operation range. Moreover, the relation between laser current and the emitted wavelength at a constant laser temperature should be continuous, indicating mode-hop-free operation.

The results of the laser characterization for the four DFB-QCLs are plotted in Figure 4.1. One can see that the devices for CO (Figure 4.1a) and SO₂ (Figure 4.1d) emit single-mode and mode-hop free, as the data-sets of different temperatures do not cross/overlap. In contrast, the QCLs AdTech 17-15 (Figure 4.1b) and AdTech 17-17 (Figure 4.1c) have mode-hops. In the case of the laser for NO, this effects only a relatively narrow spectral range. As mode-hops affect the measurements by a sudden change in the wavelength and emitted intensity, it is not recommended to employ this QCL for any precise 2f-WMS experiments around $\approx 1902 \text{ cm}^{-1}$, to avoid misleading results. By increasing the laser temperature and reducing the injection current or vice versa, it is possible to find laser parameters where the laser emits at the desired wavelength without risking mode-hops during the measurement.

4.1.2. Fine-Tuning the Laser Parameters and Modulation Depth

The results from the characterization with the FTIR-spectrometer deliver coarse values for the laser current and temperature. After installing the QCLs in the setup, aligning the optics and filling the gas measurement cell with the target analyte at the desired pressure, the final laser parameters have been selected. Considering the data acquisition rate of 1 MSPS and requiring 1000 data points for each lock-in process step, the final 2f-WMS spectrum consists of 1000 points. To guarantee a reasonable resolution, the laser parameters have been adjusted that the FWHM of the absorption line corresponds to ≈ 200 data points. This guarantees a fast acquisition rate of one spectrum per second and a reasonable resolution of the characteristic 2f-WMS signal.

As the peak height and the shape of the recorded spectra depend strongly on the modulation index of the laser, this parameter has been optimized too. Again, the gas cell has been filled

4.2. 2f-WMS Performance Under Laboratory Conditions

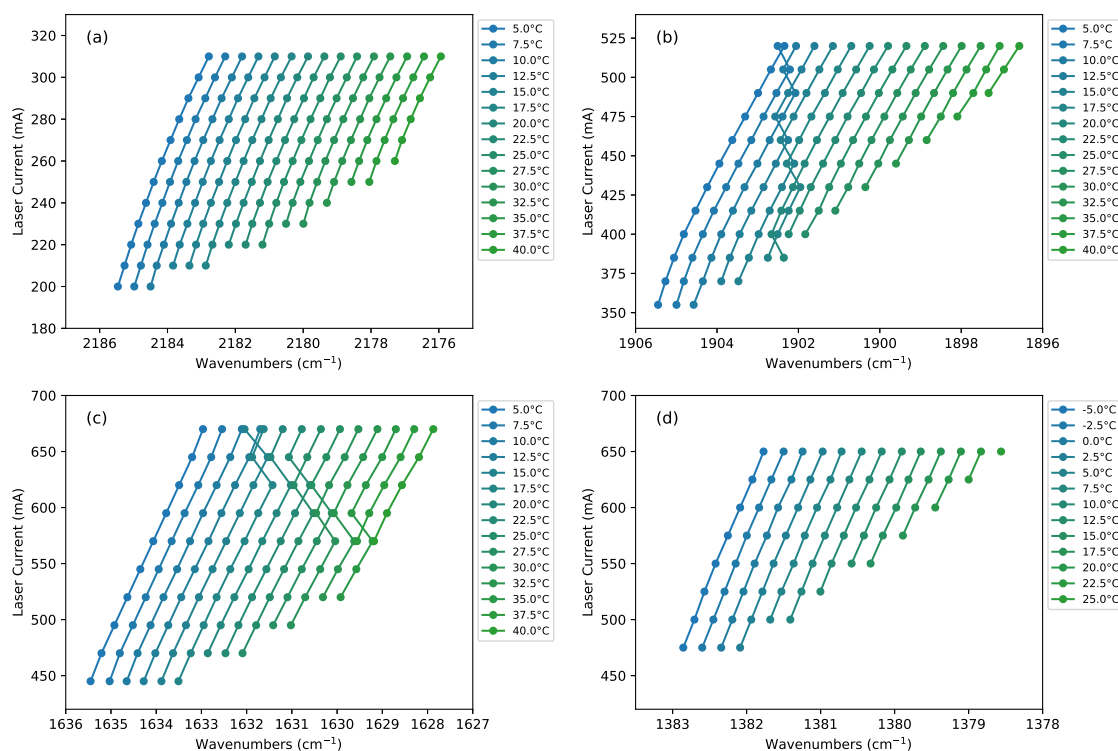


Figure 4.1.: Results of the characterization of the DFB-QCLs. Spectra at different laser currents and gain-element-temperatures have been recorded and the wavelength of its peak maximum is plotted. (a) AdTech 15-06, (b) AdTech 17-15, (c) AdTech 17-17, (d) Alpes 507.

with a defined concentration and set to a pressure of 100 mbar. The amplitude of the sine-wave modulation has been increased in a step-wise manner and the maximum of the 2f-WMS peak was recorded. The normalized peak amplitude for all analytes is plotted in Figure 4.2 and the maximum signal is achieved with a modulation index m between 2.2 and 2.5. This is in good agreement with theory, which expects an optimum modulation index of 2.2. The final laser parameters, including the laser temperature, the range of the sawtooth-shaped current ramp and the amplitude of the sine-wave modulation, are listed in Table 4.1.

4.2. 2f-WMS Performance Under Laboratory Conditions

4.2.1. Calibration Curves

A common way to characterize the performance of a sensor is to test if the output signal/the generated values correlate with the analyte content. From the already discussed theory, one

4. Experiments and Results

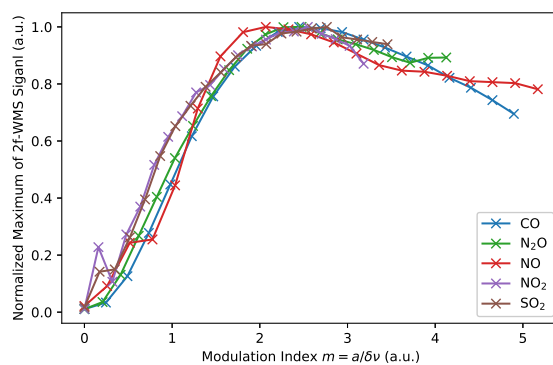


Figure 4.2.: The 2f-WMS signal is maximized if the modulation amplitude corresponds to ≈ 2.2 times the HWHM of the absorption line.

Target Analyte	Laser	Wave-numbers (cm^{-1})	Temperature ($^{\circ}\text{C}$)	Current Ramp (mA)	Modulation (mA)
CO	AdTech 15-06	2179.77	20.85	297.0-300.2	1.0
N ₂ O	AdTech 15-06	2180.40	17.61	297.0-300.2	1.1
NO	AdTech 17-15	1900.08	21.09	514.0-520.0	1.6
NO ₂	AdTech 17-17	1630.33	27.57	640.2-646.5	2.8
SO ₂	Alpes 507	1380.93	3.95	625.0-640.0	5.2

Table 4.1.: Laser parameters used for the experiments.

4.2. 2f-WMS Performance Under Laboratory Conditions

Target Analyte	Calibration R ²	SNR at 100 ppbv, 1 Hz Sample Rate	1 σ Detection Limit (ppbv), 1 Hz Sample Rate
CO	0.99918	308	0.32
N ₂ O	0.99798	40	2.51
NO	0.99998	224	0.45
NO ₂	0.99990	233	0.43
SO ₂	0.99978	71	1.40

Table 4.2.: Linear response and detection limits calculated from the calibration for the individual target analytes.

expects a linear relation between the peak height of the 2f-spectrum and the concentration of the target analytes (to be more precise: concentrations ≤ 500 ppbv with this prototype and the target analytes).

Although it would be possible to perform calibration-free 2f-WMS measurements [217–219], the prototype has been calibrated with an in-house developed gas mixing rig. It consists of four mass flow controllers (GSC-B9TS-BB23, Vögtlin Instruments, Aesch, CH) and allows to combine up to four different gas streams. For the experiments, test gas bottles, filled with the target analyte (≈ 1 ppmv in N₂, Air Liquide Austria, Schwechat, AT), and pure N₂ (N₂ 5.0, Messer Austria, Gumpoldskirchen, AT) have been connected to two of the mass flow controllers and a LabVIEW-based software increased the concentration of the target analyte in a step-wise manner. Each step was held constant for 5 min and the calibration range was 0-500 ppbv for the analytes CO, N₂O, NO and NO₂. Due to the relatively small cross-section of SO₂, the calibrated concentration range was set to 0-1000 ppbv and the number of measurement steps was reduced as well. The 2f-spectra, the peak-height during the calibration sequence as time-trace and the final linear fits are plotted in Figure 4.3. The insets in the column "Calibration Time-Series" show the signal at 100 ppbv of the analyte. The residuals of the linear fit are also plotted as an inset (3rd column). For completeness, the 1f- and 3f-spectra can be found in Appendix B.

The limit of detection (LOD, 1σ) has been derived from the signal to noise ratio at an analyte concentration of 100 ppbv and 30 data points (corresponding a measurement time of 30 s) have been used for the calculation. The detailed results are listed in Table 4.2.

4. Experiments and Results

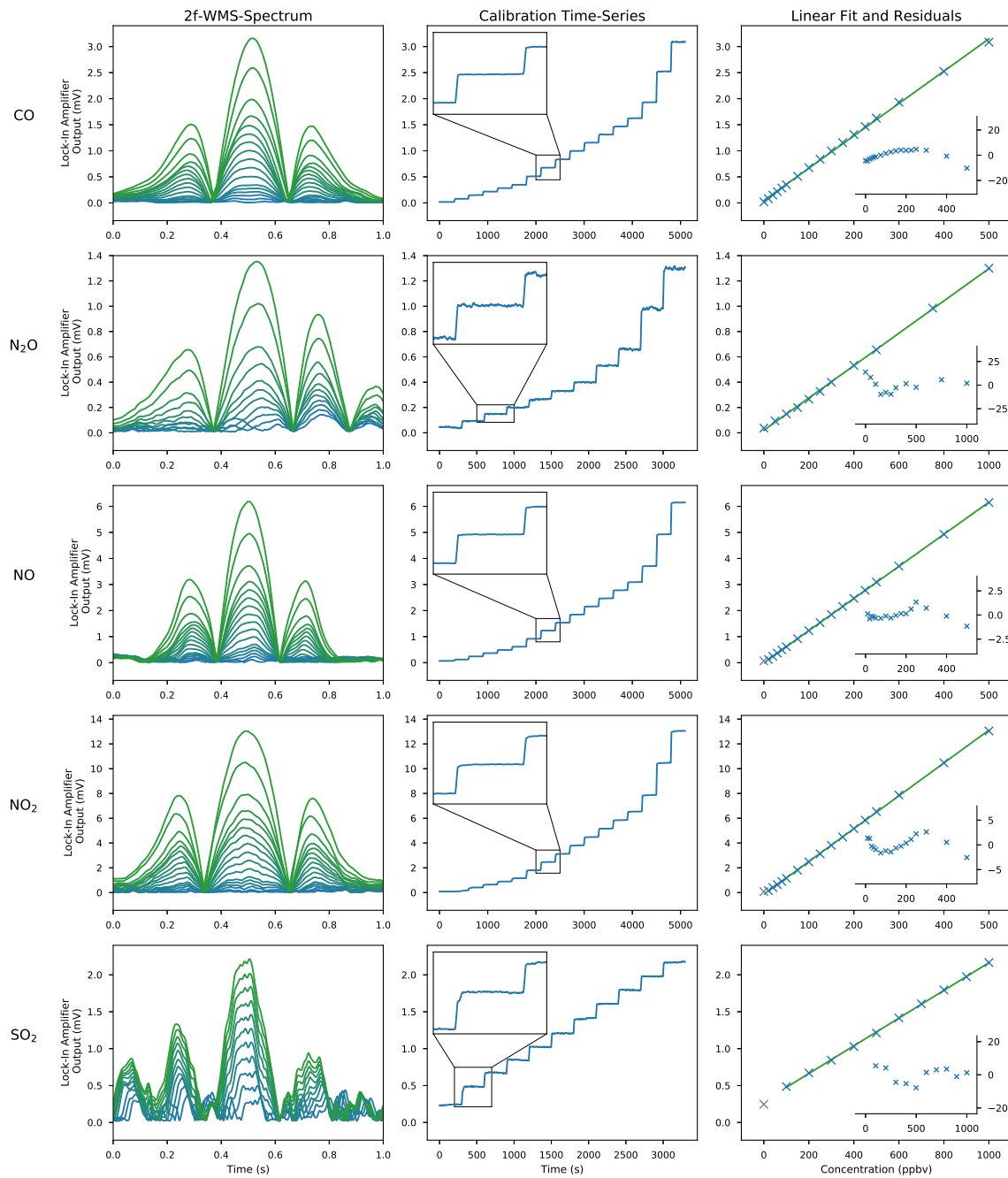


Figure 4.3.: Calibration experiments for CO, N₂O, NO, NO₂ and SO₂. The first column are the recorded 2f-spectra, the second plot is the trace of the maximum of the 2f-WMS peak (the inset corresponds to 100 ppbv of the target analyte). The third column shows the linear calibration and the residuals as inset. Measurement points indicated in grey were identified as outliers and have been excluded for the calculation of the calibration.

4.2.2. Allan-Werle Plot

Similar important, like the LOD, is the temporal stability of the prototype. This property limits the chance to improve the Signal-to-Noise ratio by averaging a higher number of measurement points. One way to characterize the long term stability is to calculate the Allan-Werle variance and plot the resulting data. The basic idea behind this is that the deviation decreases until it reaches a minimum. After this point, it increases again as slow fluctuations, such as thermal drifts in the lab, begin to dominate the noise level.

To record such an Allan-Werle plot, the concentration and pressure within the gas measurement cell has been kept constant for 1 h and the multi-gas-analyzer measures the concentration. Each target analyte has been studied after another and the combined plot is shown in Figure 4.4. One can clearly see that the optimum averaging time is between 30 and 120 s, which is comparable to results of other publications [247, 313, 314].

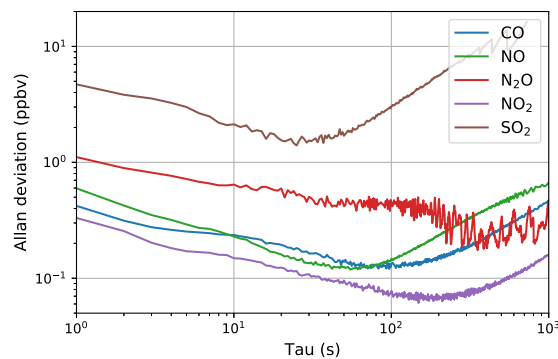


Figure 4.4.: Allan-Werle Plots for CO, N₂O, NO, NO₂ and SO₂.

4.3. Calibration Curves Recorded With HPSDS

The initial experiments to quantify CO with HPSDS were done with the laboratory signal generator Rigol DG4162 and the first aim was to reproduce the typical shape of the spectra, as known from literature. Therefore, the laser parameters have been adjusted to ensure sufficient amplitude modulation with the sine-wave signal, injected via the bias-tee-module. While it is common to operate a QCL at its maximum output power to maximize the optical path length or to optimize the signal at the detector, the highest amplitude modulation is typically found at moderate laser currents. Decreasing the laser current, however, causes a lower output power

4. Experiments and Results

	Initial Experiments with Rigol 4162	Field Experiments with AD9959
CO Absorption Line	2183.22 cm ⁻¹	2179.77 cm ⁻¹
Laser Current Ramp	238.0-242.0 mA	297.0-300.2 mA
Laser Temperature	11.28 °C	20.85 °C

Table 4.3.: Laser parameters for the first HPSDS experiments in the lab (with the Rigol 4162) and the field campaign (with the AD9959).

and a higher detector noise. The consequence was to select a different ro-vibrational absorption line of CO, located at 2183.22 cm⁻¹. Subsequently, the laser current and temperature, listed in Table 4.3, have been identified as useful.

From [237] it is known, that the maximum phase shift is generated, if the sine-wave frequency is approximately 0.58 times the FWHM of the absorption line. Considering a pressure of 100 mbar in the gas measurement cell, the FWHM of the probed absorption line is ≈ 0.014 cm⁻¹, which corresponds to ≈ 420 MHz. Subsequently, the optimum modulation frequency would be ≈ 244 MHz, which is, neither supported by the signal generator, nor by the MCT detector (electrical bandwidth: 200 MHz).

To avoid this hardware limitation, the pressure in the gas measurement cell was reduced to 30 mbar, resulting in an FWHM of ≈ 127 MHz. As a higher modulation frequency affect the maximum phase shift less than lower ones (here: ≈ 5 % smaller), this parameter has been set to 100 MHz.

As HPSDS has been implemented in the prototype to quantify rather high levels of CO in the ambient air, the calibration range was adjusted too. The test gas bottle contained CO with a concentration of 100 ppmv in N₂ (Air Liquide Austria, Schwechat, AT) and has been diluted with N₂ 5.0. The measured concentrations covered the range 0-20 ppmv whereas each step was held for 5 min. A selection of HPSDS spectra, recorded during the calibration experiment, and the resulting calibration curve are shown in Figure 4.5. One can clearly see that the shape of the spectra are as expected from the theory (compare with Figure 2.23). The linearity of the calibration and the LOD derived from the SNR at 10 ppmv are listed in Table 4.4.

The mechanical dimensions of the prototype, however, prevented an integration of the laboratory signal generator and it was replaced by a development board, based on the chip AD9959. In addition, the laser settings have been adjusted to measure CO again at 2179.77 cm⁻¹, avoiding possible influences from the significantly different laser parameters (295.0-300.2 mA, 22.45 °C).

4.4. Field Experiments

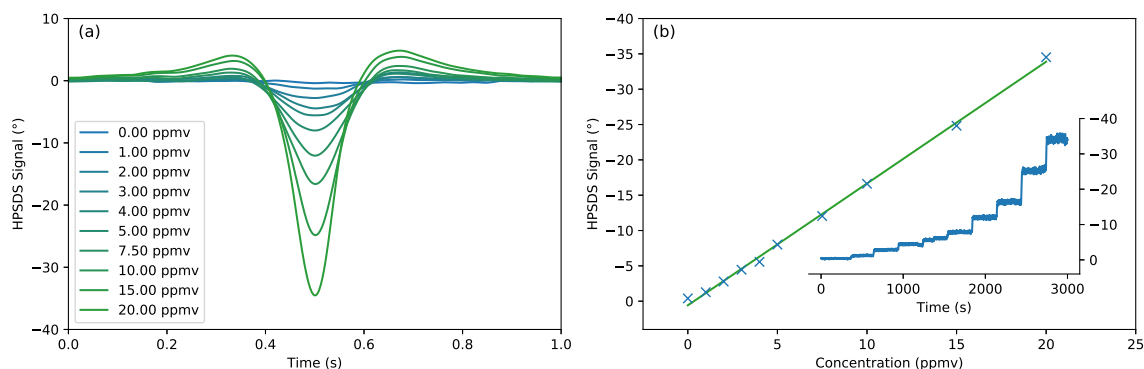


Figure 4.5.: HPSDS spectra of CO at 2183.77 cm^{-1} , recorded with the prototype. The minimum in the HPSDS spectrum correlates with the concentration of the target analyte, as one can see from the linear calibration.

Signal Generator	Calibration R^2	SNR at 10 ppmv, 1 Hz Sample Rate	1σ Detection Limit (ppmv), 1 Hz Sample Rate
Rigol 4162	0.99802	32	0.31
AD9959	0.99880	124	0.08

Table 4.4.: Linear response and detection limits for CO, recorded with HPSDS and two different signal generators.

Figure 4.6 shows HPSDS spectra recorded at different CO concentrations, the decreasing phase signal (caused by the presence of the analyte), and the linear calibration curve. It is immediately visible that the spectra are different, compared to the first HPSDS calibration. This is most likely caused by operating the QCL at a relatively high laser current, which reduces the effectiveness of amplitude modulation and, although not further investigated, optical side bands with different amplitudes. Again, the minimum of the HPSDS spectrum is in linear relationship with the concentration, defined by the gas mixing rig.

4.4. Field Experiments

While it is sufficient to demonstrate the functionality of a prototype for the TRLs 3 to 5 under optimized lab conditions, achieving TRL 6 requires already testing in the intended environment. Experiments in the lab differ significantly from field campaigns and additional challenges are, to name a few, transportation, remote location/limited access and durability. Their effect on the measurements and possible solutions shall be briefly mentioned, before discussing the performed field campaigns.

4. Experiments and Results

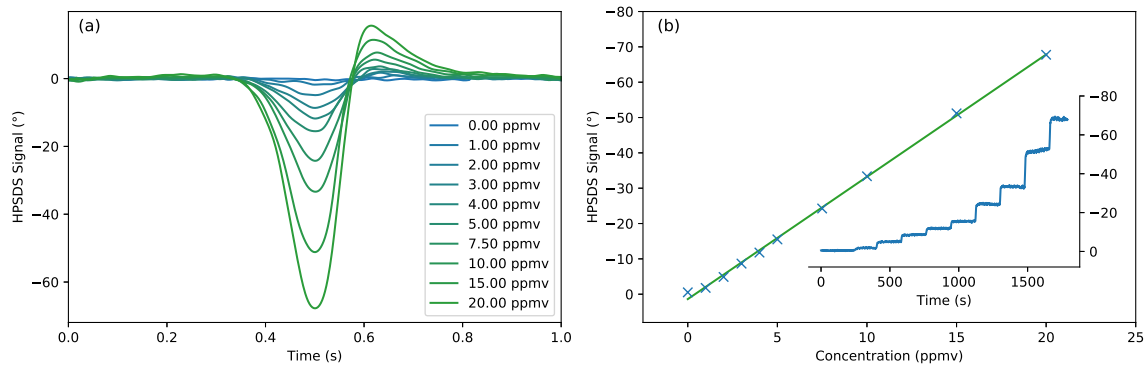


Figure 4.6.: HPSDS spectra of CO and the calculated calibration curve. The laser parameters are similar to the ones used in 2f-WMS and the sine-wave for modulating the QCL was generated by the AD9959.

It is known that experimental setups equipped with optical components are sensitive to vibrations and mechanical impacts. Compared to the electronics rack, special care has to be taken when the optics rack of the prototype is transported. This issue can, for example, be addressed by simplifying and reducing the number of optical elements, installing the components in a rigid construction, or by employing a mechanically more robust measurement technique.

Closely related with transportation is the geographical location of measurement sites and the limited access. Performing experiments in the laboratory or on the University campus allows usually easy access to the equipment. In contrast, servicing a prototype at a remote measurement site includes often traveling (even if the location is within the same city) and, in many cases, coordination with project partners. Installing a cellular modem gives simple remote-access to the measurement-software and allows monitoring the hardware functionality.

The third identified challenge is durability. A prototype in the lab is often only turned on if, e.g., the optics need to be adjusted, the software is tested, calibration experiments are performed or Allan-Werle plots are recorded. Subsequently, the hardware/software runs only a few hours per day and long-term issues, like buffer overflows in the software, a filling hard drive or an unexpected software update, are a minor issue. Measurement campaigns, in contrast, require the sensor to operate autonomously, 24/7, without any interruptions.

With these challenges in mind, two successful measurement campaigns have been performed with the multi-gas-analyzer and will be discussed in detail.

4.4.1. Szombathely - January 2019

The first field test has been carried out in the city Szombathely (HU), together with the project partner *Green Lab Hungary Engineering* (Budapest, HU). The measurement site (Vépi út 12, 9700 Szombathely, HU, 47°13'55.4"N, 16°38'52.7"E) has been selected, because the project partner already operates there a mobile laboratory for ambient air monitoring. It is installed in a van (Peugeot Boxer) and two 19" racks hold reference devices to monitor the following pollutants:

- Particle counter (MP 101M, ENVEA, Poissy, FR)
- NO, NO₂, NO_x (Model 42i, Thermo Fisher Scientific, Waltham, MA, USA)
- SO₂ (Model 43i, Thermo Fisher Scientific, Waltham, MA, USA)
- CO (Model 48i, Thermo Fisher Scientific, Waltham, MA, USA)
- O₃ (Model 49i, Thermo Fisher Scientific, Waltham, MA, USA)

In addition, the mobile laboratory is equipped with an automated calibration system (Sonimix 6000, LNI Swissgas, Versoix, CH), test-gas bottles, two sample inlets, a manifold, air-condition, an industrial computer and various meteorologic sensors (temperature, wind-speed and direction). The measurement site itself is located in the industrial part of the town and close to a wood-processing company. An ambient air monitoring station, operated by the Hungarian Air Quality Network (Ministry of Agriculture, HU) is in 2.1 km distance and its data has been evaluated as well.

The prototype has been installed in the van and data has been recorded between January 11 and 22, 2019. As the focus of ambient air monitoring is rather gaining information over long periods of time than measuring short time events, like a truck passing by the measurement site, the sequential monitoring (one analyte after another and switching the active QCL every 10 min) is sufficient. Similar, the data supported by the project partner are average-values of 15 min and the temporal resolution of the Hungarian Air Quality Network is 1 h.

Due to the development state of the multi-gas-analyzer, the focus was on the analytes NO, NO₂ and CO. Moreover, only 2f-WMS has been employed to quantify the pollutants, as at that time HPSDS has not yet been implemented in the prototype.

Figure 4.7 shows the results from that measurement campaign in Szombathely. One can see that the values, derived from the prototype follow the trends of both, the reference values from the project partner, as well as the ones from the air quality network. A possible explanation for the similar trends in the concentration of the pollutants is that the source is in significant distance

4. Experiments and Results

to the town. This could be, for example, the slowly changing traffic on a local highway, or a changing wind direction, transporting pollutants from a distant factory towards the town. Further investigations on its origin, however, would require additional information on the wind-direction and wind-speed, and would be part of a dedicated study.

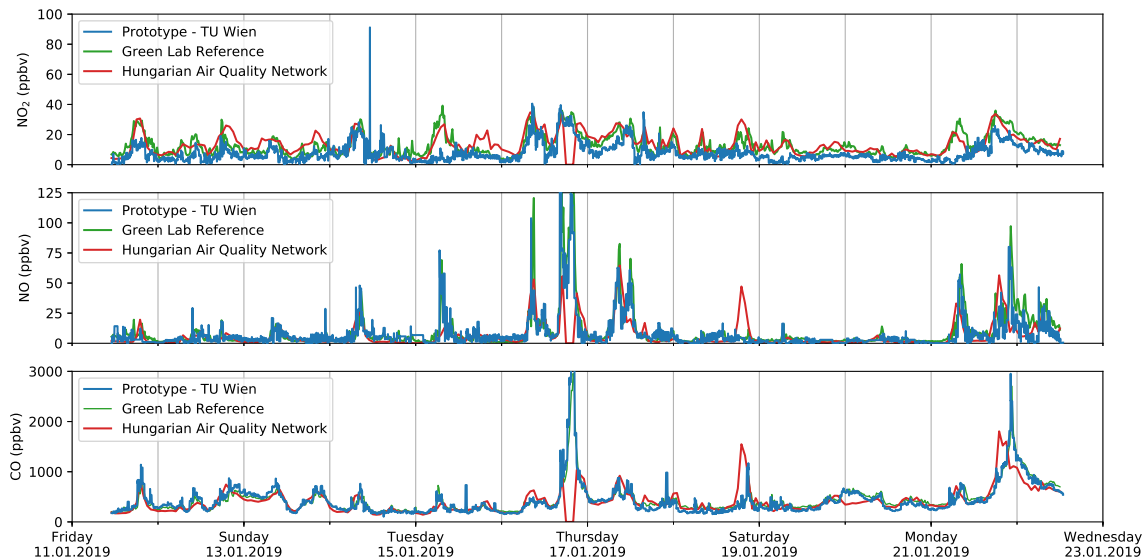


Figure 4.7.: Results of the measurement campaign in Szombathely in January 2019. The results gained with the multi-gas-analyzer are comparable with the ones from the reference equipment, installed at the same location, and the data from the Hungarian Air Quality Network.

4.4.2. Vienna - October and November 2019

The second measurement campaign was in cooperation with the Municipal Department for Environmental Protection (MA 22) of Vienna (AT) and has been carried out between October 22 and November 29, 2019. In contrast to the first one, where the multi-gas-sensor was located in an industrial part of the city, the measurement location was in an urban area. The sample intake was next to a busy road, with an intersection in ≈ 50 m distance. The equipment has been set up in a dedicated laboratory of an administrative building (Hietzinger Kai 1-3, 1130 Vienna, AT, $48^{\circ}11'18.3''N$, $16^{\circ}18'0.0''E$).

The measurement station was equipped with a calibrator (ASGU, Horiba, Kyoto, JP), the required calibration gas bottles, an automated remote control system, a manifold and reference devices to quantify the following analytes:

- NO, NO₂, NO_x (APNA-370, Horiba, Kyoto, JP)

- CO (APMA-370, Horiba, Kyoto, JP)

4.4.2.1. Long-Term Monitoring

Again, the focus of the campaign was on the analytes CO, NO and NO₂. The greenhouse-gas N₂O was irrelevant, as the measurement site is located in a city and its most significant human source is agriculture. The pollutant SO₂ is also of minor interest, as it is known from previous studies, carried out with reference equipment, that the typical levels in Vienna are below 3 ppbv and, if they are slightly increased, usually caused by a refinery, close to Vienna.

Like during the field campaign in Szombathely, the multi-gas-analyzer has been operated in automated switching mode, where each pollutant was monitored for 10 min, before activating the next QCL. With keeping in mind that the *Directive 2008/50/EC* aims to ensure a clean air on a long term perspective, the 10 min-average-values have been accepted to be comparable with the official average-values of 30 min.

The results of the prototype and the reference hardware can be found in Appendix E, and a representative plot, showing the concentrations of the three pollutants of one week can be seen in Figure 4.8.

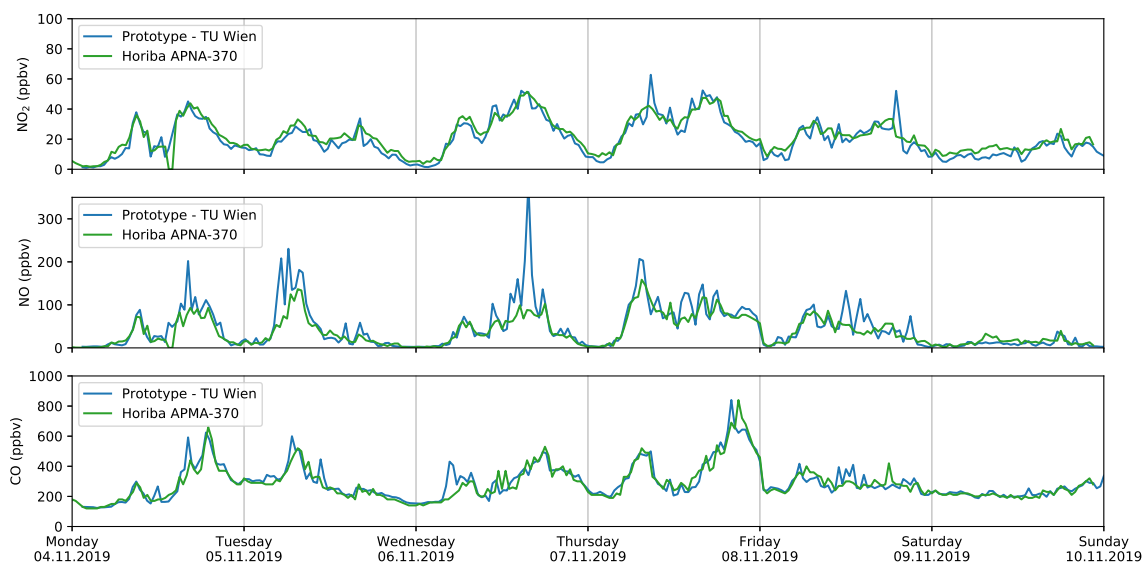


Figure 4.8.: Exemplary concentration profile of the pollutants CO, NO and NO₂, recorded during the measurement campaign in Hietzing (Vienna, AT), in October/November 2019.

Compared to the first field test, the concentrations of the pollutants reach much higher levels during the day. This can be traced back to the traffic on the road next to the the sample intake.

4. Experiments and Results

As the traffic is at a minimum during the night, NO and NO₂ levels reach almost 0 ppbv and CO is reduced to its natural ambient air concentration of ~200 ppbv. Together with the increasing number of vehicles during the morning hours, the pollution increases too, as it can be seen in the diagrams. Around midday, the concentrations decrease slightly, and reach the levels from the morning again in the late afternoon/early evening. This daily rhythm is clearly visible during the working days from Monday to Friday. On the weekends, in contrast, the traffic is less and this effect is significantly reduced.

From a technical point of view, the relevant result is the good agreement of the values derived with the prototype and the data retrieved from the reference equipment. A better way to visualize this, is a scatter plot, as shown in Figure 4.9. Here, the values from the reference devices are plotted on the x-axis and the data from the prototype on the y-axis. If the equipment was ideal and both would deliver identical results, all points would be on a single line, with the slope $k = 1$ and no offset. Keeping in mind, that the measurement principles of the prototype and the reference equipment are different and that simplifications have been made by assuming that the average of 10 min (laser-based sensor) and the average of 30 min are equal, it is obvious that the scatter-plot cannot deliver a perfect line. However, as one can see in Figure 4.9, the individual data points are located in vicinity of the slope with $k = 1$. The different colors in the plot shall indicate the data quality and comparability of the laser based and the reference sensors. Dots in blue represent 90 % of the data points, sorted by their distance to the ideal behavior. The red ones are the remaining 10 % of the data points and one could argue that these are outliers.

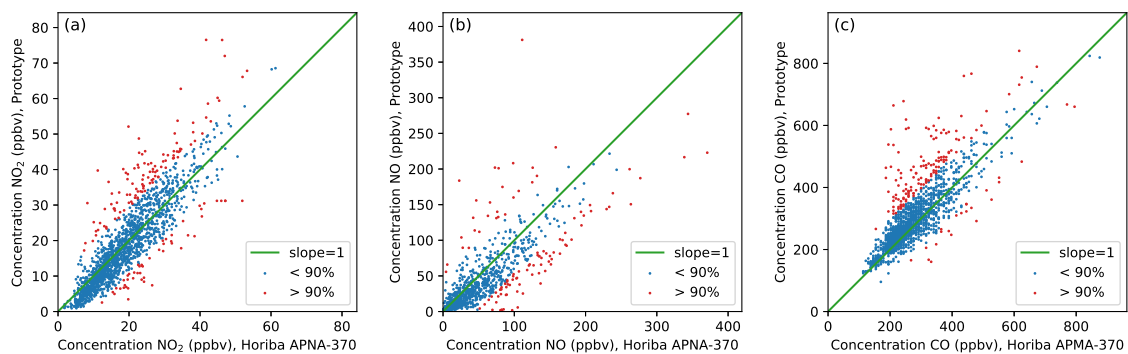


Figure 4.9.: Visualization of the recorded data of the reference equipment and the prototype as a scatter plot. The colors indicate the match of the different sensors. The green line has a slope of $k = 1$ and represents the ideal situation, where the prototype delivers the same values as the reference equipment. (a): NO₂, (b): NO, (c): CO.

4.4.2.2. Monitoring One Pollutant in Detail for Several Hours

Although the focus during this second field campaign was again on the evaluation of the long-term applicability for ambient air monitoring, two additional experiments have been carried out. The first one took place between October 30 and November 2 and it investigated the rapidly changing concentrations of the pollutants, that are usually suppressed by averaging the sensor data to produce the 30 min values. To do so, the automatic switching between the lasers has been deactivated and a single analyte has been monitored with a temporal resolution of 1 s over 8 h. The recorded data has been filtered with a moving-average filter over 10 s and the resulting data is plotted together with the reference values (temporal resolution: 1 min) in Figure 4.10.

As expected, the results recorded with the prototype are almost identical to the data, delivered by the commercial reference equipment. Similar to the already discussed long-term results, the concentration of the pollutants is significantly reduced during the night and concentration levels increase in the morning hours. With the higher temporal resolution, it is now possible to identify sharp peaks in the pollution during the night and strong fluctuations of the analyte concentration during the the day. For a better visualization of these events, the grey sections in Figure 4.10 are magnified in the plots below.

With the information that a light-controlled intersection is located in ≈ 50 m distance to the sample intake, it is obvious, that these peaks of pollution are caused by the traffic. In detail, the total light cycle is 120 s, whereas the main road (Hietzinger Kai/B1) is active for 95 s and the side road (Dommayergasse) for 25 s. The periodic stops of the traffic have been identified in the time diagram but should be visible in the frequency domain of the recorded signal as well. Therefore, the data has been analyzed with an FFT algorithm and the frequency components are plotted for the individual analytes in Figure 4.11.

The FFT revealed clear peaks at the frequencies 0.010 Hz and 0.008 Hz for the analytes NO_2 and NO, respectively. This fits perfectly to the light cycle of the intersection. For CO, however, the FFT has not been able to identify any periodic signal, which is most likely due to the relatively long intervals between events during the night.

4. Experiments and Results

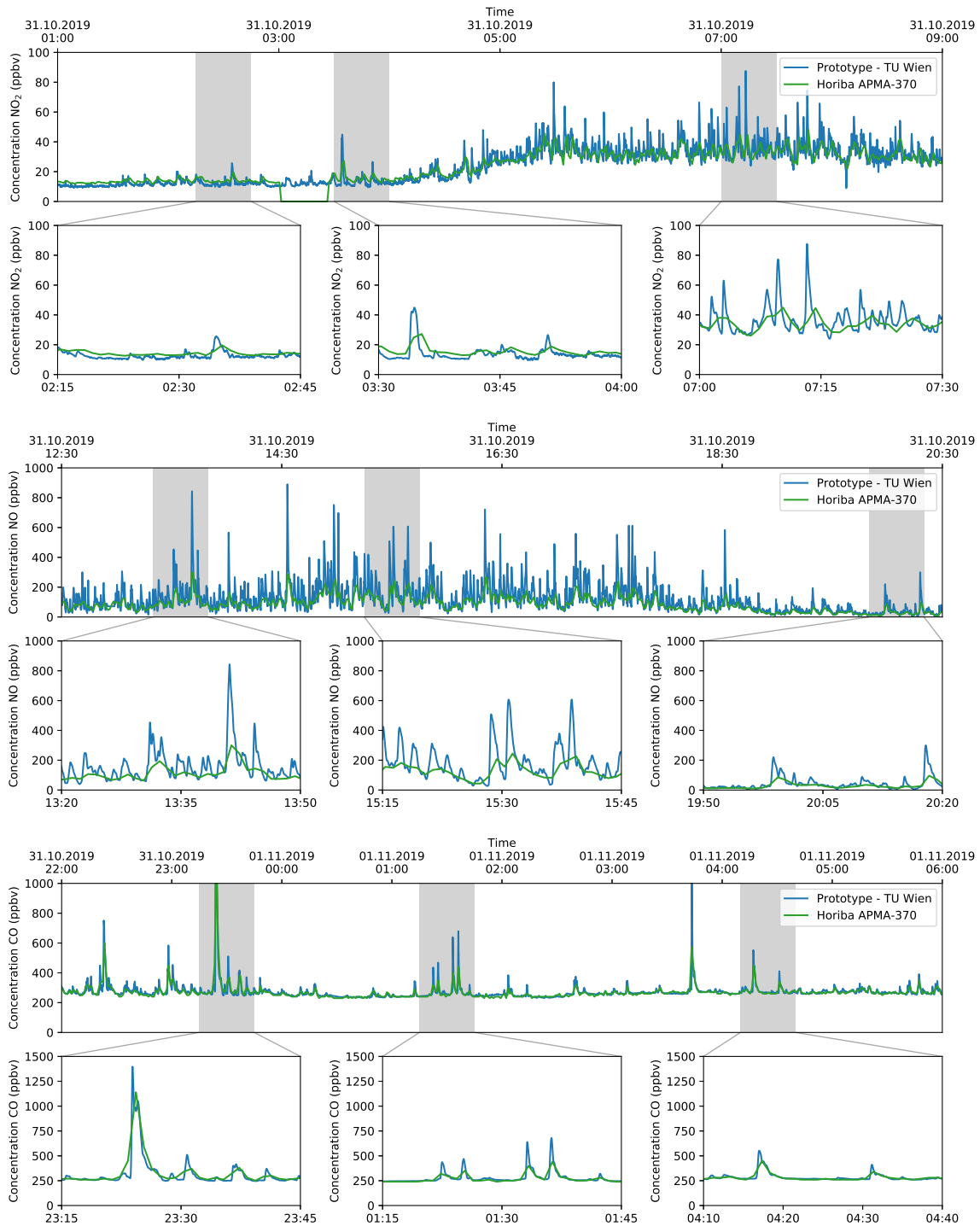


Figure 4.10.: Observing each analyte for 8 h with a increased temporal resolution (prototype: 1 s, reference equipment: 1 min).

4.4. Field Experiments

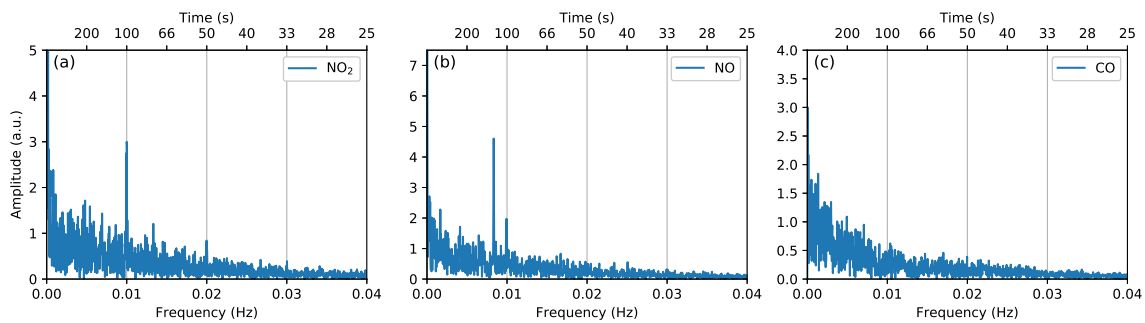


Figure 4.11.: Converting the time-series of a single pollutant into the frequency domain helps to identify repeating events.

4.4.2.3. Field Measurements with HPSDS

Closely related to the experiments, where one pollutant was measured for an extended time period with 2f-WMS, is a long-term test of HPSDS. Here, the pollutant CO has been monitored with the dispersion based technique for 42 h (November 26-28) to evaluate and verify the applicability in the field. The results of the reference hardware and the prototype are plotted in Figure 4.12 and the time diagrams are again almost identical. The relatively high CO concentration (average: ≈ 500 -700 ppbv, with several peaks > 1.5 ppmv) and the subsequent high absorbance, have been the optimum conditions to test the applicability of HPSDS.

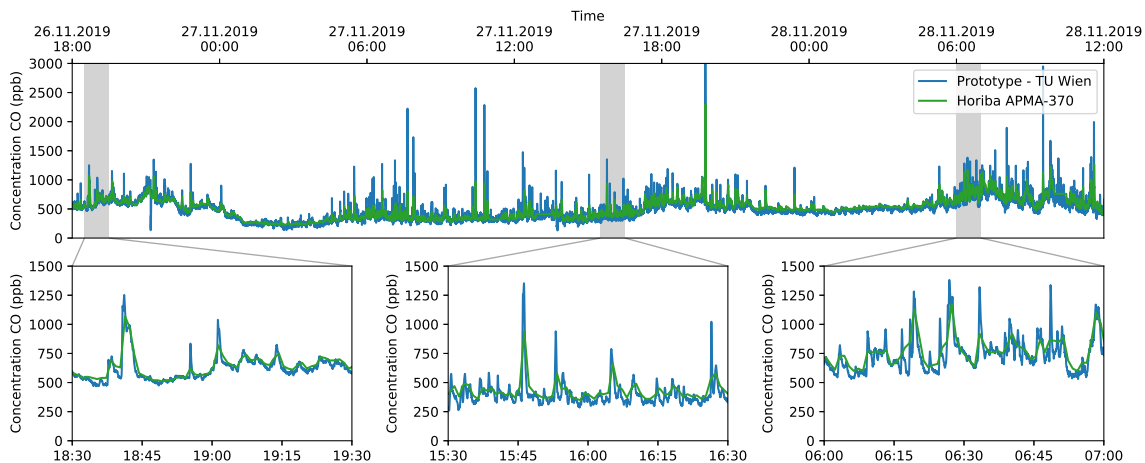


Figure 4.12.: CO concentration recorded with HPSDS and the commercial NDIR-based reference equipment.

Converting the time series of the CO concentration to the frequency domain reveals, as shown in Figure 4.13, a significant peak at 0.008 Hz. This corresponds to the already discussed light-cycle of 120 s and emphasizes the readiness of HPSDS for field campaigns.

4. Experiments and Results

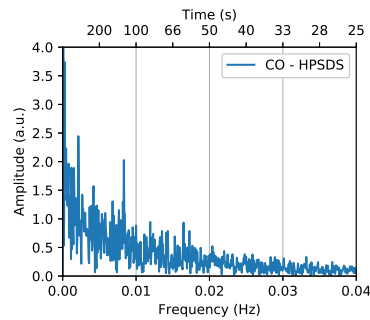


Figure 4.13.: Similar to the measurements of NO and NO₂, the FFT of the time series recorded with HPSDS shows a repeating event with 0.008 Hz.

The results from the measurement campaigns in Szombathely and Vienna show that the performance of the prototype is comparable to the reference equipment. As the intention of ambient air monitoring lies in improving the air quality for the inhabitants in an area/city/country, it has been acceptable to quantify each pollutant for 10 min and to compare its average with the official 30 min-value, derived from the reference equipment.

The additional experiments in Vienna, where a single analyte has been monitored over several hours, have proven the fast response of the laser-based prototype. The light-controlled intersection close to the measurement site has been the perfect benchmark to test this property of the multi-gas-analyzer.

Finally, it has been possible to test the applicability of HPSDS in the field together with established reference equipment. As it is a dispersion based technique, its main advantage lies in the reduced sensitivity towards the transmitted light. The increased CO concentrations, caused by the traffic close to the sample intake, have been the perfect test conditions to verify this.

5. Conclusion, Outlook

Over the decades, numerous research projects have shown the applicability of infrared lasers to quantify greenhouse gases, pollutants and other trace gases in the ambient air by probing their ro-vibrational absorption lines. Depending on the applied measurement technique and the selected wavelength, concentration measurements in the ppbv-, pptv- and even ppqv-range have been achieved. The ongoing improvements of the light sources (e.g. ICLs and recently frequency combs) and the progress in measurement techniques (especially photo-acoustic, photo-thermal and dispersion based ones) are the key to develop high-precision sensors and novel prototypes.

They have the chance to outperform established measurement techniques, like the gas chromatography or fluorescence-based devices, in terms of lower detection limits, reduced measurement time or by recovering more information from the sample. Quantifying multiple analytes with one device simultaneously reduces the required space in mobile laboratories, makes them more energy efficient and can also help to extend the service intervals. In the simplest case, it is sufficient to adjust the temperature/laser current of the (DFB-) QCL to quantify a different analyte than the initially intended one. Although QCLs with an external cavity cover a significantly wider spectral range ($\sim 200 \text{ cm}^{-1}$), they are often avoided for trace gas measurements, as their mode-hop-free range is limited and their modulation properties do not compete with DFB-QCLs. Subsequently, it is still preferred to install one dedicated DFB-QCL for each analyte and to combine them with either beamsplitters, dichroic mirrors or even galvo mirrors.

The presented multi-gas-analyzer is not the first prototype that tries to revolutionize the equipment installed in mobile laboratories. Other research groups and start-ups have, for example, developed open-path sensors with an optical path length of several hundreds of meters, prototypes that can quantify more than seven gases or ultra compact devices measuring down to the ppqv-region. How this prototype contributes to the commercialization of QCL-based ambient air monitors in detail shall be summarized in the following section.

5. Conclusion, Outlook

5.1. Achievements

Within this work, a QCL based multi-gas-analyzer has been developed to quantify the pollutants CO, NO, NO₂ and SO₂ in the ambient air. In addition, it is possible to quantify the greenhouse gas N₂O too, as it features a ro-vibrational absorption line that is accessible with the laser for CO. A careful wavelength selection of the required QCLs and reducing the pressure in the gas cell allows interference-free measurements of the target analytes. In contrast to fundamental research projects, one aim was to rely on commercially available components in this setup. Subsequently, the optics, electronics and most of the mechanical parts, have been ordered from established companies, which helps to reduce the development time significantly.

The employed measurement technique is 2f-WMS, which is commonly used in near- and mid-IR laser spectroscopy. Here, the laser diode is modulated with a sine-wave and slowly tuned across an absorption feature. The detector signal is then demodulated with a software-based lock-in-amplifier at the 2nd harmonic, which delivers the 2f-spectrum. With this, it has been possible to achieve detection limits in the low single-digit ppbv-range for the target analytes, which is required to be applicable for ambient air measurements.

The precise planning with CAD software and minor simplifications made it possible to keep the overall dimensions of the prototype within the defined limits. Placing the optical components and (most of) the required electronics in two separate 19" racks makes it transportable and already competitive to commercial reference equipment.

Two successful measurement campaigns underline the performance and readiness of the 2f-WMS based sensor for ambient air monitoring. Both revealed that the values derived from the prototype are comparable with the 30 min-average values that are demanded by the *Directive 2008/50/EC*. Additional experiments during the field evaluation in Vienna showed, that if only a single analyte is monitored, the responsiveness of the setup is sufficient to resolve the cycle of a signal controlled intersection.

Finally, HPSDS has been integrated in the 2f-WMS setup to quantify CO. The additional components included off-the-shelf parts and, in the final version, an evaluation board to modulate the QCL in the high MHz-region. The dispersion based technique has been tested during the 2nd campaign for 42 h and delivered almost identical results as the reference equipment.

5.2. Future Improvements

Several simplifications have been made to achieve the desired Technology Readiness Level 6 within the project's time-frame. Subsequently, the prototype could be improved in different ways to deliver even more precise results and to quantify all target analytes simultaneously.

First of all, one could adopt the 2f-WMS technique with an algorithm for calibration-free measurements. To do so, it is necessary to characterize the tuning behavior of the QCL in more detail and to include the lock-in-signal of higher harmonics to the calculations.

Operating all QCLs simultaneously is another important feature, but it involves major hardware modifications. In particular, each QCL would require its dedicated laser-driver, sine-wave generator and lock-in amplifier. While the demodulation is done in software and therefore a minor issue, three additional high-precision current-sources are difficult to fit into the electronics rack and also a cost-factor.

Closely related is the improvement of the lock-in amplifier and the control of the laser driver in general. One could replace the installed measurement-PC with a more efficient single-board-computer and reduce the complexity of the system. In addition, the lock-in amplifier could be either designed in hardware (analog), on a DSP or even on an FPGA. The simultaneous modulation of all QCLs would also benefit from the chip integration, as it involves only copy/paste of the individual code-blocks.

A major topic is to quantify as many pollutants and greenhouse gases as possible with a single analyzer. Due to the different molecular properties, this would require additional wavelengths and therefore additional QCLs. Depending on the application and the analytes of interest, one could employ QCL-arrays, where multiple DFB-QCLs are processed from a single gain chip. Assuming that each gain chip covers a gain range of $\approx 250 \text{ cm}^{-1}$, six gain chips could cover the range $1000\text{-}2500 \text{ cm}^{-1}$, in which most of the interesting analytes show absorption lines.

More information on the composition of the ambient air could also be delivered by installing additional, specialized sensors. In detail, one could use low-cost sensors to quantify CO_2 or the humidity.



Die approbierte gedruckte Originalversion dieser Dissertation ist an der TU Wien Bibliothek verfügbar.
The approved original version of this doctoral thesis is available in print at TU Wien Bibliothek.

Bibliography

- [1] S. L. Olson et al. “Earth: Atmospheric Evolution of a Habitable Planet”. In: *Handbook of Exoplanets*. Cham: Springer International Publishing, 2018, pp. 2817–2853. DOI: 10.1007/978-3-319-55333-7_189.
- [2] T. W. Lyons, C. T. Reinhard, and N. J. Planavsky. “The rise of oxygen in Earth’s early ocean and atmosphere”. In: *Nature* 506.7488 (Feb. 2014), pp. 307–315. DOI: 10.1038/nature13068.
- [3] D. Vallero. *Fundamentals of Air Pollution*. 5th. Academic Press, 2014, pp. 267–459.
- [4] L. Makra. “Anthropogenic Air Pollution in Ancient Times”. In: *History of Toxicology and Environmental Health*. Vol. 2. Elsevier, 2015, pp. 21–41. DOI: 10.1016/B978-0-12-801506-3.00003-0.
- [5] Y. Mamane. “Air pollution control in Israel during the first and second century”. In: *Atmospheric Environment (1967)* 21.8 (Jan. 1987), pp. 1861–1863. DOI: 10.1016/0004-6981(87)90128-4.
- [6] W. C. Turner. “ATMOSPHERIC POLLUTION”. In: *Weather* 10.4 (Apr. 1955), pp. 110–119. DOI: 10.1002/j.1477-8696.1955.tb00165.x.
- [7] K. C. Heidorn. “A Chronology of Important Events in the History of Air Pollution Meteorology to 1970”. In: *Bulletin of the American Meteorological Society* 59.12 (Dec. 1978), pp. 1589–1597. DOI: 10.1175/1520-0477(1978)059<1589:ACOIIEI>2.0.CO;2.
- [8] A. C. César, J. A. Carvalho, and L. F. Nascimento. “Association between NO_x exposure and deaths caused by respiratory diseases in a medium-sized Brazilian city”. In: *Brazilian Journal of Medical and Biological Research* 48.12 (2015), pp. 1130–1135. DOI: 10.1590/1414-431X20154396.
- [9] The European Parliament and the Council of the European Union. “Directive 2008/50/EC of the European Parliament and of the Council of 21 May 2008 on Ambient Air Quality and Cleaner Air for Europe”. 2008.
- [10] WHO. *WHO Air quality guidelines for particulate matter, ozone, nitrogen dioxide and sulfur dioxide*. Tech. rep. WHO, 2005.
- [11] EN 14211. *Ambient air - Standard method for the measurement of the concentration of nitrogen dioxide and nitrogen monoxide by chemiluminescence*. 2012.
- [12] EN 14212. *Ambient air - Standard method for the measurement of the concentration of sulphur dioxide by ultraviolet fluorescence*. 2014.
- [13] EN 14626. *Ambient air - Standard method for the measurement of the concentration of carbon monoxide by non-dispersive infrared spectroscopy*. 2012.
- [14] EN 14625. *Ambient air - Standard method for the measurement of the concentration of ozone by ultraviolet photometry*. 2013.

Bibliography

- [15] C. Wang et al. “Metal Oxide Gas Sensors: Sensitivity and Influencing Factors”. In: *Sensors* 10.3 (Mar. 2010), pp. 2088–2106. DOI: 10.3390/s100302088.
- [16] L. Chatzidiakou et al. “Characterising low-cost sensors in highly portable platforms to quantify personal exposure in diverse environments”. In: *Atmospheric Measurement Techniques* 12.8 (2019), pp. 4643–4657. DOI: 10.5194/amt-12-4643-2019.
- [17] F. Karagulian et al. “Review of the Performance of Low-Cost Sensors for Air Quality Monitoring”. In: *Atmosphere* 10.9 (Aug. 2019), p. 506. DOI: 10.3390/atmos10090506.
- [18] C. Borrego et al. “Assessment of air quality microsensors versus reference methods: The EuNetAir joint exercise”. In: *Atmospheric Environment* 147.2 (Dec. 2016), pp. 246–263. DOI: 10.1016/j.atmosenv.2016.09.050.
- [19] N. Masson, R. Piedrahita, and M. Hannigan. “Approach for quantification of metal oxide type semiconductor gas sensors used for ambient air quality monitoring”. In: *Sensors and Actuators B: Chemical* 208 (Mar. 2015), pp. 339–345. DOI: 10.1016/j.snb.2014.11.032.
- [20] W. Jiao et al. “Community Air Sensor Network (CAIRSENSE) project: evaluation of low-cost sensor performance in a suburban environment in the southeastern United States”. In: *Atmospheric Measurement Techniques* 9.11 (Nov. 2016), pp. 5281–5292. DOI: 10.5194/amt-9-5281-2016.
- [21] L. Spinelle et al. “Field calibration of a cluster of low-cost available sensors for air quality monitoring. Part A: Ozone and nitrogen dioxide”. In: *Sensors and Actuators B: Chemical* 215 (Aug. 2015), pp. 249–257. DOI: 10.1016/j.snb.2015.03.031.
- [22] L. Spinelle et al. “Field calibration of a cluster of low-cost commercially available sensors for air quality monitoring. Part B: NO, CO and CO₂”. In: *Sensors and Actuators B: Chemical* 238 (Jan. 2017), pp. 706–715. DOI: 10.1016/j.snb.2016.07.036.
- [23] P. Schneider et al. “Mapping urban air quality in near real-time using observations from low-cost sensors and model information”. In: *Environment International* 106. December 2016 (Sept. 2017), pp. 234–247. DOI: 10.1016/j.envint.2017.05.005.
- [24] E. G. Snyder et al. “The changing paradigm of air pollution monitoring”. In: *Environmental Science and Technology* 47.20 (2013), pp. 11369–11377. DOI: 10.1021/es4022602.
- [25] I. Lazovic, Z. Ristovski, and A. Bartonova. “Four Years’ Experience of Application of Low-Cost Sensors in Belgrade in the Framework of the CITI-SENSE Project”. In: (2016), pp. 3–6. DOI: 10.5162/6EuNetAir2016/12.
- [26] J. M. Cordero, R. Borge, and A. Narros. “Using statistical methods to carry out in field calibrations of low cost air quality sensors”. In: *Sensors and Actuators B: Chemical* 267.2 (Aug. 2018), pp. 245–254. DOI: 10.1016/j.snb.2018.04.021.
- [27] A. Hickman et al. “Evaluation of air quality at the Birmingham New Street Railway Station”. In: *Proceedings of the Institution of Mechanical Engineers, Part F: Journal of Rail and Rapid Transit* 232.6 (July 2018), pp. 1864–1878. DOI: 10.1177/0954409717752180.
- [28] S. Kumar and A. Jasuja. “Air quality monitoring system based on IoT using Raspberry Pi”. In: *Proceeding - IEEE International Conference on Computing, Communication and Automation, ICCCA 2017* 2017-Janua (2017), pp. 1341–1346. DOI: 10.1109/CCAA.2017.8230005.
- [29] R. Piedrahita et al. “The next generation of low-cost personal air quality sensors for quantitative exposure monitoring”. In: *Atmospheric Measurement Techniques* 7.10 (Oct. 2014), pp. 3325–3336. DOI: 10.5194/amt-7-3325-2014.

- [30] J. Silva et al. “An Online Platform For Real-Time Air Quality Monitoring”. In: *2019 5th Experiment International Conference (exp.at'19)*. Vol. 0569. IEEE, June 2019, pp. 320–325. DOI: 10.1109/EXPAT.2019.8876486.
- [31] G. F. Fine et al. “Metal Oxide Semi-Conductor Gas Sensors in Environmental Monitoring”. In: *Sensors* 10.6 (June 2010), pp. 5469–5502. DOI: 10.3390/s100605469.
- [32] A. Kumar and B. Gurjar. “Low-Cost Sensors for Air Quality Monitoring in Developing Countries – A Critical View”. In: *Asian Journal of Water, Environment and Pollution* 16.2 (Apr. 2019), pp. 65–70. DOI: 10.3233/AJW190021.
- [33] N. Castell et al. “Can commercial low-cost sensor platforms contribute to air quality monitoring and exposure estimates?” In: *Environment International* 99 (Feb. 2017), pp. 293–302. DOI: 10.1016/j.envint.2016.12.007.
- [34] Q. M. Konopacky et al. “Detection of Carbon Monoxide and Water Absorption Lines in an Exoplanet Atmosphere”. In: *Science* 339.6126 (Mar. 2013), pp. 1398–1401. DOI: 10.1126/science.1232003.
- [35] T. S. Barman et al. “SIMULTANEOUS DETECTION OF WATER, METHANE, AND CARBON MONOXIDE IN THE ATMOSPHERE OF EXOPLANET HR 8799 b”. In: *The Astrophysical Journal* 804.1 (May 2015), p. 61. DOI: 10.1088/0004-637X/804/1/61.
- [36] L. Kaltenegger and D. Sasselov. “DETECTING PLANETARY GEOCHEMICAL CYCLES ON EXOPLANETS: ATMOSPHERIC SIGNATURES AND THE CASE OF SO₂”. In: *The Astrophysical Journal* 708.2 (Jan. 2010), pp. 1162–1167. DOI: 10.1088/0004-637X/708/2/1162.
- [37] M. P. Minitti et al. “Imaging Molecular Motion: Femtosecond X-Ray Scattering of an Electrocyclic Chemical Reaction”. In: *Physical Review Letters* 114.25 (June 2015), p. 255501. DOI: 10.1103/PhysRevLett.114.255501.
- [38] K. Pande et al. “Femtosecond structural dynamics drives the trans/cis isomerization in photoactive yellow protein”. In: *Science* 352.6286 (May 2016), pp. 725–729. DOI: 10.1126/science.aad5081.
- [39] C. S. Joseph et al. “Imaging of ex vivo nonmelanoma skin cancers in the optical and terahertz spectral regions”. In: *Journal of Biophotonics* 7.5 (2014), pp. 295–303. DOI: 10.1002/jbio.201200111.
- [40] P. Doradla, C. Joseph, and R. H. Giles. “Terahertz endoscopic imaging for colorectal cancer detection: Current status and future perspectives”. In: *World Journal of Gastrointestinal Endoscopy* 9.8 (2017), p. 346. DOI: 10.4253/wjge.v9.i8.346.
- [41] M. Arumugam. “Optical fiber communication - An overview”. In: *Pramana* 57.5-6 (Nov. 2001), pp. 849–869. DOI: 10.1007/s12043-001-0003-2.
- [42] M. N. O. Sadiku, S. Musa, and S. R. Nelatury. “Free Space Optical Communications: An Overview”. In: *European Scientific Journal, ESJ* 12.9 (Mar. 2016), p. 55. DOI: 10.19044/esj.2016.v12n9p55.
- [43] E. Leitgeb et al. “Analysis and evaluation of optimum wavelengths for free-space optical transceivers”. In: *2010 12th International Conference on Transparent Optical Networks*. IEEE, June 2010, pp. 1–7. DOI: 10.1109/ICTON.2010.5549009.
- [44] M. Ijaz et al. “Comparison of 830 nm and 1550 nm based free space optical communications link under controlled fog conditions”. In: *2012 8th International Symposium on Communication Systems, Networks & Digital Signal Processing (CSNDSP)*. IEEE, July 2012, pp. 1–5. DOI: 10.1109/CSNDSP.2012.6292739.

Bibliography

- [45] F. Fidler et al. “Optical Communications for High-Altitude Platforms”. In: *IEEE Journal of Selected Topics in Quantum Electronics* 16.5 (Sept. 2010), pp. 1058–1070. DOI: 10.1109/JSTQE.2010.2047382.
- [46] D. Micheli et al. “Measurement of Electromagnetic Field Attenuation by Building Walls in the Mobile Phone and Satellite Navigation Frequency Bands”. In: *IEEE Antennas and Wireless Propagation Letters* 14 (2015), pp. 698–702. DOI: 10.1109/LAWP.2014.2376811.
- [47] B. P. Abbott et al. “LIGO: the Laser Interferometer Gravitational-Wave Observatory”. In: *Reports on Progress in Physics* 72.7 (July 2009), p. 076901. DOI: 10.1088/0034-4885/72/7/076901.
- [48] B. C. Barish and R. Weiss. “LIGO and the Detection of Gravitational Waves”. In: *Physics Today* 52.10 (Oct. 1999), pp. 44–50. DOI: 10.1063/1.882861.
- [49] S. Vitale. “Space-borne gravitational wave observatories”. In: *General Relativity and Gravitation* 46.5 (May 2014), p. 1730. DOI: 10.1007/s10714-014-1730-2.
- [50] J. C. Maxwell. “A dynamical theory of the electromagnetic field”. In: *Philosophical Transactions of the Royal Society of London* 155.2986 (Dec. 1865), pp. 459–512. DOI: 10.1098/rstl.1865.0008.
- [51] J. W. Arthur. “The Evolution of Maxwell’s Equations from 1862 to the Present Day”. In: *IEEE Antennas and Propagation Magazine* 55.3 (June 2013), pp. 61–81. DOI: 10.1109/MAP.2013.6586627.
- [52] ISO 20473. *Optics and photonics - Spectral bands*. 2007.
- [53] R. K. Hanson, R. M. Spearrin, and C. S. Goldenstein. *Spectroscopy and Optical Diagnostics for Gases*. Cham: Springer International Publishing, 2016, pp. 1–279. DOI: 10.1007/978-3-319-23252-2.
- [54] W. Demtröder. *Atoms, Molecules and Photons*. Berlin/Heidelberg: Springer-Verlag, 2006. DOI: 10.1007/3-540-32346-5.
- [55] W. Demtröder. *Laser Spectroscopy - Volume 1 - Basic Principles*. Berlin, Heidelberg: Springer Berlin Heidelberg, 2008. DOI: 10.1007/978-3-540-73418-5.
- [56] J. M. Hollas. *Modern Spectroscopy*. 4th ed. John Wiley & Sons, Ltd, 2004.
- [57] F. Merkt and M. Quack. *Handbook of High-resolution Spectroscopy*. Ed. by M. Quack and F. Merkt. Chichester, UK: John Wiley & Sons, Ltd, Jan. 2011. DOI: 10.1002/9780470749593.
- [58] P. R. Griffiths and J. A. de Haseth. *Fourier Transform Infrared Spectrometry*. Second. Hoboken, NJ, USA: John Wiley & Sons, Inc., Apr. 2007. DOI: 10.1002/047010631X.
- [59] R. Kochanov et al. “HITRAN Application Programming Interface (HAPI): A comprehensive approach to working with spectroscopic data”. In: *Journal of Quantitative Spectroscopy and Radiative Transfer* 177 (July 2016), pp. 15–30. DOI: 10.1016/j.jqsrt.2016.03.005.
- [60] I. Gordon et al. “The HITRAN2016 molecular spectroscopic database”. In: *Journal of Quantitative Spectroscopy and Radiative Transfer* 203 (Dec. 2017), pp. 3–69. DOI: 10.1016/j.jqsrt.2017.06.038.
- [61] S. P. Davis, M. C. Abrams, and J. W. Brault. *Fourier Transform Spectrometry*. Elsevier, 2001. DOI: 10.1016/B978-0-12-042510-5.X5000-8.
- [62] W. D. Perkins. “Fourier transform infrared spectroscopy. Part II. Advantages of FT-IR”. In: *Journal of Chemical Education* 64.11 (Nov. 1987), A269. DOI: 10.1021/ed064pA269.

- [63] P. Fellgett. “I. — les principes généraux des méthodes nouvelles en spectroscopie interférentielle - A propos de la théorie du spectromètre interférentiel multiplex”. In: *Journal de Physique et le Radium* 19.3 (1958), pp. 187–191. DOI: 10.1051/jphysrad:01958001903018700.
- [64] P. Jacquinot. “The Luminosity of Spectrometers with Prisms, Gratings, or Fabry-Perot Etalons”. In: *Journal of the Optical Society of America* 44.10 (Oct. 1954), p. 761. DOI: 10.1364/JOSA.44.000761.
- [65] J. Connes and P. Connes. “Near-Infrared Planetary Spectra by Fourier Spectroscopy I Instruments and Results”. In: *Journal of the Optical Society of America* 56.7 (July 1966), p. 896. DOI: 10.1364/JOSA.56.000896.
- [66] D. Landgrebe et al. “On-line infrared spectroscopy for bioprocess monitoring”. In: *Applied Microbiology and Biotechnology* 88.1 (Sept. 2010), pp. 11–22. DOI: 10.1007/s00253-010-2743-8.
- [67] O. Anjos et al. “FTIR–ATR spectroscopy applied to quality control of grape-derived spirits”. In: *Food Chemistry* 205 (Aug. 2016), pp. 28–35. DOI: 10.1016/j.foodchem.2016.02.128.
- [68] C. Koch et al. “Multi-analyte quantification in bioprocesses by Fourier-transform-infrared spectroscopy by partial least squares regression and multivariate curve resolution”. In: *Analytica Chimica Acta* 807 (Jan. 2014), pp. 103–110. DOI: 10.1016/j.aca.2013.10.042.
- [69] Z. Bacsik, J. Mink, and G. Keresztury. “FTIR Spectroscopy of the Atmosphere Part 2. Applications”. In: *Applied Spectroscopy Reviews* 40.4 (Nov. 2005), pp. 327–390. DOI: 10.1080/05704920500230906.
- [70] R. N. Hall et al. “Coherent Light Emission From GaAs Junctions”. In: *Physical Review Letters* 9.9 (Nov. 1962), pp. 366–368. DOI: 10.1103/PhysRevLett.9.366.
- [71] N. Holonyak and S. F. Bevacqua. “COHERENT (VISIBLE) LIGHT EMISSION FROM Ga(As 1- x P x) JUNCTIONS”. In: *Applied Physics Letters* 1.4 (Dec. 1962), pp. 82–83. DOI: 10.1063/1.1753706.
- [72] M. I. Nathan et al. “STIMULATED EMISSION OF RADIATION FROM GaAs p-n JUNCTIONS”. In: *Applied Physics Letters* 1.3 (Nov. 1962), pp. 62–64. DOI: 10.1063/1.1777371.
- [73] I. Melngailis. “MASER Action in InAs Diodes”. In: *Applied Physics Letters* 2.9 (May 1963), pp. 176–178. DOI: 10.1063/1.1753832.
- [74] R. J. Phelan et al. “Infrared InSb Laser Diode in High Magnetic Fields”. In: *Applied Physics Letters* 3.9 (Nov. 1963), pp. 143–145. DOI: 10.1063/1.1753905.
- [75] C. R. Webster et al. “Tunable diode laser IR spectrometer for in situ measurements of the gas phase composition and particle size distribution of Titan’s atmosphere”. In: *Applied Optics* 29.7 (Mar. 1990), p. 907. DOI: 10.1364/AO.29.000907.
- [76] J. Roths et al. “Four-laser airborne infrared spectrometer for atmospheric trace gas measurements”. In: *Applied Optics* 35.36 (Dec. 1996), pp. 7075–7084. DOI: 10.1364/AO.35.007075.
- [77] P. Werle and R. Kormann. “Fast chemical sensor for eddy-correlation measurements of methane emissions from rice paddy fields”. In: *Applied Optics* 40.6 (Feb. 2001), pp. 846–858. DOI: 10.1364/AO.40.000846.
- [78] P. Werle et al. “Spectroscopic gas analyzers based on indium-phosphide, antimonide and lead-salt diode-lasers”. In: *Spectrochimica Acta Part A: Molecular and Biomolecular Spectroscopy* 58.11 (Sept. 2002), pp. 2361–2372. DOI: 10.1016/S1386-1425(02)00051-3.

Bibliography

- [79] J. A. Silver and A. C. Stanton. “Airborne measurements of humidity using a single-mode Pb–salt diode laser”. In: *Applied Optics* 26.13 (July 1987), pp. 2558–2566. DOI: 10.1364/AO.26.002558.
- [80] M. Tacke. “Lead–salt lasers”. In: *Philosophical Transactions of the Royal Society of London. Series A: Mathematical, Physical and Engineering Sciences* 359.1780 (Mar. 2001). Ed. by A. R. Adams et al., pp. 547–566. DOI: 10.1098/rsta.2000.0742.
- [81] U. P. Schießl and J. Rohr. “60°C lead salt laser emission near 5- μm wavelength”. In: *Infrared Physics & Technology* 40.4 (Aug. 1999), pp. 325–328. DOI: 10.1016/S1350-4495(99)00028-6.
- [82] K. J. Linden. “Single Mode, Short Cavity, Pb-Salt Diode Lasers Operating”. In: QE-21.4 (1985), p. 391. DOI: 10.1109/JQE.1985.1072650.
- [83] R. F. Kazarinov and R. A. Suris. “Possibility of the amplification of electromagnetic waves in a semiconductor with a superlattice”. In: *Soviet Physics - Semiconductors* 5.4 (1971), pp. 707–709.
- [84] J. Faist et al. “Quantum Cascade Laser”. In: *Science* 264.5158 (Apr. 1994), pp. 553–556. DOI: 10.1126/science.264.5158.553.
- [85] J. Faist et al. “Continuous wave operation of a vertical transition quantum cascade laser above T = 80 K”. In: *Applied Physics Letters* 67.21 (Nov. 1995), pp. 3057–3059. DOI: 10.1063/1.114863.
- [86] J. Faist et al. “High power mid-infrared ($\lambda \sim 5 \mu\text{m}$) quantum cascade lasers operating above room temperature”. In: *Applied Physics Letters* 68.26 (June 1996), pp. 3680–3682. DOI: 10.1063/1.115741.
- [87] A. Hugi et al. “External cavity quantum cascade laser tunable from 7.6 to 11.4 μm ”. In: *Applied Physics Letters* 95.6 (Aug. 2009), p. 061103. DOI: 10.1063/1.3193539.
- [88] C. Gmachl et al. “Recent progress in quantum cascade lasers and applications”. In: *Reports on Progress in Physics* 64.11 (Nov. 2001), pp. 1533–1601. DOI: 10.1088/0034-4885/64/11/204.
- [89] C. Gmachl et al. “Quantum cascade lasers with a heterogeneous cascade: Two-wavelength operation”. In: *Applied Physics Letters* 79.5 (July 2001), pp. 572–574. DOI: 10.1063/1.1383806.
- [90] J. R. Arthur. “Molecular beam epitaxy”. In: *Surface Science* 500.1-3 (Mar. 2002), pp. 189–217. DOI: 10.1016/S0039-6028(01)01525-4.
- [91] K. Kosiel. “MBE - Technology for nanoelectronics”. In: *Vacuum* 82.10 (June 2008), pp. 951–955. DOI: 10.1016/j.vacuum.2008.01.033.
- [92] S. Slivken et al. “Gas-source molecular beam epitaxy growth of an 8.5 μm quantum cascade laser”. In: *Applied Physics Letters* 71.18 (1997), p. 2593. DOI: 10.1063/1.119338.
- [93] R. P. Green et al. “High-performance distributed feedback quantum cascade lasers grown by metalorganic vapor phase epitaxy”. In: *Applied Physics Letters* 85.23 (Dec. 2004), pp. 5529–5531. DOI: 10.1063/1.1830072.
- [94] O. Malis et al. “The quantum cascade laser: A versatile high-power semiconductor laser for mid-infrared applications”. In: *Bell Labs Technical Journal* 10.3 (Nov. 2005), pp. 199–214. DOI: 10.1002/bltj.20114.
- [95] M. Razeghi et al. “Recent progress of quantum cascade laser research from 3 to 12 μm at the Center for Quantum Devices [Invited]”. In: *Applied Optics* 56.31 (Nov. 2017), H30. DOI: 10.1364/AO.56.000H30.
- [96] P. Rauter and F. Capasso. “Multi-wavelength quantum cascade laser arrays”. In: *Laser & Photonics Reviews* 9.5 (Sept. 2015), pp. 452–477. DOI: 10.1002/lpor.201500095.

- [97] M. S. Vitiello et al. “Quantum cascade lasers: 20 years of challenges”. In: *Optics Express* 23.4 (2015), p. 5167. DOI: 10.1364/oe.23.005167.
- [98] M. Razeghi et al. “Quantum cascade lasers: from tool to product”. In: *Optics Express* 23.7 (Apr. 2015), p. 8462. DOI: 10.1364/OE.23.008462.
- [99] E. Tournié and A. N. Baranov. “Mid-Infrared Semiconductor Lasers”. In: *Semiconductors and Semimetals*. 1st ed. Vol. 86. Elsevier Inc., 2012, pp. 183–226. DOI: 10.1016/B978-0-12-391066-0.00005-8.
- [100] R. Pecharroman-Gallego. “An Overview on Quantum Cascade Lasers: Origins and Development”. In: *Quantum Cascade Lasers*. InTech, Apr. 2017. DOI: 10.5772/65003.
- [101] E. Tournie and L. Cerutti. *Mid-infrared Optoelectronics: Materials, Devices, and Applications*. 2019.
- [102] R. Q. Yang et al. “Interband cascade light emitting diodes in the 5–8 μm spectrum region”. In: *Applied Physics Letters* 70.15 (Apr. 1997), pp. 2013–2015. DOI: 10.1063/1.118806.
- [103] R. Yang. “Mid-infrared interband cascade lasers based on type-II heterostructures”. In: *Microelectronics Journal* 30.10 (Oct. 1999), pp. 1043–1056. DOI: 10.1016/S0026-2692(99)00061-0.
- [104] I. Vurgaftman et al. “Interband cascade lasers”. In: *Journal of Physics D: Applied Physics* 48.12 (Apr. 2015), p. 123001. DOI: 10.1088/0022-3727/48/12/123001.
- [105] A. Bauer et al. “Mid-infrared semiconductor heterostructure lasers for gas sensing applications”. In: *Semiconductor Science and Technology* 26.1 (Jan. 2011), p. 014032. DOI: 10.1088/0268-1242/26/1/014032.
- [106] K. J. Franz. *Erwin Jr.* 2012.
- [107] Zhijun Liu et al. “Room-temperature continuous-wave quantum cascade lasers grown by MOCVD without lateral regrowth”. In: *IEEE Photonics Technology Letters* 18.12 (June 2006), pp. 1347–1349. DOI: 10.1109/LPT.2006.877006.
- [108] S. Ahn et al. “Enhanced light output power of quantum cascade lasers from a tilted front facet”. In: *Optics Express* 21.13 (July 2013), p. 15869. DOI: 10.1364/OE.21.015869.
- [109] D.-B. Wang et al. “Stable Single-Mode Operation of Distributed Feedback Quantum Cascade Laser by Optimized Reflectivity Facet Coatings”. In: *Nanoscale Research Letters* 13.1 (Dec. 2018), p. 37. DOI: 10.1186/s11671-018-2455-z.
- [110] Y. Bai et al. “Optimizing facet coating of quantum cascade lasers for low power consumption”. In: *Journal of Applied Physics* 109.5 (Mar. 2011), p. 053103. DOI: 10.1063/1.3553863.
- [111] R. Maulini et al. “High power thermoelectrically cooled and uncooled quantum cascade lasers with optimized reflectivity facet coatings”. In: *Applied Physics Letters* 95.15 (Oct. 2009), p. 151112. DOI: 10.1063/1.3246799.
- [112] Y. Matsuoka et al. “Broadband multilayer antireflection coating for quantum cascade laser facets”. In: *Optics Letters* 43.19 (2018), p. 4723. DOI: 10.1364/ol.43.004723.
- [113] Y. Yoon et al. “Time resolved characterization of Fabry-Perot quantum cascade lasers for use in a broadband “white light” source”. In: *Optics Express* 27.22 (Oct. 2019), p. 32609. DOI: 10.1364/OE.27.032609.
- [114] B. Lendl et al. “Mid-Infrared Quantum Cascade Lasers for Flow Injection Analysis”. In: *Analytical Chemistry* 72.7 (Apr. 2000), pp. 1645–1648. DOI: 10.1021/ac990833b.

Bibliography

- [115] S. Schaden, A. Domínguez-Vidal, and B. Lendl. “Simultaneous measurement of two compounds in aqueous solution with dual quantum cascade laser absorption spectroscopy”. In: *Applied Physics B* 83.1 (Apr. 2006), pp. 135–139. DOI: 10.1007/s00340-006-2133-1.
- [116] S. Schaden, A. Domínguez-Vidal, and B. Lendl. “On-Line Reaction Monitoring in the Liquid Phase Using Two Mid-Infrared Quantum Cascade Lasers Simultaneously”. In: *Applied Spectroscopy* 60.5 (May 2006), pp. 568–571. DOI: 10.1366/000370206777412068.
- [117] M. Kölhed et al. “Assessment of quantum cascade lasers as mid infrared light sources for measurement of aqueous samples”. In: *Vibrational Spectroscopy* 29.1-2 (July 2002), pp. 283–289. DOI: 10.1016/S0924-2031(01)00190-4.
- [118] A. Lambrecht et al. “Continuous Glucose Monitoring by Means of Fiber-Based, Mid-Infrared Laser Spectroscopy”. In: *Applied Spectroscopy* 60.7 (July 2006), pp. 729–736. DOI: 10.1366/000370206777887071.
- [119] S. Barbieri et al. “Gas detection with quantum cascade lasers: An adapted photoacoustic sensor based on Helmholtz resonance”. In: *Review of Scientific Instruments* 73.6 (2002), pp. 2458–2461. DOI: 10.1063/1.1480463.
- [120] A. Elia et al. “Quantum cascade laser-based photoacoustic spectroscopy of volatile chemicals: Application to hexamethyldisilazane”. In: *Spectrochimica Acta Part A: Molecular and Biomolecular Spectroscopy* 64.2 (May 2006), pp. 426–429. DOI: 10.1016/j.saa.2005.07.041.
- [121] C. J. Hawthorn, K. P. Weber, and R. E. Scholten. “Littrow configuration tunable external cavity diode laser with fixed direction output beam”. In: *Review of Scientific Instruments* 72.12 (Dec. 2001), pp. 4477–4479. DOI: 10.1063/1.1419217.
- [122] G. P. Luo et al. “Grating-tuned external-cavity quantum-cascade semiconductor lasers”. In: *Applied Physics Letters* 78.19 (May 2001), pp. 2834–2836. DOI: 10.1063/1.1371524.
- [123] M. G. Littman and H. J. Metcalf. “Spectrally narrow pulsed dye laser without beam expander”. In: *Applied Optics* 17.14 (July 1978), p. 2224. DOI: 10.1364/AO.17.002224.
- [124] Y. Cunyun. *Tunable External Cavity Diode Lasers*. Ed. by T. K. Wei. Singapore: WORLD SCIENTIFIC, Dec. 2004. DOI: 10.1142/5694.
- [125] T. Tsai and G. Wysocki. “External-cavity quantum cascade lasers with fast wavelength scanning”. In: *Applied Physics B* 100.2 (Aug. 2010), pp. 243–251. DOI: 10.1007/s00340-009-3865-5.
- [126] R. Centeno et al. “High power, widely tunable, mode-hop free, continuous wave external cavity quantum cascade laser for multi-species trace gas detection”. In: *Applied Physics Letters* 105.26 (Dec. 2014), p. 261907. DOI: 10.1063/1.4905281.
- [127] J. Wagner et al. “Widely tunable quantum cascade lasers for spectroscopic sensing”. In: *Quantum Sensing and Nanophotonic Devices XII*. Ed. by M. Razeghi, E. Tournié, and G. J. Brown. Vol. 9370. Feb. 2015, p. 937012. DOI: 10.1117/12.2082794.
- [128] M. Tormen et al. “Deformable MEMS grating for wide tunability and high operating speed”. In: *Journal of Optics A: Pure and Applied Optics* 8.7 (July 2006), S337–S340. DOI: 10.1088/1464-4258/8/7/S07.
- [129] X. Jia et al. “Fast Swept-Wavelength, Low Threshold-Current, Continuous-Wave External Cavity Quantum Cascade Laser”. In: *Nanoscale Research Letters* 13.1 (Dec. 2018), p. 341. DOI: 10.1186/s11671-018-2765-1.

- [130] G. Wysocki et al. “Widely tunable mode-hop free external cavity quantum cascade laser for high resolution spectroscopic applications”. In: *Applied Physics B* 81.6 (Oct. 2005), pp. 769–777. DOI: 10.1007/s00340-005-1965-4.
- [131] C. Peng, G. Luo, and H. Q. Le. “Broadband, continuous, and fine-tune properties of external-cavity thermoelectric-stabilized mid-infrared quantum-cascade lasers”. In: *Applied Optics* 42.24 (Aug. 2003), p. 4877. DOI: 10.1364/AO.42.004877.
- [132] R. Ghorbani and F. M. Schmidt. “Real-time breath gas analysis of CO and CO₂ using an EC-QCL”. In: *Applied Physics B: Lasers and Optics* 123.5 (2017), pp. 1–11. DOI: 10.1007/s00340-017-6715-x.
- [133] Y. Yu et al. “CW EC-QCL-based sensor for simultaneous detection of H₂O, HDO, N₂O and CH₄ using multi-pass absorption spectroscopy”. In: *Optics Express* 24.10 (May 2016), p. 10391. DOI: 10.1364/OE.24.010391.
- [134] A. Schwaighofer et al. “Recent advancements of EC-QCL based mid-IR transmission spectroscopy of proteins and application to analysis of bovine milk¹”. In: *Biomedical Spectroscopy and Imaging* 7.1-2 (May 2018), pp. 35–45. DOI: 10.3233/BSI-180177.
- [135] M. Brandstetter et al. “Tunable external cavity quantum cascade laser for the simultaneous determination of glucose and lactate in aqueous phase”. In: *The Analyst* 135.12 (Dec. 2010), p. 3260. DOI: 10.1039/c0an00532k.
- [136] G. Ramer, V. A. Aksyuk, and A. Centrone. “Quantitative Chemical Analysis at the Nanoscale Using the Photothermal Induced Resonance Technique”. In: *Analytical Chemistry* 89.24 (Dec. 2017), pp. 13524–13531. DOI: 10.1021/acs.analchem.7b03878.
- [137] J. Faist et al. “Distributed feedback quantum cascade lasers”. In: *Applied Physics Letters* 70.20 (1997), pp. 2670–2672. DOI: 10.1063/1.119208.
- [138] S. Golka et al. “Quantum cascade lasers with lateral double-sided distributed feedback grating”. In: *Applied Physics Letters* 86.11 (Mar. 2005), p. 111103. DOI: 10.1063/1.1883332.
- [139] C. Gmachl et al. “Continuous-wave and high-power pulsed operation of index-coupled distributed feedback quantum cascade laser at $\lambda \approx 8.5 \mu\text{m}$ ”. In: *Applied Physics Letters* 72.12 (Mar. 1998), pp. 1430–1432. DOI: 10.1063/1.120585.
- [140] C. Gmachl et al. “High-power, continuous-wave, current-tunable, single-mode quantum-cascade distributed-feedback lasers at $\lambda = 52$ and $\lambda = 795 \mu\text{m}$ ”. In: *Optics Letters* 25.4 (Feb. 2000), p. 230. DOI: 10.1364/OL.25.000230.
- [141] J. C. Zhang et al. “High power buried sampled grating distributed feedback quantum cascade lasers”. In: *Journal of Applied Physics* 113.15 (Apr. 2013), p. 153101. DOI: 10.1063/1.4801906.
- [142] Z. Jia et al. “Improvement of Buried Grating DFB Quantum Cascade Lasers by Small-Angle Tapered Structure”. In: *IEEE Photonics Technology Letters* 29.10 (May 2017), pp. 783–785. DOI: 10.1109/LPT.2017.2681127.
- [143] W. Schrenk et al. “Surface-emitting distributed feedback quantum-cascade lasers”. In: *Applied Physics Letters* 77.14 (Oct. 2000), pp. 2086–2088. DOI: 10.1063/1.1313807.
- [144] E. Mujagić et al. “Low divergence single-mode surface emitting quantum cascade ring lasers”. In: *Applied Physics Letters* 93.16 (2008), p. 161101. DOI: 10.1063/1.3000630.
- [145] C. Schwarzer et al. “Grating duty-cycle induced enhancement of substrate emission from ring cavity quantum cascade lasers”. In: *Applied Physics Letters* 100.19 (May 2012), p. 191103. DOI: 10.1063/1.4712127.

Bibliography

- [146] C. Schwarzer et al. “Linearly polarized light from substrate emitting ring cavity quantum cascade lasers”. In: *Applied Physics Letters* 103.8 (Aug. 2013), p. 081101. DOI: 10.1063/1.4819034.
- [147] R. Szedlak et al. “On-chip focusing in the mid-infrared: Demonstrated with ring quantum cascade lasers”. In: *Applied Physics Letters* 104.15 (Apr. 2014), p. 151105. DOI: 10.1063/1.4871520.
- [148] Y. Bai et al. “High power, continuous wave, quantum cascade ring laser”. In: *Applied Physics Letters* 99.26 (Dec. 2011), p. 261104. DOI: 10.1063/1.3672049.
- [149] A. Harrer et al. “Mid-infrared surface transmitting and detecting quantum cascade device for gas-sensing”. In: *Scientific Reports* 6.21795 (Apr. 2016), pp. 1–6. DOI: 10.1038/srep21795.
- [150] E. Mujagić et al. “Two-dimensional broadband distributed-feedback quantum cascade laser arrays”. In: *Applied Physics Letters* 98.14 (Apr. 2011), p. 141101. DOI: 10.1063/1.3574555.
- [151] M. Brandstetter et al. “Time-resolved spectral characterization of ring cavity surface emitting and ridge-type distributed feedback quantum cascade lasers by step-scan FT-IR spectroscopy”. In: *Optics Express* 22.3 (Feb. 2014), p. 2656. DOI: 10.1364/OE.22.002656.
- [152] H. Moser et al. “Application of a ring cavity surface emitting quantum cascade laser (RCSE-QCL) on the measurement of H₂S in a CH₄ matrix for process analytics”. In: *Optics Express* 24.6 (Mar. 2016), p. 6572. DOI: 10.1364/OE.24.006572.
- [153] B. Meng and Q. J. Wang. “Broadly tunable single-mode mid-infrared quantum cascade lasers”. In: *Journal of Optics* 17.2 (Feb. 2015), p. 023001. DOI: 10.1088/2040-8978/17/2/023001.
- [154] P. Fuchs et al. “Single mode quantum cascade lasers with shallow-etched distributed Bragg reflector”. In: *Optics Express* 20.4 (2012), p. 3890. DOI: 10.1364/oe.20.003890.
- [155] S. Slivken et al. “Sampled grating, distributed feedback quantum cascade lasers with broad tunability and continuous operation at room temperature”. In: *Applied Physics Letters* 100.26 (2012). DOI: 10.1063/1.4732801.
- [156] S. Kalchmair et al. “High tuning stability of sampled grating quantum cascade lasers”. In: *Optics Express* 23.12 (June 2015), p. 15734. DOI: 10.1364/OE.23.015734.
- [157] T. S. Mansuripur et al. “Widely tunable mid-infrared quantum cascade lasers using sampled grating reflectors”. In: *Optics Express* 20.21 (2012), p. 23339. DOI: 10.1364/oe.20.023339.
- [158] X.-F. Jia et al. “Multi-wavelength sampled Bragg grating quantum cascade laser arrays”. In: *Photonics Research* 6.7 (July 2018), p. 721. DOI: 10.1364/PRJ.6.000721.
- [159] H. Yoshinaga et al. “Mid-infrared quantum cascade laser integrated with distributed Bragg reflector”. In: *SEI Technical Review*. Ed. by M. Razeghi. Vol. 9755. 85. Feb. 2016, p. 97552V. DOI: 10.1117/12.2212332.
- [160] F. Kapsalidis et al. “Dual-wavelength DFB quantum cascade lasers: sources for multi-species trace gas spectroscopy”. In: *Applied Physics B* 124.107 (2018), p. 17. DOI: 10.1007/s00340-018-6973-2.
- [161] S. Höfling et al. “Widely tunable single-mode quantum cascade lasers with two monolithically coupled Fabry-Pérot cavities”. In: *Applied Physics Letters* 89.24 (Dec. 2006), p. 241126. DOI: 10.1063/1.2404933.
- [162] B. Meng et al. “Tunable single-mode slot waveguide quantum cascade lasers”. In: *Applied Physics Letters* 104.20 (May 2014), p. 201106. DOI: 10.1063/1.4875711.

- [163] B. Meng et al. “Broadly continuously tunable slot waveguide quantum cascade lasers based on a continuum-to-continuum active region design”. In: *Applied Physics Letters* 107.11 (2015), p. 111110. DOI: 10.1063/1.4931444.
- [164] C. C. Nshii et al. “A unidirectional quantum cascade ring laser”. In: *Applied Physics Letters* 97.23 (2010). DOI: 10.1063/1.3524200.
- [165] B. Schwarz et al. “A bi-functional quantum cascade device for same-frequency lasing and detection”. In: *Applied Physics Letters* 101.19 (Nov. 2012), p. 191109. DOI: 10.1063/1.4767128.
- [166] B. Schwarz et al. “Monolithically Integrated Mid-Infrared Quantum Cascade Laser and Detector”. In: *Sensors* 13.2 (Feb. 2013), pp. 2196–2205. DOI: 10.3390/s130202196.
- [167] P. Malara et al. “External ring-cavity quantum cascade lasers”. In: *Applied Physics Letters* 102.14 (2013). DOI: 10.1063/1.4800073.
- [168] J. H. Lambert. *Photometria sive de mensura et gradibus luminis, colorum et umbrae*. Augsburg, 1760, p. 547. DOI: 10.3931/e-rara-9488.
- [169] Beer. “Bestimmung der Absorption des rothen Lichts in farbigen Flüssigkeiten”. In: *Annalen der Physik und Chemie* 162.5 (1852), pp. 78–88. DOI: 10.1002/andp.18521620505.
- [170] C. Reidl-Leuthner and B. Lendl. “Toward Stand-Off Open-Path Measurements of NO and NO₂ in the Sub-Parts Per Million Meter Range Using Quantum Cascade Lasers (QCLs) in the Intra-Pulse Absorption Mode”. In: *Applied Spectroscopy* 67.12 (Dec. 2013), pp. 1368–1375. DOI: 10.1366/13-07104.
- [171] C. Reidl-Leuthner et al. “Simultaneous open-path determination of road side mono-nitrogen oxides employing mid-IR laser spectroscopy”. In: *Atmospheric Environment* 112.2 (July 2015), pp. 189–195. DOI: 10.1016/j.atmosenv.2015.04.010.
- [172] M. Taslakov et al. “Open-path ozone detection by quantum-cascade laser”. In: *Applied Physics B* 82.3 (Nov. 2005), pp. 501–506. DOI: 10.1007/s00340-005-2010-3.
- [173] D. J. Miller et al. “Open-path, quantum cascade-laser-based sensor for high-resolution atmospheric ammonia measurements”. In: *Atmospheric Measurement Techniques* 7.1 (Jan. 2014), pp. 81–93. DOI: 10.5194/amt-7-81-2014.
- [174] A. P. M. Michel et al. “Open-path spectroscopic methane detection using a broadband monolithic distributed feedback-quantum cascade laser array”. In: *Applied Optics* 56.11 (Apr. 2017), E23. DOI: 10.1364/ao.56.000e23.
- [175] V. Simeonov, H. van den Bergh, and M. Parlange. “Long open-path, TDL based system for monitoring methane background concentration for deployment at Jungfraujoeh High Altitude Research Station- Switzerland”. In: 41.0 (2012).
- [176] P. M. Hundt et al. “Multi-species trace gas sensing with dual-wavelength QCLs”. In: *Applied Physics B* 124.6 (June 2018), p. 108. DOI: 10.1007/s00340-018-6977-y.
- [177] C. Reidl-Leuthner et al. “Quasi-Simultaneous In-Line Flue Gas Monitoring of NO and NO₂ Emissions at a Caloric Power Plant Employing Mid-IR Laser Spectroscopy.” In: *Analytical chemistry* 86.18 (Sept. 2014), pp. 9058–9064. DOI: 10.1021/ac5020244.
- [178] F. Hempel et al. “Quantum Cascade Laser Absorption Spectroscopy: A Modern Technique for Online Plasma Process Monitoring and Trace Gas Diagnostics”. In: (2005), pp. 3–5.
- [179] D. T. Cassidy and J. Reid. “Atmospheric pressure monitoring of trace gases using tunable diode lasers”. In: *Applied Optics* 21.7 (1982), p. 1185. DOI: 10.1364/ao.21.001185.

Bibliography

- [180] J. Reid et al. “High sensitivity pollution detection employing tunable diode lasers”. In: *Applied Optics* 17.2 (1978), p. 300. DOI: 10.1364/ao.17.000300.
- [181] J. Reid et al. “High sensitivity point monitoring of atmospheric gases employing tunable diode lasers”. In: *Applied Optics* 17.11 (1978), p. 1806. DOI: 10.1364/ao.17.001806.
- [182] J. Reid, B. K. Garside, and J. Shewchun. “Detection of sulphur dioxide at, and below, the part per billion level using a tunable diode laser”. In: *Optical and Quantum Electronics* 11.5 (Sept. 1979), pp. 385–391. DOI: 10.1007/BF00619820.
- [183] J. Reid et al. “Sensitivity limits of a tunable diode laser spectrometer, with application to the detection of NO₂ at the 100-ppt level”. In: *Applied Optics* 19.19 (1980), p. 3349. DOI: 10.1364/ao.19.003349.
- [184] J. Reid and D. Labrie. “Second-harmonic detection with tunable diode lasers - Comparison of experiment and theory”. In: *Applied Physics B Photophysics and Laser Chemistry* 26.3 (Nov. 1981), pp. 203–210. DOI: 10.1007/BF00692448.
- [185] M. El-Sherbiny et al. “High sensitivity point monitoring of ozone, and high resolution spectroscopy of the ν_3 band of ozone using a tunable semiconductor diode laser”. In: *Applied Optics* 18.8 (1979), p. 1198. DOI: 10.1364/ao.18.001198.
- [186] M. Loewenstein. “Diode laser harmonic spectroscopy applied to in situ measurements of atmospheric trace molecules”. In: *Journal of Quantitative Spectroscopy and Radiative Transfer* 40.3 (Sept. 1988), pp. 249–256. DOI: 10.1016/0022-4073(88)90118-5.
- [187] H. Li et al. “Extension of wavelength-modulation spectroscopy to large modulation depth for diode laser absorption measurements in high-pressure gases”. In: *Applied Optics* 45.5 (Feb. 2006), p. 1052. DOI: 10.1364/AO.45.001052.
- [188] G. B. Rieker, J. B. Jeffries, and R. K. Hanson. “Calibration-free wavelength-modulation spectroscopy for measurements of gas temperature and concentration in harsh environments”. In: *Applied Optics* 48.29 (Oct. 2009), p. 5546. DOI: 10.1364/AO.48.005546.
- [189] L. Che et al. “Calibration-free wavelength modulation spectroscopy for gas concentration measurements under low-absorbance conditions”. In: *Chinese Physics B* 21.12 (2012). DOI: 10.1088/1674-1056/21/12/127803.
- [190] R. Arndt. “Analytical line shapes for Lorentzian signals broadened by modulation”. In: *Journal of Applied Physics* 36.8 (1965), pp. 2522–2524. DOI: 10.1063/1.1714523.
- [191] P. Kluczynski and O. Axner. “Theoretical description based on Fourier analysis of wavelength-modulation spectrometry in terms of analytical and background signals”. In: *Applied Optics* 38.27 (1999), p. 5803. DOI: 10.1364/ao.38.005803.
- [192] P. Kluczynski et al. “Wavelength modulation absorption spectrometry — an extensive scrutiny of the generation of signals”. In: *Spectrochimica Acta Part B: Atomic Spectroscopy* 56.8 (Aug. 2001), pp. 1277–1354. DOI: 10.1016/S0584-8547(01)00248-8.
- [193] H. Chang et al. “Immunity to Laser Power Variation in a DFB Diode Laser Based Optical Gas Sensor Using a Division Process”. In: *Sensors* 15.4 (Apr. 2015), pp. 9582–9591. DOI: 10.3390/s150409582.
- [194] M. L. Meade. “Advances in lock-in amplifiers”. In: *Journal of Physics E: Scientific Instruments* 15.4 (Apr. 1982), pp. 395–403. DOI: 10.1088/0022-3735/15/4/001.

- [195] L. Orozco. “Synchronous Detectors Facilitate Precision, Low-Level Measurements”. In: *Analog Dialogue* 48.12 (2014), pp. 1–5.
- [196] M. L. Meade. *Lock-in amplifiers: principles and applications*. London: Peregrinus on behalf of the Institution of Electrical Engineers, 1983, p. 232.
- [197] S. K. Sengupta, J. M. Farnham, and J. E. Whitten. “A Simple Low-Cost Lock-In Amplifier for the Laboratory”. In: *Journal of Chemical Education* 82.9 (Sept. 2005), p. 1399. DOI: 10.1021/ed082p1399.
- [198] A. D. Marcellis et al. “A Fully-Analog Lock-In Amplifier With Automatic Phase Alignment for Accurate Measurements of ppb Gas Concentrations”. In: *IEEE Sensors Journal* 12.5 (2012), pp. 1377–1383. DOI: 10.1109/JSEN.2011.2172602.
- [199] A. Dorrington and R. Kunemeyer. “A simple microcontroller based digital lock-in amplifier for the detection of low level optical signals”. In: *Proceedings First IEEE International Workshop on Electronic Design, Test and Applications '2002*. IEEE Comput. Soc, 2002, pp. 486–488. DOI: 10.1109/DELTA.2002.994680.
- [200] G. Gervasoni, M. Carminati, and G. Ferrari. “FPGA-based lock-in amplifier with sub-ppm resolution working up to 6 MHz”. In: *2016 IEEE International Conference on Electronics, Circuits and Systems, ICECS 2016* (2017), pp. 117–120. DOI: 10.1109/ICECS.2016.7841146.
- [201] A. Chighine et al. “An FPGA-based lock-in detection system to enable Chemical Species Tomography using TDLAS”. In: *2015 IEEE International Conference on Imaging Systems and Techniques (IST)*. IEEE, Sept. 2015, pp. 1–5. DOI: 10.1109/IST.2015.7294460.
- [202] M. A. Luda et al. “Compact embedded device for lock-in measurements and experiment active control”. In: *Review of Scientific Instruments* 90.2 (2019). DOI: 10.1063/1.5080345.
- [203] G. A. Stimpson et al. “An open-source high-frequency lock-in amplifier”. In: *Review of Scientific Instruments* 90.9 (Sept. 2019), p. 094701. DOI: 10.1063/1.5083797.
- [204] J. Sinlapanuntakul et al. “Digital lock-in amplifier based on soundcard interface for physics laboratory”. In: *Journal of Physics: Conference Series* 901 (Sept. 2017), p. 012065. DOI: 10.1088/1742-6596/901/1/012065.
- [205] J. T. Liu, J. B. Jeffries, and R. K. Hanson. “Wavelength modulation absorption spectroscopy with 2f detection using multiplexed diode lasers for rapid temperature measurements in gaseous flows”. In: *Applied Physics B: Lasers and Optics* 78.3-4 (2004), pp. 503–511. DOI: 10.1007/s00340-003-1380-7.
- [206] X. Chao, J. B. Jeffries, and R. K. Hanson. “Absorption sensor for CO in combustion gases using 2.3 μm tunable diode lasers”. In: *Measurement Science and Technology* 20.11 (2009). DOI: 10.1088/0957-0233/20/11/115201.
- [207] X. Chao, J. B. Jeffries, and R. K. Hanson. “Wavelength-modulation-spectroscopy for real-time, in situ NO detection in combustion gases with a 5.2 μm quantum-cascade laser”. In: *Applied Physics B: Lasers and Optics* 106.4 (Mar. 2012), pp. 987–997. DOI: 10.1007/s00340-011-4839-y.
- [208] K. Sun et al. “Analysis of calibration-free wavelength-scanned wavelength modulation spectroscopy for practical gas sensing using tunable diode lasers”. In: *Measurement Science and Technology* 24.12 (Dec. 2013), p. 125203. DOI: 10.1088/0957-0233/24/12/125203.
- [209] R. M. Spearrin et al. “Simultaneous sensing of temperature, CO, and CO₂ in a scramjet combustor using quantum cascade laser absorption spectroscopy”. In: *Applied Physics B* 117.2 (Nov. 2014), pp. 689–698. DOI: 10.1007/s00340-014-5884-0.

Bibliography

- [210] L. C. Philippe and R. K. Hanson. “Laser diode wavelength-modulation spectroscopy for simultaneous measurement of temperature, pressure, and velocity in shock-heated oxygen flows”. In: *Applied Optics* 32.30 (1993), p. 6090. DOI: 10.1364/ao.32.006090.
- [211] C. S. Goldenstein et al. “Infrared laser-absorption sensing for combustion gases”. In: *Progress in Energy and Combustion Science* 60 (2017), pp. 132–176. DOI: 10.1016/j.pecs.2016.12.002.
- [212] G. Stewart et al. “Recovery of Absolute Gas Absorption Line Shapes Using Tuneable Diode Laser Spectroscopy with Wavelength Modulation - Part I: Theoretical Analysis”. In: *Journal of Lightwave Technology* 29.6 (2011), pp. 811–821. DOI: 10.1109/JLT.2011.2107312.
- [213] A. J. McGettrick et al. “Tunable Diode Laser Spectroscopy With Wavelength Modulation: A Phasor Decomposition Method for Calibration-Free Measurements of Gas Concentration and Pressure”. In: *Journal of Lightwave Technology* 26.4 (2008), pp. 432–440. DOI: 10.1109/JLT.2007.912519.
- [214] A. Hangauer et al. “Multi-harmonic detection in wavelength modulation spectroscopy systems”. In: *Applied Physics B* 110.2 (Feb. 2013), pp. 177–185. DOI: 10.1007/s00340-012-5049-y.
- [215] A. Behera and A. Wang. “Calibration-free wavelength modulation spectroscopy: symmetry approach and residual amplitude modulation normalization”. In: *Applied Optics* 55.16 (June 2016), p. 4446. DOI: 10.1364/AO.55.004446.
- [216] G. Zhao et al. “Calibration-free wavelength-modulation spectroscopy based on a swiftly determined wavelength-modulation frequency response function of a DFB laser”. In: *Optics Express* 24.2 (2016), p. 1723. DOI: 10.1364/oe.24.001723.
- [217] Z. Qu et al. “Calibration-free scanned wavelength modulation spectroscopy – application to H₂O and temperature sensing in flames”. In: *Optics Express* 23.12 (June 2015), p. 16492. DOI: 10.1364/OE.23.016492.
- [218] A. Upadhyay and A. L. Chakraborty. “Calibration-free 2f WMS with in situ real-time laser characterization and 2f RAM nulling”. In: *Optics Letters* 40.17 (2015), p. 4086. DOI: 10.1364/ol.40.004086.
- [219] A. Upadhyay et al. “Calibration-Free WMS Using a cw-DFB-QCL, a VCSEL, and an Edge-Emitting DFB Laser With In-Situ Real-Time Laser Parameter Characterization”. In: *IEEE Photonics Journal* 9.2 (Apr. 2017), pp. 1–17. DOI: 10.1109/JPHOT.2017.2655141.
- [220] J. S. Toll. “Causality and the Dispersion Relation: Logical Foundations”. In: *Physical Review* 104.6 (Dec. 1956), pp. 1760–1770. DOI: 10.1103/PhysRev.104.1760.
- [221] J. Chamberlain. “On a relation between absorption strength and refractive index”. In: *Infrared Physics* 5.4 (Dec. 1965), pp. 175–178. DOI: 10.1016/0020-0891(65)90020-5.
- [222] J. Hayden et al. “A quantum cascade laser-based Mach–Zehnder interferometer for chemical sensing employing molecular absorption and dispersion”. In: *Applied Physics B* 124.2 (Feb. 2018), p. 29. DOI: 10.1007/s00340-018-6899-8.
- [223] S. Lindner et al. “External Cavity Quantum Cascade Laser-Based Mid-Infrared Dispersion Spectroscopy for Qualitative and Quantitative Analysis of Liquid-Phase Samples”. In: *Applied Spectroscopy* 74.4 (Apr. 2020), pp. 452–459. DOI: 10.1177/0003702819892646.
- [224] A. Hangauer et al. “High frequency modulation capabilities and quasi single-sideband emission from a quantum cascade laser”. In: *Optics Express* 22.19 (Sept. 2014), p. 23439. DOI: 10.1364/oe.22.023439.

- [225] M. Gehrtz et al. “High-frequency-modulation spectroscopy with a lead-salt diode laser”. In: *Optics Letters* 11.3 (Mar. 1986), p. 132. DOI: 10.1364/OL.11.000132.
- [226] J. A. Silver. “Frequency-modulation spectroscopy for trace species detection: theory and comparison among experimental methods”. In: *Applied Optics* 31.24 (Aug. 1992), p. 4927. DOI: 10.1364/AO.31.004927.
- [227] G. C. Bjorklund. “Frequency-modulation spectroscopy: a new method for measuring weak absorptions and dispersions”. In: *Optics Letters* 5.1 (Jan. 1980), p. 15. DOI: 10.1364/OL.5.000015.
- [228] G. C. Bjorklund et al. “Frequency modulation (FM) spectroscopy - Theory of lineshapes and signal-to-noise analysis”. In: *Applied Physics B Photophysics and Laser Chemistry* 32.3 (1983), pp. 145–152. DOI: 10.1007/BF00688820.
- [229] D. E. Cooper and T. F. Gallagher. “Double frequency modulation spectroscopy: high modulation frequency with low-bandwidth detectors”. In: *Applied Optics* 24.9 (May 1985), p. 1327. DOI: 10.1364/AO.24.001327.
- [230] J. Ye, L.-S. Ma, and J. L. Hall. “Ultrasensitive detections in atomic and molecular physics: demonstration in molecular overtone spectroscopy”. In: *Journal of the Optical Society of America B* 15.1 (Jan. 1998), p. 6. DOI: 10.1364/JOSAB.15.000006.
- [231] B. M. Siller et al. “Noise immune cavity enhanced optical heterodyne velocity modulation spectroscopy”. In: *Optics Express* 19.24 (Nov. 2011), p. 24822. DOI: 10.1364/OE.19.024822.
- [232] A. Foltynowicz et al. “Noise-immune cavity-enhanced optical heterodyne molecular spectroscopy: Current status and future potential”. In: *Applied Physics B* 92.3 (Sept. 2008), pp. 313–326. DOI: 10.1007/s00340-008-3126-z.
- [233] G. Wysocki and D. Weidmann. “Molecular dispersion spectroscopy for chemical sensing using chirped mid-infrared quantum cascade laser”. In: *Optics Express* 18.25 (Dec. 2010), p. 26123. DOI: 10.1364/OE.18.026123.
- [234] M. Nikodem and G. Wysocki. “Molecular dispersion spectroscopy - new capabilities in laser chemical sensing”. In: *Annals of the New York Academy of Sciences* 1260.1 (2012), pp. 101–111. DOI: 10.1111/j.1749-6632.2012.06660.x.
- [235] M. Nikodem, D. Weidmann, and G. Wysocki. “Chirped laser dispersion spectroscopy with harmonic detection of molecular spectra”. In: *Applied Physics B* 109.3 (Nov. 2012), pp. 477–483. DOI: 10.1007/s00340-012-5060-3.
- [236] G. Plant et al. “Field test of a remote multi-path CLaDS methane sensor”. In: *Sensors (Switzerland)* 15.9 (2015), pp. 21315–21326. DOI: 10.3390/s150921315.
- [237] P. Martín-Mateos and P. Acedo. “Heterodyne phase-sensitive detection for calibration-free molecular dispersion spectroscopy”. In: *Optics Express* 22.12 (June 2014), p. 15143. DOI: 10.1364/OE.22.015143.
- [238] P. Martín-Mateos, B. Jerez, and P. Acedo. “Heterodyne architecture for tunable laser chirped dispersion spectroscopy using optical processing”. In: *Optics Letters* 39.9 (May 2014), p. 2611. DOI: 10.1364/OL.39.002611.
- [239] W. Ding et al. “Dual-sideband heterodyne of dispersion spectroscopy based on phase-sensitive detection”. In: *Applied Optics* 55.31 (2016), p. 8698. DOI: 10.1364/ao.55.008698.
- [240] P. Martín-Mateos et al. “Heterodyne Phase-Sensitive Dispersion Spectroscopy in the Mid-Infrared with a Quantum Cascade Laser”. In: *Analytical Chemistry* 89.11 (June 2017), pp. 5916–5922. DOI: 10.1021/acs.analchem.7b00303.

Bibliography

- [241] L. Ma et al. “Temperature and H₂O sensing in laminar premixed flames using mid-infrared heterodyne phase-sensitive dispersion spectroscopy”. In: *Applied Physics B* 124.6 (June 2018), p. 117. DOI: 10.1007/s00340-018-6990-1.
- [242] L. Ma et al. “Mid-infrared heterodyne phase-sensitive dispersion spectroscopy in flame measurements”. In: *Proceedings of the Combustion Institute* 37.2 (2019), pp. 1329–1336. DOI: 10.1016/j.proci.2018.06.184.
- [243] S. Viciani et al. “A Portable Quantum Cascade Laser Spectrometer for Atmospheric Measurements of Carbon Monoxide”. In: *Sensors* 18.7 (July 2018), p. 2380. DOI: 10.3390/s18072380.
- [244] J. Kostinek et al. “Modification, Characterization and Evaluation of a Quantum/Interband Cascade Laser Spectrometer for simultaneous airborne in situ observation of CH₄, C₂H₆, CO₂, CO and N₂O”. In: *Atmospheric Measurement Techniques Discussions* October (2018), pp. 1–23.
- [245] R. Maamary et al. “A quantum cascade laser-based optical sensor for continuous monitoring of environmental methane in Dunkirk (France)”. In: *Sensors* 16.2 (2016). DOI: 10.3390/s16020224.
- [246] J. Li et al. “Simultaneous atmospheric CO, N₂O and H₂O detection using a single quantum cascade laser sensor based on dual-spectroscopy techniques”. In: *Sensors & Actuators B: Chemical* 231 (2016), pp. 723–732. DOI: 10.1016/j.snb.2016.03.089.
- [247] J. Dang et al. “Development a low-cost carbon monoxide sensor using homemade CW-DFB QCL and board-level electronics”. In: *Optics and Laser Technology* 101 (2018), pp. 57–67. DOI: 10.1016/j.optlastec.2017.10.037.
- [248] L. Tao et al. “Compact and portable open-path sensor for simultaneous measurements of atmospheric N₂O and CO using a quantum cascade laser”. In: *Optics Express* 20.27 (2012), pp. 28106–28118. DOI: 10.1007/s00340-012-5231-2.
- [249] T.-V. Dinh et al. “A review on non-dispersive infrared gas sensors: Improvement of sensor detection limit and interference correction”. In: *Sensors and Actuators B: Chemical* 231 (Aug. 2016), pp. 529–538. DOI: 10.1016/j.snb.2016.03.040.
- [250] J. Hodgkinson et al. “Non-dispersive infra-red (NDIR) measurement of carbon dioxide at 4.2 μm in a compact and optically efficient sensor”. In: *Sensors and Actuators B: Chemical* 186 (Sept. 2013), pp. 580–588. DOI: 10.1016/j.snb.2013.06.006.
- [251] M. Ebermann, S. Lehmann, and N. Neumann. “Tunable filter and detector technology for miniature infrared gas sensors”. In: *2017 ISOCS/IEEE International Symposium on Olfaction and Electronic Nose (ISOEN)*. IEEE, May 2017, pp. 1–3. DOI: 10.1109/ISOEN.2017.7968846.
- [252] R. Frodl and T. Tille. “A High-Precision NDIR CO₂ Gas Sensor for Automotive Applications”. In: *IEEE Sensors Journal* 6.6 (Dec. 2006), pp. 1697–1705. DOI: 10.1109/JSEN.2006.884440.
- [253] A. Genner et al. “On-line monitoring of methanol and methyl formate in the exhaust gas of an industrial formaldehyde production plant by a mid-IR gas sensor based on tunable Fabry-Pérot filter technology”. In: *Analytical and Bioanalytical Chemistry* 409.3 (Jan. 2017), pp. 753–761. DOI: 10.1007/s00216-016-0040-9.
- [254] C. Gasser et al. “Application of a tunable Fabry-Pérot filter to mid-infrared gas sensing”. In: *Sensors and Actuators B: Chemical* 242 (Apr. 2017), pp. 9–14. DOI: 10.1016/j.snb.2016.11.016.
- [255] R. Bogue. “Detecting gases with light: a review of optical gas sensor technologies”. In: *Sensor Review* 35.2 (Mar. 2015), pp. 133–140. DOI: 10.1108/SR-09-2014-696.

- [256] M. S. Rauscher et al. “Dual-channel mid-infrared sensor based on tunable Fabry-Pérot filters for fluid monitoring applications”. In: *Sensors and Actuators B: Chemical* 259 (Apr. 2018), pp. 420–427. DOI: 10.1016/j.snb.2017.12.032.
- [257] J. Kuligowski et al. “Recent advances in on-line liquid chromatography - infrared spectrometry (LC-IR)”. In: *TrAC Trends in Analytical Chemistry* 29.6 (June 2010), pp. 544–552. DOI: 10.1016/j.trac.2010.03.004.
- [258] K. H. Michaelian. *Photoacoustic IR Spectroscopy: Instrumentation, Applications and Data Analysis: Second Edition*. 2010. DOI: 10.1002/9783527633197.
- [259] M. da Silva et al. “Photoacoustic detection of ozone using a quantum cascade laser”. In: *Applied Physics B* 78.6 (Apr. 2004), pp. 677–680. DOI: 10.1007/s00340-004-1513-7.
- [260] M. W. Sigrist. “Trace gas monitoring by laser photoacoustic spectroscopy and related techniques (plenary)”. In: *Review of Scientific Instruments* 74.1 (Jan. 2003), pp. 486–490. DOI: 10.1063/1.1512697.
- [261] J. Li, W. Chen, and B. Yu. “Recent Progress on Infrared Photoacoustic Spectroscopy Techniques”. In: *Applied Spectroscopy Reviews* 46.6 (Aug. 2011), pp. 440–471. DOI: 10.1080/05704928.2011.570835.
- [262] A. Elia et al. “Photoacoustic Spectroscopy with Quantum Cascade Lasers for Trace Gas Detection”. In: *Sensors* 6.10 (Oct. 2006), pp. 1411–1419. DOI: 10.3390/s6101411.
- [263] F. J. Harren and S. M. Cristescu. “Photoacoustic Spectroscopy in Trace Gas Monitoring”. In: *Encyclopedia of Analytical Chemistry* (Mar. 2019), pp. 1–29. DOI: 10.1002/9780470027318.a0718.pub3.
- [264] M. Sigrist, S. Bernegger, and P. Meyer. “Infrared-laser photoacoustic spectroscopy”. In: *Infrared Physics* 29.2-4 (May 1989), pp. 805–814. DOI: 10.1016/0020-0891(89)90129-2.
- [265] T. Chen, G. Su, and H. Yuan. “In situ gas filter correlation: photoacoustic CO detection method for fire warning”. In: *Sensors and Actuators B: Chemical* 109.2 (Sept. 2005), pp. 233–237. DOI: 10.1016/j.snb.2004.12.055.
- [266] K. Kuhn, E. Pignanelli, and A. Schutze. “Versatile Gas Detection System Based on Combined NDIR Transmission and Photoacoustic Absorption Measurements”. In: *IEEE Sensors Journal* 13.3 (Mar. 2013), pp. 934–940. DOI: 10.1109/JSEN.2012.2224104.
- [267] S. Li et al. “Ppb-Level Quartz-Enhanced Photoacoustic Detection of Carbon Monoxide Exploiting a Surface Grooved Tuning Fork”. In: *Analytical Chemistry* 91.9 (May 2019), pp. 5834–5840. DOI: 10.1021/acs.analchem.9b00182.
- [268] J. P. Waclawek et al. “Quartz-enhanced photoacoustic spectroscopy-based sensor system for sulfur dioxide detection using a CW DFB-QCL”. In: *Applied Physics B: Lasers and Optics* 117.1 (2014), pp. 113–120. DOI: 10.1007/s00340-014-5809-y.
- [269] L. Gong et al. “Atmospheric ammonia measurements in Houston, TX using an external-cavity quantum cascade laser-based sensor”. In: *Atmospheric Chemistry and Physics* 11.18 (2011), pp. 9721–9733. DOI: 10.5194/acp-11-9721-2011.
- [270] A. A. Kosterev et al. “QEPAS detector for rapid spectral measurements”. In: *Applied Physics B: Lasers and Optics* 100.1 (2010), pp. 173–180. DOI: 10.1007/s00340-010-3975-0.
- [271] P. Patimisco et al. “Quartz-enhanced photoacoustic spectroscopy: a review”. In: *Sensors* 14.4 (Mar. 2014), pp. 6165–6206. DOI: 10.3390/s140406165.

Bibliography

- [272] M. Giglio et al. “Nitrous oxide quartz-enhanced photoacoustic detection employing a broadband distributed-feedback quantum cascade laser array”. In: *Applied Physics Letters* 113.17 (2018), pp. 1–5. DOI: 10.1063/1.5049872.
- [273] Y. Ma. “Review of Recent Advances in QEPAS-Based Trace Gas Sensing”. In: *Applied Sciences* 8.10 (Oct. 2018), p. 1822. DOI: 10.3390/app8101822.
- [274] K. Krzempek et al. “Multi-pass cell-assisted photoacoustic/photothermal spectroscopy of gases using quantum cascade laser excitation and heterodyne interferometric signal detection”. In: *Applied Physics B* 124.5 (May 2018), p. 74. DOI: 10.1007/s00340-018-6941-x.
- [275] K. Krzempek. “A Review of Photothermal Detection Techniques for Gas Sensing Applications”. In: *Applied Sciences* 9.14 (July 2019), p. 2826. DOI: 10.3390/app9142826.
- [276] J. P. Waclawek et al. “2f-wavelength modulation Fabry-Perot photothermal interferometry”. In: 24.25 (2016), pp. 28958–28967. DOI: 10.1364/OE.24.028957.
- [277] J. P. Waclawek et al. “Balanced-detection interferometric cavity-assisted photothermal spectroscopy”. In: *Optics Express* 27.9 (Apr. 2019), p. 12183. DOI: 10.1364/OE.27.012183.
- [278] S. E. Bialkowski, N. G. C. Astrath, and M. A. Proskurnin. *Photothermal Spectroscopy Methods*. Wiley, Apr. 2019. DOI: 10.1002/9781119279105.
- [279] Y. Tan et al. “Cavity-Enhanced Photothermal Gas Detection With a Hollow Fiber Fabry-Perot Absorption Cell”. In: *Journal of Lightwave Technology* 37.17 (Sept. 2019), pp. 4222–4228. DOI: 10.1109/JLT.2019.2922001.
- [280] H. Bao et al. “Modeling and performance evaluation of in-line Fabry-Perot photothermal gas sensors with hollow-core optical fibers”. In: *Optics Express* 28.4 (Feb. 2020), p. 5423. DOI: 10.1364/OE.385670.
- [281] A. Elefante et al. “Environmental Monitoring of Methane with Quartz-Enhanced Photoacoustic Spectroscopy Exploiting an Electronic Hygrometer to Compensate the H₂O Influence on the Sensor Signal”. In: *Sensors* 20.10 (May 2020), p. 2935. DOI: 10.3390/s20102935.
- [282] R. Lewicki et al. “Current Status of Mid-infrared Semiconductor-Laser-based Sensor Technologies for Trace-Gas Sensing Applications”. In: *The Wonder of Nanotechnology: Quantum Optoelectronic Devices and Applications*. Society of Photo-Optical Instrumentation Engineers, 2013. Chap. 23. DOI: 10.1117/3.1002245.ch23.
- [283] J. Hodgkinson and R. P. Tatam. “Optical gas sensing: a review”. In: *Measurement Science and Technology* 24.1 (Jan. 2013), p. 012004. DOI: 10.1088/0957-0233/24/1/012004.
- [284] J. Haas and B. Mizaikoff. “Advances in Mid-Infrared Spectroscopy for Chemical Analysis”. In: *Annual Review of Analytical Chemistry* 9.1 (2016), pp. 45–68. DOI: 10.1146/annurev-anchem-071015-041507.
- [285] Z. Du et al. “Mid-Infrared Tunable Laser-Based Broadband Fingerprint Absorption Spectroscopy for Trace Gas Sensing: A Review”. In: *Applied Sciences* 9.2 (Jan. 2019), p. 338. DOI: 10.3390/app9020338.
- [286] A. Lambrecht and K. Schmitt. “Mid-infrared gas-sensing systems and applications”. In: *Mid-infrared Optoelectronics*. Elsevier, 2020, pp. 661–715. DOI: 10.1016/B978-0-08-102709-7.00016-4.
- [287] S. Palzer. “Photoacoustic-Based Gas Sensing: A Review”. In: *Sensors (Basel, Switzerland)* 20.9 (2020). DOI: 10.3390/s20092745.

- [288] Y. Ma, A. Vicet, and K. Krzempek. *State-of-the-art Laser Gas Sensing Technologies*. Vol. 10. 2. MDPI, Mar. 2020. DOI: 10.3390/books978-3-03928-399-6.
- [289] E. Commission. *Horizon 2020 - Work Programme 2014-2015 - Annex G. Technology readiness levels (TRL)*. 2014.
- [290] EN 60297-3-100. *Mechanical structures for electronic equipment - Dimensions of mechanical structures of the 482,6 mm (19 in) series*. 2009.
- [291] A. N. Cox. *Allen's Astrophysical Quantities*. Ed. by A. N. Cox. New York, NY: Springer New York, 2002. DOI: 10.1007/978-1-4612-1186-0.
- [292] J. U. White. "Long Optical Paths of Large Aperture". In: *Journal of the Optical Society of America* 32.5 (May 1942), p. 285. DOI: 10.1364/JOSA.32.000285.
- [293] M. L. Thoma, R. Kaschow, and F. J. Hindelang. "A multiple-reflection cell suited for absorption measurements in shock tubes". In: *Shock Waves* 4.1 (July 1994), pp. 51–53. DOI: 10.1007/BF01414633.
- [294] D. R. Herriott and H. J. Schulte. "Folded Optical Delay Lines". In: *Applied Optics* 4.8 (Aug. 1965), p. 883. DOI: 10.1364/AO.4.000883.
- [295] D. Horn and G. C. Pimentel. "2.5-km Low-Temperature Multiple-Reflection Cell". In: *Applied Optics* 10.8 (Aug. 1971), p. 1892. DOI: 10.1364/AO.10.001892.
- [296] J.-F. Doussin, R. Dominique, and C. Patrick. "Multiple-pass cell for very-long-path infrared spectrometry". In: *Applied Optics* 38.19 (July 1999), p. 4145. DOI: 10.1364/AO.38.004145.
- [297] W. S. Dalton and H. Sakai. "Absorption cell for the infrared spectroscopy of heated gas". In: *Applied Optics* 19.14 (1980), p. 2413. DOI: 10.1364/ao.19.002413.
- [298] M. Mangold et al. "Circular paraboloid reflection cell for laser spectroscopic trace gas analysis". In: *Journal of the Optical Society of America A* 33.5 (2016), p. 913. DOI: 10.1364/JOSAA.33.000913.
- [299] M. Zou et al. "Acetylene sensing system based on wavelength modulation spectroscopy using a triple-row circular multi-pass cell". In: *Optics Express* 28.8 (2020), p. 11573. DOI: 10.1364/oe.388343.
- [300] Z. Yang, M. Zou, and L. Sun. "Generalized optical design of the multiple-row circular multi-pass cell with dense spot pattern". In: *Optics Express* 27.23 (Nov. 2019), p. 32883. DOI: 10.1364/OE.27.032883.
- [301] M. Graf, L. Emmenegger, and B. Tuzson. "Compact, circular, and optically stable multipass cell for mobile laser absorption spectroscopy". In: *Optics Letters* 43.11 (2018), p. 2434. DOI: 10.1364/OL.43.002434.
- [302] D. Herriott, H. Kogelnik, and R. Kompfner. "Off-Axis Paths in Spherical Mirror Interferometers". In: *Applied Optics* 3.4 (1964), p. 523. DOI: 10.1364/ao.3.000523.
- [303] J. B. McManus, P. L. Kebabian, and M. S. Zahniser. "Astigmatic mirror multipass absorption cells for long-path-length spectroscopy". In: *Applied Optics* 34.18 (June 1995), pp. 3336–3348. DOI: 10.1364/AO.34.003336.
- [304] K. G. Libbrecht and J. L. Hall. "A low-noise high-speed diode laser current controller". In: *Review of Scientific Instruments* 64.8 (Aug. 1993), pp. 2133–2135. DOI: 10.1063/1.1143949.
- [305] C. M. Seck et al. "Noise reduction of a Libbrecht–Hall style current driver". In: *Review of Scientific Instruments* 87.6 (June 2016), p. 064703. DOI: 10.1063/1.4953330.

Bibliography

- [306] C. J. Erickson et al. “An ultrahigh stability, low-noise laser current driver with digital control”. In: *Review of Scientific Instruments* 79.7 (July 2008), p. 073107. DOI: 10.1063/1.2953597.
- [307] N. Li et al. “A portable low-power integrated current and temperature laser controller for high-sensitivity gas sensor applications”. In: *Review of Scientific Instruments* 89.10 (Oct. 2018), p. 103103. DOI: 10.1063/1.5044230.
- [308] D. L. Troxel, C. J. Erickson, and D. S. Durfee. “Note: Updates to an ultra-low noise laser current driver”. In: *Review of Scientific Instruments* 82.9 (Sept. 2011), p. 096101. DOI: 10.1063/1.3630950.
- [309] C. Liu et al. “Laser driving and data processing concept for mobile trace gas sensing: Design and implementation”. In: *Review of Scientific Instruments* 89.6 (June 2018), p. 065107. DOI: 10.1063/1.5026546.
- [310] D. B. Oh, M. E. Paige, and D. S. Bomse. “Frequency modulation multiplexing for simultaneous detection of multiple gases by use of wavelength modulation spectroscopy with diode lasers”. In: *Applied Optics* 37.12 (1998), p. 2499. DOI: 10.1364/ao.37.002499.
- [311] National Instruments. *Application Design Patterns: Producer/Consumer*. Tech. rep. National Instruments, 2012.
- [312] EN 60715. *Dimensions of low-voltage switchgear and controlgear - Standardized mounting on rails for mechanical support of electrical devices in switchgear and controlgear installations*. 2016.
- [313] X. Chen et al. “Highly-sensitive NO, NO₂, and NH₃ measurements with an open-multipass cell based on mid-infrared wavelength modulation spectroscopy”. In: *Chinese Physics B* 27.4 (Apr. 2018), p. 040701. DOI: 10.1088/1674-1056/27/4/040701.
- [314] J. Li et al. “Real-Time Measurements of Atmospheric CO Using a Continuous-Wave Room Temperature Quantum Cascade Laser Spectrometer”. In: *2012 Symposium on Photonics and Optoelectronics*. Vol. 20. 7. IEEE, May 2012, pp. 1–4. DOI: 10.1109/SOPO.2012.6271103.

Appendix A.

Simulated Gas Spectra



Die approbierte gedruckte Originalversion dieser Dissertation ist an der TU Wien Bibliothek verfügbar.
The approved original version of this doctoral thesis is available in print at TU Wien Bibliothek.

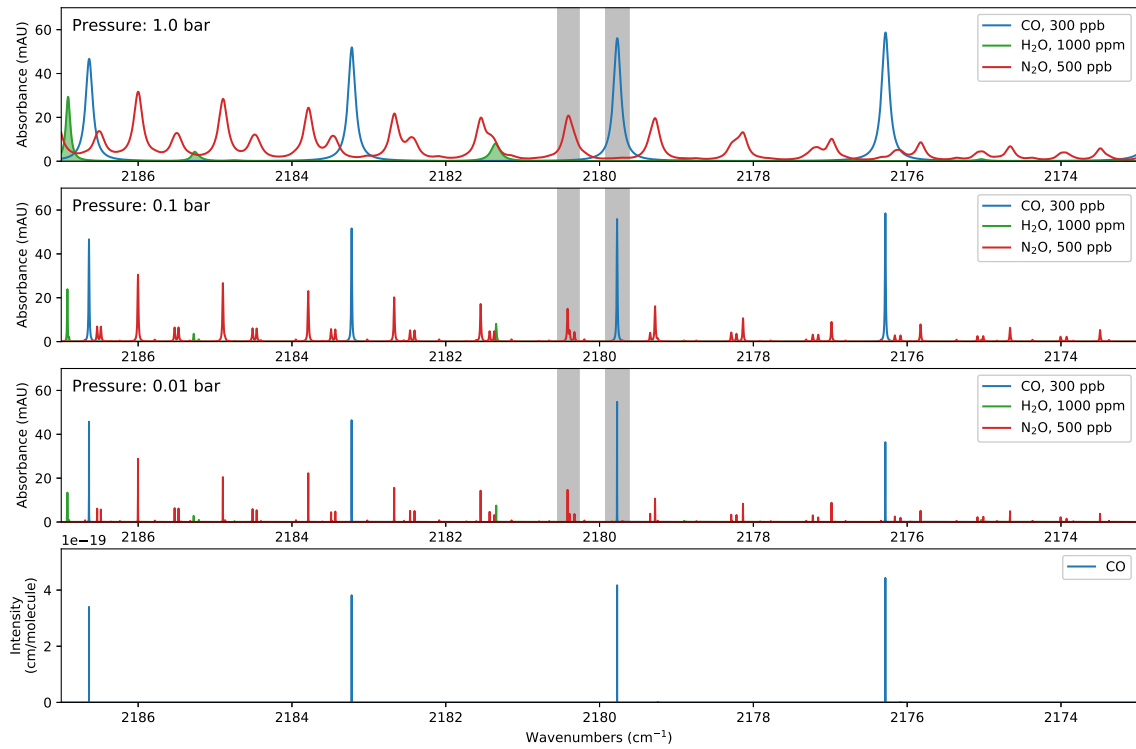


Figure A.1.: Simulated spectra of CO and its possible interferants at different pressures.

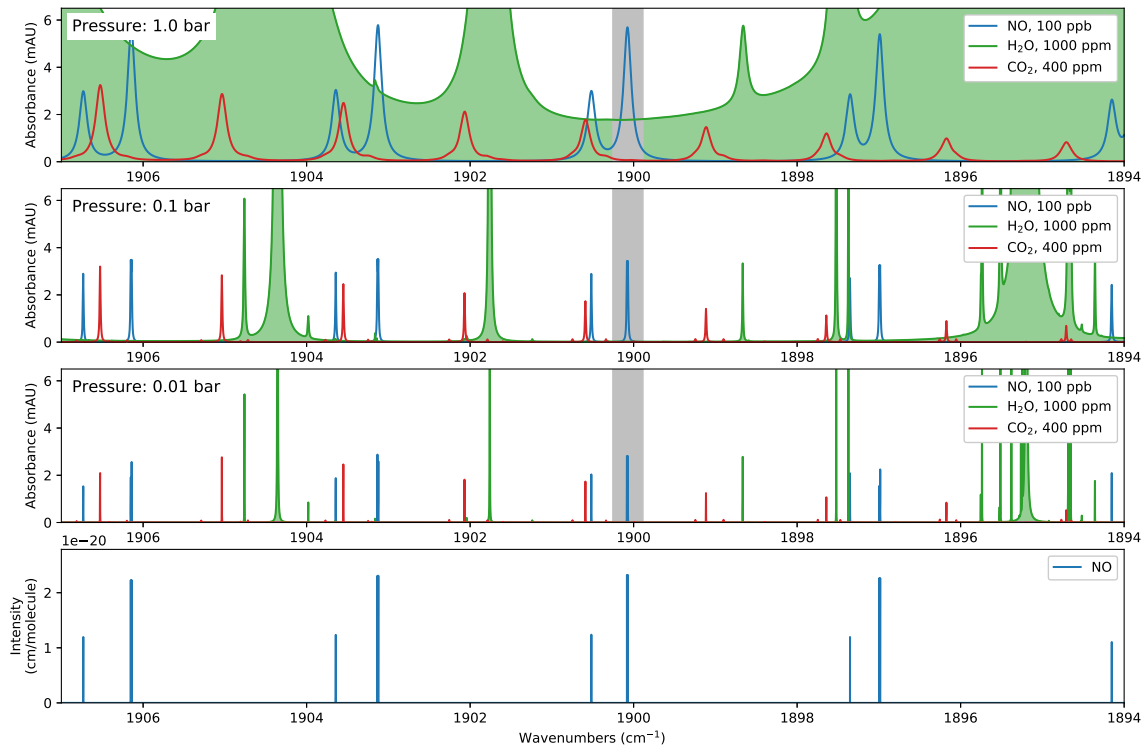


Figure A.2.: Simulated spectra of NO and its possible interferants at different pressures.

Appendix A. Simulated Gas Spectra

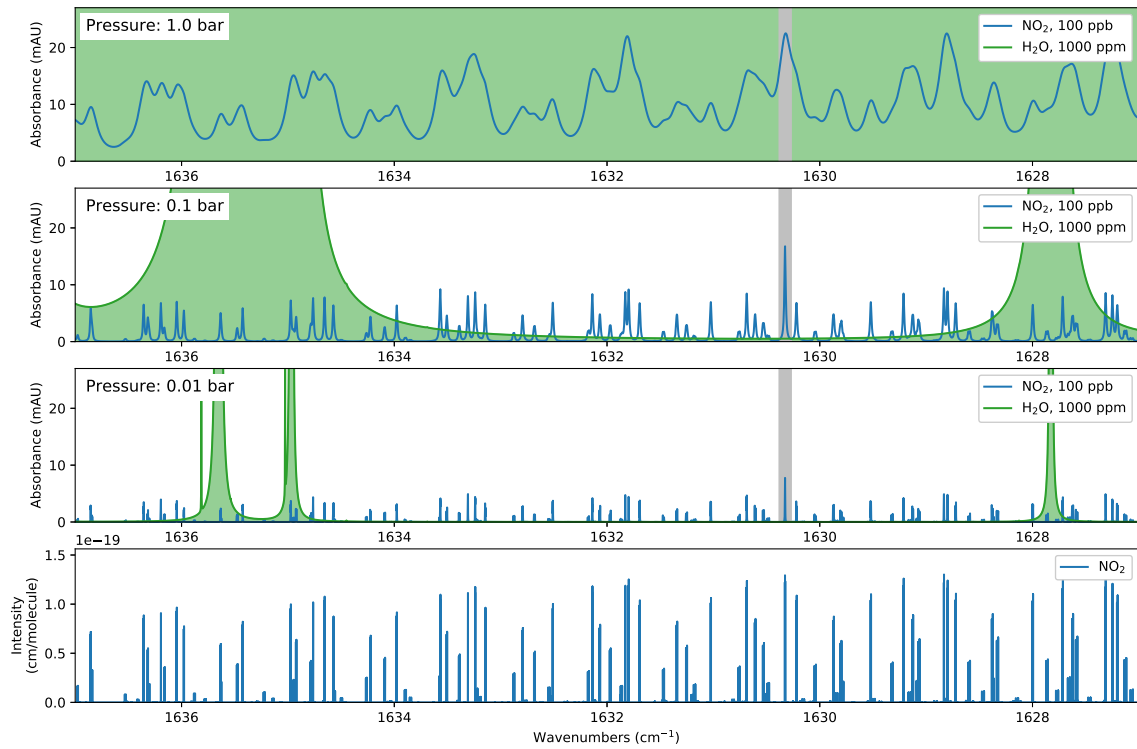


Figure A.3.: Simulated spectra of NO₂ and its possible interferants at different pressures.

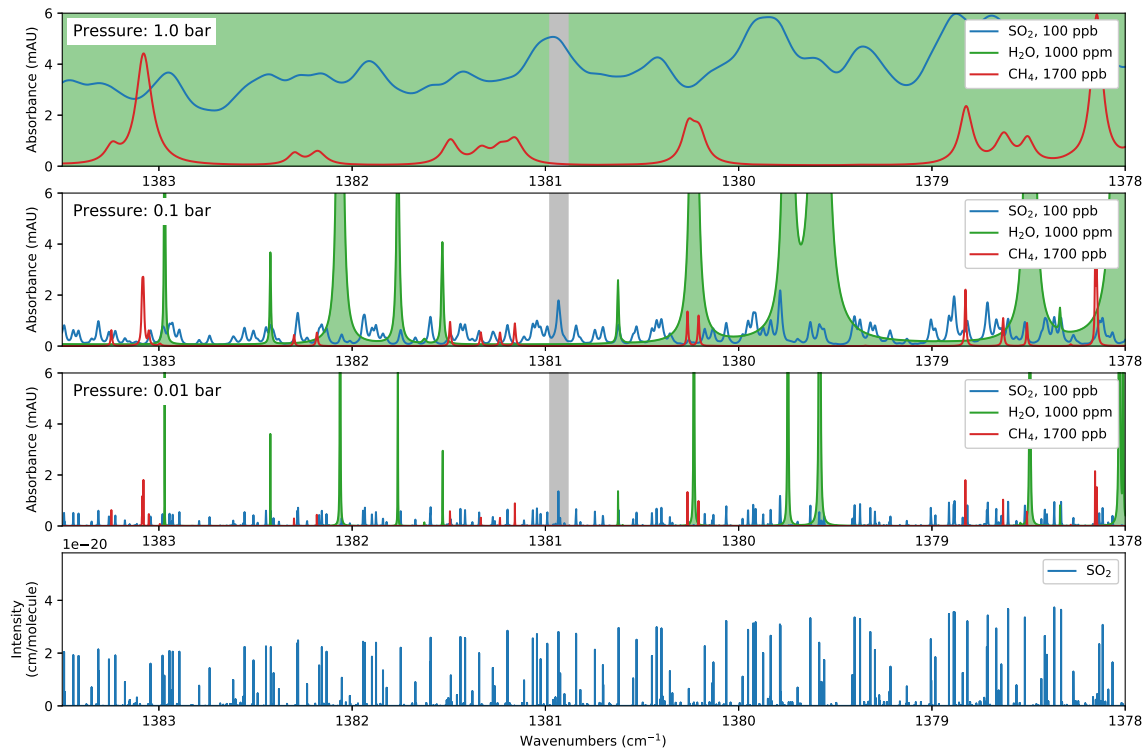


Figure A.4.: Simulated spectra of SO₂ and its possible interferants at different pressures.

Appendix B.

1f-, 2f- and 3f-WMS-Spectra

Appendix B. 1f-, 2f- and 3f-WMS-Spectra

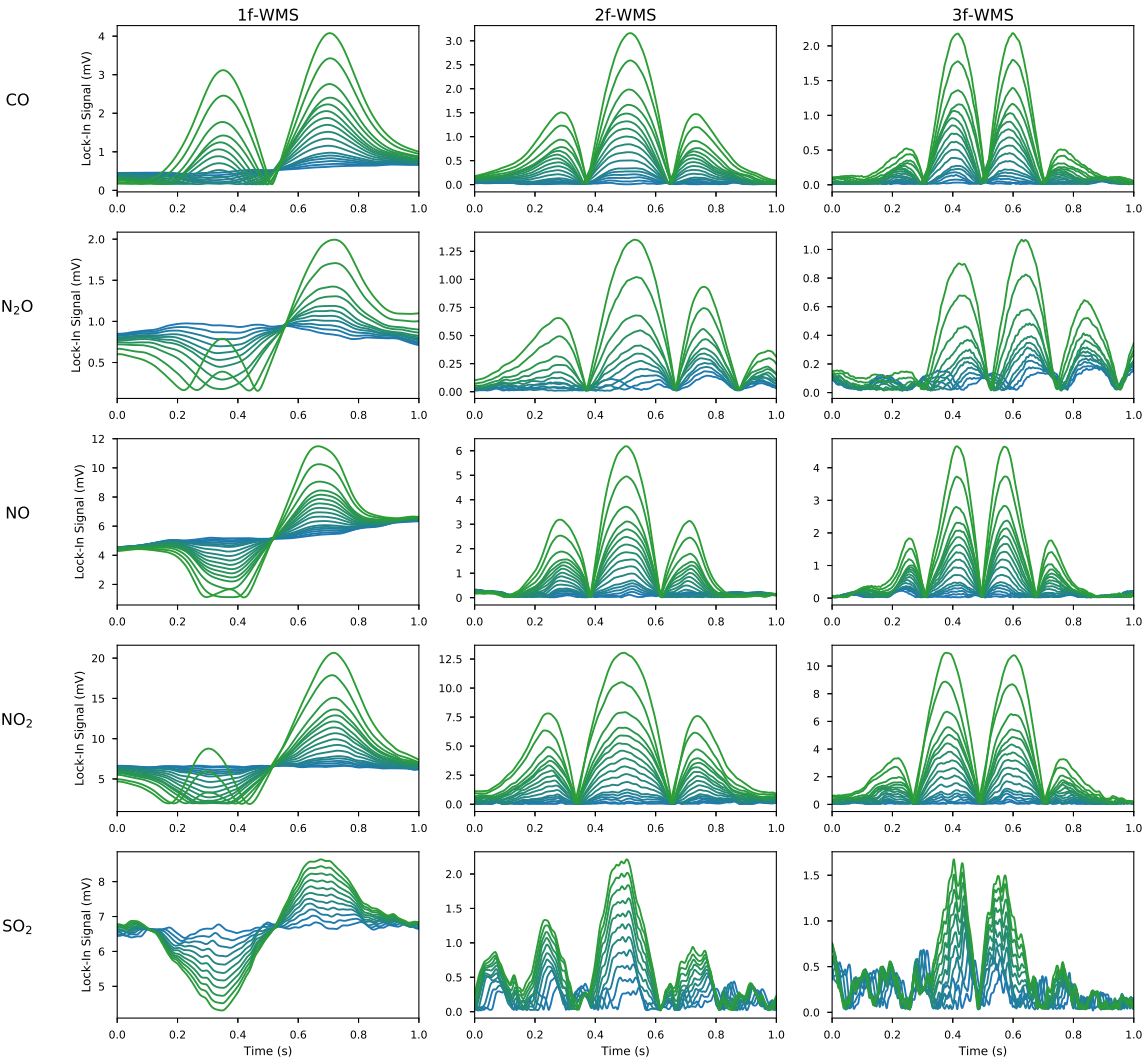


Figure B.1.: 1f, 2f and 3f-WMS-spectra, recorded during the calibrations.

Die approbierte gedruckte Originalversion dieser Dissertation ist an der TU Wien Bibliothek verfügbar.
 The approved original version of this doctoral thesis is available in print at TU Wien Bibliothek.

Appendix C.

Demultiplexer



Die approbierte gedruckte Originalversion dieser Dissertation ist an der TU Wien Bibliothek verfügbar.
The approved original version of this doctoral thesis is available in print at TU Wien Bibliothek.



Die approbierte gedruckte Originalversion dieser Dissertation ist an der TU Wien Bibliothek verfügbar.
The approved original version of this doctoral thesis is available in print at TU Wien Bibliothek.

Appendix D.

Mechanical Parts, CAD Drawings



Die approbierte gedruckte Originalversion dieser Dissertation ist an der TU Wien Bibliothek verfügbar.
The approved original version of this doctoral thesis is available in print at TU Wien Bibliothek.

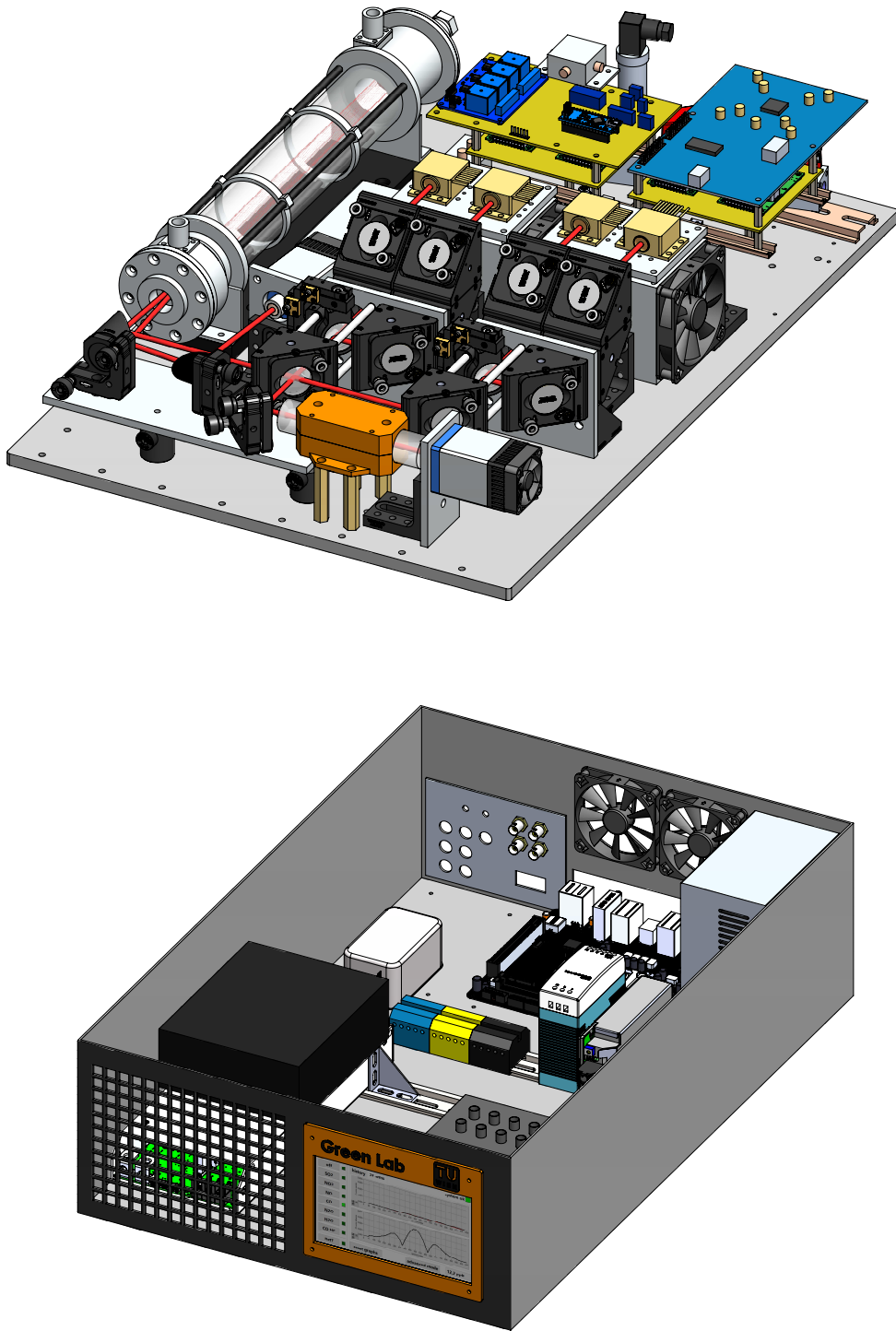


Figure D.1.: CAD drawings of the optical setup (without enclosure, top) and the electronics racks (without cover plate, bottom).

Appendix D. Mechanical Parts, CAD Drawings

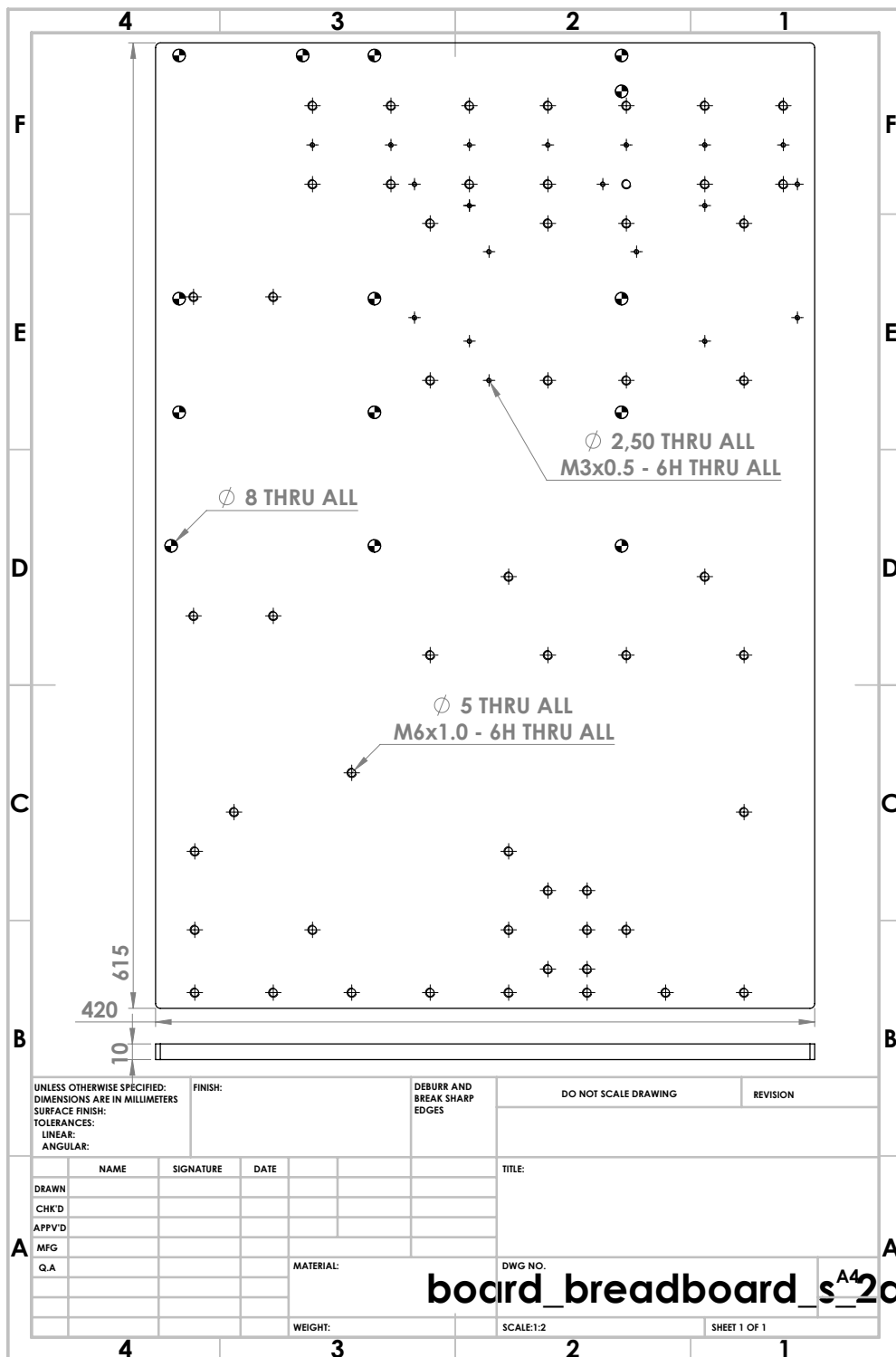


Figure D.2.: Technical drawing of the custom-built breadboard.

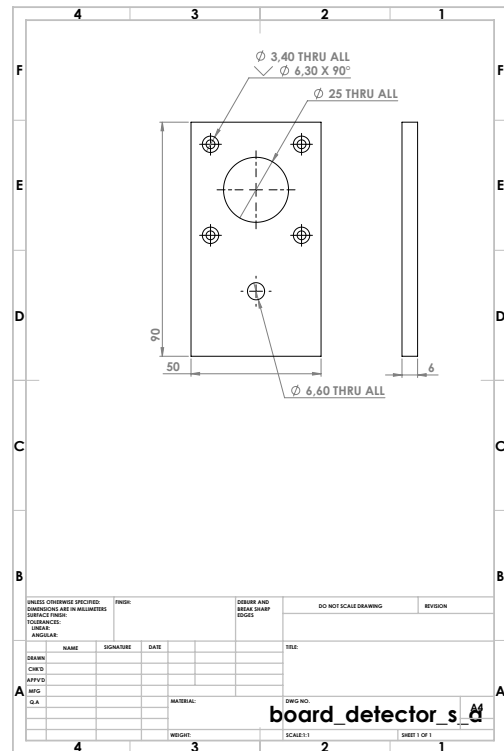
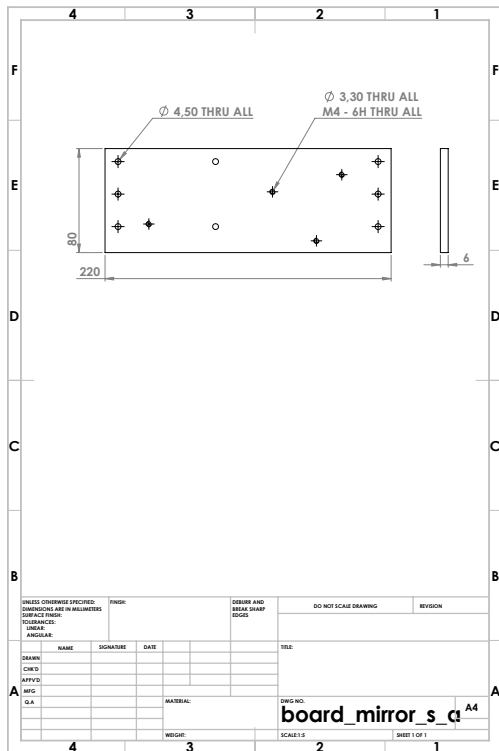
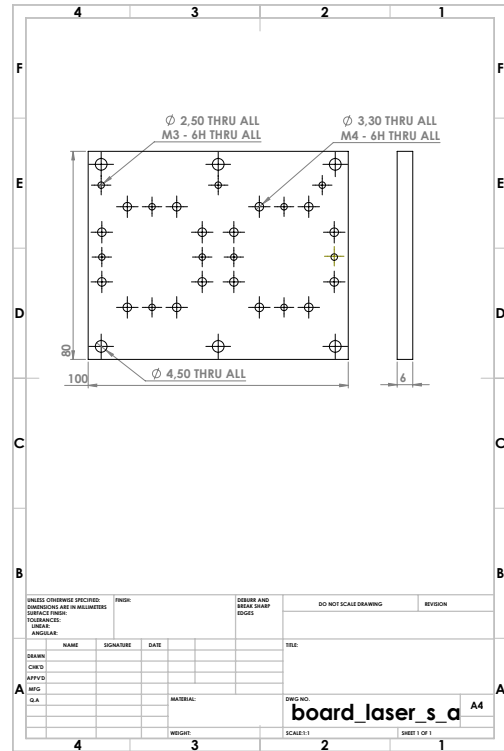
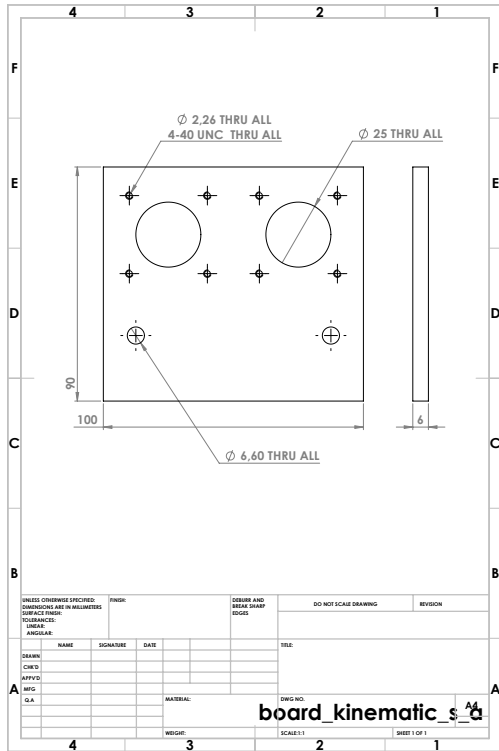


Figure D.3.: Additional custom-built parts.



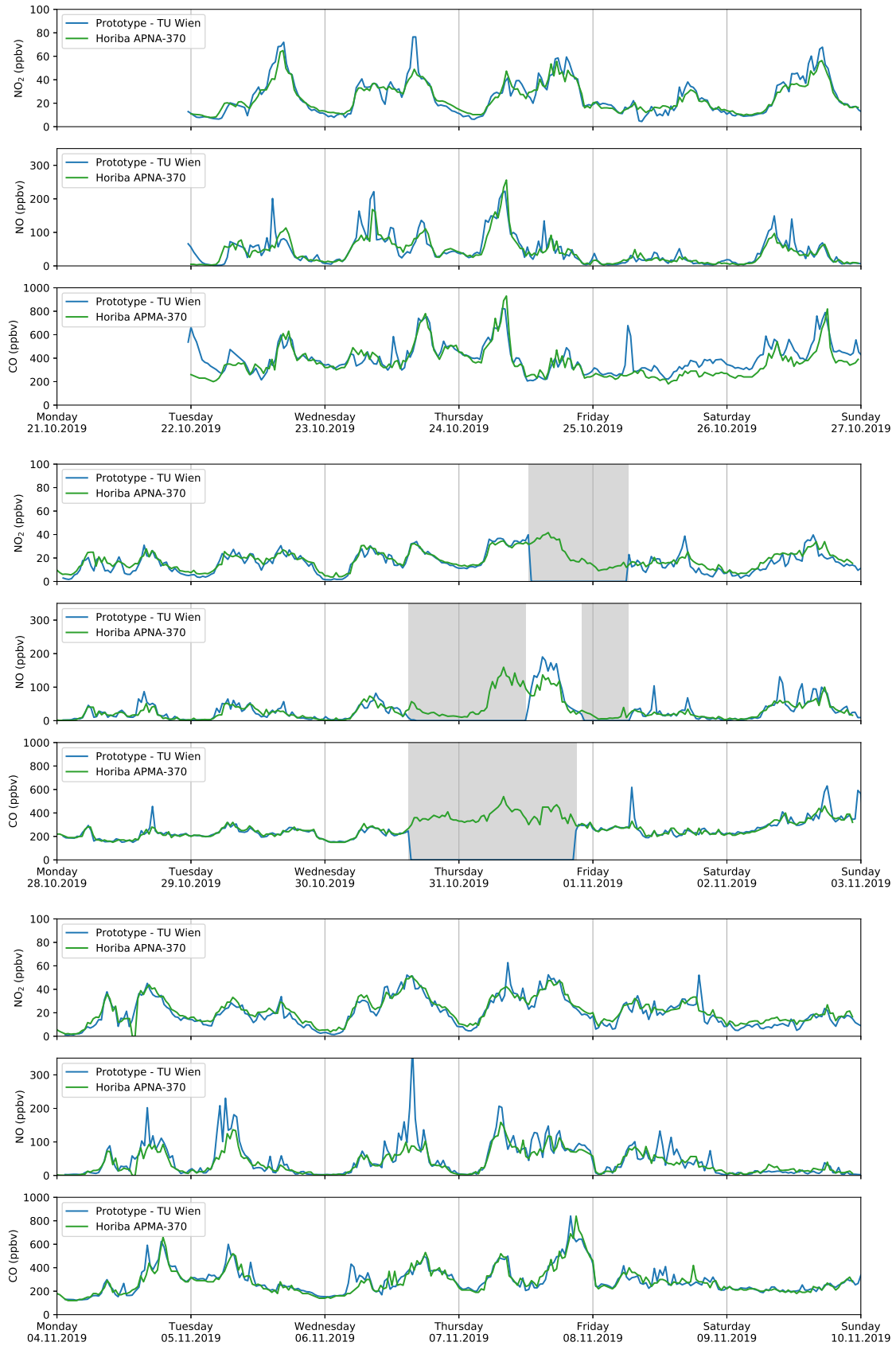
Die approbierte gedruckte Originalversion dieser Dissertation ist an der TU Wien Bibliothek verfügbar.
The approved original version of this doctoral thesis is available in print at TU Wien Bibliothek.

Appendix E.

Results Vienna, October 22 - November 29, 2019

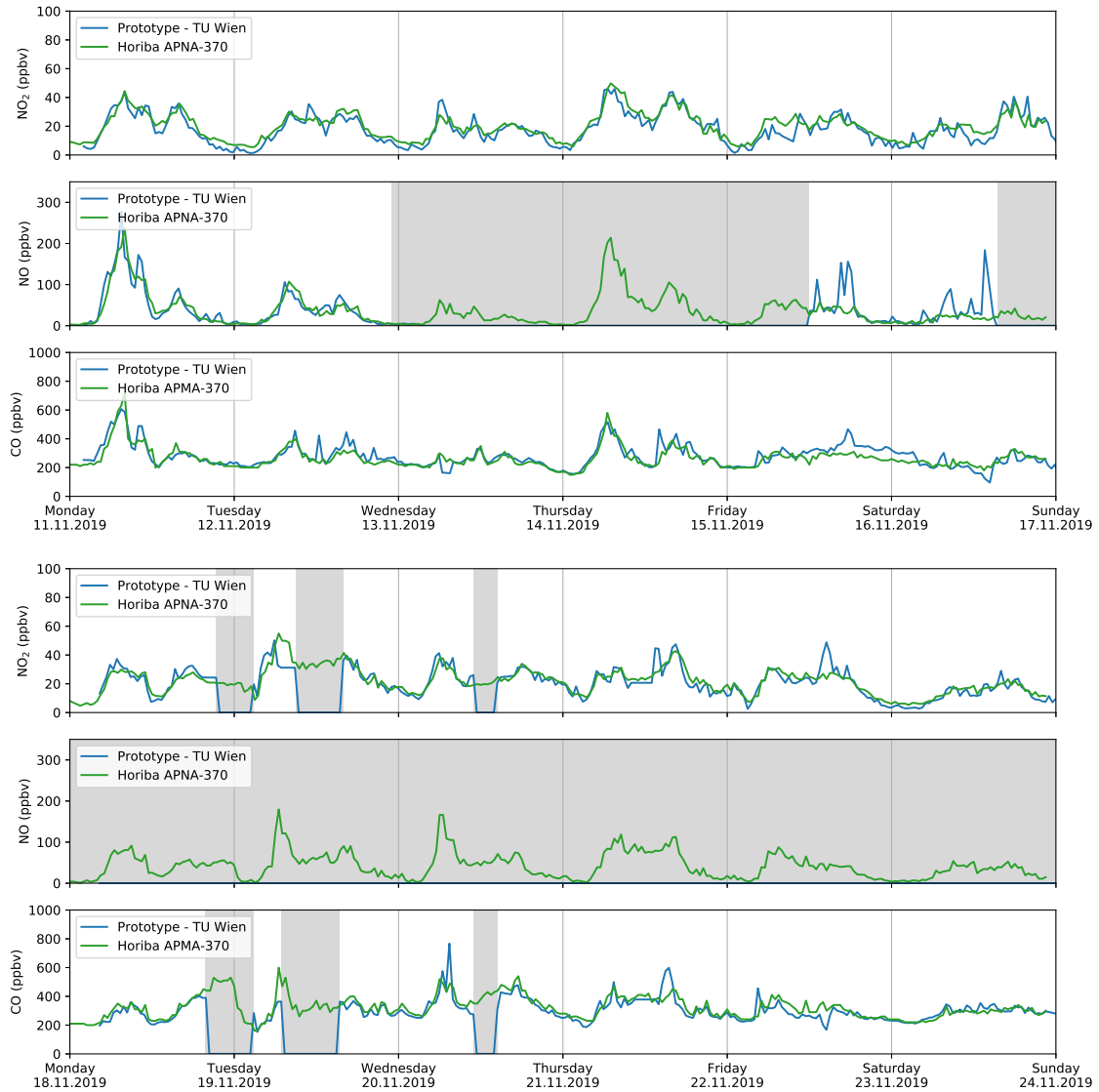


Die approbierte gedruckte Originalversion dieser Dissertation ist an der TU Wien Bibliothek verfügbar.
The approved original version of this doctoral thesis is available in print at TU Wien Bibliothek.



Appendix E. Results Vienna, October 22 - November 29, 2019

Die approbierte gedruckte Originalversion dieser Dissertation ist an der TU Wien Bibliothek verfügbar.
The approved original version of this doctoral thesis is available in print at TU Wien Bibliothek.



Appendix F.

Scientific Publications on Infrared-Based Gas Sensing

Publication I

A Quantum Cascade Laser-Based Multi-Gas Sensor for Ambient Air Monitoring


Authors: Andreas Genner, Pedro Martín-Mateos, Harald Moser and Bernhard Lendl



Die approbierte gedruckte Originalversion dieser Dissertation ist an der TU Wien Bibliothek verfügbar.
The approved original version of this doctoral thesis is available in print at TU Wien Bibliothek.

Article

A Quantum Cascade Laser-Based Multi-Gas Sensor for Ambient Air Monitoring

Andreas Genner ¹, Pedro Martín-Mateos ², Harald Moser ¹  and Bernhard Lendl ^{1,*}

¹ Institute of Chemical Technologies and Analytics, TU Wien, Getreidemarkt 9/164, 1060 Vienna, Austria; andreas.genner@tuwien.ac.at (A.G.); harald.moser@tuwien.ac.at (H.M.)

² Electronics Technology Department, Universidad Carlos III de Madrid, C/Butarque 15, 28911 Leganés, Madrid, Spain; pmmateos@ing.uc3m.es

* Correspondence: bernhard.lendl@tuwien.ac.at

Received: 28 February 2020; Accepted: 25 March 2020; Published: 26 March 2020



Abstract: A quantum cascade laser-based sensor for ambient air monitoring is presented and five gases, affecting the air quality, can be quantified. The light sources are selected to measure CO, NO, NO₂, N₂O and SO₂. The footprint of the measurement setup is designed to fit in two standard 19" rack (48 cm × 65 cm) with 4 height units (18 cm) whereas one is holding the optical components and the other one contains the electronics and data processing unit. The concentrations of the individual analytes are measured using 2f-Wavelength Modulation Spectroscopy (2f-WMS) and a commercially available multipass gas cell defines the optical path. In addition, CO can also be measured with a dispersion-based technique, which allows one to cover a wider concentration range than 2f-WMS. The performance of this prototype has been evaluated in the lab and detection limits in the range of 1ppbv have been achieved. Finally, the applicability of this prototype for ambient air monitoring is shown in a five-week measurement campaign in cooperation with the Municipal Department for Environmental Protection (MA 22) of Vienna, Austria.

Keywords: quantum cascade laser; infrared; ambient air; wavelength modulation spectroscopy; heterodyne phase sensitive dispersion spectroscopy

1. Introduction

Measuring the air quality has become an important task in analytical chemistry over the last decades and it was mainly caused by the combustion of fossil fuels. While CO₂ is the primary product of the oxidation process, toxic gases, such as CO, NO, NO₂ and SO₂, are formed as well. Measures, such as the desulfurizing of diesel, gasoline or the resulting flue gas already improved the air quality in industrial cities significantly during the last decades [1,2]. A recent example of further efforts to reduce air pollution is the limitation of diesel cars in cities with high NO_x levels, which are considered to cause respiratory diseases [3]. Nevertheless, the effectiveness of those measures needs to be evaluated and are therefore in the interest of (non-) governmental air-quality measurement networks. The requirements for such a measurement station are typically regulated in local laws and the globally important regulations, such as the Directive 2008/50/EC (EU), the Clean Air Act (USA) and the Law on Prevention and Control of Air Pollution (China) should be noted.

The instrumental equipment can differ between the measurement stations but in general, it can be said that each analyte/measurement parameter requires different equipment. For example, SO₂ is measured with UV fluorescence, the NO_x detection relies on chemiluminescence and the CO/CO₂ is quantified with a non-dispersive infrared sensor. One way to reduce the investment/operation costs and the required space of the measurement station is to combine and simplify the equipment/components. As the previously listed analytes are gaseous and rather small molecules, an infrared based technique

could be applied. In infrared spectroscopy, Fourier transformation-based spectrometers are still the “golden standard” and cover the whole mid-IR. However, the typical concentrations of the target analytes require an optical path length >20 m, which is difficult to achieve in combination with standard Fourier transform infrared (FTIR) equipment.

An alternative is to replace the light source with a collimated semiconductor laser. Beside the higher optical power and the better beam quality, they do not require an interferometer. Instead, the emitted wavelength can be controlled by the temperature of the gain element and the injected current.

Lead–salt diode lasers were the first successful semiconductor based mid-IR diode lasers [4–11], but only a decent number of gas sensors, working in the mid-IR, have been demonstrated and published [12–19]. This has changed with the development of the quantum cascade laser (QCL) [20]. The first devices required liquid nitrogen for cooling and allowed only pulsed operation, but they are currently commercially available in continuous wave mode at room temperature and emit up to several hundreds of mW. So far, numerous measurement techniques with QCLs have been applied to ambient air monitoring—ranging from Tunable Diode Laser Absorption Spectroscopy (TDLAS) [21–23], 2f-Wavelength Modulation Spectroscopy (2f-WMS) [24], photoacoustic [25–27] photothermal spectroscopy [28], cavity enhanced absorption spectroscopy [29] and also dispersion-based ones [30] have been demonstrated.

In this work, we present a sensor based on 2f-WMS that is capable to quantify the analytes CO, NO, N₂O, NO₂ and SO₂ in the single digit ppbv-range in ambient air. With the exception of the breadboard and a 3d-printed mount for a reference cell, all other parts are off-the-shelf components and easily available. In addition, we show the integration of Heterodyne Phase Sensitive Dispersion Spectroscopy (HPSDS) to cover a significantly higher CO concentration range and present results of a measurement campaign in Vienna.

2. Design Considerations for the Multi-Gas Sensor

Due to the molecular properties of the analytes of interest, their absorption lines are clearly separated, in the range between 4 and 8 μm (Figure 1a) and could easily be quantified with filter-based IR sensors. As the ambient air contains other IR active molecules like H₂O, CO₂ or CH₄ as well, only a few absorption lines are interference-free and suited for quantification with IR spectroscopy. This situation is illustrated in Figure 1b whereas the line strengths of the individual analytes are plotted on a logarithmic scale.

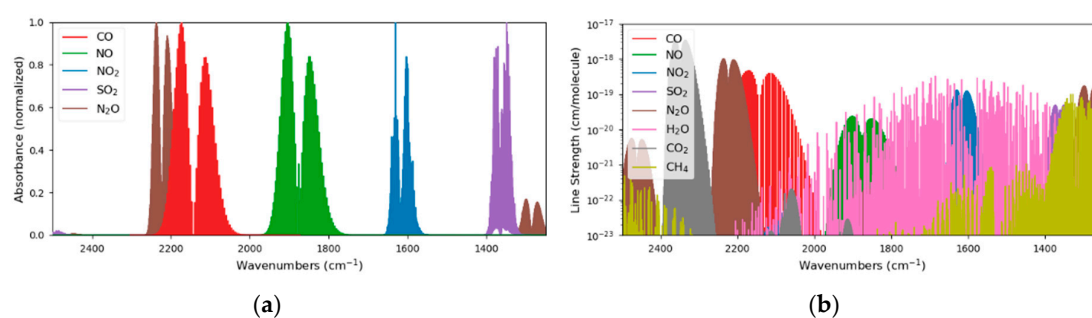


Figure 1. Although the target analytes show nicely separated absorption regions (a), the presence of other gases in the ambient air, such as H₂O, CH₄ and CO₂, require a precise wavelength selection of the laser sources (b).

QCLs with an external cavity (EC-QCLs) can already cover a spectral range of >400 cm⁻¹ [31], but they are rather unsuited for gas phase measurement. This is caused by the mechanical parts that are required to select the emitted wavelength and mode hops are a common issue. They are mainly used for measuring solids [32,33], liquids [34,35] or polyatomic gasses and vapors with broad absorption bands [36,37]. During the last decades, QCLs with distributed feedback (DFB) gratings [38] have

proven as reliable light sources for gas phase spectroscopy. An optical grating, which is etched into the waveguide during the manufacturing process, is responsible for single mode emission. Subsequently, the emitted wavelength can only be tuned by either changing the injected current or the temperature of the gain element. Common values for this tuning range are a few wavenumbers and usually more than one absorption line of the target analyte is within the accessible range.

As the absorption lines of our target analytes are distributed over the mid IR range and cannot be covered by a single DFB-QCL, multiple lasers are necessary. On the wafer scale level, QCL-arrays in different geometries have been demonstrated [39–42] and even the integration of infrared detectors is possible [43]. Due to the weak demand of such arrays, they can still be seen as research devices and the preferred way is to employ individually packaged DFB-QCLs that are then combined with dichroic mirrors or beamsplitters.

2.1. Spectral Coverage of the QCLs and Absorption Lines of the Analytes

The DFB-QCLs that are used in this multi-gas sensor are commercially available (AdTech Optics, City of Industry, CA, USA and Alpes Lasers, St. Blaise, CH) and mounted in a high heat load (HHL) package. Each device was characterized with a high resolution FTIR spectrometer (Vertex 80v, Bruker Optics, Ettlingen, DE) whereas spectra were recorded at different gain element temperatures and laser currents. The emitted wavelength, depending on the operation parameters, is plotted in Figure 2a–d and spectra of the target analytes and their major interferences are shown as well. The data is derived from the HITRAN database [44,45] and calculated for a pressure of 100 mbar, room temperature and 76 m optical path length. The laser parameters used for the further experiments are listed in Table 1.

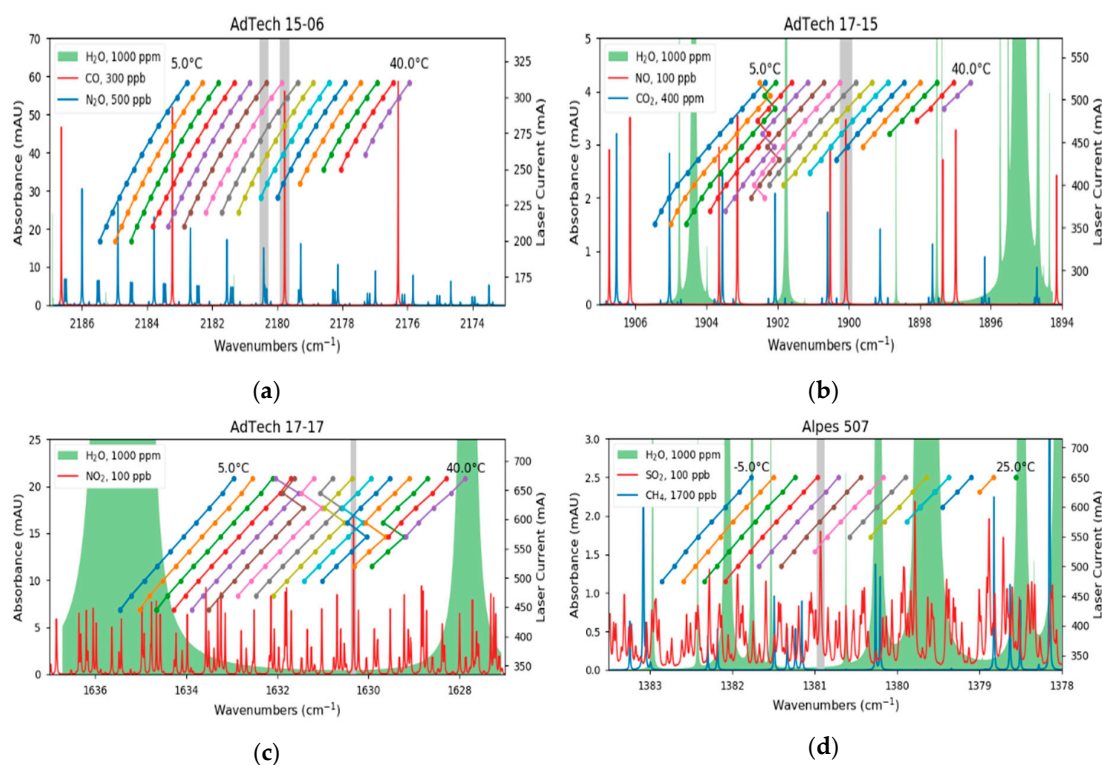


Figure 2. Characterization of the cw-QCLs. While the lasers for CO (a) and SO₂ (d) are mode-hop-free, the devices for NO (b) and NO₂ (c) have mode-hops within their operation range. In addition, absorption spectra of the analytes and other interfering species are plotted. The grey sections indicate the investigated absorption lines of the analytes.

Table 1. Laser parameters used for 2f-Wavelength Modulation Spectroscopy (2f-WMS). The amplitudes of the sine wave modulation were adjusted to achieve the maximum lock-in amplifier signal, according to [46].

Manufacturer	Analyte	Wavenumbers (cm ⁻¹)	Temperature (°C)	Current Ramp (mA)	Modulation (mA)
AdTech Optics	CO	2179.77	20.85	297.0–300.2	1.0
	N ₂ O	2180.42	17.61	297.0–300.2	1.1
AdTech Optics	NO	1900.08	21.09	514.0–520.0	1.6
AdTech Optics	NO ₂	1630.33	27.57	640.2–646.5	2.8
Alpes Lasers	SO ₂	1380.93	3.95	625.0–640.0	5.2

Although the QCLs emit typically single-mode, two devices showed mode hops during the characterization. In the case of the QCL for NO, this occurs at laser parameters where the analyte is not absorbing and therefore not relevant (Figure 2b). In contrast, the laser for NO₂ has a mode hop at the same wavelength as the probed absorption line (Figure 2c). However, the thermal and electrical parameters of the gain element allowed us to find suitable laser parameters where the mode hop does not influence the measurements.

2.2. Opto-Mechanics

The laser beams were collimated and then directed with gold mirrors (PF-10-M03, Thorlabs, Newton, NJ, USA) to the first beam splitter stage (CaF₂, BSW510, Thorlabs, Newton, NJ, USA). Here, two lasers that were on the same aluminum heat sink were combined. A third beam splitter allowed us to combine the beams from the first stages. Approximately 45% of the light was redirected with a flat mirror (PFE10-M01, Thorlabs, Newton, NJ, USA) into the 76 m long Herriott-type multipass gas cell (AMAC 76, Aerodyne, USA) and then focused (MPD149-M01, Thorlabs, Newton, NJ, USA) onto a thermoelectrically cooled MCT detector (PCI-2-TE-12, 200 MHz bandwidth, Vigo Systems, Ozarow Mazowiecki, PL). The other half can be used to track the laser parameters by passing a gas reference cell (Wavelength References, Corvallis, OR, USA) and an additional reference detector (PCI-4TE-9, 20 MHz bandwidth, Vigo Systems, Ozarow Mazowiecki, PL). The overall dimensions of the optical setup were 45 cm × 65 cm, making it perfectly fit in a 19" server rack (IPC 4U-4129-N, Inter-Tech Elektronik, Langenhagen, DE), as shown in Figure 3.

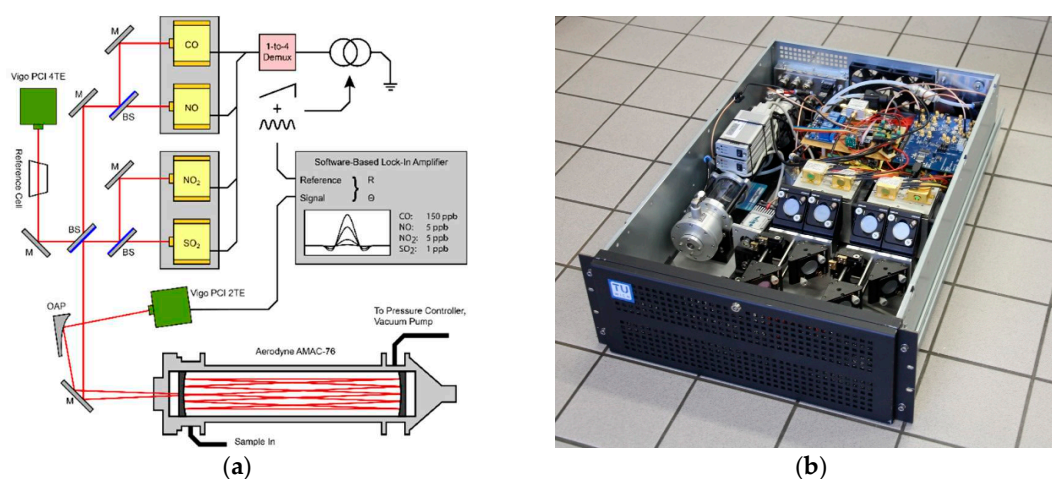


Figure 3. Schematic layout of the individual components for the 2f-WMS based sensor (a) and the assembly of the optical setup in a standard 19" server rack (b). The laser driver, data-acquisition-card, power supplies and the measurement PC are installed in a second rack (not shown).

2.3. 2f-Wavelength Modulation Spectroscopy

The prototype is based on Wavelength Modulation Spectroscopy (WMS), which is closely related to the TDLAS. Here, the laser is tuned over an absorption line (e.g., by changing the injected current, tuning an external cavity grating, etc.) and attenuated by the presence of the analyte. After passing the gas measurement cell, the light hits a detector and its signal can directly be used for the Beer–Lambert relation. In contrast, WMS uses a sine wave on top of the slow sawtooth ramp and a lock-in amplifier processes the received detector signal. An ideal lock-in-amplifier recovers only the signal components that arise from the sine wave modulation and suppresses all other frequencies with a low pass filter. It is therefore perfectly suited to extract the desired signals from noisy environments. By demodulating at the harmonics of the sine wave, one gains information on the shape of the absorption line and the peak height of the second harmonic is proportional to the absorption of the analyte. The noise at the maximum of the 2f-spectrum is further reduced by fitting the center of the spectrum with a parabolic function.

2.4. Electronic Parts

A data acquisition card (NI 6366, National Instruments, Austin, TX, USA) produced the control signal for the laser driver (QCL 1000 OEM, Wavelength Electronics, Bozeman, MT, USA). It consisted of a 1 Hz sawtooth ramp with a 20 kHz sine wave on top. The rather slow sawtooth function was responsible for tuning the emitted wavelength over the absorption line and the sine wave was responsible for the wavelength modulation. Each QCL requires specific amplitudes of the individual signal components as the material properties and dimensions of the gain chips differ. Considering the additional costs and the required space of individual laser drivers, a low-cost 1-to-4 demultiplexer (4 channel relay module, SainSmart Technology, Lenexa, KS, USA) redirects the laser current to the desired QCL. Each laser was protected with a dedicated fuse and an electrostatic discharge (ESD) absorber (LA44-2000, Lasorb, Sanford, FL, USA).

The detector signal was digitized with the data acquisition (DAQ) card at 1 MSPS and demodulated with a software-based lock-in-amplifier (120 dB/decade, time constant=1 ms, FIR). The demodulation was set to the second harmonic of the sine wave modulation ($1f = 20$ kHz) and, as the laser was tuning over an absorption line with 1 Hz, a 2f-WMS spectrum was recorded every second. The hardware for the signal processing, the measurement PC and the required power supplies were installed in a second, dedicated 19" rack (IPC 4U-4129-N, Inter-Tech Elektronik, Langenhagen, DE) and the overall power consumption was 280 W.

Beside the high precision laser driver, DAQ card and demultiplexer, the sensor requires an accurate temperature control of the laser gain chips. Therefore, each HHL package had its own thermoelectric cooling (TEC) controller (TEC 1091, Meerstetter Engineering, Rubigen, CH), which read out an NTC and adjusts the current for the Peltier element. An additional dual-channel TEC controller (TEC 1122, Meerstetter Engineering, Rubigen, CH) was installed to stabilize the temperature of the aluminum plate where the HHL packages were mounted. The pressure in the multipass gas cell was adjusted with a pressure controller (GSP-C5SA, Vögtlin Instruments, Aesch, CH) and set to 100 mbar. To avoid mechanical vibrations, the required vacuum pump (N860.3FT.40.18, KNF Neuberger, Freiburg, DE) was placed next to the prototype.

3. Experiments with 2f-Wavelength Modulation Spectroscopy

3.1. Lab Evaluation

The sensor was calibrated with an inhouse built gas mixing rig whereas two mass flow controllers (GSC-B9TS-BB23, Vögtlin Instruments, Aesch, CH) defined the mixing ratio of the gas from the individual test gas bottle and nitrogen (N₂ 5.0, Messer Austria, Gumpoldskirchen, AT). The concentration was increased in a stepwise manner, covering the range between 0 and 500 ppbv. The flow rate was set to 1 L/min and each concentration step was held for 5 min to exchange and stabilize

the sample composition in the gas cell. As the gas sensor allows only sequential quantification of the analytes, the QCLs were not switched during the calibration runs. The fitted peak amplitude of the 2f-WMS-spectrum were averaged over 10 s and the resulting graphs are shown in Figure 4. The minimum detection limits were calculated from the signal to noise ratios at 100 ppbv and are listed in Table 2.

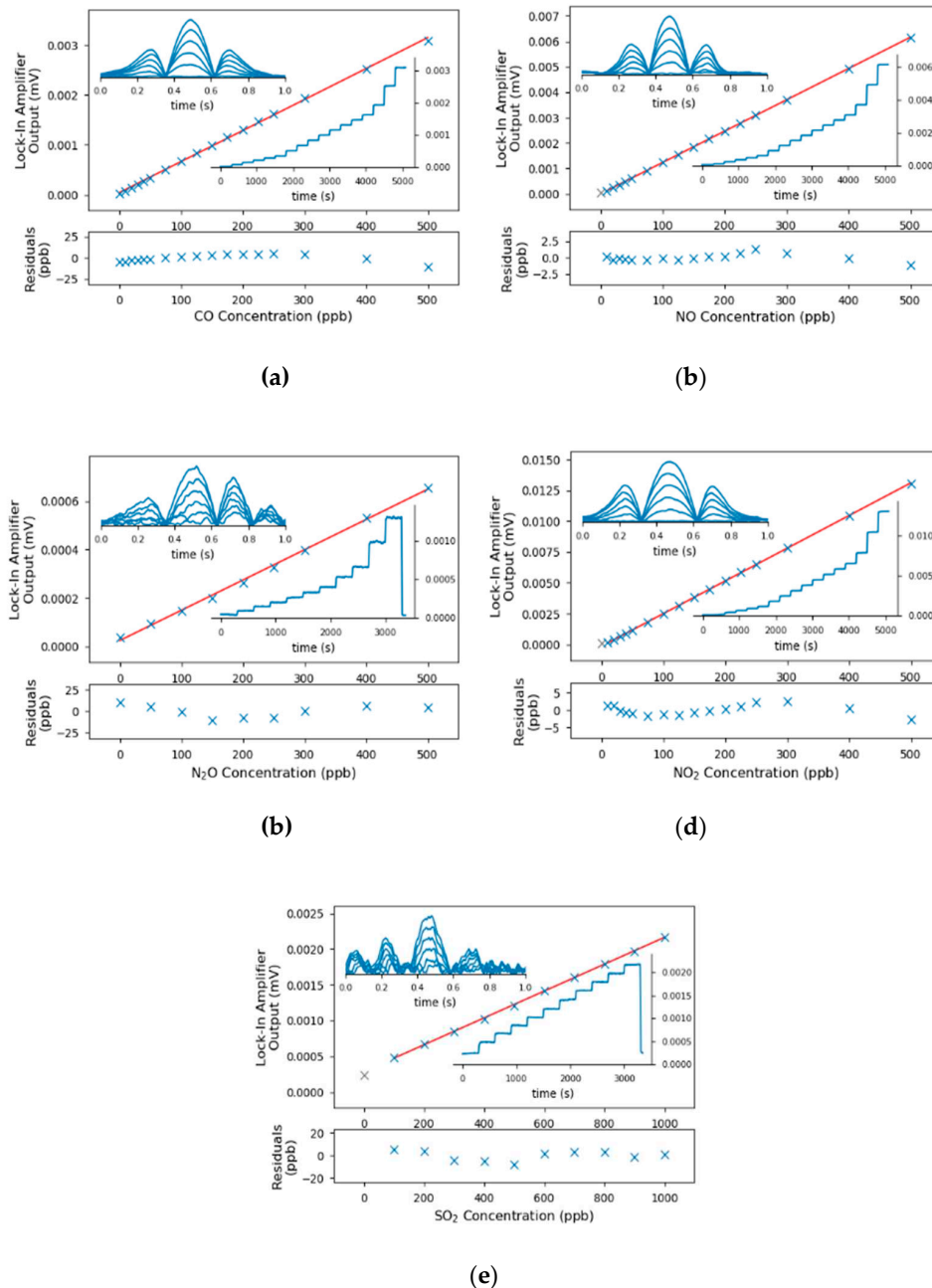


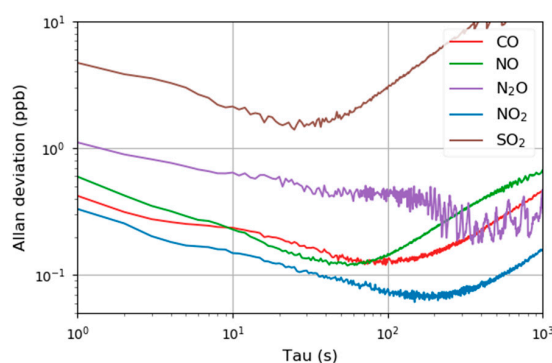
Figure 4. Calibration curves (center), the associated residuals (bottom), the peak signal of the lock-in-amplifier and selected spectra (insets) for the accessible pollutants. The calibration points indicated in grey have been identified as outliers and were excluded from the linear calibrations. The concentrations for the presented spectra in (a–d) were 0, 100, 200, 300, 400 and 500 ppbv; the concentrations for SO₂ (e) were 0, 200, 400, 600, 800 and 1000 ppbv.

Table 2. Linear response and detection limits derived from the calibration for the individual target analytes.

Analyte	Calibration R ²	SNR at 100 ppbv, 1 Hz Sample Rate	1 σ Detection Limit (ppbv), 1 Hz Sample Rate
CO	0.99918	308	0.32
NO	0.99998	224	0.45
N ₂ O	0.99798	40	2.51
NO ₂	0.99990	233	0.43
SO ₂	0.99978	71	1.40

One can see from the calibrations, that the LODs for SO₂ and N₂O were significantly higher than the other components. In the case for N₂O, the increased noise can be traced back to fringes as the mirrors and detector signal were optimized for the laser parameters to quantify CO. For the SO₂, in contrast, the interference free absorption lines of SO₂ were in general rather weak, which resulted in higher detection limits.

The temporal stability of the sensor was evaluated by measuring a constant concentration of the analyte for 1 h (CO, NO, N₂O and NO₂: 100 ppbv, SO₂: 500 ppbv). The Allan–Werle variance (Figure 5) retrieved an optimum integration time between 30 and 100 s. This result is in the same region as other publications [47–49] and it is assumed that thermal drifts in the lab (air conditioner) limit the maximum integration time.

**Figure 5.** Allan–Werle plot for five pollution relevant analytes that can be detected with the multi-gas sensor.

3.2. Field Evaluation of CO, NO and NO₂

A measurement campaign was carried out in Vienna, Austria, in October/November 2019 and the focus was on the analytes CO, NO and NO₂. As the sensor can only quantify one component at a time, it was set to monitor one analyte for 10 min and then to switch to the next one. This guaranteed a reasonable measurement duration for each component but also an acceptable interval. Additional reference data was gained at the installation site using commercially available equipment, based on chemiluminescence (NO, NO₂ and NO_x, Horiba APNA-370, Kyoto, JP) and non-dispersive IR measurements (CO, Horiba APMA-370, Kyoto, JP). The data from one week is plotted in Figure 6 and one can clearly see that the results of the QCL based sensor were very similar to the values from the reference methods.

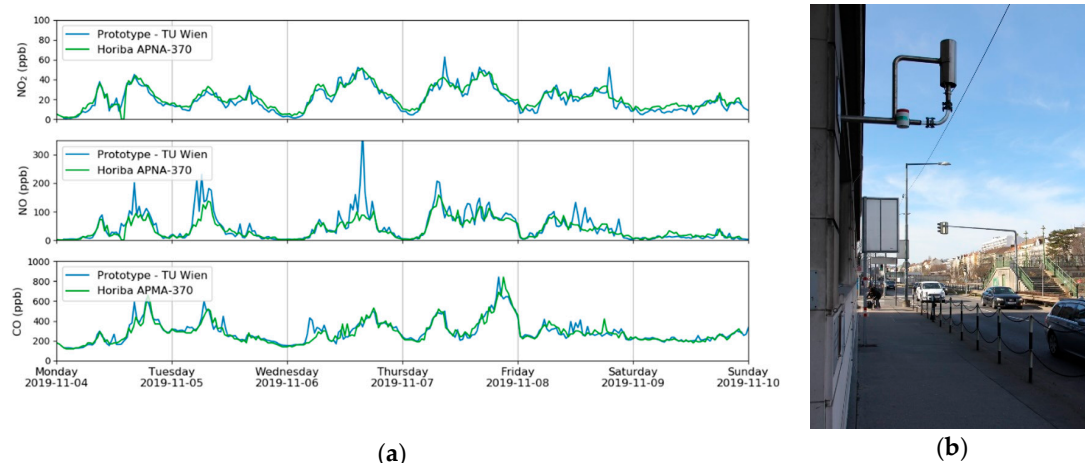


Figure 6. Time series of CO, NO and NO₂ during one week of the measurement campaign in Vienna. Beside data from the QCL sensor, values from the MA 22 are plotted too (a). The intake of the measurement station (b) is located close to an intersection of a busy road.

While the analytes NO and NO₂ were always within the linear calibration range of the sensor, several short time events with significantly higher CO concentrations occurred during the field test. They exceeded the linear range of the calibration and the resulting data is therefore not reliable. One solution would have been to modify the hardware by, for example, reducing the optical path length or diluting the sample stream. However, these options have not been applicable in the experimental setup and it was solved by integrating the Heterodyne Phase Sensitive Dispersion Spectroscopy as a second measurement modality.

4. Heterodyne Phase Sensitive Dispersion Spectroscopy to Quantify High CO Concentrations

4.1. Required Modifications

As one can see from the recorded calibrations, 2f-WMS was perfectly suited for the quantification of low-ppbv-concentrations, but it shows a non-linear behavior at rather high concentrations. In particular, the gained 2f-WMS signal from CO concentrations higher than 1 ppmv was not linear anymore and the calibration would require a non-linear fitting-function. This limitation originates from the Beer–Lambert–Bouguer law and can be solved by changing the measurement technique. Photo-thermal and photoacoustic methods, for example, enable a linear range over several magnitudes, but they require special designed gas cells and cannot be implemented in the existing system. A method that can be easily integrated in this direct absorption-based sensor is Heterodyne Phase Sensitive Dispersion Spectroscopy [50]. Instead of quantifying the attenuation of the laser beam caused by the presence of the analyte, the phase shift of the laser beam, introduced by the dispersion of the gas, is measured.

The basic principle is to superimpose the laser current with a sine wave in the high MHz range, causing the emission of two additional sidebands. They are separated from the emitted center wavelength by the applied modulation frequency. Each optical tone undergoes different refractive indices while passing the gas measurement cell. These optical phase shifts are proportional to the wavelength dependent dispersion of the analyte, its concentration and the optical path length. To detect these phase shifts, the bandwidth of the detector must be in the same range as the modulation frequency. The relevant information is the phase and it is, for a wide concentration range, independent of the amplitude.

The required hardware modification involves standard components for radio-frequency experiments that are commercially available. A four-channel frequency source (AD9959, Analog Devices, Norwood, MA, USA) generated a sine wave with 100.00 MHz, which was added to the laser current with a bias-tee (ZFBT-6g+, Mini-Circuits, Brooklyn, NY, USA). As the software-based

lock-in-amplifier was not capable to demodulate at the resulting frequency, the detector signal must be downmixed with an analog mixer (ZAD-1-1+, Mini-Circuits, Brooklyn, NY, USA). The required reference signal was slightly higher (100.01 MHz) and synthesized on the second channel of the AD9959. The third channel generated the difference frequency (10 kHz), which allowed us to demodulate the downmixed signal with the software-based lock-in-amplifier (Figure 7). Like TDLAS and 2f-WMS, the absorption line was probed by tuning the center-wavelength of the QCL (1 Hz sawtooth current ramp).

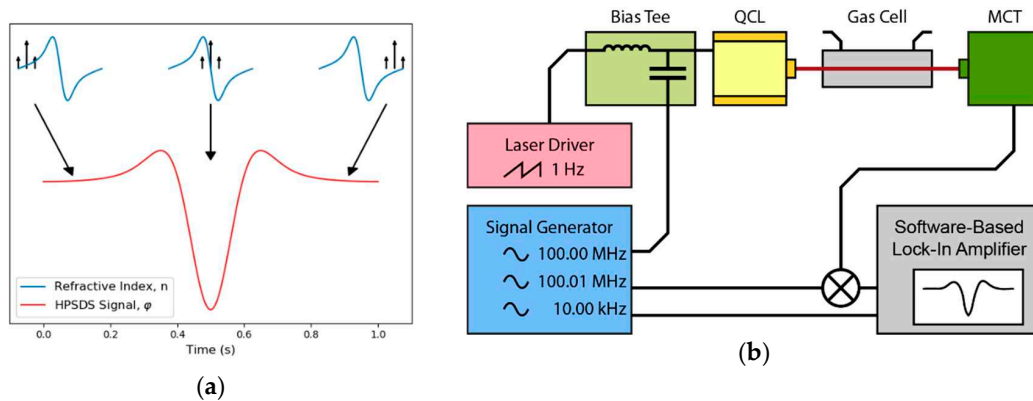


Figure 7. (a) The laser source is intensity-modulated and generates an optical three-tone-signal. While the laser is tuned across the absorption line, the phases of the three wavelengths are differently shifted because of the wavelength dependent refractive indices. (b) The detector signal is downmixed to a lower frequency and a software-based lock-in-amplifier recovers the phase information.

4.2. Calibration of CO

Again, the applicability of this hardware upgrade of the prototype was verified in the lab by recording a calibration of CO in N₂ whereas a concentration range of 0–20 ppmv was covered. In contrast to the 2f-WMS measurements, the pressure in the gas cell was reduced to 30 mbar. This was necessary because the maximum phase signal is achieved if the modulation frequency is 0.6 times the full width at half maximum (FWHM) of the spectral line [51]. As the electrical bandwidth of the detector and the signal generator are limited, one can only improve the signal by reducing the FWHM of the spectral feature. To compensate the additional phase caused by the cables and optical elements, a HPSDS background spectrum (only N₂ in the gas cell) was subtracted. Then, the phase at the minimum was used to calculate the linear regression. The HPSDS spectra and calibration curve ($R^2 = 0.9988$) were plotted in Figure 8 and the detection limit was 0.08 ppmv.

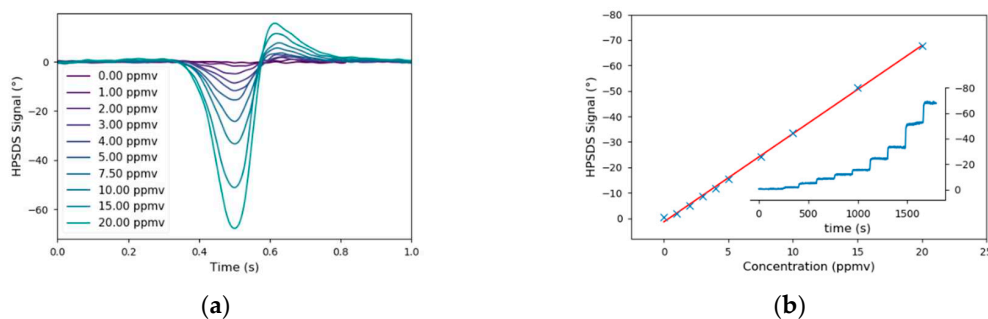


Figure 8. Heterodyne Phase Sensitive Dispersion Spectroscopy (HPSDS) spectra (a) from the calibration of CO (b). The asymmetry of the spectra is the result of the rather high laser current, which is necessary to achieve a sufficient signal on the detector.

4.3. Field Test and Discussion

The applicability of HPSDS for measuring CO in the ambient air has also been tested during the campaign and compared with values from the commercial reference sensor. To show the performance of this advanced technique, only CO has been measured during this 42 h experiment. The retrieved concentrations were compared with the one-minute-average values from the reference equipment and are shown in Figure 9.

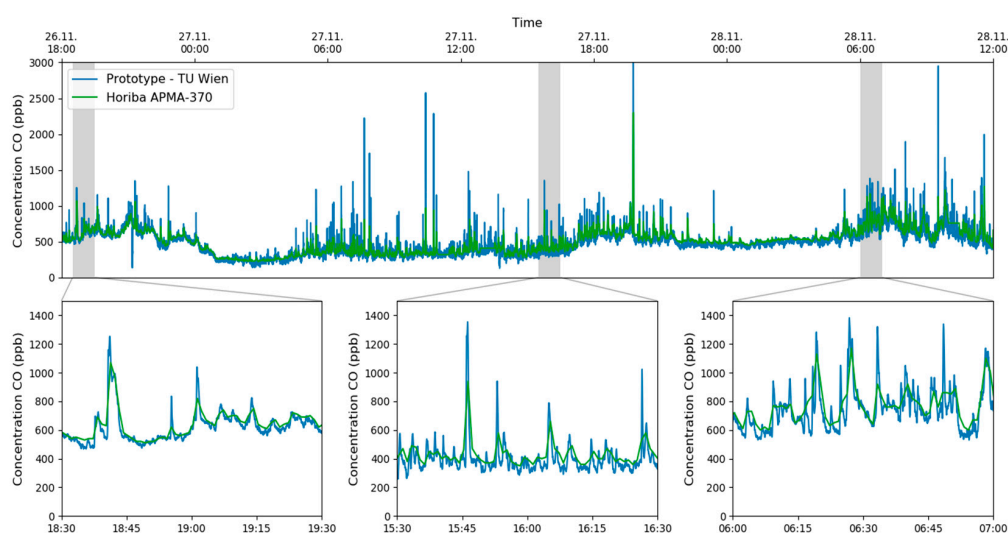


Figure 9. Time series of the CO concentration measured with HPSDS and the data from the NDIR based reference equipment. The responsiveness of setup can be seen in the zoomed in plots.

Considering the different temporal resolutions of the multi-gas sensor and the reference equipment, one can see that the graphs matched perfectly. The sudden increase of CO at the sampling point of the measurement station was caused by the traffic light-controlled intersection, shown in Figure 6b. One can clearly identify phases with a lower CO concentration during the night (e.g., 27 November 0:00–4:00, 28 November 0:00–5:00) and increased levels during the rush hours in the morning and evening.

5. Conclusions

In this paper, we demonstrated a QCL based sensor for monitoring gaseous analytes that strongly contributed to the overall air quality. The electrical and optical components of the setup are commercially available and can be, due to the installation in a standard 19" server rack, easily installed next to commercial ambient air monitors and maybe even replace them in the future. By default, the analytes were measured with 2f-WMS and the characterization in the lab revealed LODs <1 ppbv for the main analytes (CO, NO and NO₂) and slightly higher values for N₂O and SO₂. According to the Allan variance plots, this could be improved by averaging over 30–60 s, however, an integration time of 10 s was used to guarantee a reasonable response time. Comparing the results to other multi-components QCL sensors, it was suspected that the wedged beamsplitters and the lack of not perfectly optimized electronics are the main reasons for the slightly higher detection limits.

In addition, HPSDS was integrated in the sensor that was originally designed for 2f-WMS measurements. The calibration of CO in the lab showed that the linear range of the prototype could be extended to cover concentrations of up to 20 ppmv without replacing the gas measurement cell or installing an additional gas dilution system.

Both techniques, the 2f-WMS and HPSDS, were applied in a measurement campaign in Vienna and the results were in good agreement with the reference values. Subsequently, this QCL-based multi-gas sensor can be seen as a step forward to a new generation of high precision and still very flexible gas monitoring systems.

Author Contributions: Conceptualization, A.G.; software, A.G.; calibration and field experiments, A.G.; writing—original draft preparation, A.G.; writing—review and editing, A.G., H.M., and B.L.; visualization, A.G.; supervision, H.M., P.M.-M.; project administration, B.L.; All authors have read and agreed to the published version of the manuscript.

Funding: This research received no external funding.

Acknowledgments: The authors acknowledge TU Wien Bibliothek for financial support through its Open Access Funding Program.

Conflicts of Interest: The authors declare no conflict of interest.

References

1. Van der A, R.J.; Mijling, B.; Ding, J.; Koukouli, M.E.; Liu, F.; Li, Q.; Mao, H.; Theys, N. Cleaning up the Air: Effectiveness of Air Quality Policy for SO₂ and NO_x Emissions in China. *Atmos. Chem. Phys.* **2017**, *17*, 1775–1789. [[CrossRef](#)]
2. Zhang, H.; Wang, S.; Hao, J.; Wang, X.; Wang, S.; Chai, F.; Li, M. Air Pollution and Control Action in Beijing. *J. Clean. Prod.* **2016**, *112*, 1519–1527. [[CrossRef](#)]
3. César, A.C.G.; Carvalho, J.A.; Nascimento, L.F.C. Association between NO_x Exposure and Deaths Caused by Respiratory Diseases in a Medium-Sized Brazilian City. *Braz. J. Med. Biol. Res.* **2015**, *48*, 1130–1135. [[CrossRef](#)] [[PubMed](#)]
4. Roths, J.; Zenker, T.; Parchatka, U.; Wienhold, F.G.; Harris, G.W. Four-Laser Airborne Infrared Spectrometer for Atmospheric Trace Gas Measurements. *Appl. Opt.* **1996**, *35*, 7075–7084. [[CrossRef](#)] [[PubMed](#)]
5. Silver, J.A.; Stanton, A.C. Airborne Measurements of Humidity Using a Single-Mode Pb–Salt Diode Laser. *Appl. Opt.* **1987**, *26*, 2558–2566. [[CrossRef](#)]
6. Werle, P.; Maurer, K.; Kormann, R.; Mücke, R.; D’Amato, F.; Lancia, T.; Popov, A. Spectroscopic Gas Analyzers Based on Indium-Phosphide, Antimonide and Lead-Salt Diode-Lasers. *Spectrochim. Acta A Mol. Biomol. Spectrosc.* **2002**, *58*, 2361–2372. [[CrossRef](#)]
7. Werle, P.; Kormann, R. Fast Chemical Sensor for Eddy-Correlation Measurements of Methane Emissions from Rice Paddy Fields. *Appl. Opt.* **2001**, *40*, 846–858. [[CrossRef](#)]
8. Schiff, H.I.; Karecki, D.R.; Harris, G.W. A Tunable Diode Laser System for Aircraft Measurements of Trace Gases. *J. Geophys. Res.* **1990**, *95*, 10147–10153. [[CrossRef](#)]
9. Webster, C.R.; Menzies, R.T. In Situ Measurement of Stratospheric Nitric Oxide Using a Balloon-Borne Tunable Diode Laser Spectrometer. *Appl. Opt.* **1984**, *23*, 1140–1142. [[CrossRef](#)]
10. Butler, J.F.; Calawa, A.R.; Phelan, R.J.; Harman, T.C.; Strauss, A.J.; Rediker, R.H. PbTe Diode Laser. *Appl. Phys. Lett.* **1964**, *5*, 75–77. [[CrossRef](#)]
11. Butler, J.F.; Calawa, A.R.; Phelan, R.J.; Strauss, A.J.; Rediker, R.H. PbSe Diode Laser. *Solid State Commun.* **1964**, *2*, 303–304. [[CrossRef](#)]
12. Wormhoudt, J.; Herndon, S.C.; Yelvington, P.E.; Miake-Lye, R.C.; Wey, C. Nitrogen Oxide (NO/NO₂/HONO) Emissions Measurements in Aircraft Exhausts. *J. Propuls. Power* **2007**, *23*, 906–911. [[CrossRef](#)]
13. McManus, J.B.; Shorter, J.H.; Nelson, D.D.; Zahniser, M.S.; Glenn, D.E.; McGovern, R.M. Pulsed Quantum Cascade Laser Instrument with Compact Design for Rapid, High Sensitivity Measurements of Trace Gases in Air. *Appl. Phys. B Lasers Opt.* **2008**, *92*, 387–392. [[CrossRef](#)]
14. Schiller, C.L.; Bozem, H.; Gurk, C.; Parchatka, U.; Königstedt, R.; Harris, G.W.; Lelieveld, J.; Fischer, H. Applications of Quantum Cascade Lasers for Sensitive Trace Gas Measurements of CO, CH₄, N₂O and HCHO. *Appl. Phys. B* **2008**, *92*, 419–430. [[CrossRef](#)]
15. Khan, A.; Sun, K.; Miller, D.J.; Zondlo, M.A. Simultaneous Detection of Atmospheric Nitrous Oxide and Carbon Monoxide Using a Quantum Cascade Laser. In Proceedings of the SPIE 2011, Orlando, FL, USA, 25–29 April 2011.
16. Hübner, M.; Welzel, S.; Marinov, D.; Guaitella, O.; Glitsch, S.; Rousseau, A.; Röpcke, J. TRIPLE Q: A Three Channel Quantum Cascade Laser Absorption Spectrometer for Fast Multiple Species Concentration Measurements. *Rev. Sci. Instrum.* **2011**, *82*, 093102. [[CrossRef](#)]

17. Nelson, D.D.; McManus, J.B.; Herndon, S.C.; Shorter, J.H.; Zahniser, M.S.; Blaser, S.; Hvozdar, L.; Muller, A.; Giovannini, M.; Faist, J. Characterization of a Near-Room-Temperature, Continuous-Wave Quantum Cascade Laser for Long-Term, Unattended Monitoring of Nitric Oxide in the Atmosphere. *Opt. Lett.* **2006**, *31*, 2012–2014. [[CrossRef](#)]
18. Li, J.; Parchatka, U.; Fischer, H. Development of Field-Deployable QCL Sensor for Simultaneous Detection of Ambient N₂O and CO. *Sens. Actuators B. Chem.* **2013**, *182*, 659–667. [[CrossRef](#)]
19. Ma, Y.; Lewicki, R.; Rzeghzi, M.; Tittel, F.K. QEPAS Based Ppb-Level Detection of CO and N₂O Using a High Power CW DFB-QCL. *Opt. Express* **2013**, *21*, 1008–1019. [[CrossRef](#)]
20. Faist, J.; Capasso, F.; Sivco, D.L.; Sirtori, C.; Hutchinson, A.L.; Cho, A.Y. Quantum Cascade Laser. *Science* **1994**, *264*, 553–556. [[CrossRef](#)]
21. Maamary, R.; Cui, X.; Fertein, E.; Augustin, P.; Fourmentin, M.; Dewaele, D.; Cazier, F.; Guinet, L.; Chen, W. A Quantum Cascade Laser-Based Optical Sensor for Continuous Monitoring of Environmental Methane in Dunkirk (France). *Sensors* **2016**, *16*, 224. [[CrossRef](#)]
22. Hundt, P.M.; Tuzson, B.; Aseev, O.; Liu, C.; Scheidegger, P.; Looser, H.; Kapsalidis, F.; Shahmohammadi, M.; Faist, J.; Emmenegger, L. Multi-Species Trace Gas Sensing with Dual-Wavelength QCLs. *Appl. Phys. B* **2018**, *124*, 108. [[CrossRef](#)]
23. Reidl-Leuthner, C.; Ofner, J.; Tomischko, W.; Lohninger, H.; Lendl, B. Simultaneous Open-Path Determination of Road Side Mono-Nitrogen Oxides Employing Mid-IR Laser Spectroscopy. *Atmos. Environ.* **2015**, *112*, 189–195. [[CrossRef](#)]
24. Yu, Y.; Sanchez, N.P.; Lou, M.; Zheng, C.; Wu, H.; Gluszek, A.K.; Hudzikowski, A.J.; Griffin, R.J.; Tittel, F.K. CW DFB-QCL- and EC-QCL-Based Sensor for Simultaneous NO and NO₂ Measurements via Frequency Modulation Multiplexing Using Multi-Pass Absorption Spectroscopy. *Proceedings* **2017**, *10111*, 1011108.
25. Wu, H.; Yin, X.; Dong, L.; Jia, Z.; Zhang, J.; Liu, F.; Ma, W.; Zhang, L.; Yin, W.; Xiao, L.; et al. Ppb-Level Nitric Oxide Photoacoustic Sensor Based on a Mid-IR Quantum Cascade Laser Operating at 52 °C. *Sens. Actuators B Chem.* **2019**, *290*, 426–433. [[CrossRef](#)]
26. Li, S.; Dong, L.; Wu, H.; Sampaolo, A.; Patimisco, P.; Spagnolo, V.; Tittel, F.K. Ppb-Level Quartz-Enhanced Photoacoustic Detection of Carbon Monoxide Exploiting a Surface Grooved Tuning Fork. *Anal. Chem.* **2019**, *91*, 5834–5840. [[CrossRef](#)]
27. Chen, K.; Liu, S.; Zhang, B.; Gong, Z.; Chen, Y.; Zhang, M.; Deng, H.; Guo, M.; Ma, F.; Zhu, F.; et al. Highly Sensitive Photoacoustic Multi-Gas Analyzer Combined with Mid-Infrared Broadband Source and near-Infrared Laser. *Opt. Lasers Eng.* **2020**, *124*, 105844. [[CrossRef](#)]
28. Waclawek, J.P.; Kristament, C.; Moser, H.; Lendl, B. Balanced-Detection Interferometric Cavity-Assisted Photothermal Spectroscopy. *Opt. Express* **2019**, *27*, 12183–12195. [[CrossRef](#)]
29. Mikołajczyk, J.; Bielecki, Z.; Wojtas, J.; Chojnowski, S. Cavity Enhanced Absorption Spectroscopy in Air Pollution Monitoring. *Sens. Transducers* **2015**, *193*, 63–66.
30. Daghestani, N.S.; Brownsword, R.; Weidmann, D. Analysis and Demonstration of Atmospheric Methane Monitoring by Mid-Infrared Open-Path Chirped Laser Dispersion Spectroscopy. *Opt. Express* **2014**, *22*, 1731–1743. [[CrossRef](#)]
31. Hugi, A.; Terazzi, R.; Bonetti, Y.; Wittmann, A.; Fischer, M.; Beck, M.; Faist, J.; Gini, E. External Cavity Quantum Cascade Laser Tunable from 7.6 to 11.4 Mm. *Appl. Phys. Lett.* **2009**, *95*, 061103. [[CrossRef](#)]
32. Wieland, K.; Lendl, B.; Ramer, G.; Centrone, A.; Weiss, V.U.; Allmaier, G. Nanoscale Chemical Imaging of Individual Chemotherapeutic Cytarabine-Loaded Liposomal Nanocarriers. *Nano Res.* **2019**, *12*, 197–203. [[CrossRef](#)] [[PubMed](#)]
33. Ramer, G.; Reisenbauer, F.; Steindl, B.; Tomischko, W.; Lendl, B. Implementation of Resonance Tracking for Assuring Reliability in Resonance Enhanced Photothermal Infrared Spectroscopy and Imaging. *Appl. Spectrosc.* **2017**, *71*, 2013–2020. [[CrossRef](#)] [[PubMed](#)]
34. Schwaighofer, A.; Brandstetter, M.; Lendl, B. Quantum Cascade Lasers (QCLs) in Biomedical Spectroscopy. *Chem. Soc. Rev.* **2017**, *46*, 5903–5924. [[CrossRef](#)]
35. Alcaráz, M.R.; Schwaighofer, A.; Kristament, C.; Ramer, G.; Brandstetter, M.; Goicoechea, H.; Lendl, B. External-Cavity Quantum Cascade Laser Spectroscopy for Mid-IR Transmission Measurements of Proteins in Aqueous Solution. *Anal. Chem.* **2015**, *87*, 6980–6987. [[CrossRef](#)]

36. Sun, J.; Ding, J.; Liu, N.; Yang, G.; Li, J. Detection of Multiple Chemicals Based on External Cavity Quantum Cascade Laser Spectroscopy. *Spectrochim. Acta A Mol. Biomol. Spectrosc.* **2018**, *191*, 532–538. [[CrossRef](#)] [[PubMed](#)]
37. Kosterev, A.A.; Buerki, P.R.; Dong, L.; Reed, M.; Day, T.; Tittel, F.K. QEPAS Detector for Rapid Spectral Measurements. *Appl. Phys. B Lasers Opt.* **2010**, *100*, 173–180. [[CrossRef](#)]
38. Faist, J.; Gmachl, C.; Capasso, F.; Sirtori, C.; Sivco, D.L.; Baillargeon, J.N.; Cho, A.Y. Distributed Feedback Quantum Cascade Lasers. *Appl. Phys. Lett.* **1997**, *70*, 2670–2672. [[CrossRef](#)]
39. Lee, B.G.; Belkin, M.A.; Pflugl, C.; Diehl, L.; Zhang, H.A.; Audet, R.M.; MacArthur, J.; Bour, D.P.; Corzine, S.W.; Hofler, G.E.; et al. DFB Quantum Cascade Laser Arrays. *IEEE J. Quantum Electron.* **2009**, *45*, 554–565. [[CrossRef](#)]
40. Rauter, P.; Capasso, F. Multi-Wavelength Quantum Cascade Laser Arrays. *Laser Photonics Rev.* **2015**, *9*, 452–477. [[CrossRef](#)]
41. Kapsalidis, F.; Shahmohammadi, M.; Süess, M.J.; Wolf, J.M.; Gini, E.; Beck, M.; Hundt, M.; Tuzson, B.; Emmenegger, L.; Faist, J. Dual-wavelength DFB Quantum Cascade Lasers: Sources for Multi-species Trace Gas Spectroscopy. *Appl. Phys. B* **2018**, *124*, 107. [[CrossRef](#)]
42. Mujagić, E.; Schwarzer, C.; Yao, Y.; Chen, J.; Gmachl, C.; Strasser, G. Two-Dimensional Broadband Distributed-Feedback Quantum Cascade Laser Arrays. *Appl. Phys. Lett.* **2011**, *98*, 141101. [[CrossRef](#)]
43. Harrer, A.; Szedlak, R.; Schwarz, B.; Moser, H.; Zederbauer, T.; MacFarland, D.; Detz, H.; Andrews, A.M.; Schrenk, W.; Lendl, B.; et al. Mid-Infrared Surface Transmitting and Detecting Quantum Cascade Device for Gas-Sensing. *Sci. Rep.* **2016**, *6*, 21795. [[CrossRef](#)] [[PubMed](#)]
44. Kochanov, R.V.; Gordon, I.E.; Rothman, L.S.; Wcisło, P.; Hill, C.; Wilzewski, J.S. HITRAN Application Programming Interface (HAPI): A Comprehensive Approach to Working with Spectroscopic Data. *J. Quant. Spectrosc. Radiat. Transf.* **2016**, *177*, 15–30. [[CrossRef](#)]
45. Gordon, I.E.; Rothman, L.S.; Hill, C.; Kochanov, R.V.; Tan, Y.; Bernath, P.F.; Birk, M.; Boudon, V.; Campargue, A.; Chance, K.V.; et al. The HITRAN2016 Molecular Spectroscopic Database. *J. Quant. Spectrosc. Radiat. Transf.* **2017**, *203*, 3–69. [[CrossRef](#)]
46. Reid, J.; Labrie, D. Second-Harmonic Detection with Tunable Diode Lasers—Comparison of Experiment and Theory. *Appl. Phys. B* **1981**, *26*, 203–210. [[CrossRef](#)]
47. Chen, X.; Yang, C.G.; Hu, M.; Shen, J.K.; Niu, E.C.; Xu, Z.Y.; Fan, X.L.; Wei, M.; Yao, L.; He, Y.B.; et al. Highly-Sensitive NO, NO₂, and NH₃ Measurements with an Open-Multipass Cell Based on Mid-Infrared Wavelength Modulation Spectroscopy. *Chin. Phys. B* **2018**, *27*, 040701. [[CrossRef](#)]
48. Dang, J.; Yu, H.; Zheng, C.; Wang, L.; Sui, Y.; Wang, Y. Development a Low-Cost Carbon Monoxide Sensor Using Homemade CW-DFB QCL and Board-Level Electronics. *Opt. Laser Technol.* **2018**, *101*, 57–67. [[CrossRef](#)]
49. Li, J.; Parchatka, U.; Königstedt, R.; Fischer, H. Real-Time Measurements of Atmospheric CO Using a Continuous-Wave Room Temperature Quantum Cascade Laser Based Spectrometer. *Opt. Express* **2012**, *20*, 7590–7601. [[CrossRef](#)]
50. Martín-Mateos, P.; Hayden, J.; Acedo, P.; Lendl, B. Quantum-Cascade-Laser-Based Heterodyne Phase-Sensitive Dispersion Spectroscopy in the Mid-IR Range: Capabilities and Limitations. In Proceedings of the SPIE 2017, San Diego, CA, USA, 6–10 August 2017.
51. Martín-Mateos, P.; Acedo, P. Heterodyne Phase-Sensitive Detection for Calibration-Free Molecular Dispersion Spectroscopy. *Opt. Express* **2014**, *22*, 15143–15153. [[CrossRef](#)]



© 2020 by the authors. Licensee MDPI, Basel, Switzerland. This article is an open access article distributed under the terms and conditions of the Creative Commons Attribution (CC BY) license (<http://creativecommons.org/licenses/by/4.0/>).



Die approbierte gedruckte Originalversion dieser Dissertation ist an der TU Wien Bibliothek verfügbar.
The approved original version of this doctoral thesis is available in print at TU Wien Bibliothek.

Publication II

Implementation and characterization of a thermal infrared laser heterodyne radiometer based on a wavelength modulated local oscillator laser

Authors: Pedro Martín-Mateos, Andreas Genner, Harald Moser and Bernhard Lendl



Die approbierte gedruckte Originalversion dieser Dissertation ist an der TU Wien Bibliothek verfügbar.
The approved original version of this doctoral thesis is available in print at TU Wien Bibliothek.



Implementation and characterization of a thermal infrared laser heterodyne radiometer based on a wavelength modulated local oscillator laser

PEDRO MARTÍN-MATEOS,^{1,*} ANDREAS GENNER,² HARALD MOSER,² AND BERNHARD LENDL²

¹*Electronics Technology Department, Universidad Carlos III de Madrid, C/Butarque 15, 28911 Leganés, Madrid, Spain*

²*Institute of Chemical Technologies and Analytics, Technische Universität Wien, Getreidemarkt 9/164-UPA, 1060 Vienna, Austria*

*pmmateos@ing.uc3m.es

Abstract: This article presents the first implementation and the experimental characterization of a thermal infrared wavelength modulation laser heterodyne radiometer (WM-LHR) based on an external cavity quantum cascade laser. This novel WM-LHR system has demonstrated calibration-free operation, a superior signal to noise ratio and, more importantly, has opened the door for cost-efficient wide spectral range laser heterodyne radiometry in the near future.

© 2019 Optical Society of America under the terms of the [OSA Open Access Publishing Agreement](#)

1. Introduction

Optical spectroscopy is arguably the technique with the highest potential for atmospheric sounding: the Total Carbon Column Observing Network (TCCON) [1,2], the Thermal and Near infrared Sensor onboard the Greenhouse Gases Observing Satellite (GOSAT) [3] or the Orbiting Carbon Observatory 2 spectrometers [4,5] are indeed some of the most outstanding examples of the capabilities of the approach. The sophisticated spectral analyzers mentioned above, which provide reliable estimations of the concentrations of atmospheric constituents such as water vapor, carbon dioxide, methane, and nitrous oxide, have been implemented utilizing Fourier Transform (FTS) or grating spectrometers (as virtually any other, ground-based or spaceborne, optical atmospheric sounding infrastructure nowadays). However, and strongly supported by the advent of high quality, robust and compact laser sources, many stunning instrument designs and experimental demonstrations are paving the way for Laser Heterodyne Radiometers (LHR) to become the terrestrial and planetary atmospheric optical sounding tool of the future [6–12].

LHR systems provide very high sensitivity, ultra-narrow optical resolution, very confined field-of-view, and, due to low component count, reduced cost, high reliability, and a huge potential for ruggedization and miniaturization [13,14]. The LHR method has, nevertheless, remained essentially unchanged from the very first demonstrations performed by Menzies and Shumate [15,16] in the early seventies and, up to this day, most developments have been focused on the adoption of higher-performing components. It was only very recently that a new LHR spectral interrogation procedure, Wavelength Modulation Laser Heterodyne Radiometry (WM-LHR) [17], was proposed as a noteworthy performance enhancement step. WM-LHR is based on the use of a wavelength-modulated local oscillator (LO) laser in a manner similar to the vastly used Wavelength Modulation Spectroscopy (WMS) technique [18]. A preliminary WM-LHR near-infrared system implementation [17], based on optical communication components, recently demonstrated a very promising boost in performance and consistency. This paper now presents the first implementation of a thermal infrared (TIR) WM-LHR based on an external cavity quantum cascade laser (EC-QCL) and provides a

through characterization of the system and a comprehensive comparison of performance with the traditional LHR method. This novel WM-LHR system has demonstrated calibration-free operation, a superior signal to noise ratio and, more importantly, has opened the door for wide spectral range radiometric measurements in the near future. The results yield a very clear and conclusive representation of the new and unique capabilities of this novel spectral analysis approach.

2. Wavelength modulation laser heterodyne radiometry

2.1 Fundamentals of the method

The block diagram of the WM-LHR architecture can be seen in Fig. 1. The incoming optical signal is combined with the LO on a beam splitter and focused into the detector. The RF chain maintains a classical design based on amplification, band-pass filtering, RF power detection and lock-in signal demodulation. A ramp modulation signal is applied to the laser for frequency sweeping in order to facilitate the spectral interrogation of the incoming signal. Contrary to traditional LHR [19], WM-LHR adds a sinusoidal frequency modulation to the ramp signal of the laser that completely redefines the functioning of the heterodyne radiometer. In this way, the traditional spectral intensity detection performed by LHR is now converted into optical intensity differentiation (the presence of an absorption line gives rise to harmonics of the modulation signal that can be utilized to infer the composition of the gas sample under analysis) providing several noteworthy advantages in the process.

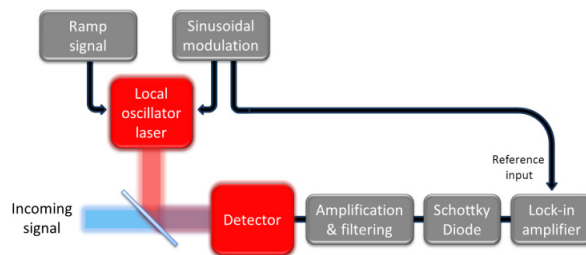


Fig. 1. Schematic of a WM-LHR system.

2.2 Thermal infrared wavelength modulation laser heterodyne radiometry with an external cavity quantum cascade laser

A photograph of the experimental TIR WM-LHR implementation based on an EC-QCL is shown in Fig. 2. A continuous wave mode-hop-free EC-QCL (41078-MHF, Daylight Solutions, Inc., USA) with a wavelength tuning range from 7.64 to 8.22 μm (1319 to 1217 cm^{-1}) and a maximum power output of 225 mW is employed. The laser frequency is slowly swept across the spectrum of interest using a ramp signal generator connected to the piezo element that controls the external cavity length. A much faster sinusoidal modulation of the laser is achieved by the direct modulation of the QCL current through the internal bias Tee circuit.

The first optical component of the set-up is an uncoated 4 mm thick calcium fluoride window acting as a beam splitter that sends roughly the 95% of the power emitted by the laser to a beam block. The remaining light is redirected to the next stages of the heterodyne radiometer (a second beam-stopper eliminates the reflection on the backside of the beam-splitter). This approach is preferred over the traditional laser intensity control based on polarizers, as it provides an improved performance with respect to interference fringes. Subsequently, beam expansion, required for an adequate spatial overlapping with the optical signal, is realized by means of two 90 degrees gold-coated off-axis parabolic mirrors with focal lengths of 1 and 6 inches. The total diameter of the laser beam is, in this manner, expanded up to 12 mm. A second calcium fluoride window combines the LO light with the

signal (5:95) and redirects the resulting beam to a parabolic mirror that focus the light into the thermal detector. A thermoelectrically cooled photovoltaic detector (PVI-4TE-10.6-1x1, Vigo Systems S. A., Poland) with a high speed (450 MHz) transimpedance preamplifier has been employed in the experimental demonstrations presented in this paper. The use of a thermoelectrically cooled detector instead of the conventional liquid nitrogen unit is utterly important to facilitate the eventual field deployment of the radiometer. No modifications were made to the detector to reduce the noise level. To ensure maximum consistency in the experimental results, a regular optical signal is replicated with a 12 V silicon carbide IR source (an area of roughly $70 \times 10^{-9} \text{ m}^2$ of the source is imaged into the detector) and an off-axis parabolic mirror that collimates part of the emitted radiation through a 30 mm gas cell with calcium fluoride windows. A band-pass optical filter (7.5 to 8.5 μm) finally restricts the optical bandwidth of the incoming signal before combination with the LO for spectral interrogation. Different gas concentrations were pumped into the cell for the characterization of the performance of the system. An optical chopper, which is disabled during WM operation, is also included to benchmark the performance of WM-LHR with the traditional LHR method. The RF processing chain is comprised of a low-noise 24 dB amplifier (ZFL-500LN, Mini-Circuits Inc., USA), a 50 MHz to 100 MHz band-pass filter and a Schottky detector (EZR0120A3, Eclipse Microwave Inc., U.S.A.). The dual-sideband optical resolution of the spectrometer is, therefore, 100 MHz or 0.003 cm^{-1} .

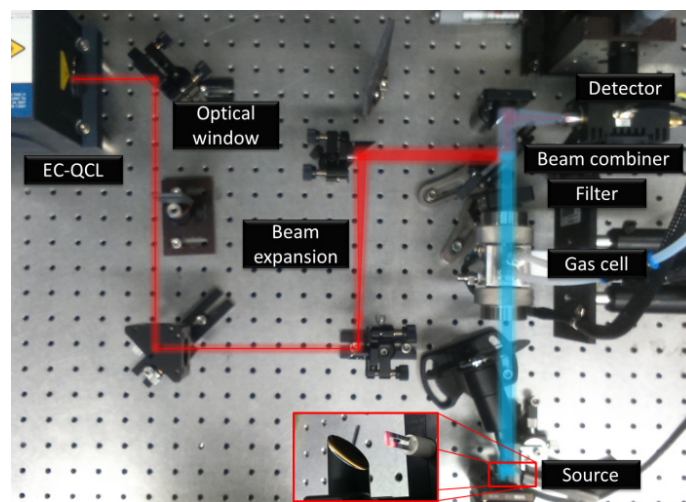


Fig. 2. Photograph of the WM-LHR implemented in the laboratory. The red and blue lines represent the optical path of the local oscillator laser and the thermal signal respectively.

The EC-QCL was tuned to $7.87 \mu\text{m}$ (1270.8 cm^{-1}) to target methane inside the cell. The laser was operated at a forward current of 375 mA to ensure a LO power reaching the detector of $150 \mu\text{W}$; this intensity level was found to be the optimum operation point of our detector (the power passing through the cell in these conditions is approximately 5 mW). The sinusoidal modulation of the current of the EC-QCL was performed at 185 Hz and 1 V_p (for a total frequency deviation of 0.0002 pm or 0.033 cm^{-1}) in order to achieve a fast wavelength modulation of the LO with an optimum modulation index of about 2.2 times the linewidth of the molecular transition [17]. Besides this, a sawtooth signal, amplified by a piezo driver up to 20 V peak to peak, was utilized for fine spectral interrogation. The power dissipated by the infrared source and the gas concentration in the cell were widely tuned during several tests to accurately characterize the effectiveness of the WM-LHR method.

3. Experimental results

3.1 Experimental validation and WM-LHR calibration-free operation

The WM-LHR output signals for a CH₄ sample with a concentration of 20% in nitrogen at 60 mbar (restricted by the maximum modulation current of the laser) using a 30 mm gas cell, an electrical power of 12.5 W dissipated on the thermal infrared emitter, 330 ms of integration time in the lock-in amplifier and a total sweep time of 15 s are shown in Fig. 3. Interference fringes within the cavity of the laser employed in the set-up generate a strong residual amplitude modulation (RAM) in the first harmonic of the modulation signal. This RAM, for a measurement in which only the LO signal is allowed to reach the detector is shown in red in Fig. 3(a) (red) together with an actual measurement of the methane sample (blue). The abscissa axis was calibrated prior to the measurements using a 50.815 mm germanium etalon. The 1f WM-LHR signal can be straightforwardly baseline-compensated by a quadratic curve fitting ($R^2 = 0.9995$) and the resulting waveform is plotted in Fig. 3(b) (which corresponds directly to the first derivative of the spectrum of the input signal). The second (2f) and third (3f) harmonics of the modulation frequency can be seen in Figs. 3(c) and 3(d) correspondingly.

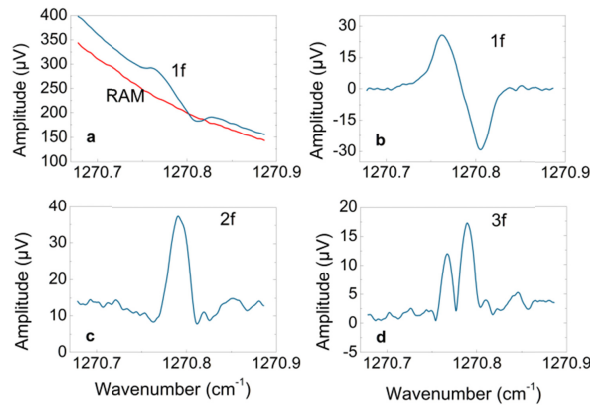


Fig. 3. WM-LHR signals: (a) RAM and 1f, (b) baseline-compensated 1f, (c) 2f and (d) 3f.

As expected from WMS, the amplitudes of the harmonics depend on both the concentration of gas in the sample and the power emitted by the thermal source, therefore a normalization procedure is required to enable calibration-free operation. Luckily, the baseline level of the 1f harmonic provides a direct measurement of the optical power at the entrance of the spectrometer that can, hence, be used to enable calibration-free WM-LHR sample characterization. The RAM of the laser source has been long used in calibration-free WMS approaches for intensity normalization [20] and a similar procedure can now also be employed for WM-LHR. As seen in Fig. 3(a), the incoming optical intensity generates an increase in the baseline level beyond the signal caused by the RAM of the laser. As a matter of fact, this increase is directly proportional to the source light intensity, and therefore the intensity of the incoming optical signal can be accurately determined. Then, the intensity-normalization of the 1f, 2f and 3f output signals will provide a set of waveforms that depend exclusively on the absorption line depth and that can hence be directly related to the gas concentration (column density).

In the experiments presented in this paper, the best calibration-free performance has been obtained by dividing the peak-to-peak 1f signal by the offset of the quadratic fitting of the baseline. For the evaluation of this calibration-free strategy, six individual measurements were taken at three methane concentrations (4%, 6% and 10%) and for electrical power levels

dissipated in the thermal source of 6.5, 8.5, 9.75 and 12.75 W (for a total of 72 spectral measurements). The normalized 1f amplitudes averaged for each set of six measurements are shown in Fig. 4. The experimentally obtained precision of the normalization procedure is 2.4% for an integration time of the lock-in amplifier of 330 ms and a sweep time of 15 s. This result demonstrates that WM-LHR can accurately operate in calibration-free conditions with independence of the intensity of the source and providing high consistency and fast measurement rates. In experimental scenarios in which non-absorbing spectral regions are unavailable or precluded by the limited tunability of the laser source, any other regular WMS signal normalization strategy, such as the widely used WMS-2f/1f, could be employed.

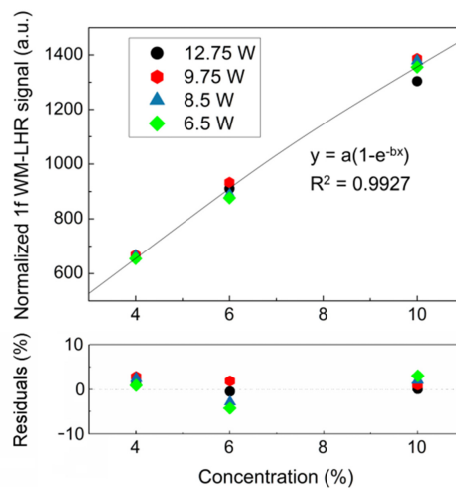


Fig. 4. Calibration-free WM-LHR performance.

4. Analysis of performance and comparison with laser heterodyne radiometry

Some of the features and advantages provided by WM-LHR can be better illustrated when the technique is benchmarked against LHR. Therefore, as presented before, an optical chopper was included in the set-up and WM-LHR and conventional LHR measurements were alternatively taken under the same operational conditions. During WM-LHR operation the chopper is stopped, the blades set out of the optical path of the signal and the LO frequency is modulated as described in the previous sections of the paper. In LHR mode, the frequency modulation of the LO source is disabled and the optical chopper is activated. The modulation and chopping frequencies were set to the same value: 185 Hz, to avoid misleading results due to the frequency response of the detectors or the RF processing chain.

4.1 Baseline and signal normalization in LHR

An LHR measurement taken in the same conditions described for Fig. 3 can be seen in Fig. 5 for a straightforward comparison. Three separate areas have been highlighted to differentiate different situations: in (1) both the signal and the laser beams are blocked, only residual noise is visible, in section (2) the LO is blocked and the incoming signal is let through to reach the photodetector, a noticeable baseline signal is generated under these circumstances, and in (3) both the signal and the LO are allowed to impinge on the detector, the overlap between the spectrum of the incoming light and the intensity response to frequency-sweeping of the laser is apparent. With a system implementation based on an off-the-shelf thermoelectrically cooled detector and a 1000 nm band-pass optical filter, an LO-independent baseline (shown in section (2) of the Fig.) appears as a consequence of the non-linearities in the gain profile of

the detection chain. The strong changes in DC level induced by chopping the optical signal produce the modulation of the gain of the preamplifier (the baseline is a consequence of the modulated amplification of the noise generated by the system front-end). Even though narrower optical filters would lessen the baseline level, this issue has still to be considered in order to guarantee the accuracy of the measurements. In the same way, gain non-linearities also produce the compression of the absorption line-shape by factors that depend on the intensity of the incoming signal, which complicates LHR calibration-free operation. As a matter of fact, if not compensated, the raw transmittance measurement presented in Fig. 5 induces an error by a factor of approximately 8 in the estimation of the concentration of methane in the sample due to non-linearities.

By contrast, in WM-LHR no signal chopping is required and therefore the DC operation point and the gain of the detection chain remains constant during the whole spectral acquisition (regardless of the quality of the detector) producing no spectral distortion and thus enabling a straightforward compensation. The gain non-linearity issue is often overlooked by papers on the topic, but it is a very important factor to consider when implementing a LHR system with cost-effective components. This first comparison reveals that WM-LHR puts far less strain than LHR in the performance of the components required for the implementation of the set-up.

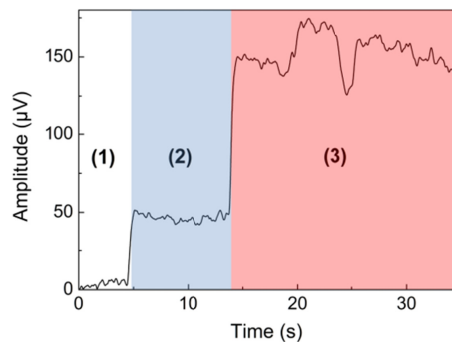


Fig. 5. LHR measurement. The different zones identify (1) signal and LO blocked, (2) signal reaching the detector and LO block and (3) both signal and LO in the detector.

4.2 Signal to noise ratio

The characterization of the SNR provided by the two techniques was carried out through a data set in which ten consecutive spectra are digitized for both methods for different integration times of the lock-in amplifier. A gas concentration of 20% and 12 W of electrical power in the thermal source were employed. The SNR of the WM-LHR harmonics is determined as the peak to peak signal divided by the standard deviation of the baseline far from the molecular resonance (in a nearby region not affected by the spectral line) calculated for a wavelength range equal to three times the linewidth of the transition covering several background fringes. In the case of LHR, the SNR is obtained as the ratio between the depth of the absorption line and, as before, the standard deviation of the baseline out of the molecular transition.

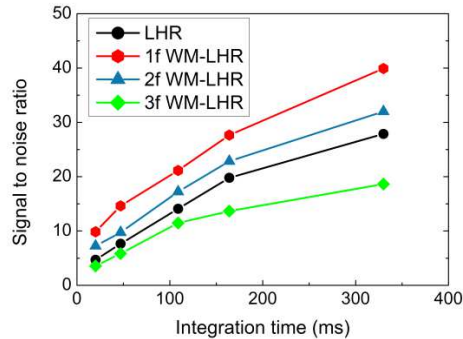


Fig. 6. Signal to noise ratio with respect to the integration time of the lock-in amplifier.

As shown in Fig. 6, the SNR of the thermal infrared radiometer provided by 1f and 2f WM-LHR noticeably exceeds that of the conventional LHR method. This is expected, as in WM-LHR the modulation is performed directly by an electronic reference signal, while a mechanical system with far greater phase jitter and frequency drifts is utilized by LHR. Interference fringes in the cavity of the particular laser employed are the main SNR restricting factor in the implemented WM-LHR system. The differences in SNR could be even more apparent when laser diodes (with much lower RAM) are employed in systems in which a great level of amplification is required [17].

4.3 Out-of-band signal rejection

Even though the use of LHR has routinely been restricted to very narrow (single absorption line) spectral ranges, the surge of robust widely tunable laser technology promises to permit the development of a new generation of wide span heterodyne radiometers. In the traditional LHR approximation highly selective optical filters are employed to narrow down the spectral span of the signal to be analyzed because of the reasons presented in Section 4.1. Set-ups with a wide spectral coverage require a method with a superior out-of-band intensity rejection such as WM-LHR. In this section, the ability of the traditional and the WM-LHR approaches to operate without optical filters are analyzed. A series of measurements were carried out in which the optical filter that restricts the wavelength range of the incoming signal is placed in the system and subsequently removed. A gas sample with 10% methane diluted in nitrogen at 60 mbar was pumped into the cell, the integration time of the lock in amplifier was adjusted to 100 ms and the period of the ramp signal to 20 s. A traditional LHR measurement in which four line sweeps are performed, two with optical filter and two without the optical filter, is shown in Fig. 7(a). Even though the optical power density of the signal in the spectral range interrogated by the laser rises only by roughly 40% (due to the absence of the optical losses of the filter), the baseline is increased by more than an order of magnitude due to optical power reaching the detector at wavelengths that are far from the region of interest. As previously presented, the pronounced step changes in the intensity of the incoming power (that result from the need of chopping the input signal) generate a substantial gain modulation due to the non-linearities of regular detectors and amplifiers. This issue is strongly noticed if out-of-band radiation is allowed into the detector, as is this case. On the contrary, both the baseline and the WM-LHR signal, shown in Fig. 7(b), are incremented by a factor that is equal to the inverse of the transmittance of the optical filter, not being influenced by out-of-band optical radiation. The reason being that, whereas signal chopping in LHR generates high amplitude optical pulses, in WM-LHR the only intensity fluctuations are those from the RAM of the laser that are miniscule compared to the DC intensity level. Therefore, WM-LHR measurements are consistently taken at a constant gain value (and with no distortion of the

line shape due to the gain saturation profile) allowing for a far greater dynamic range. This behavior becomes even clearer in Figs. 7(c) and 7(d), in which the baseline-compensated LHR and WM-LHR signals measured with and without the optical filter are represented. Whereas LHR is unable to operate without the filter, WM-LHR performs without issues, even providing an improved SNR due to the higher amplitude of the 1f signal (shot-noise in the system is not the main noise contributor).

Summarizing, the increased dynamic range and the possibility to operate without optical filters provided by WM-LHR enable the implementation of highly flexible wide coverage radiometers that allow taking full advantage of the characteristics of modern widely tunable laser sources.

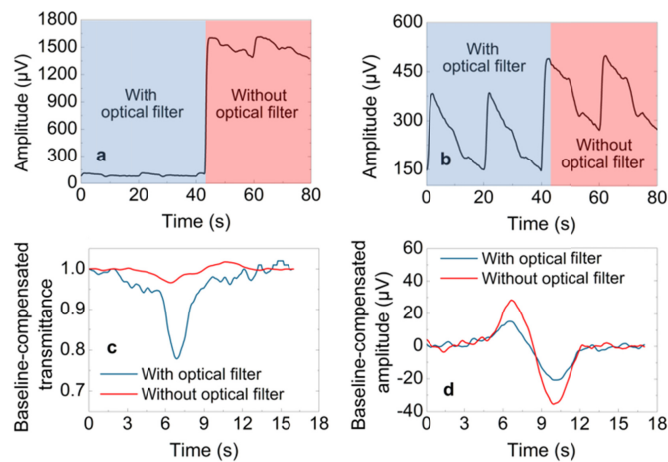


Fig. 7. Behavior of LHR and WM-LHR with and without optical filter: raw (a) LHR and (b) WM-LHR measurements; baseline-compensated (c) LHR and (d) WM-LHR signals.

5. Conclusion

LHR is nowadays a mature and very promising technology that is destined to replace current methods as the main optical tool for the targeted exploration of the chemical make-up of the atmosphere [6–12]. LHR instruments are robust, compact and cost-efficient, and feature an ultra-high sensitivity and an unmatched optical resolution. Besides this, and as demonstrated in this paper, a very simple modification of the traditional LHR spectral interrogation approach, such as that proposed by WM-LHR, provides outstanding improvements in many aspects of the LHR system operation that further qualify these systems as the atmospheric sounding tools of the future.

WM-LHR is based on a LHR system with a wavelength modulated LO laser that simplifies the optical architecture of the system by removing the optical chopper. On the TIR WM-LHR based on an EC-QCL presented in this paper, calibration-free WM-LHR has been demonstrated through a simple procedure that compensates intensity fluctuations from the RAM amplification level. This set-up, in comparison to a traditional LHR instrument, has demonstrated a superior SNR, a lessening in the requirements on the quality of the components and has opened the door for very wide range spectral characterization. These new features provide the potential to increase the accuracy and lower the cost of implementing a ground-based network of radiometers based on off-the-shelf components. Moreover, WM-LHR makes it feasible to tremendously multiply the spectral range of current systems by combining, when operated in conjunction with widely tunable monochromatic sources, a spectral range comparable to that of a FTS with ultra-high optical resolution and an enhanced

sensitivity. These characteristics promise to enable a new palette of applications that would range from atmospheric multiple analyte detection to deep space exploration.

Funding

Ministerio de Economía y Competitividad (TEC2017-86271-R); Österreichische Forschungsförderungsgesellschaft (861581 (ATMOSENSE)); Ministerio de Educación, Cultura y Deporte (Estancias de movilidad José Castillejo).

Acknowledgments

The work by P.M.-M. has been performed in the frame of the “Estancias de movilidad José Castillejo” from the Spanish Ministry of Education, Culture and Sports. P.M.-M. would also like to thank the Spanish Ministry of Economy and Competitiveness for supporting the project under the TEC2017-86271-R Grant. A.G., H. M. and B.L. acknowledge financial support received from the Austrian Research Promotion Agency FFG within the project 861581 (ATMOSENSE) of the ERA-NET Photonics program.

References

1. D. Wunch, G. C. Toon, J.-F. L. Blavier, R. A. Washenfelder, J. Notholt, B. J. Connor, D. W. T. Griffith, V. Sherlock, and P. O. Wennberg, “The total carbon column observing network,” *Philos Trans A Math Phys Eng Sci* **369**(1943), 2087–2112 (2011).
2. F. Chevallier, N. M. Deutscher, T. J. Conway, P. Ciais, L. Ciattaglia, S. Dohe, M. Fröhlich, A. J. Gomez-Pelaez, D. Griffith, F. Hase, L. Haszpra, P. Krummel, E. Kyrö, C. Labuschagne, R. Langenfelds, T. Machida, F. Maignan, H. Matsueda, I. Morino, J. Notholt, M. Ramonet, Y. Sawa, M. Schmidt, V. Sherlock, P. Steele, K. Strong, R. Sussmann, P. Wennberg, S. Wofsy, D. Worthy, D. Wunch, and M. Zimnoch, “Global CO₂ fluxes inferred from surface air-sample measurements and from TCCON retrievals of the CO₂ total column,” *Geophys. Res. Lett.* **38**(24), L24810 (2011).
3. A. Kuze, H. Suto, M. Nakajima, and T. Hamazaki, “Thermal and near infrared sensor for carbon observation Fourier-transform spectrometer on the Greenhouse Gases Observing Satellite for greenhouse gases monitoring,” *Appl. Opt.* **48**(35), 6716–6733 (2009).
4. C. Frankenberg, R. Pollock, R. A. M. Lee, R. Rosenberg, J.-F. Blavier, D. Crisp, C. W. O’Dell, G. B. Osterman, C. Roehl, P. O. Wennberg, and D. Wunch, “The Orbiting Carbon Observatory (OCO-2): spectrometer performance evaluation using pre-launch direct sun measurements,” *Atmos. Meas. Tech.* **8**, 301–313 (2015).
5. D. R. Thompson, D. Chris Benner, L. R. Brown, D. Crisp, V. Malathy Devi, Y. Jiang, V. Natraj, F. Oyafuso, K. Sung, D. Wunch, R. Castañón, and C. E. Miller, “Atmospheric validation of high accuracy CO₂ absorption coefficients for the OCO-2 mission,” *J. Quant. Spectrosc. Radiat. Transf.* **113**(17), 2265–2276 (2012).
6. P. I. Palmer, E. L. Wilson, G. L. Villanueva, G. Liuzzi, L. Feng, A. J. DiGregorio, J. Mao, L. Ott, and B. Duncan, “Potential improvements in global carbon flux estimates from a network of laser heterodyne radiometer measurements of column carbon dioxide,” *Atmos. Meas. Tech. Discuss.* (in review).
7. D. Weidmann, A. Hoffmann, N. Macleod, K. Middleton, J. Kurtz, S. Barraclough, and D. Griffin, “The methane isotopologues by solar occultation (MISO) nanosatellite mission: spectral channel optimization and early performance analysis,” *Remote Sens.* **9**(10), 1073 (2017).
8. E. L. Wilson, A. J. DiGregorio, V. J. Riot, M. S. Ammons, W. W. Bruner, D. Carter, J. Mao, A. Ramanathan, S. E. Strahan, L. D. Oman, C. Hoffman, and R. M. Garner, “A 4 U laser heterodyne radiometer for methane (CH₄) and carbon dioxide (CO₂) measurements from an occultation-viewing CubeSat,” *Meas. Sci. Technol.* **28**(3), 035902 (2017).
9. A. Hoffmann, N. A. Macleod, M. Huebner, and D. Weidmann, “Thermal infrared laser heterodyne spectroradiometry for solar occultation atmospheric CO₂ measurements,” *Atmos. Meas. Tech.* **9**(12), 5975–5996 (2016).
10. E. L. Wilson, M. L. McLinden, J. H. Miller, G. R. Allan, L. E. Ott, H. R. Melroy, and G. B. Clarke, “Miniaturized laser heterodyne radiometer for measurements of CO₂ in the atmospheric column,” *Appl. Phys. B* **114**(3), 385–393 (2014).
11. T. Stangier, T. Hewagama, M. Sornig, G. Sonnabend, T. Kostiuk, M. Herrmann, and T. Livengood, “Thermal structure of Venus’ nightside mesosphere as observed by infrared heterodyne spectroscopy at 10 μm,” *Planet. Space Sci.* **113–114**, 359–368 (2015).
12. H. Nakagawa, S. Aoki, H. Sagawa, Y. Kasaba, I. Murata, G. Sonnabend, M. Sornig, S. Okano, J. R. Kuhn, J. M. Ritter, M. Kagitani, T. Sakanoi, M. Taguchi, and K. Takami, “IR heterodyne spectrometer MILAHI for continuous monitoring observatory of Martian and Venusian atmospheres at Mt. Haleakalā, Hawaii,” *Planet. Space Sci.* **126**, 34–48 (2016).
13. H. R. Melroy, E. L. Wilson, G. B. Clarke, L. E. Ott, J. Mao, A. K. Ramanathan, and M. L. McLinden, “Autonomous field measurements of CO₂ in the atmospheric column with the miniaturized laser heterodyne radiometer (Mini-LHR),” *Appl. Phys. B* **120**(4), 609–615 (2015).

Appendix F. Scientific Publications on Infrared-Based Gas Sensing

14. D. Weidmann and G. Wysocki, "High-resolution broadband ($>100\text{ cm}^{-1}$) infrared heterodyne spectro-radiometry using an external cavity quantum cascade laser," *Opt. Express* **17**(1), 248–259 (2009).
15. R. T. Menzies, "Remote detection of SO_2 and CO_2 with a heterodyne radiometer," *Appl. Phys. Lett.* **22**(11), 592–593 (1973).
16. R. T. Menzies and M. S. Shumate, "Air pollution: remote detection of several pollutant gases with a laser heterodyne radiometer," *Science* **184**(4136), 570–572 (1974).
17. P. Martín-Mateos, O. E. Bonilla-Manrique, and C. Gutiérrez-Escobero, "Wavelength modulation laser heterodyne radiometry," *Opt. Lett.* **43**(12), 3009–3012 (2018).
18. J. Hodgkinson and R. P. Tatam, "Optical gas sensing: a review," *Meas. Sci. Technol.* **24**(1), 012004 (2013).
19. A. Hoffmann, M. Huebner, N. Macleod, and D. Weidmann, "Spectrally resolved thermal emission of atmospheric gases measured by laser heterodyne spectrometry," *Opt. Lett.* **43**(16), 3810–3813 (2018).
20. G. B. Rieker, J. B. Jeffries, and R. K. Hanson, "Calibration-free wavelength-modulation spectroscopy for measurements of gas temperature and concentration in harsh environments," *Appl. Opt.* **48**(29), 5546–5560 (2009).

Publication III

Application of a ring cavity surface emitting quantum cascade laser (RCSE-QCL) on the measurement of H₂S in a CH₄ matrix for process analytics

Authors: Harald Moser, Andreas Genner, Johannes Ofner, Clemens Schwarzer, Gottfried Strasser and Bernhard Lendl

Die approbierte gedruckte Originalversion dieser Dissertation ist an der TU Wien Bibliothek verfügbar.
The approved original version of this doctoral thesis is available in print at TU Wien Bibliothek.



Die approbierte gedruckte Originalversion dieser Dissertation ist an der TU Wien Bibliothek verfügbar.
The approved original version of this doctoral thesis is available in print at TU Wien Bibliothek.

Application of a ring cavity surface emitting quantum cascade laser (RCSE-QCL) on the measurement of H₂S in a CH₄ matrix for process analytics

Harald Moser,¹ Andreas Genner,¹ Johannes Ofner,¹ C. Schwarzer,² Gottfried Strasser,² and Bernhard Lendl^{1,*}

¹Institute of Chemical Technologies and Analytics, Vienna University of Technology, Austria

²Institute of Solid State Electronics, Vienna University of Technology, Austria

*bernhard.lendl@tuwien.ac.at

Abstract: The present work reports on the first application of a ring-cavity-surface-emitting quantum-cascade laser (RCSE-QCL) for sensitive gas measurements. RCSE-QCLs are promising candidates for optical gas-sensing due to their single-mode, mode-hop-free and narrow-band emission characteristics along with their broad spectral coverage. The time resolved down-chirp of the RCSE-QCL in the 1227-1236 cm⁻¹ (8.15-8.09 μm) spectral range was investigated using a step-scan FT-IR spectrometer (Bruker Vertex 80v) with 2 ns time and 0.1 cm⁻¹ spectral resolution. The pulse repetition rate was set between 20 and 200 kHz and the laser device was cooled to 15-17°C. Employing 300 ns pulses a spectrum of ~1.5 cm⁻¹ could be recorded. Under these laser operation conditions and a gas pressure of 1000 mbar a limit of detection (3σ) of 1.5 ppmv for hydrogen sulfide (H₂S) in nitrogen was achieved using a 100 m Herriott cell and a thermoelectric cooled MCT detector for absorption measurements. Using 3 μs long pulses enabled to further extend the spectral bandwidth to 8.5 cm⁻¹. Based on this increased spectral coverage and employing reduced pressure conditions (50 mbar) multiple peaks of the target analyte H₂S as well as methane (CH₄) could be examined within one single pulse.

©2016 Optical Society of America

OCIS codes: (300.6340) Spectroscopy, infrared; (140.5965) Semiconductor lasers, quantum cascade; (280.3420) Laser sensors.

References and links

1. B. Lendl, J. Frank, R. Schindler, A. Müller, M. Beck, and J. Faist, "Mid-infrared quantum cascade lasers for flow injection analysis," *Anal. Chem.* **72**(7), 1645–1648 (2000).
2. J. Kuligowski, G. Quintás, and B. Lendl, "High performance liquid chromatography with on-line dual quantum cascade laser detection for the determination of carbohydrates, alcohols and organic acids in wine and grape juice," *Appl. Phys. B* **99**(4), 833–840 (2010).
3. Y. Wang, M. G. Soskind, W. Wang, and G. Wysocki, "High-resolution multi-heterodyne spectroscopy based on Fabry-Perot quantum cascade lasers," *Appl. Phys. Lett.* **104**(3), 031114 (2014).
4. J. Faist, C. Gmachl, F. Capasso, C. Sirtori, D. L. Sivco, J. N. Baillargeon, and A. Y. Cho, "Distributed feedback quantum cascade lasers," *Appl. Phys. Lett.* **70**(20), 2670 (1997).
5. G. P. Luo, C. Peng, H. Q. Le, S. S. Pei, W.-Y. Hwang, B. Ishaug, J. Um, J. N. Baillargeon, and C.-H. Lin, "Grating-tuned external-cavity quantum-cascade semiconductor lasers," *Appl. Phys. Lett.* **78**(19), 2834 (2001).
6. G. Wysocki, R. F. Curl, F. K. Tittel, R. Maulini, J. M. Bulliard, and J. Faist, "Widely tunable mode-hop free external cavity quantum cascade laser for high resolution spectroscopic applications," *Appl. Phys. B* **81**(6), 769–777 (2005).
7. S. Slivken, N. Bandyopadhyay, Y. Bai, Q. Y. Lu, and M. Razeghi, "Extended electrical tuning of quantum cascade lasers with digital concatenated gratings," *Appl. Phys. Lett.* **103**(23), 231110 (2013).
8. A. Bismuto, Y. Bidaux, C. Tardy, R. Terazzi, T. Gresch, J. Wolf, S. Blaser, A. Muller, and J. Faist, "Extended tuning of mid-ir quantum cascade lasers using integrated resistive heaters," *Opt. Express* **23**(23), 29715–29722

#257291

Received 12 Jan 2016; revised 25 Feb 2016; accepted 26 Feb 2016; published 15 Mar 2016

© 2016 OSA

21 Mar 2016 | Vol. 24, No. 6 | DOI:10.1364/OE.24.006572 | OPTICS EXPRESS 6572

Appendix F. Scientific Publications on Infrared-Based Gas Sensing

- (2015).
9. Y. Bidaux, A. Bismuto, C. Tardy, R. Terazzi, T. Gresch, S. Blaser, A. Muller, and J. Faist, "Extended and quasi-continuous tuning of quantum cascade lasers using superstructure gratings and integrated heaters," *Appl. Phys. Lett.* **107**(22), 29715–29722 (2015).
 10. S. Slivken, S. Sengupta, and M. Razeghi, "High power continuous operation of a widely tunable quantum cascade laser with an integrated amplifier," *Appl. Phys. Lett.* **107**(25), 251101 (2015).
 11. J. Buus, M.-C. Amann, and D. J. Blumenthal, *Tunable Laser Diodes and Related Optical Sources* (Wiley-Interscience, 2005).
 12. M. Brandstetter, A. Genner, C. Schwarzer, E. Mujagic, G. Strasser, and B. Lendl, "Time-resolved spectral characterization of ring cavity surface emitting and ridge-type distributed feedback quantum cascade lasers by step-scan FT-IR spectroscopy," *Opt. Express* **22**(3), 2656–2664 (2014).
 13. J. Hodgkinson and R. P. Tatam, "Optical gas sensing: a review," *Meas. Sci. Technol.* **24**(1), 012004 (2013).
 14. J. H. van Helden, N. Lang, U. Macherius, H. Zimmermann, and J. Röpcke, "Sensitive trace gas detection with cavity enhanced absorption spectroscopy using a continuous wave external-cavity quantum cascade laser," *Appl. Phys. Lett.* **103**(13), 131114 (2013).
 15. J. P. Waclawek, R. Lewicki, H. Moser, M. Brandstetter, F. K. Tittel, and B. Lendl, "Quartz-enhanced photoacoustic spectroscopy-based sensor system for sulfur dioxide detection using a CW DFB-QCL," *Appl. Phys. B* **117**(1), 113–120 (2014).
 16. C. Reidl-Leuthner and B. Lendl, "Toward stand-off open-path measurements of NO and NO₂ in the sub-parts per million meter range using quantum cascade lasers (QCLs) in the intra-pulse absorption mode," *Appl. Spectrosc.* **67**(12), 1368–1375 (2013).
 17. C. Reidl-Leuthner, A. Viernstein, K. Wieland, W. Tomischko, L. Sass, G. Kinger, J. Ofner, and B. Lendl, "Quasi-simultaneous in-line flue gas monitoring of NO and NO₂ emissions at a caloric power plant employing mid-IR laser spectroscopy," *Anal. Chem.* **86**(18), 9058–9064 (2014).
 18. C. Reidl-Leuthner, J. Ofner, W. Tomischko, H. Lohninger, and B. Lendl, "Simultaneous open-path determination of road side mono-nitrogen oxides employing mid-IR laser spectroscopy," *Atmos. Environ.* **112**(2), 189–195 (2015).
 19. J. B. McManus, D. D. Nelson, S. C. Herndon, J. H. Shorter, M. S. Zahniser, S. Blaser, L. Hvozdar, A. Muller, M. Giovannini, and J. Faist, "Comparison of cw and pulsed operation with a TE-cooled quantum cascade infrared laser for detection of nitric oxide at 1900 cm⁻¹," *Appl. Phys. (Berl.)* **85**(2), 235–241 (2006).
 20. B. Tuzson, M. Mangold, H. Looser, A. Manninen, and L. Emmenegger, "Compact multipass optical cell for laser spectroscopy," *Opt. Lett.* **38**(3), 257–259 (2013).
 21. D. Herriott, H. Kogelnik, and R. Kompfner, "Off-axis paths in spherical mirror interferometers," *Appl. Opt.* **3**(4), 523–526 (1964).
 22. J. B. McManus, M. S. Zahniser, and D. D. Nelson, "Dual quantum cascade laser trace gas instrument with astigmatic Herriott cell at high pass number," *Appl. Opt.* **50**(4), A74–A85 (2011).
 23. B. H. Lee, E. C. Wood, M. S. Zahniser, J. B. McManus, D. D. Nelson, S. C. Herndon, G. W. Santoni, S. C. Wofsy, and J. W. Mungler, "Simultaneous measurements of atmospheric HONO and NO₂ via absorption spectroscopy using tunable mid-infrared continuous-wave quantum cascade lasers," *Appl. Phys. (Berl.)* **2**, 417–423 (2010).
 24. B. G. Lee, M. Belkin, C. Pflugl, L. Diehl, H. Zhang, R. M. Audet, J. MacArthur, D. P. Bour, S. W. Corzine, G. E. Hufler, and F. Capasso, "DFB Quantum Cascade Laser Arrays," *IEEE J. Quantum Electron.* **45**(5), 554–565 (2009).
 25. B. G. Lee, H. Zhang, C. Pflugl, L. Diehl, M. Belkin, M. Fischer, A. Wittmann, J. Faist, and F. Capasso, "Broadband Distributed-Feedback Quantum Cascade Laser Array Operating From 8.0 to 9.8 μm," *IEEE Photonics Technol. Lett.* **21**(13), 914–916 (2009).
 26. M. Carras, G. Maisons, B. Simozrag, V. Trinite, M. Brun, G. Grand, P. Labeye, and S. Nicoletti, "Monolithic tunable single source in the mid-IR for spectroscopy," *Proc. SPIE* **8631**, 863113 (2013).
 27. E. Mujagic, S. Schartner, L. K. Hoffmann, W. Schrenk, M. P. Semtsiv, M. Wienold, W. T. Masselink, and G. Strasser, "Grating-coupled surface emitting quantum cascade ring lasers," *Appl. Phys. Lett.* **93**(1), 011108 (2008).
 28. E. Mujagic, L. K. Hoffmann, S. Schartner, M. Nobile, W. Schrenk, M. P. Semtsiv, M. Wienold, W. T. Masselink, and G. Strasser, "Low divergence single-mode surface emitting quantum cascade ring lasers," *Appl. Phys. Lett.* **93**(16), 161101 (2008).
 29. E. Mujagic, M. Nobile, H. Detz, W. Schrenk, J. Chen, C. Gmachl, and G. Strasser, "Ring cavity induced threshold reduction in single-mode surface emitting quantum cascade lasers," *Appl. Phys. Lett.* **96**(3), 031111 (2010).
 30. E. Mujagic, C. Schwarzer, Y. Yao, J. Chen, C. Gmachl, and G. Strasser, "Two-dimensional broadband distributed-feedback quantum cascade laser arrays," *Appl. Phys. Lett.* **98**(14), 141101 (2011).
 31. C. Schwarzer, E. Mujagic, S. Il Ahn, A. M. Andrews, W. Schrenk, W. Charles, C. Gmachl, and G. Strasser, "Grating duty-cycle induced enhancement of substrate emission from ring cavity quantum cascade lasers," *Appl. Phys. Lett.* **100**(19), 191103 (2012).
 32. C. Schwarzer, R. Szedlak, S. Il Ahn, T. Zederbauer, H. Detz, A. Maxwell Andrews, W. Schrenk, and G. Strasser, "Linearly polarized light from substrate emitting ring cavity quantum cascade lasers," *Appl. Phys. Lett.* **103**(8), 081101 (2013).

#257291

Received 12 Jan 2016; revised 25 Feb 2016; accepted 26 Feb 2016; published 15 Mar 2016

© 2016 OSA

21 Mar 2016 | Vol. 24, No. 6 | DOI:10.1364/OE.24.006572 | OPTICS EXPRESS 6573

33. R. Szedlak, C. Schwarzer, T. Zederbauer, H. Detz, A. Maxwell Andrews, W. Schrenk, and G. Strasser, "On-chip focusing in the mid-infrared: Demonstrated with ring quantum cascade lasers," *Appl. Phys. Lett.* **104**(15), 151105 (2014).
34. B. Schwarz, P. Reiningger, H. Detz, T. Zederbauer, A. Maxwell Andrews, S. Kalchmair, W. Schrenk, O. Baumgartner, H. Kosina, and G. Strasser, "A bi-functional quantum cascade device for same-frequency lasing and detection," *Appl. Phys. Lett.* **101**(19), 191109 (2012).
35. A. Harrer, R. Szedlak, B. Schwarz, H. Moser, T. Zederbauer, D. MacFarland, H. Detz, A. M. Andrews, W. Schrenk, B. Lendl, and G. Strasser, "Mid-infrared surface transmitting and detecting quantum cascade device for gas-sensing," *Sci. Rep.* **6**, 21795 (2016).
36. Z. Liu and D. Wasserman, "Room-temperature continuous-wave quantum cascade lasers grown by MOCVD without lateral regrowth," *Photonics* **18**(12), 1347–1349 (2006).
37. W. Uhmann, A. Becker, C. Taran, and F. Siebert, "Time-Resolved FT-IR Absorption Spectroscopy Using a Step-Scan Interferometer," *Appl. Spectrosc.* **45**(3), 390–397 (1991).
38. T. J. Johnson, A. Simon, J. M. Weil, and G. W. Harris, "Applications of time-resolved step-scan and rapid-scan FT-IR spectroscopy: dynamics from ten seconds to ten nanoseconds," *Appl. Spectrosc.* **47**(9), 1376–1381 (1993).
39. J. B. McManus, P. L. P. Kebabian, and M. S. M. Zahniser, "Astigmatic mirror multipass absorption cells for long-path-length spectroscopy," *Appl. Opt.* **34**(18), 3336–3348 (1995).
40. H. Siebert, *Anwendungen der Schwingungsspektroskopie in der Anorganischen Chemie* (Springer Verlag, 1966).
41. H. a. Jahn, "A New Coriolis Perturbation in the Methane Spectrum. I. Vibrational-Rotational Hamiltonian and Wave Functions," *Proc. R. Soc. A Math. Phys. Eng. Sci.* **168**(935), 469–495 (1938).
42. S. N. Mikhailenko, Y. L. Babikov, and V. F. Golovko, "Information-calculating system Spectroscopy of Atmospheric Gases. The structure and main functions," *Atmos. Oceanic Opt.* **18**(9), 685–695 (2005).
43. L. S. Rothman, I. E. Gordon, Y. Babikov, A. Barbe, D. Chris Benner, P. F. Bernath, M. Birk, L. Bizzocchi, V. Boudon, L. R. Brown, A. Campargue, K. Chance, E. A. Cohen, L. H. Coudert, V. M. Devi, B. J. Drouin, A. Fayt, J.-M. Flaud, R. R. Gamache, J. J. Harrison, J.-M. Hartmann, C. Hill, J. T. Hodges, D. Jacquemart, A. Jolly, J. Lamouroux, R. J. Le Roy, G. Li, D. A. Long, O. M. Lyulin, C. J. Mackie, S. T. Massie, S. Mikhailenko, H. S. P. Müller, O. V. Naumenko, A. V. Nikitin, J. Orphal, V. Perevalov, A. Perrin, E. R. Polovtseva, C. Richard, M. A. H. Smith, E. Starikova, K. Sung, S. Tashkun, J. Tennyson, G. C. Toon, V. G. Tyuterev, and G. Wagner, "The HITRAN2012 molecular spectroscopic database," *J. Quant. Spectrosc. Radiat. Transf.* **130**, 4–50 (2013).
44. R. A. McClatchey, W. S. Benedict, S. A. Clough, D. E. Burch, R. F. Calfee, K. Fox, L. S. Rothman, and J. S. Garing, "AFCL atmospheric absorption line parameters compilation," *Environ. Res. Pap.* **434**, 1–86 (1973).
45. D. Weidmann, F. K. Tittel, T. Aellen, M. Beck, D. Hofstetter, J. Faist, and S. Blaser, "Mid-infrared trace-gas sensing with a quasi-continuous-wave Peltier-cooled distributed feedback quantum cascade laser," *Appl. Phys. B* **79**(7), 907–913 (2004).
46. B. Neidhart and W. Wegscheider, *Quality in chemical measurements* (Springer Science and Business Media, 2001).
47. W. Chen, A. A. Kosterev, F. K. Tittel, X. Gao, and W. Zhao, "H₂S trace concentration measurements using off-axis integrated cavity output spectroscopy in the near-infrared," *Appl. Phys. B* **90**(2), 311–315 (2008).
48. F. Schmidt, *Laser-based Absorption Spectrometry - Development of NICE-OHMS Towards Ultra-sensitive Trace Species Detection* (2007).
49. A. Foltynowicz, F. M. Schmidt, W. Ma, and O. Axner, "Noise-immune cavity-enhanced optical heterodyne molecular spectroscopy: Current status and future potential," *Appl. Phys. B* **92**(3), 313–326 (2008).
50. A. Varga, Z. Bozóki, M. Szakáll, and G. Szabó, "Photoacoustic system for on-line process monitoring of hydrogen sulfide (H₂S) concentration in natural gas streams," *Appl. Phys. B* **85**(2), 315–321 (2006).

1. Introduction

Since their first realization in 1994, quantum cascade lasers (QCLs) have developed from research devices to powerful light sources for practical use in applied infrared spectroscopy. The first devices showing cascaded intersubband transitions in an AlInAs/GaInAs heterostructure could only be operated in pulsed mode at cryogenic temperatures and showed multi-mode emission with peak power of a few μW only. Resonator designs of such early architecture were based on Fabry-Perot (FP) [1] cavities. As FP-QCLs emit multimodal over a wide spectral range they tend to have limited applicability for applied infrared gas spectroscopy and even for condensed phase applications an external sample modulation is required for achieving the required selectivity [2]. In spite of the great progress achieved in high resolution spectroscopy using FP-QCL sources [3], for many applications the use of single mode sources is beneficial. Up to date, the spectral coverage of QCLs extends from below 3 μm over the mid-IR spectral range to the far-infrared and THz regime. Furthermore, concerning the mid-IR spectral range, single-mode emission in pulsed as well as in continuous wave (cw) mode are state of the art. Also resonator designs were improved over

Appendix F. Scientific Publications on Infrared-Based Gas Sensing

the years with the distributed feedback (DFB) [4] and the external cavity (EC) [5] approach being the most prominent ones. Depending on the application in mind different properties of a given QCL may be of special relevance. Properties to be considered include, among others, pulse peak power, cw-operation, line widths as well as spectral coverage.

A general aim with respect to the ongoing development of QCLs for sensing applications is to reduce the line width of the emitted radiation to a minimum while achieving a spectral coverage as large as possible. So far EC-QCLs offer the largest tuning range which, depending on the employed gain medium, may cover up to several hundreds of wavenumbers. Operated in pulsed mode these lasers are good candidates for condensed phase spectroscopy and have found their applications in far-field as well as near-field infrared microscopy, stand-off measurements of solid residues as well as in the measurement of liquids. Unfortunately, these devices are not ideal for gas spectroscopy as even concerning their mode-hop free version practical issues arise with regard to mono-mode emission over a few tens of wavenumbers [6].

In recent years various methods for extending the tuning range were investigated by exploiting the large width of the gain curve of semiconductor lasers and the full gain width of optical amplifiers. Promising results could be achieved by modification of the sampled grating distributed feedback laser architecture with digital concatenated gratings [7], by incorporation of a buried microscopic heater element close to the active region [8], by integration of Vernier-effect distributed Bragg reflectors based on superstructure gratings [9] or by integrating an asymmetric sampled grating distributed feedback tunable laser with an optical amplifier [10]. It is characteristic of the various schemes for extended tuning that the resulting wavelength is no longer a relatively simple monotonous function of a single control parameter. Instead, it is often necessary to use two or more control variables (quasicontinuous tuning) [11]. In this manner the reported full tuning ranges will span between 9 and 14 cm^{-1} [8], [9] and can reach up to 120-236 cm^{-1} [7], [10].

The high quality requirements in terms of single mode emission and wavelength stability as needed for trace gas sensing are, however, met by DFB-type QCLs [12]. Commercial DFB-QCLs are configured as ridge lasers which are designed for edge emission. These lasers can be tuned by changing the temperature of the gain medium. The resulting tuning range covers thus a few wavenumbers only, and this is why typically one analyte is targeted by a given DFB-QCL.

Several different optical setups for quantitative gas phase spectroscopy using QCLs have been demonstrated already and the used techniques were recently reviewed [13]. These include, cavity enhanced absorption spectroscopy [14], quartz-enhanced photoacoustic spectroscopy [15] and open-path setups [16], which were all successfully applied to industrial [17] and environmental monitoring [18]. The most 'straightforward' setups for gas measurements in the mid-infrared spectral region using QCLs are based on absorbance measurements in multi-reflection cells [19]. While special cell types were successfully tested [20], the basic cell type for laser spectroscopy is the so called Herriott cell [21]. Common multi-gas analyzers based on QCLs suffer from the required space to combine the beam lines of different lasers to one gas cell [22]. These setups are typically based on multiple QCLs in separated packages, even if the spectral distance between the target absorptions is small [23].

Recently, different strategies were proposed to improve the spectral coverage while maintaining the high quality of single-line emission of DFB-QCLs. Processing different, individually addressable, ridge type DFB-QCLs on a single chip as an array allows to produce a laser source [24], [25] covering several tens of wavenumbers that still features a spectral resolution smaller than 0.01 cm^{-1} . A further refinement of this concept concerns fusion of an optical coupler to the monolithically produced DFB-QCL array to achieve emission from a single spot [26].

Ring-cavity surface emitting (RCSE) QCLs represent a novel alternative [27] to commercially available ridge-type DFB-QCLs. In contrast to these edge emitting DFB-QCLs

wavelength selection and surface emission are made possible by radial second-order Bragg gratings etched in the top cladding of the gain material. The diameter of the surface emitting rings is in the order of a few hundreds of micrometer. Therefore, the beam divergence of RCSE-QCLs is only a few degrees [28] as compared to a few tens of degrees in case of edge emitting ridge lasers. This facilitates coupling of the emitted light in an optical system. Concerning peak optical power, threshold current and slope-efficiency the performance of RCSE-QCLs is improved when compared to ridge-type DFB-QCLs made of the same gain medium [12]. A further characteristic of these lasers is their broad tuning range, mode-hop-free operation and beam stability during operation [29]. Arrangement of several RCSE-QCLs with slightly different grating periods at each ring allows taking advantage of the whole spectral range provided by the used gain medium. An effective spectral coverage of 180 cm^{-1} was already demonstrated in 2011 [30]. In order to address the potential disadvantage of the RCSE design and its non-Gaussian output in the far-field, further improvement of the emitted radiation is possible using collimated substrate emission of RCSE-QCLs with on-chip focusing elements [31–33] or by modification of the distributed feedback grating by application of two π -phase-shifts at an angular distance of 180° . In this way a focused, central lobed and linearly polarized far field is achieved without external optics [32].

An innovative design of the QCL active region allows fabrication of a laser and a detector on the same chip [34], which reduces the sensor size and opens the door to new spectroscopic concepts [35].

Here we report on the first use of RCSE-QCL for gas spectroscopy. A widely tunable RCSE-QCL was operated in pulsed mode and coupled into an astigmatic Herriott cell and combined with a fast thermoelectrically cooled MCT detector. The laser down chirp produced by the pulsed mode-hop free RCSE-QCL was used for the simultaneous measurement of hydrogen sulfide (H_2S) and methane (CH_4).

2. Materials and methods

2.1 Laser and instrumentation for laser characterization

The QCL device used in this scope of work was based on the substrate P51 [36] and was processed as a RCSE-QCL [27]. By assuming an effective refractive index of $n_{\text{eff}} = 3.18$ and aiming for a emission wavenumber of 1234 cm^{-1} at room temperature, a grating period of the 2nd order was calculated to be $2.547\text{ }\mu\text{m}$ (481 slits) and realized. An in-house developed laser driver and TEC unit was used to control the injection current for pulsed operation of the RCSE-QCL and to adjust and stabilize the laser operation temperature to 0.1 K. Single mode emission at different operation parameters could be verified by recording spectra with an FT-IR spectrometer (Vertex 80v, Bruker Optics, Germany) equipped with a photovoltaic liquid nitrogen cooled MCT detector (Kolmar Technologies, USA) using the external source input port. Moreover, time-resolved step-scan FT-IR [37,38] measurements with a time resolution of 2 ns and a spectral resolution of 0.075 cm^{-1} were performed to characterize the laser chirp with this FT-IR spectrometer [12]. For recording the signal produced by a single laser pulse a transient recorder board (Spectrum GmbH, Germany) with an 8 bit resolution and 500 MS/s sample rate was used. The laser pulse repetition rate was set between 20 and 200 kHz and the temperature of the laser was set between 15 and 17 °C.

2.2 Optical setup for the H_2S detection in CH_4 containing nitrogen

The experimental set-up for absorbance measurements was designed to enable recording of the background spectrum as well as the sample spectrum using one detector. This was achieved by pulsed operation of the laser and splitting of the laser pulse at a beam splitter. Whereas one part of the laser pulse was directly focused onto a TE cooled MCT detector (PVI-2TE-10.6, Vigo Systems) the second part was delayed by passing a 100 m Herriott gas cell (AMAC100, Aerodyne Inc.) [39] before impinging on the same detector. This

Appendix F. Scientific Publications on Infrared-Based Gas Sensing

configuration allowed separating background and sample spectrum in time for laser pulses up to pulse lengths of 300 ns. For experiments relying on pulse durations >300 ns the beam splitter had to be removed in order to prevent overlapping of the reference and probe pulses on the same detector. In order to calculate absorbance values, a synthetic background spectrum had to be reconstructed from the probe pulses exiting the multipass cell and containing spectral features of the analytes. The synthetic background spectrum was obtained by fitting the pulse intensity envelope via a higher order polynomial function and subsequently used for calculation of the corresponding absorbance spectrum. To facilitate alignment of the optical set-up a HeNe-trace laser beam was used. The Herriott cell was operated at pressures ranging from 50 mbar to 1000 mbar. At low pressure conditions the ro-vibrational bands of the analyte H_2S could be resolved during short laser pulses. A calibration curve for H_2S in nitrogen was recorded holding the cell pressure constant at 1000 mbar. Temperature was kept at room-temperature level throughout all experiments. Recording of the amplified detector signal was performed using an oscilloscope (14 bit, 600 MHz bandwidth, LeCroy Waverunner 64 Xi, Teledyne LeCroy SA, CH). For improving the signal to noise ratio, 1 k samples were internally averaged. A schematic and a picture of the full configuration including mirrors and lenses are given in Fig. 1.

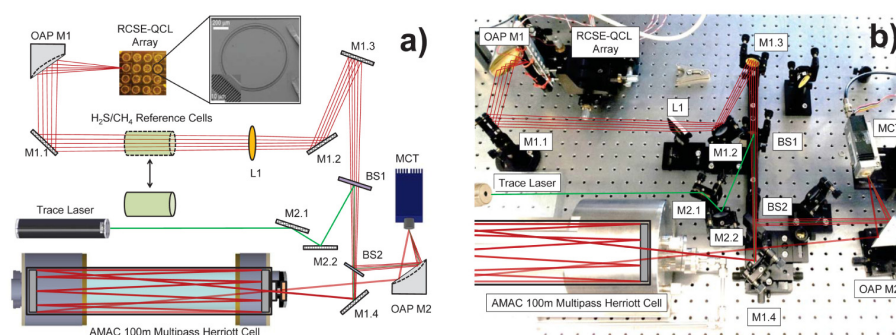


Fig. 1. Schematic (a) and actual picture (b) of the optical setup. M...mirrors, L...lenses and, OAP M...off axis parabolic mirrors.

In order to confirm the correct wavelength calibration reference gas cells were used and inserted into the optical path as required. These cells, designed with an optical path-length of 5 cm, are filled with the single target analytes with 98% H_2S and 5% CH_4 backfilled with N_2 to a total pressure of 50 mbar. They are sealed with wedged and Brewster angle tilted CaF_2 windows.

3. The $\text{H}_2\text{S} / \text{CH}_4$ system in the mid-infrared spectral region

Based on the available RCSE-QCL substrate and processing of the laser grating, the mid-infrared spectral region between 1236 and 1227 cm^{-1} was available. This region is characterized by the overlapping of the ν_2 (A_1) bending-mode transition of H_2S (C_{2v} symmetry) and the ν_4 (F_2) bending mode of CH_4 (T_d symmetry) [40]. Further a Coriolis-coupling of the $\nu_4(F_2)$ and the $\nu_2(E)$ appears, causing the presence of ν_4 - ν_2 -coupled ro-vibrational transitions [40,41] in this spectral window.

With regard to selection of the most appropriate absorption lines for measuring H_2S in the presence of CH_4 reference spectra were calculated [42] based on the HITRAN [43] database (Fig. 2). Using the available RCSE-QCL the ro-vibrational transitions corresponding to the ν_2 bending-mode of H_2S as listed in Table 1 were accessible. The rotational levels of H_2S being a three-dimensional asymmetric top rotator with three different reciprocal moment of inertia are labeled by the three standard quantum numbers J , K_a and K_c [44]. For pulses with durations of 300 ns, the accessible spectral range was limited to 1235.4 - 1233.8 cm^{-1} . Hence,

the measured H₂S band centered at 1234.5 cm⁻¹ is a sum of 4 basic ro-vibrational transitions of the ν₂ bending-mode, which could partly be resolved by measuring at reduced pressure.

Table 1. Main ro-vibrational transitions of the ν₂ bending-mode of H₂S in the spectral region 1236-1227 cm⁻¹.

Wavenumber (cm ⁻¹)	Linestrength (cmmol ⁻¹)	RVS _{low} *	RVS _{high} *	Remarks
		[J K _a K _c]	[J K _a K _c]	
1227.5925	1.37E-22	[2 2 0]	[1 1 1]	low line strength
1229.2712	4.92E-22	[5 1 4]	[5 0 5]	CH ₄ interference
1229.3305	1.64E-22	[5 2 4]	[5 1 5]	CH ₄ interference
1229.3522	1.04E-22	[7 5 3]	[7 4 4]	CH ₄ interference
1229.8447	2.10E-22	[3 2 2]	[2 1 1]	CH ₄ interference
1230.3305	1.18E-22	[7 0 7]	[7 6 1]	CH ₄ interference
1231.8627	1.74E-22	[6 4 6]	[6 1 5]	accessible only with 3 μs pulses
1232.1418	5.24E-22	[6 3 4]	[6 2 5]	accessible only with 3 μs pulses
1234.4351	3.83E-22	[7 3 4]	[7 2 5]	accessible
1234.5767	7.77E-22	[5 0 5]	[4 1 4]	accessible
1234.5830	2.59E-22	[5 1 5]	[4 0 4]	accessible
1234.6113	1.80E-22	[8 6 8]	[8 5 4]	accessible
1235.3742	1.30E-22	[7 4 4]	[7 3 5]	low line strength
1235.7048	1.26E-22	[8 7 2]	[8 6 3]	low line strength

* quantum numbers of higher and lower ro-vibrational state (RVS)

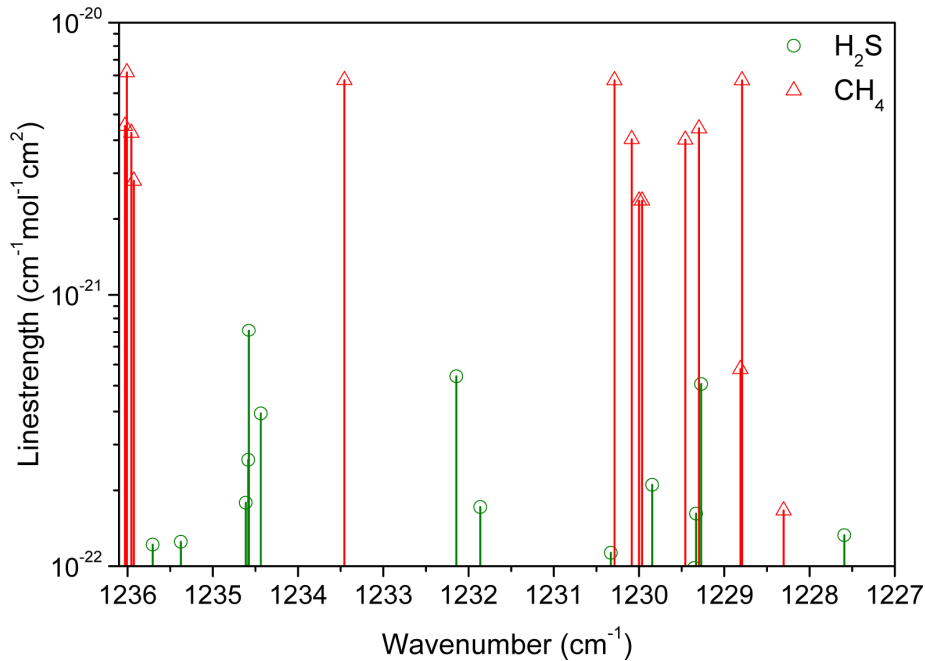


Fig. 2. Accessible linestrengths of H₂S and CH₄ in the 1236-1227 cm⁻¹ spectral region. For 300 ns pulses, the accessible spectral range was limited to 1235.4-1233.8 cm⁻¹

4. Results and discussion

4.1 Measurement of the laser chirp, determination and validation of wavenumber calibration

The temporal and spectral behavior of the pulsed laser radiation was characterized by step-scan FT-IR spectroscopy and the obtained data was subsequently used for wavelength calibration of the laser chirp and is plotted in Fig. 3. The measured laser pulse was fitted to

Appendix F. Scientific Publications on Infrared-Based Gas Sensing

the following logarithmic decay expression, termed transfer function which maps the laser emission wavelength in terms of wavenumber as a function of pulse time:

$$v(t) = v_0 - \alpha \cdot \ln(t + \beta), \quad (1)$$

where t denotes the pulse time as the independent variable and v_0 , α and β are the fitting parameters [45]. Having determined such expressions for a set of operating conditions, these transfer functions could be used for wavenumber calibration during the gas sensing experiments. As an example, $v_0 = 1154.3728$, $\alpha = 5.8419$ and $\beta = 9.3623E-7$ as the fit parameters for the logarithmic transfer function (Eq. (1)) were obtained for a 3 μs pulse length, an operation temperature of 17 °C and a pulse current of 700 mA.

As shown in Fig. 3(a)-3(c) employing an intra-pulse time of 300 ns and depending on the supplied current (400-700 mA), a spectral down-chirp range between 1.2 cm^{-1} and 1.7 cm^{-1} could be recorded. Long pulses of >3 μs and injection current levels between 400 mA and 700 mA enabled to cover a spectral bandwidth of up to 8.5 cm^{-1} . The results of the intra-pulse characteristics and tuning ranges for 3 μs pulses are outlined in Fig. 3(d)-(f).

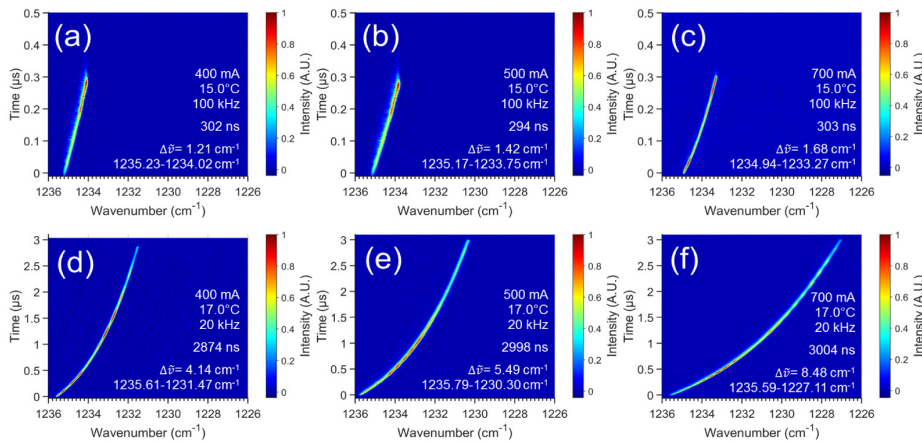


Fig. 3. Different achievable tuning ranges and intra-pulse characteristics for low current 300 ns (a), medium current 300 ns (b), high current 300 ns (c), low current 3 μs (d), medium current 3 μs (e) and high current 3 μs RCSE-QCL pulses (f).

The tuning behavior of the pulsed laser was furthermore validated using the set-up for gas sensing and by inserting the two reference cells into the optical path. In Fig. 4 the intensities recorded during a 3 μs long pulse with 98%v H_2S and 5%v CH_4 present as absorbing gases in the reference cells are given along with the previously determined transfer function. The strongly structured pulse shape between onset and $\sim 30\%$ of the total intra pulse duration can be explained by transient changes in the thermal and electrical properties of the laser material. Compared to the short pulse durations, the much larger time constant of the cooling system gives rise to dynamic shifts of the operating point caused by the temperature changes of the laser structure. In order to calculate the corresponding absorbance spectrum a synthetic background spectrum had to be reconstructed by fitting the pulse intensity envelope via a higher order polynomial function. In Fig. 5 the calculated absorbance spectrum is plotted together with the simulated spectra using information contained in the HITRAN database concerning wavenumber and strength of the corresponding lines for hydrogen sulfide as well as for methane in the investigated spectral region as well as spectral broadening at a pressure of 50 mbar.

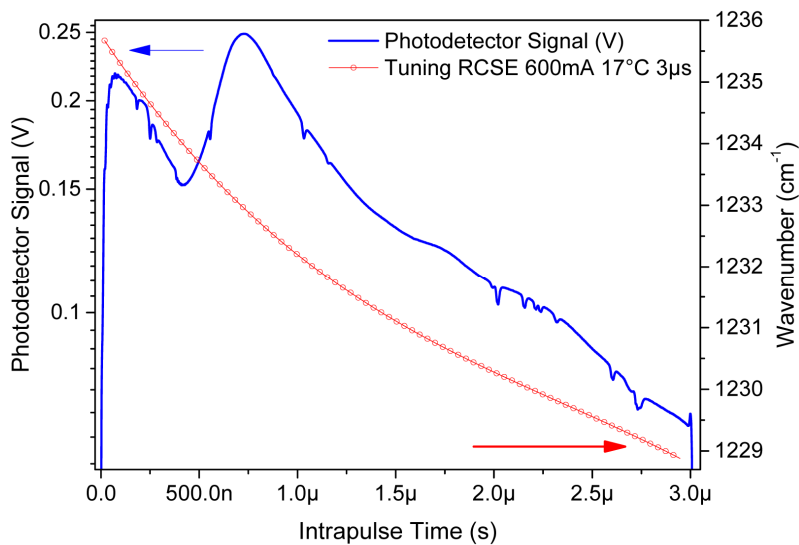


Fig. 4. A 3 μs long pulse with 98%v H_2S and 5%v CH_4 in the 5 cm reference cells at 50 mbar along with the tuning logarithmic fit.

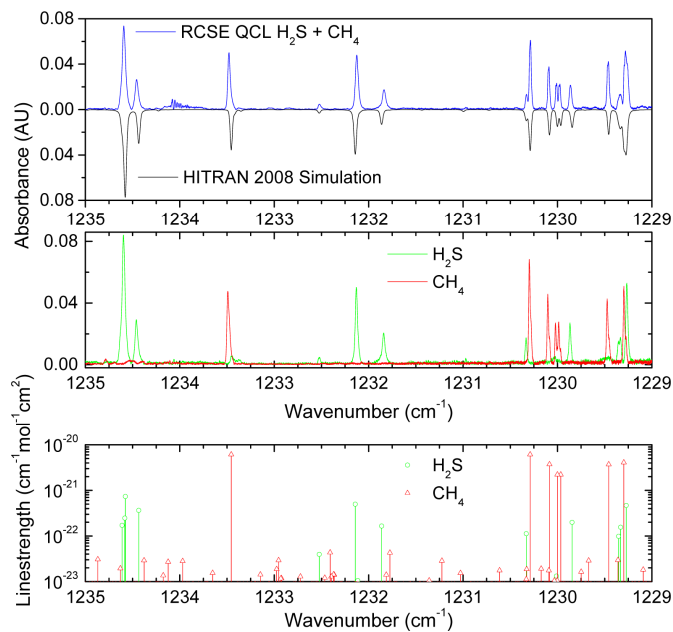


Fig. 5. Resulting absorption spectrum with the different analyte contributions of H_2S and CH_4 (top and middle) and the according line strengths of the contributing analytes (bottom).

The line positions and lineshapes of the H_2S and CH_4 features in the range between 1235 cm^{-1} and 1229 cm^{-1} could be spectrally reproduced as expected from Table 1 and are in good agreement with the HITRAN simulations.

Appendix F. Scientific Publications on Infrared-Based Gas Sensing

4.2 Resolving H_2S ro-vibrational features at reduced gas pressure

For the study of spectrally resolved ro-vibrational features a spectral region containing 4 transitions of H_2S was selected. According to the HITRAN database three, closely spaced transitions (1234.5767 , 1234.5830 and 1234.6113 cm^{-1}) as well as a fourth line at 1234.4351 cm^{-1} are to be expected. Experimental conditions were set such that a background and sample spectrum could be recorded from a single laser pulse. In Fig. 6(a) data recorded from 200 ns laser pulses measuring a gas sample containing 500 ppmv H_2S at different gas pressures are shown. Successful low pressure resolution of the ro-vibrational features can be observed starting from 400 mbar downwards. Whereas a clear separation of the transition at 1234.4351 cm^{-1} from the group of three transitions and centered at 1234.59 cm^{-1} could be achieved, the latter three transitions were not resolved even at further reduced gas pressures. The resulting absorption spectrum at 200 mbar is shown in Fig. 6(b) and compared with HITRAN simulations showing excellent agreement. However, the strongly structured features at the pulse shape edges caused by transient changes in the thermal and electrical properties of the laser material and stemming from optical fringes are eventually the cause for the baseline noise between 25 ns and 75 ns.

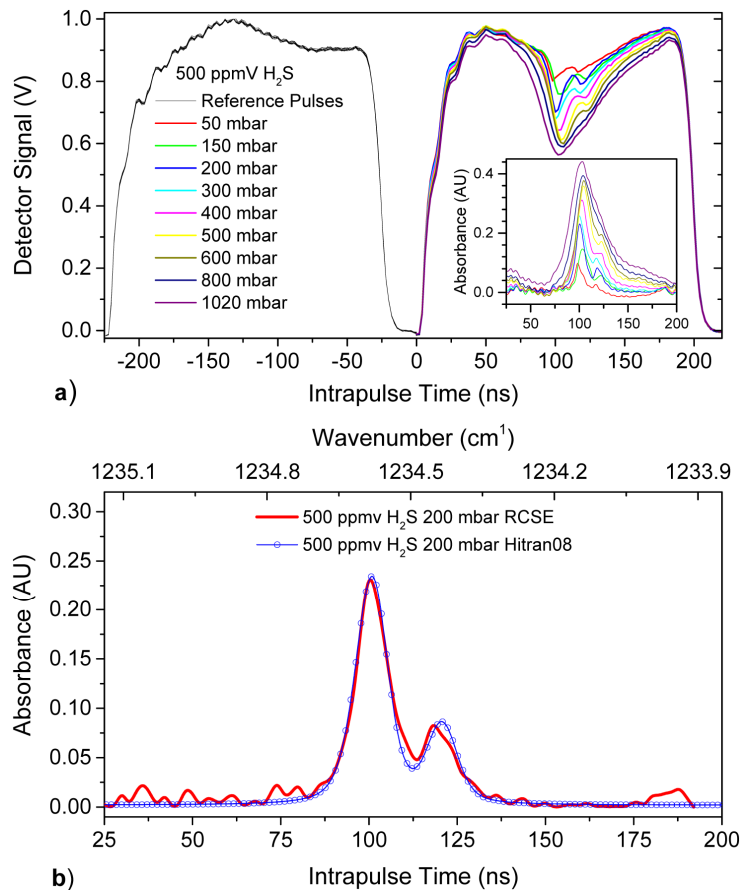


Fig. 6. (a) Short 200 ns pulses with 500 ppmv H_2S at different cell pressures and the resulting absorption spectra (inset); (b) Experimental data and HITRAN simulation of a short 200 ns pulse with 500 ppmv H_2S at 200 mbar cell pressure demonstrating low pressure resolution of the ro-vibrational features.

#257291
© 2016 OSA

Received 12 Jan 2016; revised 25 Feb 2016; accepted 26 Feb 2016; published 15 Mar 2016
21 Mar 2016 | Vol. 24, No. 6 | DOI:10.1364/OE.24.006572 | OPTICS EXPRESS 6581

4.3 Measuring H₂S in the presence of methane (CH₄)

Possible applications of measuring H₂S can be found in the petrochemical industry. In these applications hydrocarbons are important components and methane a frequently occurring constituent of a typical sample matrix. Within this work the issue was pursued whether an extended tuning range of a single pulse would allow resolving absorption features of both molecules, H₂S and methane (CH₄), simultaneously. Therefore RCSE-QCL pulses of 3 μs duration were used as they enabled to cover a bandwidth of approximately 8 cm⁻¹. Together with low pressure conditions of <500mbar selective and interference free H₂S assessments in a CH₄ matrix could be demonstrated. Figure 7(a) shows intra-pulse transmission and absorption spectra from 3 μs pulses with different isolated CH₄ contributions arising from concentrations in the range of 0- 495 ppmv. Intra-pulse transmission and absorption spectra of a constant CH₄ matrix of 495 ppmv and varying H₂S content in the range of 0-1000 ppmv are highlighted in Fig. 7(b).

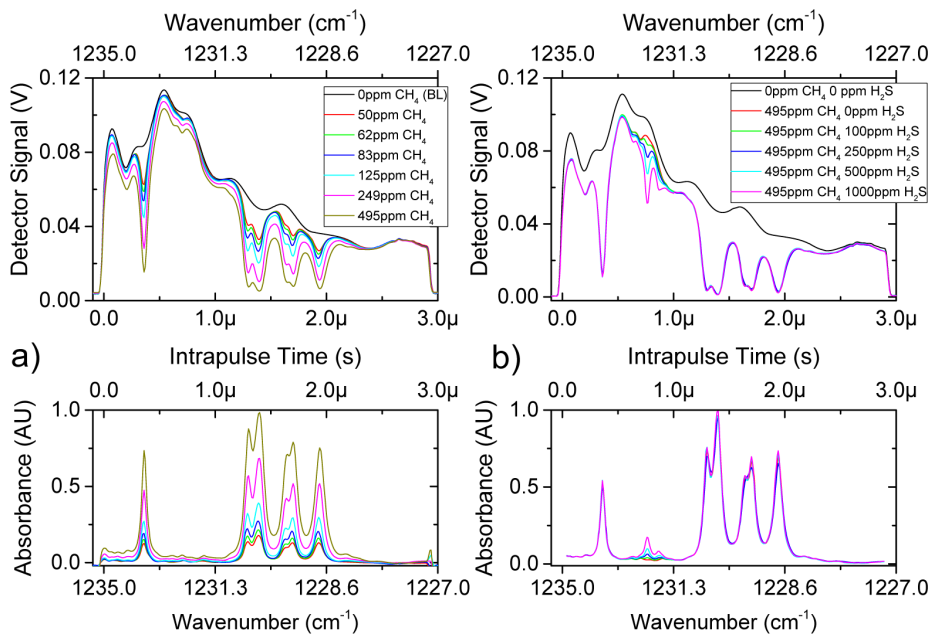


Fig. 7. 3 μs pulses with different CH₄ concentrations (a) and 3 μs pulse with constant 500 ppmv CH₄ and different H₂S concentrations (b). The cell pressure was held constant at 500 mbar.

The experimental results of the intra-pulse absorption spectrum of a 3 μs pulse with contributions of 500 ppmv CH₄ and 1000 ppmv H₂S at 500 mbar are shown in Fig. 8 together with a HITRAN simulation for comparison. Slight differences in peak positions could be observed for the CH₄ features at the beginning and pulse. The peak to peak wavenumber difference $\Delta\nu_{pp}$ was calculated to be ~ 0.07 cm⁻¹. The positions of the main three CH₄ peaks at 1230.2 cm⁻¹, 1229.4 cm⁻¹ and 1228.8 cm⁻¹ respectively, could also be spectrally reproduced, whereas the lineshapes could not be fully resolved as expected from the simulations. Due to slight TEC instabilities of the laser which led to minute wavelength shifts, the CH₄ lineshapes appear broadened. The line positions and the lineshape of the H₂S features at 1232.13 cm⁻¹ and 1231.86 cm⁻¹ could be spectrally reproduced with adequate precision.

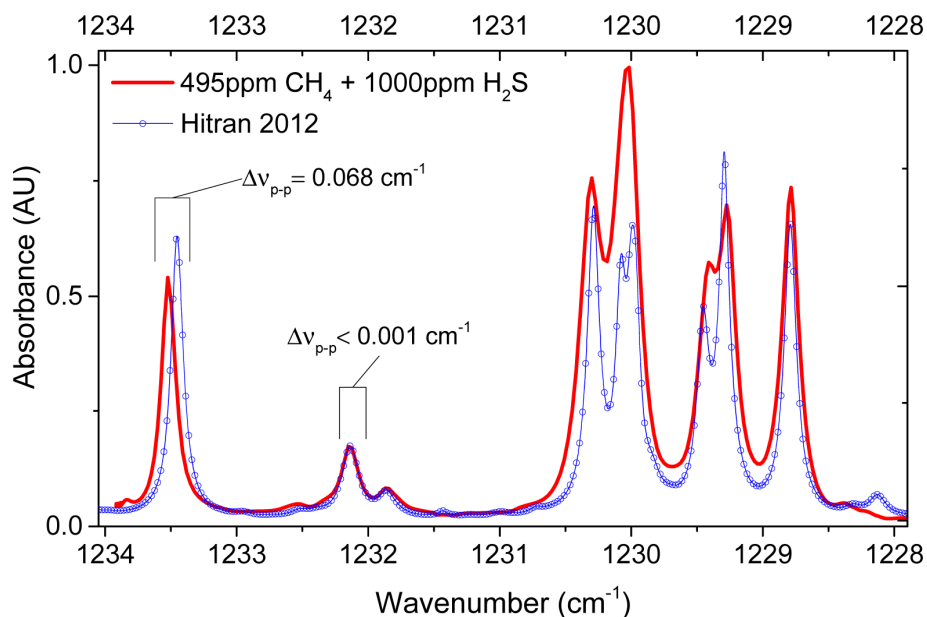


Fig. 8. Experimental data and HITRAN simulation of the intrapulse tuning of a 3 μ s pulse with contributions of 500ppmv CH_4 and 1000ppmv H_2S at 500 mbar.

4.4 Calibration of the H_2S measurements and determination of the limit of detection (LOD)

The calibration of H_2S inside the 100 m Herriott cell and the determination of the related limit of detection (LOD) was performed by applying laser pulses of 300 ns as shown in Fig. 9(a). According to the step-scan FT-IR measurements, the ro-vibrational transitions of Table 1 marked “accessible” could be probed. Different H_2S concentrations from 50 ppm down to 1 ppm were applied and the related absorption spectra calculated as outlined in Fig. 9(b). Each point of the calibration curve in Fig. 10 correlates to an averaging of 10 samples and good linearity between integrated absorbance and H_2S concentrations is observed. The corresponding limit of detection (LOD) was ascertained with the VALIDATA software package [46] at three times the standard deviation (3σ) of the intercept divided by the slope of the calibration curve, which resulted in 1.5 ppmv. Analysis of the residuals provided a convenient means of confirming the linearity of the calibration data.

In the aspect of process analytical integration and applicability sub-ppmv detection of H_2S concentration levels is essential for production control and environmental monitoring purposes. When measuring H_2S by IR spectroscopy high sensitivities are difficult to achieve due to the intrinsically weak linestrengths of the H_2S ro-vibrational features within the spectral range covered by diode lasers. Although detection of H_2S concentrations levels of several ppbv has been demonstrated by employing integrated cavity output spectroscopy approaches [47], such sensitivities are difficult to obtain in field measurements as the robustness of these kind of systems remain limited [48,49]. A fully developed and industry tailored H_2S sensor based on photoacoustic spectroscopy and a LOD of 0.5 ppmv is described in [50].

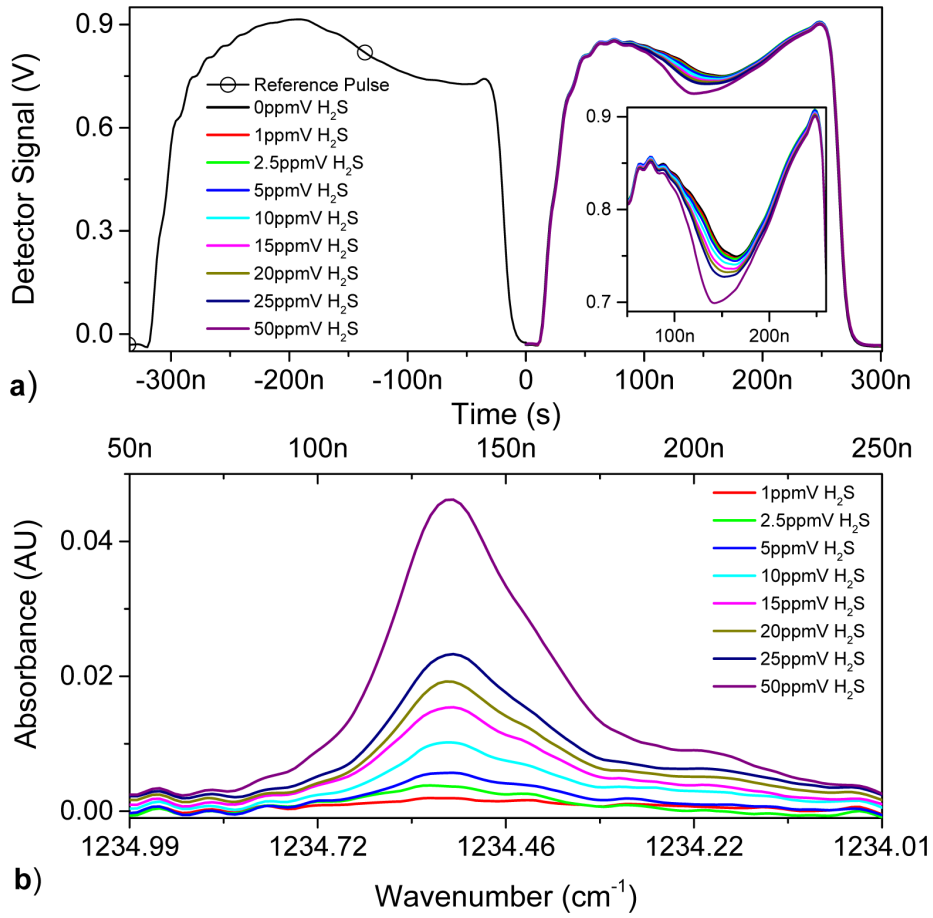


Fig. 9. (a) Short 300ns pulses with different H₂S concentrations; (b) Resulting absorption spectra from intra-pulse transmission signals.

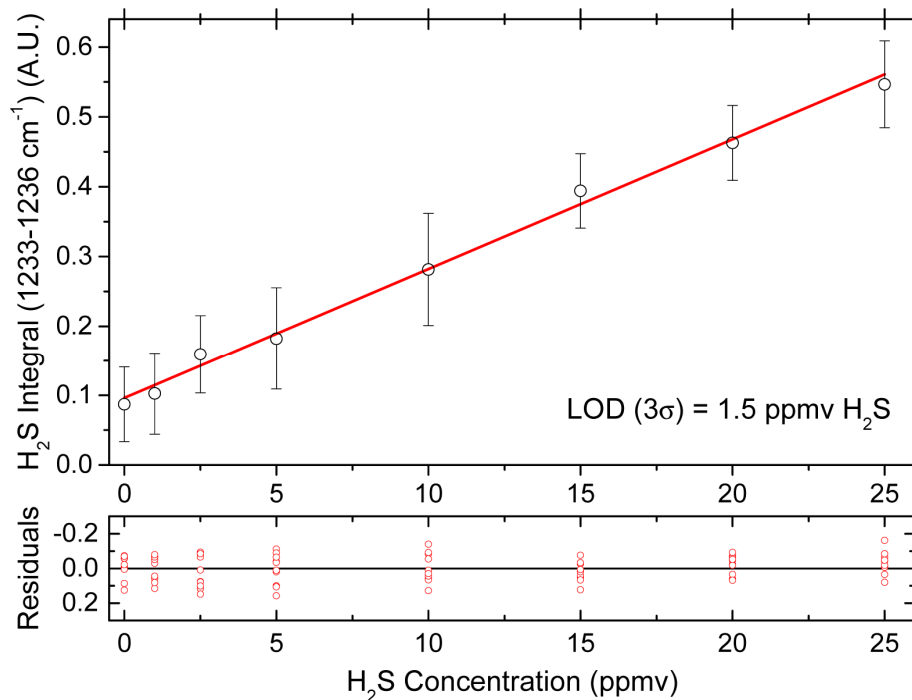


Fig. 10. Calibration curve of 0-25 ppmv H₂S. The calculated LOD was ~1.5 ppmv.

5. Conclusions

The presented work showed the applicability of pulsed ring cavity surface emitting quantum cascade lasers (RCSE QCL) for gas measurements for the first time. Pulse length between 200 ns and 3 μs as well as pulse currents ranging from 400 to 700 mA were applied covering spectral bandwidths up to 8.5 cm⁻¹, as revealed by step-scan FT-IR spectrometry. The ring-type cavity allows single-mode and mode-hop-free emission. Gas measurements were conducted in a 100 m astigmatic Herriott cell. When applying short pulses (200-300 ns) and using a beam splitter it was possible to measure a background and sample spectrum with a single thermoelectrically cooled MCT detector from a single laser pulse. The investigated target analyte was hydrogen sulfide (H₂S), present either in pure nitrogen or in nitrogen containing methane (CH₄) as possible interferent. With the developed set-up a LOD (3σ) of 1.5 ppmv for H₂S could be obtained by evaluating the corresponding transitions in the spectral region from 1234.4 to 1234.7 cm⁻¹. Planned research will benefit from the flexibility in the design of RCSE QCLs. Construction of multiple rings either side by side or in a centered configuration will allow for a further extended spectral coverage. Also integration of resonant cavities and detectors in one device is possible opening the path for highly miniaturized, sensitive gas sensors for detecting multiple gas molecules.

Acknowledgment

The authors acknowledge the Austrian Research Promotion Agency (FFG) within the K-project imPACTs (contract no. 843546) for funding.

Publication IV

On-line monitoring of methanol and methyl formate in the exhaust gas of an industrial formaldehyde production plant by a mid-IR gas sensor based on tunable Fabry-Pérot filter technology

Authors: Andreas Genner, Christoph Gasser, Harald Moser, Johannes Ofner, Josef Schreiber and Bernhard Lendl



Die approbierte gedruckte Originalversion dieser Dissertation ist an der TU Wien Bibliothek verfügbar.
The approved original version of this doctoral thesis is available in print at TU Wien Bibliothek.

On-line monitoring of methanol and methyl formate in the exhaust gas of an industrial formaldehyde production plant by a mid-IR gas sensor based on tunable Fabry-Pérot filter technology

Andreas Genner¹ · Christoph Gasser¹ · Harald Moser¹ · Johannes Ofner¹ · Josef Schreiber² · Bernhard Lendl¹

Received: 26 July 2016 / Revised: 10 October 2016 / Accepted: 18 October 2016 / Published online: 9 November 2016
© The Author(s) 2016. This article is published with open access at Springerlink.com

Abstract On-line monitoring of key chemicals in an industrial production plant ensures economic operation, guarantees the desired product quality, and provides additional in-depth information on the involved chemical processes. For that purpose, rapid, rugged, and flexible measurement systems at reasonable cost are required. Here, we present the application of a flexible mid-IR filterometer for industrial gas sensing. The developed prototype consists of a modulated thermal infrared source, a temperature-controlled gas cell for absorption measurement and an integrated device consisting of a Fabry-Pérot interferometer and a pyroelectric mid-IR detector. The prototype was calibrated in the research laboratory at TU Wien for measuring methanol and methyl formate in the concentration ranges from 660 to 4390 and 747 to 4610 ppmV. Subsequently, the prototype was transferred and installed at the project partner Metadynea Austria GmbH and linked to their Process Control System via a dedicated micro-controller and used for on-line monitoring of the process off-gas. Up to five process streams were sequentially monitored in a fully automated manner. The obtained readings for methanol and methyl formate concentrations provided useful information on the efficiency and correct functioning of the process plant. Of special interest for industry is the now added capability to

monitor the start-up phase and process irregularities with high time resolution (5 s).

Keywords Formaldehyde production · Fabry-Pérot detector · Mid-infrared · Process analytical chemistry · Methyl formate · Methanol

Introduction

In process analytical chemistry (PAC), there is clear focus on providing dedicated solutions to a given measurement problem. In this regard, emphasis is put on different parameters/features with respect to laboratory equipment. Depending on the installation, in PAC, a number of requirements have to be met. This can involve robustness against environmental conditions (e.g., humidity, vibration, chemical substances in the air), a simple user interface (soft- and hardware), avoiding sample preparation, autonomous operation, and the possibility to forward the gained measurement data to a control center (e.g., Modbus, OPC, 4–20 mA signal [1, 2]). Over the time, many analytical techniques were adopted, optimized, and successfully integrated in industrial processes. The range of different instrumental techniques that were brought on-line includes not only a broad variety of measurement principles such as conductivity-, pH-, and particle-sensors but also highly optimized gas chromatography systems, advanced mass spectrometers, and alike [3, 4]. However, if possible, simple and rugged, sensor-like solutions are the preferred way for efficient on-line monitoring with high time resolution.

A well suited measurement principle for analyzing process streams in the gas phase is infrared spectroscopy. Almost every gaseous analyte (except noble gases and homonuclear diatomic molecules) absorbs radiation in the mid-infrared

Published in the topical collection *Process Analytics in Science and Industry* with guest editor Rudolf W. Kessler.

✉ Bernhard Lendl
bernhard.lendl@tuwien.ac.at

¹ Institute of Chemical Technologies and Analytics, TU Wien, Getreidemarkt 9/164, 1060 Vienna, Austria

² Metadynea Austria GmbH, Hafentrasse 77, 3500 Krems an der Donau, Austria

region (4000–400 cm^{-1}) and both, quantitative and qualitative, measurements are possible. Moreover, different instrumental realizations of mid-IR spectroscopy were developed over time, allowing customers to select the best suiting instrument [5].

Until today, the most generic and thus flexible technology for mid-IR-based gas measurements are Fourier transform infrared (FTIR) spectrometers [6]. Usually, they cover the whole mid-IR range and are capable of recording a full spectrum of the sample. The spectral resolution is typically 1–4 wavenumbers, but it can be reduced if a higher measurement frequency is required. Depending on the analytical problem to be solved either simple integration of characteristic absorption bands or application of chemometric approaches are the preferred modes of data analysis. Concerning applicability in the chemical industry, FTIR spectrometers are available from many different suppliers and in use for in-line as well as on-line monitoring of process gases. The downsides of this technology are, for example, high cost, limited temporal resolution, and, in some cases, the need for especially trained employees, especially when it comes to maintaining multivariate calibration models.

Another group of mid-IR-based analyzers make use of recent advances in laser technology in particular of quantum cascade lasers (QCLs) or intra-cavity lasers (ICLs) [7]. Using these lasers as light sources, concentrations down to the ppb-ppt concentration can be measured at high speed [8–10]. Moreover, it is possible to avoid moving parts, allowing the design of robust and compact instruments. However, their multi-analyte capabilities are still restricted due to the limited tuning range of the corresponding lasers ([11, 12]). An important current disadvantages of these mid-IR laser-based analyzers is their rather high cost.

Alternatively, filter-based mid-IR analyzers are a different, well-established group of mid-IR-based sensors that is characterized by less analytical power but with the advantage of low cost compared to FTIR-based analyzers. Here, a filter transmits infrared radiation only in the region where the analyte of interest is absorbing. These transmission windows can be rather wide ($>20 \text{ cm}^{-1}$ [13]) and cannot compete with the resolution of FTIR spectrometers. Therefore, they are only suited for rather simple applications such as quantifying CO_2 , CO, or ethylene in air [14–17]. In filter-based gas sensors, both absorption measurements based on Beers law as well as photoacoustic measurements have been realized so far.

If several analytes have to be quantified with the same analyzer, multiple filters with distinct transmission windows are needed. In the past, this was realized by mounting filters on a rotating filter wheel. However, the number of installable filters is generally limited, reducing somehow the possibility to fine tune across a certain spectral region as well as to select varying spectral segments with one and the same instrument.

Sensors which employ the gas filter correlation spectroscopy as measurement principle are closely related to the previously mentioned filter-based systems. Hereby, a gas cell filled with the analyte to be measured acts as the optical filter and generates the reference measurement [18, 19]. This technology is not limited to the infrared region ([20]) and typical analytes are CO, CO_2 , and SO_2 .

An approach for realizing filters is to use a Fabry-Pérot interferometer. Its basic principle is that two parallel and reflective surfaces allow only certain wavelengths to transmit. The transmitted wavelength segment depends on the distance between the reflecting mirrors (d), their reflectivity (R), and the interference order (m). The mathematical relation is as follows [21]:

$$\text{FWHM}_\lambda = \frac{2d}{\pi m^2} \frac{(1-R)}{\sqrt{R}}$$

Based on this technique, full widths at half height of typically 10–20 cm^{-1} can be achieved.

There are different ways how such FP filters have been implemented in process analyzers so far. FP filters with varying but mechanically fixed distances between the mirrors can be found in circular and linear variable filters [22]. Here, the first method is typically integrated in the respective instrument like a filter wheel, thus requiring a single detector, whereas instruments employing linear variable filters also contain a detector array. In these systems, the optical configuration is such that each detector element is irradiated by a different wavelength segment.

Applying microelectromechanical systems (MEMS) made it possible to develop Fabry-Pérot (FP) interferometers with variable distance between the reflective mirrors. Commercial available detectors employ either piezos (e.g., VTT Technical Research Centre of Finland Ltd. [23]) or mechanical springs (InfraTec GmbH) in combination with an electrical field to establish a certain distance between the mirrors and thus to select a certain wavelength segment. Realization of tunable FP filters using MEMS components allowed downsizing of this functional element. A sensor consisting of a tunable FP filter, a pyroelectric detector and corresponding preamplifier electronics can thus fit in a TO-8 can. Nevertheless, a broadband filter still must be installed to suppress the transmission of harmonics. A basic scheme of such a FP filter-based detector element is illustrated in Fig. 1. A detailed mathematical description of its operation basics is available in [21, 24–26].

Production of formaldehyde

The measurement device presented in this paper was developed to monitor the concentration of side products from chemical reaction plants producing formaldehyde (FA). The

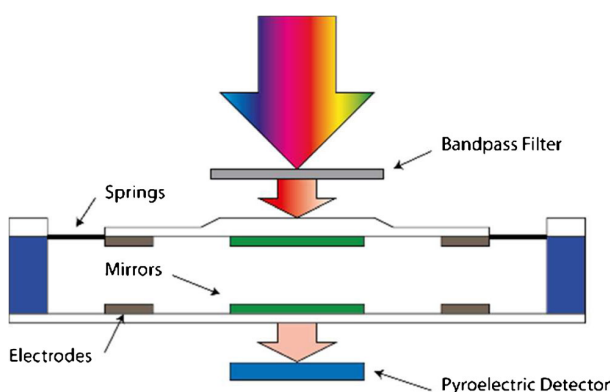
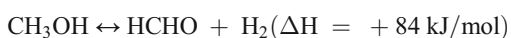
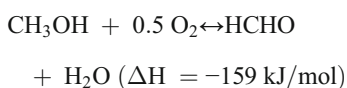


Fig. 1 Scheme of a Fabry-Pérot filter-based detector

underlying catalytic chemical reaction is the partial oxidation of methanol, leading to primarily formaldehyde. Two major processes which differ in the employed catalyst types are used to produce FA on an industrial scale. The first one, which is also known as Formox process, uses metal oxides (e.g., vanadium, molybdenum, or iron oxide) and is operated in the temperature region of 270–400 °C. The other one, which is also used at the investigated production plants of this study, is based on silver crystals and operated at significantly higher temperatures (600–720 °C) [27–30]. The formation of FA can be written as follows:

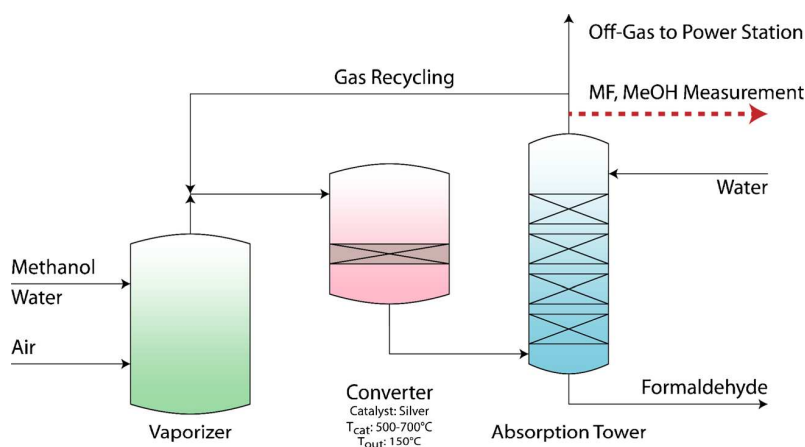


And with oxidation of the hydrogen:



After the catalytic reaction, the product stream is cooled down to approximately 150 °C and washed in counter flow with H₂O in an absorption column (a simplified scheme is given in Fig. 2).

Fig. 2 Simplified scheme of the FA production process based on the silver catalyst. The side product methyl formate (MF) and traces of not converted MeOH are quantified at the top of the absorption tower, indicated with a red arrow [31, 32]



The main part of the off-gas consists of CO₂, CO, and H₂, which are already monitored at Metadynea Austria GmbH with commercial available devices. However, also low concentrations of methanol (MeOH) and methyl formate (MF) (both <5000 ppm) and traces of not absorbed FA (<50 ppm) can be detected. While MeOH originates from not converted reactant, MF is created by a side reaction on the silver catalyst. Investigations with deuterated methanol [33], performed at lower temperatures than in commercial processes, propose the mechanism shown in Fig. 3 (Tischenko mechanism).

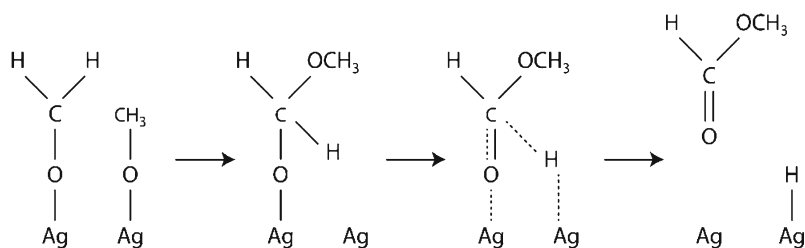
However, Wachs and Madix mention that no MF is found in industrial processes. They argue that the catalyst temperature (>600 °C) would be too high to enable a long enough surface residence time of FA on the silver catalyst to react to MF.

The task of the newly developed mid-IR-based gas sensor is quantification of MeOH and MF in the process off-gas with high time resolution (5 s.). The sensor was developed and implemented with the vision to enable accurate monitoring of the chemical status of the process and therefore to open the possibility for a more economic operation of the FA production plants.

Experimental setup

The installed mid-IR source is a JSIR350-4-AL-R-D6.0-0-0 (Micro Hybrid Electronic GmbH), which is a highly efficient blackbody emitter [34] and produced by applying MEMS processes. It is basically an electrical resistor which heats up when a voltage is applied. Due to its compact design and low thermal mass, amplitude modulation of the emitted radiation up in the hundred Hz region can be achieved. This allows to omit chopper wheels or other modulation techniques usually required by the need of the employed cost-effective pyroelectric detector. For this application, the applied voltage was 5 V and the modulation frequency was set to 3.5 Hz (duty cycle, 50 %) to achieve an optimum detector responsivity.

Fig. 3 Reaction mechanism for the formation of methyl formate as proposed by Wachs and Madix



A ZnSe lens ($f=50$ mm, ThorLabs Inc.) collimates the beam and a flat gold mirror reflects the radiation to a custom built gas cell. Its optical length is 30 cm and its steel body is heated up to 45 °C to avoid possible condensation from the humid off-gas on the cell walls. The limited space requires an additional reflection of the beam from a second plane mirror before it is focused (ZnSe, $f=50$ mm) onto the detector.

The central component of the measurement device is the tunable Fabry-Pérot (FP) filter-detector LFP-80105-337 (InfraTec GmbH) [35]. By applying a control voltage ($V_{\text{range}}=0-70$ V), the filter can be tuned through the region of 1250-950 cm^{-1} , where two vibrational transitions of MF and MeOH can be found (Fig. 5). These bands (MF: CH_3 rocking [36] at ~ 1190 cm^{-1} and MeOH: C-O str. [37] at ~ 1040 cm^{-1}) are spectrally separated well enough for the tunable filter to resolve the bands, although the low spectral resolution of the tunable FP of approximately 10 cm^{-1} (Fig. 4).

As the mid-IR source is modulated, the detector signal has to be demodulated with an in-house developed Lock-In-Amplifier. The resulting signal is digitized with an analog digital converter (ADC, ADS1115, 16 bit, Texas Instruments Inc.) and a microcontroller (ATmega328P, Atmel Corporation) averages 100 measurement points to improve the signal to noise ratio. As the measurement principle is based on the absorption of light, one can

apply the Beer-Lambert Law and calculate the concentration according to

$$A(\lambda) = \log\left(\frac{I_{\lambda}^0}{I_{\lambda}}\right) = \varepsilon(\lambda)cl$$

where $A(\lambda)$ is the absorbance, I_{λ}^0 is the intensity recorded from a reference measurement at a certain wavelength segment, I_{λ} is the intensity recorded from of the sample channel at a certain wavelength segment, $\varepsilon(\lambda)$ is the observed decadic molar absorption coefficient at that wavelength segment, c is the concentration of the analyte, and l is the pathlength.

In order to calculate absorbance and the concentration of the target analyte, one needs to know values for I_{λ} and I_{λ}^0 . Here, the reference value I_{λ}^0 is gained by flushing the gas cell with the IR inactive gas N_2 . This reference measurement, which is also helpful to compensate for long term drifts, is initiated by the microcontroller and performed every 2 h 45 min. The concentrations of the two target analytes have to be quantified consecutively which requires adjusting the filter position periodically. Therefore, a digital to analog converter (DAC, MCP4725, 12 bit, Microchip Technology Inc.) is installed and sets the control voltage of the FP filter-detector.

The concentrations are determined by applying a calibration curve and proportional voltage signals for each analyte are output on additional DACs (2xMCP4725). These analog

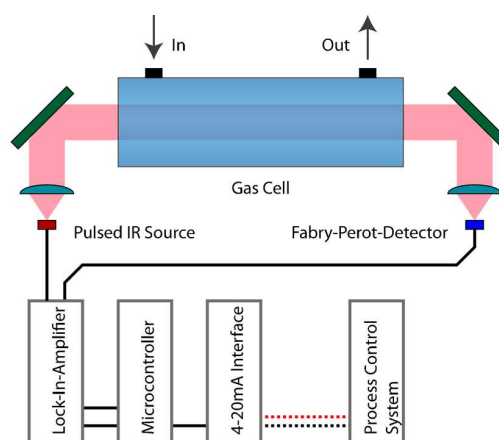


Fig. 4 *Left*: front side of the developed sensor (19" rack compatible); *right*: schematic assembly of the optical and electrical parts

signals are connected to two 4–20 mA converters (PXU-20.924/RS, Brodersen Controls A/S) to meet the requirements of the process control system (PCS) at Metadynea Austria GmbH. The 4–20 mA interface is the preferred way to monitor the concentration of the analytes of interest. However, an LCD display (HD44780, Adafruit Industries LLC) is also installed at the front panel of the sensor to check the functionality. An additional single-board-computer (Raspberry Pi 2 Model B, Raspberry Pi Foundation) and a mobile broadband modem (E3531, Huawei Co. Ltd.) allows remote monitoring and firmware upgrades of the microcontroller.

Experimental

Recording spectra of the analytes and calibration curves

Due to the conditions of the gas stream the prototype has to quantify MF and MeOH in the gas phase. At normal temperature and pressure, the analytes of interest are liquids with a significant vapor pressure (MeOH, 13.02 kPa; MF, 63.46 kPa). In order to characterize the device performance and to record calibration curves, gaseous reference samples with similar concentrations as to be expected at the intended application site had to be prepared in the laboratory. The physical properties of MF and MeOH make it difficult to prepare stable calibration gas mixtures of accurately known composition by means of static methods [38]. In addition, static calibration gas mixtures of the readily condensable gases and vapors of MF and MeOH cannot be maintained under a pressure near the saturation limit without the occurrence of condensation. Therefore, the saturation method according to ISO 6145-9:2009 was employed for preparing calibration mixtures of the analytes [39]. Following this standard a saturated gas stream is produced, where the concentration of the desired component can be calculated using pressure and temperature readings logged during the experiments. The resulting saturated gas

stream was then further diluted to the appropriate concentration with N_2 by employing mass flow controllers (MFCs, red-smart, Vögtlin Instruments AG) and a static mixer. Finally, the sample stream was fed into the developed prototype.

Reference spectra of MeOH and MF were recorded with the prototype to establish calibration curves. To do so, the control voltage of the FP filter was increased to get one data point every 10 cm^{-1} . This led to 31 points per spectrum, taking 2 min.

Online measurements

Operating the prototype at Metadynea Austria GmbH involved a modification of the microcontroller firmware, compared to the reference measurements in the academic laboratory. Instead of recording full spectra with 31 data points, only two filter positions were selected. These were selected at the maximum absorption of the analytes and resulted in one concentration value for MF and MeOH every 5 s.

Multiple FA productions plants are located at the production site. As only one plant can be monitored at a time, the process control system switches the exhaust gas to the prototype automatically. It is intended to analyze each plant at least once per working shift. The result is that in normal operation mode, each plant is monitored for 1–2 h, depending on the number of active plants. This automatic gas stream cycle is overwritten if the plant operators modify process parameters or restart individual production plants.

Results

Spectra of analytes

Two typical spectra of MF and MeOH recorded with the prototype are compared with reference spectra from the PNNL database [40] and shown in Fig. 5a. One can clearly see that the resolution obtained with the FP-interferometer-based

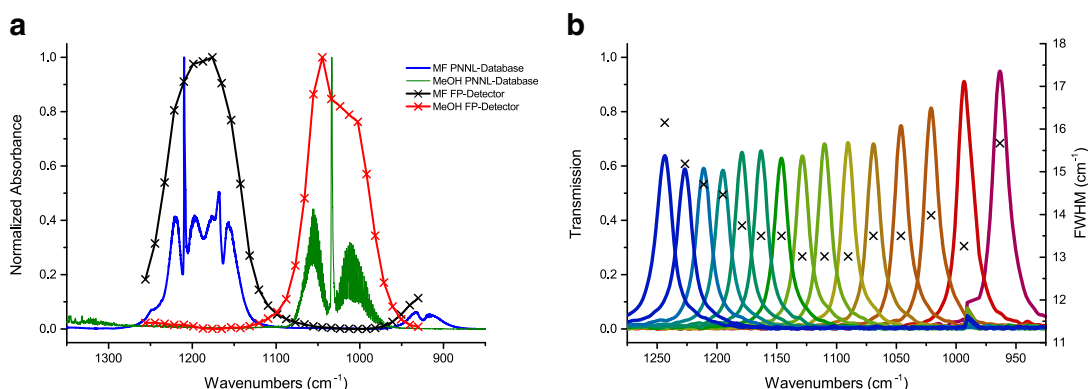


Fig. 5 a Comparison of reference spectra (PNNL) and spectra recorded with the FP-detector. All spectra were normalized to a maximum absorbance of one. b Transmission behavior and FWHM of the Fabry-Pérot filter at different control voltages

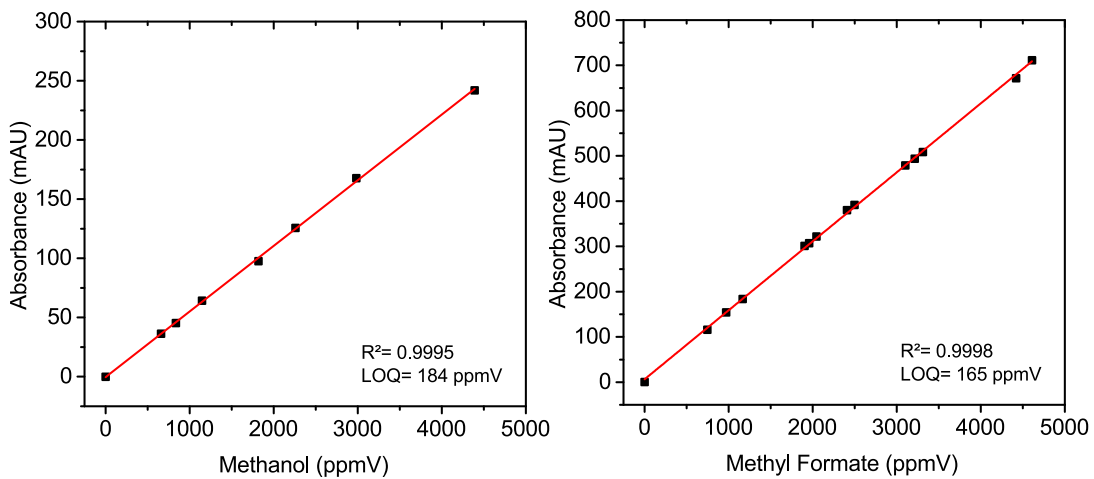


Fig. 6 Calibration curves for MeOH and methyl formate, recorded at wavelength segments centered at 1010 and 1160 cm^{-1}

instrument cannot compete with an FTIR spectrometer. Nevertheless, the absorption bands of the analytes are sufficiently isolated which allows the application of the developed instrument.

Calibration curves

Calibration samples were prepared with the gas mixing rig and spectra were acquired with the prototype. Due to the fact that

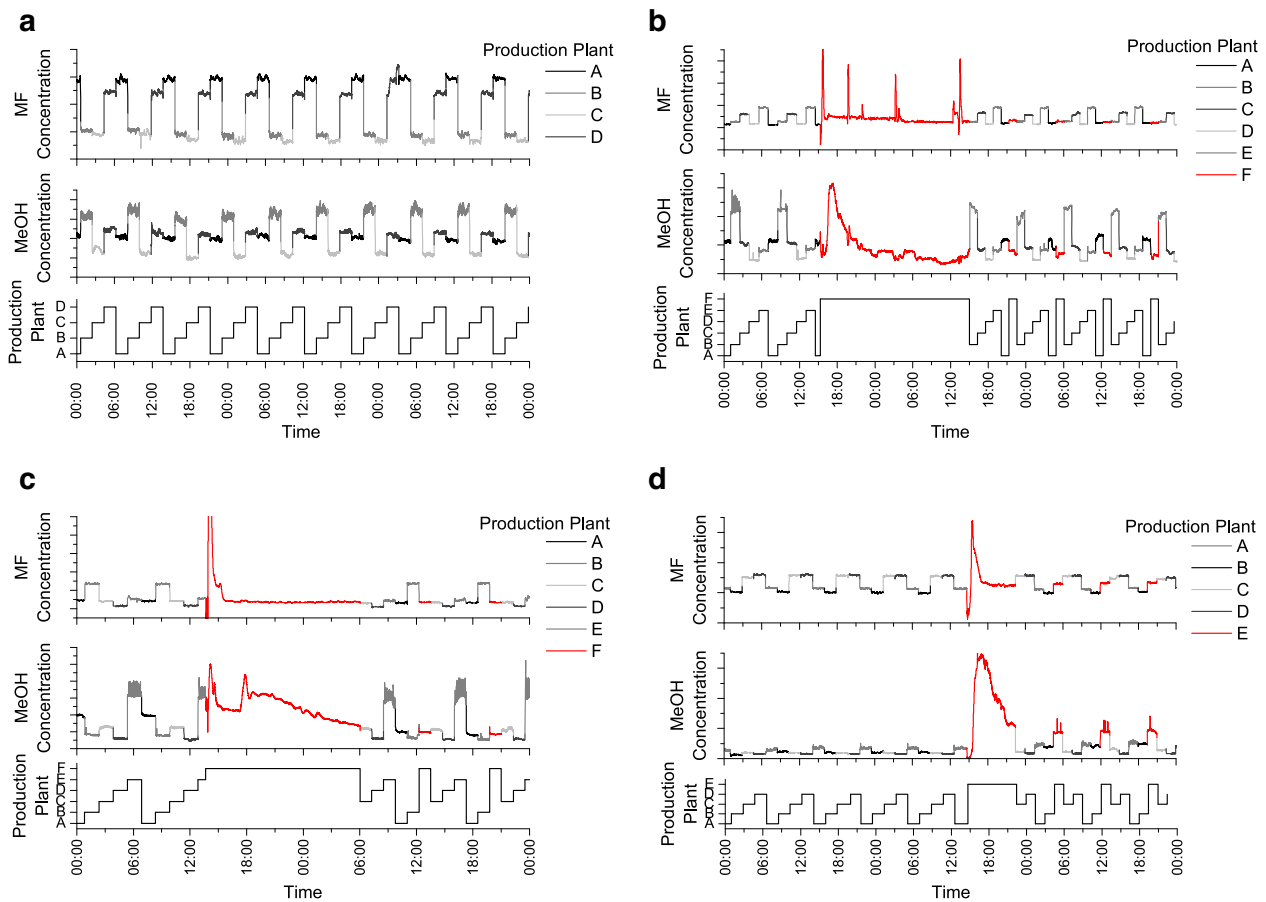
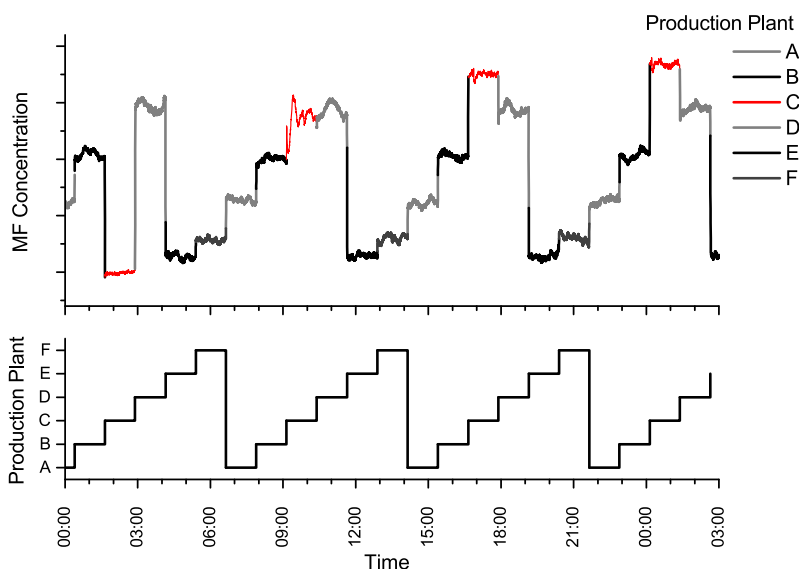


Fig. 7 a Methyl formate (MF) and MeOH concentration during 3 days at normal operation. b-d Retrieved concentration levels while starting an additional production plant (new plant indicated as red sections)

Fig. 8 Redirecting the exhaust gas to the converter causes an increase of MF as the catalyst temperature decreases



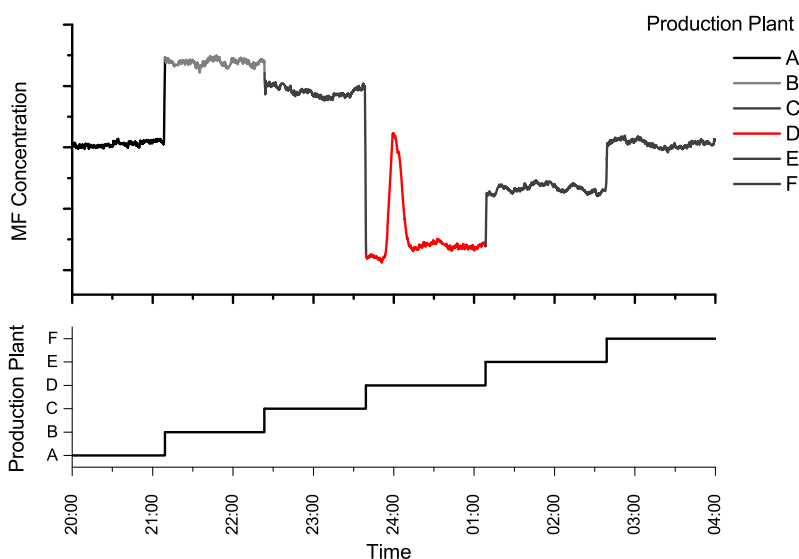
only a single point in the spectrum is used for each analyte during operation at the production plants, wavelength segments with maxima at 1010 cm^{-1} for MeOH and 1160 cm^{-1} for MF were selected as spectral positions to establish the corresponding calibration curves. No significant cross sensitivities were found in the concentration ranges of practical interest.

The resulting calibration curves are plotted in Fig. 6, with achieved limits of quantification of 184 ppmV for MeOH and 165 ppmV for MF.

Experiments at the production plants

Results from online-measurements at Metadynea Austria GmbH are depicted in the following figures. The exemplary data is

Fig. 9 A short increase of the MF concentration due to a short change of catalyst temperature



typically plotted over several hours/several days. Due to company regulations absolute values, such as concentration values and production plant IDs (which also change during different experiments) and further additional plant parameters (catalyst temperature, etc.) may not be disclosed.

If the production parameters are constant, the data recorded from the PCS is as shown in Fig. 7a. Here, the periodical switching (approx. every 2 h) between four production plants initiated by the PCS can be observed. The constant production settings lead to almost stable MF and MeOH concentrations during 3 days of operation.

The FA production has to be stopped and restarted at certain intervals. The reasons for that are, for example, degradation of the catalyst caused by sintering effects [27] or test runs for other process optimization experiments. Three examples, where

production plants have been restarted, are shown in Fig. 7b–d. During these processes, the automatic switching cycle was deactivated, to gain specific information on the selected reactor during these experiments. According to Wachs and Madix [33], MF can be produced on the silver catalyst at lower temperatures, which is the case when the FA production is started. Reaching the optimum production parameters also leads to a stable and relatively low MF concentration. The MeOH concentration does not stabilize as fast as MF which is very likely caused by its longer retention time in the absorption tower as a consequence of the higher water solubility of MeOH.

A different experiment is shown in Fig. 8. Here, the exhaust-gas was redirected to the converter, leading to a decrease in temperature at the catalyst and an increase of MF at the measurement position. In this case, the automatic switching cycle was not deactivated and the new MF concentration was not accessible until the next repetition.

Another example of the applicability of the developed process analyzer is shown in Fig. 9. An unexpected change of the catalyst temperature resulted in a quick increase of MF. The production parameters were reset within 15 min and the MF concentration stabilized immediately.

Conclusion

A cost-efficient prototype of a process analyzer for on-line monitoring of MF and MeOH in the gas phase of a formaldehyde production plant was developed and implemented. Key components of the developed dedicated process spectrometer were an electrically modulated thermal IR source, a combined Fabry-Pérot interferometer-detector device and a microcontroller for automated measurements. A custom developed gas mixing rig allowed recording reference spectra and calibration curves of the analytes of interest. The achievable limits of quantification were 184 and 165 ppmV for MeOH and MF, respectively. The applicability of the prototype was shown at the production plants of Metadynea Austria GmbH. It provided valuable data on the time-dependent changes of the concentrations of the targeted process gases. After an initial installation phase, it is now considered as a valuable tool for monitoring the production plants and for providing in-depth information on the production process under investigation.

Acknowledgments Open access funding provided by TU Wien (TUW). We would like to thank the employees of our project partner Metadynea Austria GmbH for enabling the cooperation and the access to the production plants. Moreover, we would like to acknowledge the work of Wolfgang Tomischko, for designing the analog electronics and the Lock-In-Amplifier.

Financial support was provided by the Austrian research funding association (FFG) under the scope of the COMET program within the research project “Industrial Methods for Process Analytical Chemistry – From Measurement Technologies to Information Systems (imPACTs)”

(contract # 843546). This program is promoted by BMVIT, BMWF, the federal state of Upper Austria, and the federal state of Lower Austria.

Compliance with Ethical Standards This paper does not contain any studies with human participants or animals performed by any of the authors.

Conflict of Interest The authors declare that they have no conflict of interest.

Open Access This article is distributed under the terms of the Creative Commons Attribution 4.0 International License (<http://creativecommons.org/licenses/by/4.0/>), which permits unrestricted use, distribution, and reproduction in any medium, provided you give appropriate credit to the original author(s) and the source, provide a link to the Creative Commons license, and indicate if changes were made.

References

- Berrie PG, Gut B, Lindner K-P. Fieldbuses and network protocols. In: Liptak BG, editor. Instrument engineers handbook—process control and optimization. 4th ed. Taylor & Francis Group; 2005. p. 770–789.
- Shimanuki Y. OLE for Process Control (OPC) for new industrial automation systems. IEEE SMC'99 Conf. Proceedings. 1999 I.E. Int. Conf. Syst. Man, Cybern. (Cat. No.99CH37028), vol. 6, pp. 1048–1050; 1999.
- Baakev KA. Process analytical technology. 2nd ed. Oxford: John Wiley & Sons Ltd.; 2010.
- Liptak BG. Process measurement and analysis. 4th ed., vol. 788. CRC Press; 2003.
- Hodgkinson J, Tatam RP. Optical gas sensing: a review. Meas Sci Technol. 2013;24(1):12004.
- Griffiths P, de Haseth JA. Fourier transform infrared spectrometry. 2nd ed. John Wiley & Sons Ltd.; 2007.
- Faist J, Capasso F, Sivco DL, Sirtori C, Hutchinson AL, Cho AY. Quantum cascade laser. Science. 1994;264:553–6 (80-).
- Nelson DD, Shorter JH, McManus JB, Zahniser MS. Sub-part-per-billion detection of nitric oxide in air using a thermoelectrically cooled mid-infrared quantum cascade laser spectrometer. Appl Phys B Lasers Opt. 2002;75(2–3):343–50.
- Curl RF, Capasso F, Gmachl C, Kosterev AA, McManus B, Lewicki R, et al. Quantum cascade lasers in chemical physics. Chem Phys Lett. 2010;487(1–3):1–18.
- Tittel FK, Lewicki R, Lascola R, McWhorte S. Emerging infrared laser absorption spectroscopic techniques for gas analysis. In: Geiger WM, Raynor MW, editors. Trace analysis of specialty and electronic gases. Hoboken: Wiley; 2013. p. 71–110.
- Luo GP, Peng C, Le HQ, Pei SS, Hwang WY, Ishaug B, et al. Grating-tuned external-cavity quantum-cascade semiconductor lasers. Appl Phys Lett. 2001;78(19):2834–6.
- Faist J, Gmachl C, Capasso F, Sirtori C, Sivco DL, Baillargeon JN, et al. Distributed feedback quantum cascade lasers. Appl Phys Lett. 1997;70(20):2670–2.
- InfraTec, “InfraTec - Typical Filter Plots.” [Online]. Available: <http://www.infrotec.de/fileadmin/media/Sensorik/pdf/IRFilter-Typical-Plots.pdf>.
- Hodgkinson J, Smith R, Ho WO, Saffell JR, Tatam RP. Non-dispersive infra-red (NDIR) measurement of carbon dioxide at 4.2 μm in a compact and optically efficient sensor. Sensors Actuators B Chem. 2013;186:580–8.

15. Barritault P, Brun M, Lartigue O, Willemin J, Ouvrier-Bufferet JL, Pocas S, et al. Low power CO₂ NDIR sensing using a microbolometer detector and a micro-hotplate IR-source. *Sensors Actuators B Chem.* 2013;182:565–70.
16. Frodl R, Tille T. A high-precision NDIR CO₂ gas sensor for automotive applications. *IEEE Sensors J.* 2006;6(6):1697–705.
17. Hildenbrand J, Wöllenstein J, Hartwig S, Eberhardt A, Halford B, Moreno M, et al. A compact optical multichannel system for ethylene monitoring. *Microsyst Technol.* 2008;14(4–5):637–44.
18. Dakin JP, Gunning MJ, Chambers P, Xin ZJ. Detection of gases by correlation spectroscopy. *Sensors Actuators B Chem.* 2003;90(1–3):124–31.
19. Dickerson RR, Delany AC. Modification of a commercial gas filter correlation CO detector for enhanced sensitivity. *J Atmos Ocean Technol.* 1988;5:424–31.
20. Lou XT, Somesfalean G, Zhang ZG, Svanberg S. Sulfur dioxide measurements using an ultraviolet light-emitting diode in combination with gas correlation techniques. *Appl Phys B.* 2009;94(4):699–704.
21. Ebermann M, Neumann N, Hiller K, Gittler E, Meinig M, Kurth S. Recent advances in expanding the spectral range of MEMS Fabry-Perot filters. *Proc. SPIE 7594, MOEMS Miniaturized Syst. IX;* 2010.
22. Ghaderi M, Ayerden NP, Emadi A, Enoksson P, Correia JH, de Graaf G, et al. Design, fabrication and characterization of infrared LVOFs for measuring gas composition. *J. Micromechanics Microengineering.* 2014; 24 Suppl 8.
23. Kantojärvi U, Varpula A, Antila T, Holmlund C, Mäkynen J, Näsilä A, et al. Compact large-aperture Fabry-Perot interferometer modules for gas spectroscopy at mid-IR. *SPIE Photonics West 2014-OPTO Optoelectron. Devices Mater., vol. 8992, p. 89920C;* 2014.
24. Rossberg D. Silicon micromachined infrared sensor with tunable wavelength selectivity for application in infrared spectroscopy. *Sensors Actuators A Phys.* 1995;47(1–3):413–6.
25. Neumann N, Ebermann M, Kurth S, Hiller K. Tunable infrared detector with integrated micromachined Fabry-Perot filter. *J Micro/Nanolithogr MEMS MOEMS.* 2008;7(2):21004-1–9.
26. Schuler LP, Milne JS, Dell JM, Faraone L. MEMS-based microspectrometer technologies for NIR and MIR wavelengths. *J Phys D Appl Phys.* 2009; 42.
27. Reuss G, Disteldorf W, Gamer AO, Hilt A. Formaldehyde. *Ullmann's Encycl. Industrial Chem., vol. 15, pp. 735–768;* 2012.
28. Weissermel K, Arpe H-J. *Industrial organic chemistry.* 3rd ed. VCH; 1997.
29. Lefferts L, An Ommen JG, Ross JRH. The oxidative dehydrogenation of methanol to formaldehyde over silver catalysts in relation to the oxygen-silver interaction. *Appl Catal.* 1986;23(2):385–402.
30. Yang Z, Li J, Yang X, Wu Y. Catalytic oxidation of methanol to methyl formate over silver—a new purpose of a traditional catalysis system. *Catal Lett.* 2005;100(3–4):205–11.
31. Dynea.com, Silver Catalysed Formaldehyde Plant. 2016. [Online]. Available: <http://www.dynea.com/technology-sales/silver-catalysed-formaldehyde-plant/>.
32. Bahmanpour AM, Hoadley A, Tanksale A. Critical review and exergy analysis of formaldehyde production processes. *Rev Chem Eng.* 2014;30(6):583–604.
33. Wachs IE, Madix RJ. The oxidation of methanol on a silver (110) catalyst. *Surf Sci.* 1978;76(2):531–58.
34. Micro-Hybrid, Infrared Radiation Source JSIR350-4-AL-R-D6.0-0-0. 2013. [Online]. Available: <http://www.micro-hybrid.de/fileadmin/user/IR-systems-documents/Datenblaetter/Strahler/JSIR350-4-AL-R-D6.0-0-0.pdf>.
35. InfraTec, LFP-80105-337. [Online]. Available: <http://www.infratec.de/fileadmin/media/Sensorik/pdf/LFP-80105-337.pdf>.
36. Wilmshurst JK. A vibrational assignment for methyl formate and methyl acetate. *J Mol Spectrosc.* 1957;1:201–15.
37. Larkin PJ. *IR and Raman spectroscopy—principles and spectral interpretation.* Elsevier; 2011.
38. Pratzler S, Knopf D, Ulbig P, Scholl S, Ulbig P, Scholl S. Preparation of calibration gas mixtures for the measurement of breath alcohol concentration. *J Breath Res.* 2010;4(3):36004.
39. Norm D. ISO6145-9 Herstellung von Kalibriergasgemischen (Sättigungsverfahren). 2010.
40. Sharpe SW, Johnson TJ, James RL, Chu PM, Rhoderick GC, Johnson PA. Gas phase database for quantitative infrared spectroscopy. *Appl Spectrosc.* 2004;58(12):1452–61.



Die approbierte gedruckte Originalversion dieser Dissertation ist an der TU Wien Bibliothek verfügbar.
The approved original version of this doctoral thesis is available in print at TU Wien Bibliothek.

Publication V

Application of a tunable Fabry-Pérot filter to mid-infrared gas sensing

Authors: Christoph Gasser, Andreas Genner, Harald Moser, Johannes Ofner and Bernhard Lendl



Die approbierte gedruckte Originalversion dieser Dissertation ist an der TU Wien Bibliothek verfügbar.
The approved original version of this doctoral thesis is available in print at TU Wien Bibliothek.



ELSEVIER

Contents lists available at ScienceDirect

Sensors and Actuators B: Chemical

journal homepage: www.elsevier.com/locate/snb

Application of a tunable Fabry-Pérot filterometer to mid-infrared gas sensing

Christoph Gasser*, Andreas Genner, Harald Moser, Johannes Ofner, Bernhard Lendl

Institute of Chemical Technologies and Analytics, TU Wien, Vienna, Austria

ARTICLE INFO

Article history:

Received 3 July 2016

Received in revised form 3 October 2016

Accepted 3 November 2016

Available online 5 November 2016

Keywords:

Infrared spectroscopy

Gas monitoring

Fabry-Perot interferometer

Multivariate analysis

Process analytical chemistry

ABSTRACT

The design and application of a versatile, tunable filterometer based on a Fabry-Pérot (FP) tunable filter – detector, covering the spectral range from 1250 to 1850 cm^{-1} at a spectral resolution of approximately 30 cm^{-1} , is presented. The tunable filter was characterized and calibrated using a FTIR spectrometer. Gas mixtures comprising iso-butane, 1-butene, 1,3-butadiene were prepared and measured. The obtained gas spectra were validated by FTIR measurements. Quantitative analysis based on the whole tuning range of the filterometer and employing partial least squares (PLS) calibration revealed fully satisfactory results with root mean square error of prediction (RMSEP) of 0.03, 0.04 and 0.26% for iso-butane, 1-butene and 1,3-butadiene respectively. As the tunable FP filterometer also allows measurements at pre-selected spectral windows a calibration based on multiple linear regression (MLR) was performed as well obtaining similar results. The results clearly show that tunable Fabry-Pérot filters can be used in a new generation of filterometers and provide a low-cost option for the quantitative and fast multicomponent gas sensing.

© 2016 Elsevier B.V. All rights reserved.

1. Introduction

With increasing requirements on monitoring of chemical as well as pharmaceutical processes, the demand for powerful, robust and low priced sensors increases. Trends in PAC (process analytical chemistry) or PAT (process analytical technologies) point towards portable analyzers, which can be used in different environments for at-line, but ideally for on- or in-line analysis. The sensor systems have to be fit for purpose, exhibiting adequate analytical performance for a moderate and reasonable price. In principle infrared and Raman spectroscopies are highly interesting techniques in this regard as they provide direct molecular specific information. Concerning mid-IR spectroscopy, Fourier transform spectrometers present the so far most widely used technique [1,2]. These instruments provide a broad spectral coverage and can be successfully applied to solve a broad variety of different analytical problems often by employing chemometric techniques for data analysis. As of today rugged FT-IR spectrometers for on-line or in-line applications are in generally available in every form factor, albeit at a rather high cost. An interesting alternative to established FTIR spectrometers concern spectrometer developments based on broadly tuning, but still prohibitively expensive laser sources, such as external cavity

quantum cascade lasers (EC-QCLs). Such spectrometers have been used for gas [3,4], as well as liquid sensing [5–7]. This approach, in order to be fit for purpose, needs to target applications where gas traces need to be recorded at high speed or where increased ruggedness for liquid sensing is required to justify the high cost.

For providing an answer to some sensing tasks, however, the spectroscopic performance of an FT-IR spectrometer is not required as a restricted spectral range sometimes can provide the required selectivity to solve a given problem. Furthermore, in many applications the high sensitivities as offered by mid-IR laser spectroscopy are not needed, either. This is often the case when major and minor components of industrial gas mixtures need to be monitored. A cost effective solution for addressing such applications is possible by addressing selected spectral regions by the use of filters instead of using an interferometer or lasers. Thus, analyzers using a small, but constant portion of the IR spectrum, as obtainable with static IR filters, have emerged over the years. Such filter based spectrometers are also known as filterometers, a term coined from “filter” and “photometer”. The commercial success of such filterometers made it apparent, that the compromise between performance and price allows attractive solutions for certain measurement problems. Examples are the oil-in-water analyzers by Wilks Enterprise [8] (Spectro Scientific) or first iterations of filterometers for the determination of casein content in milk and milk products [9]. Also concerning absorption or photoacoustic gas measurements filter based instruments have found their application in the recent past.

* Corresponding author.

E-mail address: christoph.gasser@tuwien.ac.at (C. Gasser).<http://dx.doi.org/10.1016/j.snb.2016.11.016>

0925-4005/© 2016 Elsevier B.V. All rights reserved.

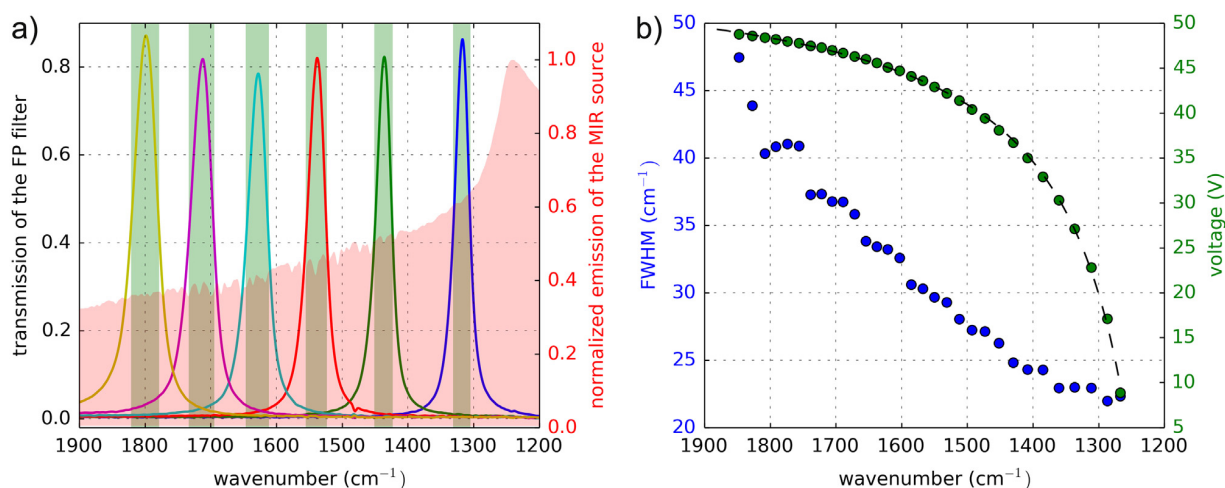


Fig. 1. Transmission windows (a) of the LFP5580 when different voltages are applied and FWHM (b, blue markers) of the transmission curves as a function of wavenumber as well as spectral center (green markers) in dependence of the applied voltage. The fitted curve is indicated as the black dashed line. (For interpretation of the references to colour in this figure legend, the reader is referred to the web version of this article.)

Here, applications of filterometers primarily include gas-phase analysis of simple molecules, such as water and CO₂ [10,11].

Whereas early technological solutions employed a filter wheel for addressing different narrow spectral ranges for measurement, new technological developments are emerging and may change the way modern filterometers operate. New designs respond to the fact that it would often be advisable to monitor more than a single or a set of predefined narrow wavelength ranges. This added capability would increase the flexibility of filterometers and turn them into a more generally applicable analytical tool at remaining low cost and small footprint.

A key enabling technology for this development is Fabry-Pérot (FP) interferometry [12], where the transmitted wavelength is defined among other by the distance between two reflective surfaces. A range of discrete distances can be realized in a small device by circular (CVF) or linear variable filters (LVF). A combination of these with a linear IR detector array [13,14] allows to create compact mid-IR spectrometers, with a spectral resolution of at best 10–20 cm⁻¹, thus approaching the capabilities of a low resolution FT-IR spectrometer but showing sensor-like performance. In these instruments, like those of Pyreos [15], the reflective surfaces of the Fabry-Pérot cavity are kept in place by a wedged spacer in such a way, that the transmission window shifts through the length of the array [14]. Another approach toward compact sensor-like spectrometers consists in changing the distances between the reflective surfaces of the Fabry-Pérot cavity on demand by MEMS (micromechanical systems) fabricated springs or piezo-actuators. These tunable filters also include pyroelectric detector elements and are available in TO8 housings. Compact arrangements of such designs are realized in Infracore's multi-color FP detectors [16] or VTT's integrated solutions [17]. Fabry-Pérot pyro-detectors can therefore be manufactured in large quantities, covering different ranges of the MIR spectrum [18] and are therefore prime candidates for the construction of dedicated spectroscopic sensors. For operation pyro-detectors require modulation of the light intensity. In FT-IR spectrometers this is achieved by using a thermal light source [19], which provides a constant emission of infrared radiation modulated by the interferometer itself. In case of using adjustable Fabry-Pérot cavities for selection of narrow spectral windows practically no intensity modulation is achieved. Therefore, in these miniature, sensor-like spectrometers the intensity of the light source itself has to be modulated. The operation principle of FP-based filterometers permits arbitrary access to selected spectral

regions, in addition to recording the whole spectra by a complete scan.

This work reports on the results obtained with a home-made prototype for gas sensing using a Fabry-Pérot pyro-detector and thermal light source, whose emitting element consists of a thin layer of diamond like carbon (DLC), that can be modulated with up to 100 Hz. A typical gas mixture found at butadiene plants of petrochemical refineries has been selected as target analyte composition (iso-butane, 1-buten, 1,3-butadiene). The obtained spectra are evaluated with multivariate data analysis techniques and the results compared.

2. Materials and methods

2.1. Tunable Fabry-Pérot (FP) filter

For characterization and wavelength calibration, the FP filter (LFP5580, InfraTec GmbH) with a tuning range from 5.5 to 8 μm (1830–1250 cm⁻¹) was coupled to a Bruker Vertex 80v FTIR spectrometer as an external detector using a parabolic off axis mirror (f = 156 mm). Spectra at different driving voltages (5–50 V) were collected by averaging 5 scans and setting the scanner velocity to 1.2 kHz (HeNe frequency). With the resulting transmission windows the filter was calibrated (Fig. 1a). The following relation between driving current and central transmission wavelength was found:

$$V_{\text{driving}} = V_{\text{max}} - \frac{c}{\bar{\nu} - \bar{\nu}_{\text{min}}} \quad (1)$$

where V_{driving} is the driving voltage of the tunable FP, V_{max} is the maximum voltage, c is a constant factor and $\bar{\nu}$ is the central wavenumber. Eq. (1) was fitted (shown in Fig. 1b as the dashed line) to the measured FTIR transmission spectra in order to calibrate the wavenumber axis and enable scanning with equidistant step size.

Furthermore, as shown in Fig. 1b, the full width at half maximum (FWHM, blue markers) of the transmission curves increases with increasing wavenumber.

2.2. FP-based MIR filterometer for gas sensing

The FP-based MIR filterometer (inset in Fig. 2) consisted of a custom built 30 cm gas cuvette employing two circular (diameter

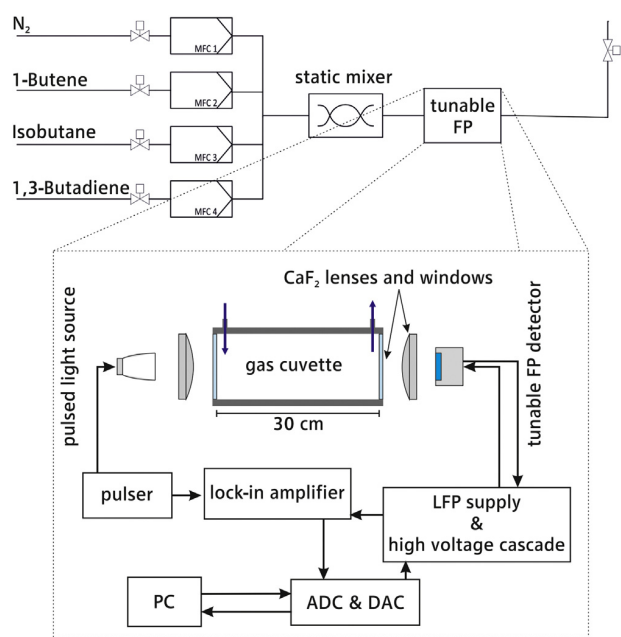


Fig. 2. Setup for the gas measurements including the gas mix rig. The inset shows the instrumentation of the tunable FP filter.

ter: 52 mm) 2 mm thick CaF_2 windows. Light from the pulsed MIR source (JSIR350-4-AL-R-D6 by Micro-Hybrid Electronics GmbH) was collimated with a CaF_2 lens ($f = 50$ mm, ThorLabs GmbH) and after passing the gas cuvette, focused with an equal lens on the active element of the tunable FP filter-detector. The light source was pulsed at 3.52 Hz with 5 V amplitude and a duty cycle of 50 %. The electronic signal from the pyroelectric element of the FP filter-detector was processed with a lock-in amplifier and the resulting voltage was digitalized (ADS1115, Texas Instruments, 16-bit resolution) and recorded. Spectra of the samples were collected by stepwise changing the control voltage (MCP4725, Microchip Technology Inc.) for the tunable filter and calculating the resulting mean intensity of an acquisition time of 1.5 s per step. A waiting period of 300 ms was applied when moving to the next position to let the filter settle. The filtermeter was thus operated by sampling from one point to the next. A step size of 10 cm^{-1} was chosen over a range of 550 cm^{-1} ($1280\text{--}1830\text{ cm}^{-1}$). Scanning across the whole spectral range thus took approximately 100 s. For reference measurements of the gases a Tensor 27 FTIR spectrometer (Bruker Optics, Germany) equipped with a 10 cm gas cell was used. For FTIR spectra acquisition 16 scans at a spectral resolution of 1 cm^{-1} were averaged. 3-term Blackman Harris apodization, a zero filling factor of 2 and Mertz phase correction were applied.

2.3. Experimental set-up including gas supply

For providing gas mixtures with defined concentrations a customized gas mixing rig (Fig. 2 top) was used. This rig consisted of four mass flow controllers (MFC red-y smart, Vögtlin Instruments AG, Switzerland), with different operating flows. To ensure homo-

geneity a helical static mixer was employed before the mixed gas was directed to the analyzers. Gas lines were made of stainless steel tubing (i.d. 4 mm) and Swagelok connections.

Gases were provided by AirLiquide Austria GmbH with the following purities: 1-butene 99.6 %, isobutane 99.5 % and 1,3-butadiene 99.6 %. The design of experiment was chosen with the built-in function in OPUS 7.2 (Bruker Optics, Germany). 20 measurement points were taken in a range from 0.12 to 1.77 % for 1,3-butadiene and isobutane and from 0.4 to 6.2 % for 1-butene. The composition for each step can be seen in Table 1.

All concentrations are given in volumetric quantities (v/v, in%) unless specified otherwise. All steps had a constant flow of 4 l/min and a duration of 8 min to ensure stable conditions in the gas cell. In addition of measuring gas mixtures spectra of pure gases were measured. The mass flow controllers and all valves switching the gas mix rig were controlled using LabVIEW® (National Instruments).

2.4. Data analysis based on partial least squares (PLS) regression

Multivariate data evaluation was performed using the software package DataLab [20]. Spectra of each concentration step were evaluated. Prior to performing PLS the dataset was mean centered. Cross validation was done by random subsets (using 5 iterations with 2 spectra). The root-mean-square error of prediction (RMSEP) was calculated by Eq. (2),

$$RMSEP = \sqrt{\frac{\sum_{i=1}^N (y_i - \hat{y}_i)^2}{N}} \quad (2)$$

where y_i are the concentrations of the respective components as prepared in the gas mixing rig, \hat{y}_i the values predicted by the PLS algorithm and N the number of samples measured.

2.5. Data analysis based on multiple linear regression (MLR)

Multiple linear regression correlates more than one independent (descriptor) to one dependent (target) variable. Usually spectroscopic methods provide a multitude of descriptors (e.g. different wavenumbers) and only one target variable (e.g. concentration). Additionally, spectra inherently show strong multicollinearities because of spectral features spanning over several wavenumbers. These facts often cause over-optimistic models by applying MLR to spectral data. This can and must be avoided by reducing the number of descriptors. This is usually done by variable selection algorithms, which identify the descriptors that are most important for the analytical problem at hand and use them explicitly to build the model. Absence of collinearities can be tested by calculating and comparing e.g. the variance inflation factor (VIF) for different sets of descriptors.

3. Results and discussion

3.1. System performance

An important parameter indicating the performance of a given experimental set-up are so called 100%-lines. These are obtained by recording two spectra without the analyte being present in the

Table 1

Composition of each concentration step set by the gas mixing rig and used for multivariate calibration and validation of the tunable FP instrument. All concentrations are given in volumetric quantities (v/v, in%).

conc. step	1	2	3	4	5	6	7	8	9	10	11	12	13	14	15	16	17	18	19	20
1-butene	0.79	1.56	1.42	1.49	4.85	0.00	4.86	2.33	3.22	1.42	2.94	0.87	3.77	1.91	2.26	4.11	1.91	6.25	0.43	0.78
isobutane	1.39	1.13	1.51	1.07	0.31	0.89	0.49	0.69	0.12	0.88	0.19	0.06	0.00	0.63	1.12	0.06	0.94	0.06	1.77	1.70
1,3-butadiene	0.77	0.85	0.34	0.94	0.50	1.72	0.22	1.10	1.43	0.94	1.52	0.35	1.26	1.28	0.51	1.09	0.85	0.33	0.43	0.43

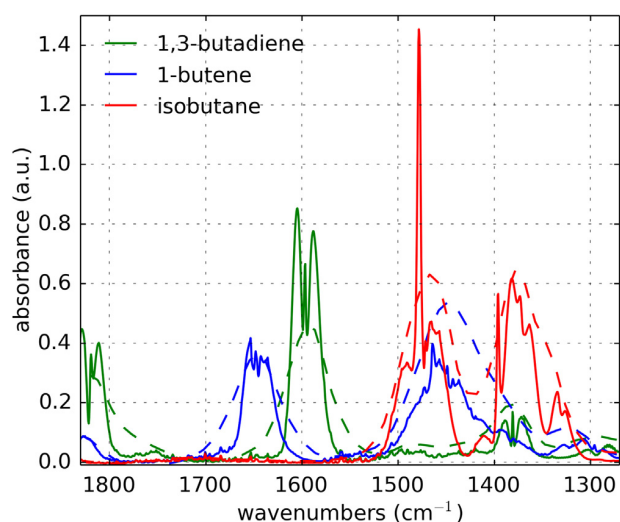


Fig. 3. Pure spectra of the three sample gases collected with the FTIR spectrometer (solid lines) and the tunable FP setup (dashed lines).

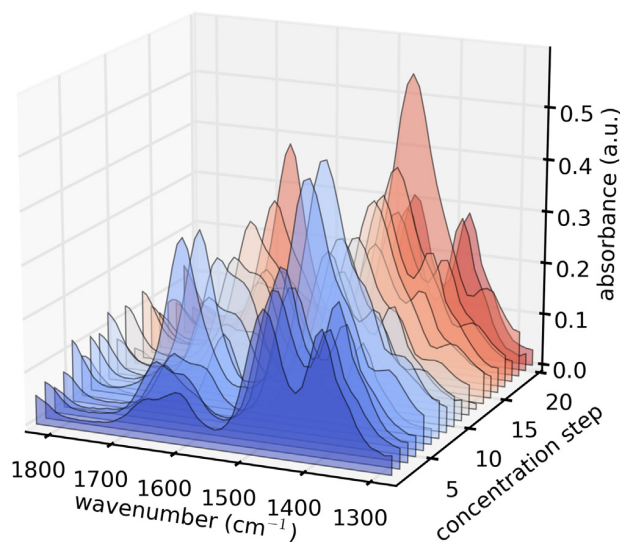


Fig. 4. All spectra of the different 3 component mixtures collected with the tunable FP setup.

gas cell and calculating the related absorbance spectra, which in absence of any noise would be straight lines. The root-mean-square (RMS) noise of these 100% lines was calculated. The peak-to-peak (PP) noise on the other hand is the difference of the absolute maximum and absolute minimum absorption value obtained in the respective 100% lines. Under the adopted conditions and covering a spectral range from 1280 to 1830 cm^{-1} the RMS noise was found to be 0.76 mAU (3.1 mAU_{PP}) for the Fabry P erot (FP)-based MIR filterometer. In Fig. 3 the spectra of the pure components collected with the FTIR spectrometer and the tunable filterometer are compared. For the FTIR spectrometer a resolution of 1 cm^{-1} was arbitrarily set, representing the highest resolution this spectrometer can offer. On the contrary, central wavenumbers for the transmission curves of the filter spaced at 10 cm^{-1} were selected considering the FWHM of the corresponding transmission curves being $25\text{--}45 \text{ cm}^{-1}$. This difference in the spectral resolution is best observed for isobutene at the band at 1470 cm^{-1} (Fig. 3). This band, assigned to the anti-symmetric deformation of the methyl group [21], should show a distinct peak at the center due to the Q-branch of the rotational

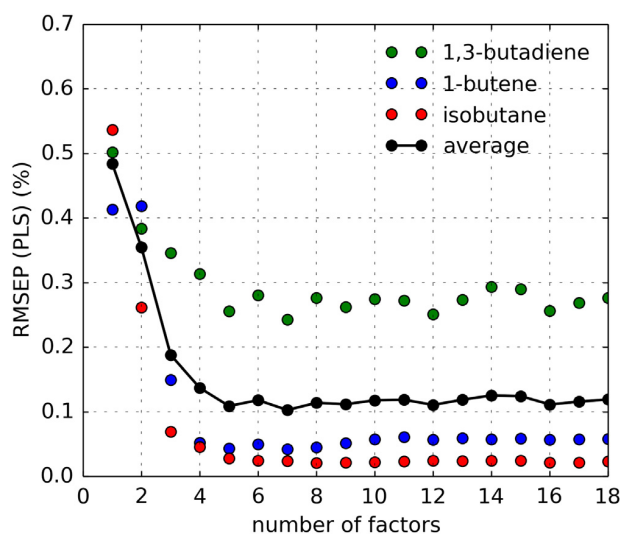


Fig. 5. RMSEP versus number of factors as calculated by cross-validation for the PLS for tunable FP setup. The black line indicates the mean RMSEP of all three components.

Table 2

Overview of the MLR regression. The results of the variable selection contain the position (in cm^{-1}) and the index of the spectral position (in parenthesis). Additionally, the variable inflation factor (VIF) of each variable, the regression coefficient (R^2) and the F-value of the model is shown.

	variable	VIF	R^2	F
1,3-butadiene	1577 (32)	1.047	0.97	282
	1448 (18)	1.047		
1-butene	1612 (36)	2.625	0.992	1078
	1662 (42)	2.625		
isobutane	1367 (10)	1.36	0.9986	4561
	1717 (49)	3.304		
	1812 (62)	3.788		

transition. While this band is visible in the FTIR spectrum it cannot be observed in the tunable FP spectrum because of the aforementioned lower resolution. The positions of absorption bands of the different analytes are consistent in both spectrometers indicating a proper calibration of the Fabry P erot (FP)-based MIR filterometer.

Using the set-up depicted in Fig. 2 acquisition of FP-based spectra (Fig. 4) for different 3 components mixtures was possible. Care was taken to avoid any carry over from one gas mixture to the next one.

3.2. Quantification employing partial least square (PLS) calibration

PLS models were calculated for the dataset using the gas concentration as set by the mass flow controllers as reference values. When establishing a PLS model the number of factors to be considered has to be selected carefully. It is recommended to choose the least possible amount of factors that describe the sample system sufficiently. For the tunable FP filterometer dataset (Fig. 5) the optimum number of factors was determined using cross-validation (2 spectra left out) to be five. With a mean RMSEP of 0.109% the developed FP filterometer provides highly satisfactory results indicating that spectral resolution as offered by the FP-based MIR filterometer does not limit the analytical performance.

Table 3
Comparison of the results of the multivariate models calculated in this study for every component. Additionally, the acquisition time is given for comparison.

	components						
	1,3-butadiene		1-butene		isobutane		acquisition time (s)
	LOD (%)	LOQ (%)	LOD (%)	LOQ (%)	LOD (%)	LOQ (%)	
PLS	0.17	0.50	0.05	0.16	0.03	0.09	100
MLR	0.20	0.57	0.06	0.17	0.04	0.11	12

3.3. MLR models for the tunable FP setup

Before setting up the MLR model for each component present in the sample mixture, a reduction of the number of descriptors is necessary. With respect to the FP-based MIR filterometer in this study it is no longer required to scan the whole spectral range, instead a few positions might be enough to predict the concentrations accurately. This in turn will allow faster measurements.

DataLab has conveniently implemented functions, which automatically select different sets of descriptors, calculate a model and report several parameters (min. t-value, Akaike Information Criterion (AIC), Bayes Information Criterion (BIC), R^2 , etc.) to decide upon the most useful descriptor set for the problem at hand. The variable selection was performed using stepwise regression. Here, the algorithm tries to improve the model by adding more suitable variables and by comparing the minimal t-value. It can also modify its selection by removing the last variable and trying another one, which may yield better results.

With the selected variables multiple linear regressions (MLRs) were performed. To investigate collinearities in the selected variables, the VIF for each selected descriptor was calculated and compared [22]. In general, VIFs should be lower than 10 so that selected variables are not strongly correlated to each other. However, the decision threshold can vary from dataset to dataset [23]. For the spectral descriptors chosen in this study, no VIF (Table 2) was obtained with values above 3.8, so there is no indication for strongly correlated variables. Thus the models can be assessed by their other figures of merit, like the regression coefficient and F value.

The prediction accuracy for the individual components reassembles the trend observed in the PLS models. For 1,3-butadiene and 1-butene two descriptors were chosen, as they gave the best results whilst showing the least correlation among them. Choosing variable sets with more than two descriptors always resulted in high VIFs and were therefore discarded. Isobutane was the only component, which allowed for three descriptors with moderate VIFs. This resulted in a better model and goodness of fit for the regression (Table 2).

3.4. Analytical figures of merit

When comparing different quantitative methods, their ability to quantify a certain component inside a given matrix can be expressed by figures of merit such as the limit of detection (LOD) or the limit of quantification (LOQ). IUPAC defines LOD as the concentration level for which the risk of false non-detects (false negatives) has a probability β [24,25]. Beforehand, a critical concentration level has to be defined, involving a certain risk of false detects (false positives) with a probability α [26]. Whereas these figures of merit are well known and used for a long time in univariate analysis, it is not straight forward to apply these to multivariate datasets. This is because calibration curves obtained from multivariate datasets by different chemometric algorithms may contain different unknown signal contributions for each component. Usually, this is the case when large datasets are generated from complex sample material where the presence of unknown contributions from unknown

components cannot be omitted. However, if the sample systems is known to not include such interferences, it is valid to use the IUPAC method for evaluating the resulting calibration curve of each component [27]. Equivalently, the LOQ was determined based on the standard deviation of the response of the model and the slope of the obtained calibration curve, where the tenfold of the standard deviation is divided by slope.

The LOD and LOQ of the different methods MLR and PLS can now be compared (Table 3). The resulting values for each component are similar, with the PLS having the upper hand by a small margin. This is to be expected, because PLS uses the whole dataset (has a higher information depth) as MLR, where only a couple of descriptors were chosen to represent the components. However, the acquisition time differs quite heavily, with the MLR method only needing 12 s, which in turn significantly improves time resolution. This might be of benefit in fast changing processes, where quick reaction to certain changes is required.

4. Conclusions

A compact, robust and low-cost Fabry P erot (FP)-based MIR filterometer for gas sensing was built and tested for multicomponent gas analysis on the example of measuring 1,3-butadiene, 1-butene and isobutene. The spectra obtained with the FP filterometer were compared with spectra recorded on a FTIR spectrometer and successfully validated. Multivariate analysis based on partial least squares (PLS) and multiple linear regression (MLR) for simultaneous quantification of the target analytes were carried out and compared. The PLS model gave best results using 5 factors with a mean RMSEP of 0.109 %. Mainly due to the slow response time of the pyroelectric detector employed in the FP-based MIR filterometer, it took about 100 s to collect a full spectrum. Given a defined target application (as a dedicated sensor) it is, however, often not required to record a full spectrum and still achieve multicomponent sensitivity. This was shown here by performing MLR based on the obtained dataset. Variable selection was applied to find the most significant descriptors which were then chosen for further analysis. The absence of collinearities was verified by calculating VIFs for the selected descriptors. MLR yielded a LOQ of 0.57 %, 0.17 % and 0.11 % for 1,3-butadiene, 1-butene and isobutane respectively, which is comparable to the results obtained from PLS analysis. The advantage of using MLR over PLS is that only data from seven positions have to be measured, which reduces the time of analysis by a factor of 8 to approximately 12 s. Thus we could show that this compact and low-cost sensor paired with chemometric processing methods is able to quantify gas mixtures composed of three different analytes. In light of the steadily increasing need for cost effective gas sensing in process applications the presented FP-based MIR filterometer provides an attractive and versatile option. The drawbacks of the FP-based MIR filterometer certainly lay in the restricted range covered and the limited spectral resolution, which can still be sufficient for certain process applications, as shown in this study on selected C_4 hydrocarbons. Apart from the low cost of the employed components a rapid reprogramming allows also adaption to different measurement problems. This versatility combined with a small electrical as well as physical footprint pave the way

Appendix F. Scientific Publications on Infrared-Based Gas Sensing

14

C. Gasser et al. / Sensors and Actuators B 242 (2017) 9–14

for this technique to establish itself as useful chemical sensors in process monitoring and control.

Acknowledgements

We sincerely acknowledge Hans Lohninger from the Vienna University of Technology for providing us with a full version of DataLab [20], which we used to construct the PLS and MLR models. Financial support was provided by the Austrian research funding association (FFG) under the scope of the COMET programme within the research project “Industrial Methods for Process Analytical Chemistry – From Measurement Technologies to Information Systems (imPACTs)” (contract # 843546).

This programme is promoted by BMVIT, BMWFW, the federal state of Upper Austria and the federal state of Lower Austria.

References

- [1] J. Workman, B. Lavine, R. Chrisman, M. Koch, Process analytical chemistry, *Anal. Chem.* 83 (2011) 4557–4578, <http://dx.doi.org/10.1021/ac200974w>.
- [2] D. Landgrebe, C. Haake, T. Höpfner, S. Beutel, B. Hitzmann, T. Scheper, M. Rhiel, K.F. Reardon, On-line infrared spectroscopy for bioprocess monitoring, *Appl. Microbiol. Biotechnol.* 88 (2010) 11–22, <http://dx.doi.org/10.1007/s00253-010-2743-8>.
- [3] M. Brandstetter, A. Genner, K. Anic, B. Lendl, Tunable external cavity quantum cascade laser for the simultaneous determination of glucose and lactate in aqueous phase, *Analyst* 135 (2010) 3260–3265, <http://dx.doi.org/10.1039/c0an00532k>.
- [4] M.C. Phillips, M.S. Taubman, B.E. Bernacki, B.D. Cannon, R.D. Stahl, J.T. Schiffern, T.L. Myers, Real-time trace gas sensing of fluorocarbons using a swept-wavelength external cavity quantum cascade laser, *Analyst* 139 (2014) 2047–2056, <http://dx.doi.org/10.1039/c3an01642k>.
- [5] G.N. Rao, A. Karpf, External cavity tunable quantum cascade lasers and their applications to trace gas monitoring, *Appl. Opt.* 50 (2011) A100–A115, <http://dx.doi.org/10.1364/AO.50.00A100>.
- [6] M.R. Alcaráz, A. Schwaighofer, C. Kristament, G. Ramer, M. Brandstetter, H. Goicoechea, B. Lendl, External-cavity quantum cascade laser spectroscopy for mid-IR transmission measurements of proteins in aqueous solution, *Anal. Chem.* 87 (2015) 6980–6987, <http://dx.doi.org/10.1021/acs.analchem.5b01738>.
- [7] M.R. Alcaráz, A. Schwaighofer, H. Goicoechea, B. Lendl, EC-QCL mid-IR transmission spectroscopy for monitoring dynamic changes of protein secondary structure in aqueous solution on the example of β -aggregation in alcohol-denaturated α -chymotrypsin, *Anal. Bioanal. Chem.* (2016), <http://dx.doi.org/10.1007/s00216-016-9464-5>.
- [8] B.P.A. Wilks, In-line infrared sensors covering the mid infrared from 2 to 14 μm (5000–700 cm^{-1}), *Proc. SPIE*. 4577 (2002) 76–82.
- [9] W. Luginbu, Evaluation of designed calibration samples for casein calibration in Fourier transform infrared analysis of milk, *Leb. Technol.* 35 (2002) 554–558, <http://dx.doi.org/10.1006/fstl.902>.
- [10] E. Vargas-Rodríguez, H.N. Rutt, Design of CO, CO₂ and CH₄ gas sensors based on correlation spectroscopy using a Fabry–Perot interferometer, *Sens. Actuators B Chem.* 137 (2009) 410–419, <http://dx.doi.org/10.1016/j.snb.2009.01.013>.
- [11] M. Noro, K. Suzuki, N. Kishi, H. Hara, T. Watanabe, H. Iwaoka, CO₂/H₂O gas sensor using a tunable Fabry–Perot filter with wide wavelength range, 2003. 319–322. doi: 10.1109/MEMSYS.2003.1189750.
- [12] G. Chantry, The use of Fabry–Perot interferometers, etalons and resonators at infrared and longer wavelengths—an overview, *J. Phys. E* 3 (1982) (accessed March 31, 2014) <http://iopscience.iop.org/0022-3735/15/1/001>.
- [13] B.R. Wiesent, D.G. Dorigo, Ö. Simsek, A.W. Koch, Linear variable filter based oil condition monitoring systems for offshore wind turbines, *Proc. SPIE* 8105 8105 (2011) 81050D, <http://dx.doi.org/10.1117/12.891505>.
- [14] B.R. Wiesent, D.G. Dorigo, A.W. Koch, Limits of IR-spectrometers based on linear variable filters and detector arrays, *Proc. SPIE* 7767 7767 (2010) 77670L, <http://dx.doi.org/10.1117/12.860532>.
- [15] D.S. Kim, T. Lee, Development of an ultra-compact mid-infrared attenuated total reflectance spectrophotometer, *Opt. Eng.* 53 (2014), <http://dx.doi.org/10.1117/1.OE.53.7.074108>, 74108–1–74108–7.
- [16] N. Neumann, M. Ebermann, K. Hiller, S. Kurth, Tunable infrared detector with integrated micromachined Fabry–Perot filter, *Proc. SPIE* (2007) 646606–646612 <http://dx.doi.org/10.1117/12.698871>.
- [17] J. Antila, M. Tuohiniemi, A. Rissanen, U. Kantojärvi, M. Lahti, K. Viherkanto, M. Kaarre, J. Malinen, MEMS- and MOEMS-Based Near-Infrared Spectrometers, 2000. doi: 10.1002/9780470027318.a9376.
- [18] N. Neumann, M. Ebermann, S. Kurth, K. Hiller, Tunable infrared detector with integrated micromachined Fabry–Perot filter, *J. Micro/Nanolithography MEMS MOEMS* 7 (2008) 21004, <http://dx.doi.org/10.1117/1.2909206>.
- [19] D.A. Long, Handbook of vibrational spectroscopy, vol. 1–5. (Ed.) J.M. Chalmers, P.R. Griffiths, John Wiley & Sons, Chichester, 2002, pp. 3862, *J. Raman Spectrosc.* 36 (2005) 271–271. doi: 10.1002/jrs.1309.
- [20] H.H. Lohninger, DataLab 3.5, 2000 <http://datalab.epina.at/> (accessed May 6, 2016).
- [21] J.C. Evans, J. Bernstein, The vibrational spectra of isobutane and isobutane-d₁, *Can. J. Chem.* (1956) 1037–1045.
- [22] M.C.U. Araújo, T.C.B. Saldanha, R.K.H. Galvão, T. Yoneyama, H.C. Chame, V. Visani, The successive projections algorithm for variable selection in spectroscopic multicomponent analysis, *Chemom. Intell. Lab. Syst.* 57 (2001) 65–73, [http://dx.doi.org/10.1016/S0169-7439\(01\)00119-8](http://dx.doi.org/10.1016/S0169-7439(01)00119-8).
- [23] R.M. O'Brien, A caution regarding rules of thumb for variance inflation factors, *Qual. Quant.* 41 (2007) 673–690, <http://dx.doi.org/10.1007/s11135-006-9018-6>.
- [24] K. Danzer, L.A. Currie, Guidelines for calibration in analytical chemistry. Part I. Fundamentals and single component calibration (IUPAC Recommendations 1998), *Pure Appl. Chem.* 70 (1998) 993–1014, <http://dx.doi.org/10.1351/pac199870040993>.
- [25] K. Danzer, M. Otto, L.A. Currie, Guidelines for calibration in analytical chemistry part 2 multispecies calibration (IUPAC technical report), *Pure Appl. Chem.* 76 (2004) 1215–1225.
- [26] N.M. Faber, The limit of detection is not the analyte level for deciding between detected and not detected, *Accredit. Qual. Assur.* 13 (2008) 277–278, <http://dx.doi.org/10.1007/s00769-007-0351-9>.
- [27] A.C. Olivieri, Analytical figures of merit: from univariate to multiway calibration, *Chem. Rev.* 114 (2014) 5358–5378, <http://dx.doi.org/10.1021/cr400455s>.

Biographies

Christoph Gasser is a PhD student in the Lendl group. So far he worked on the development of stand-off spatial offset Raman spectroscopy. He is now working on a new infrared sensing technique for process analytical applications.

Andreas Genner is a PhD student in the Lendl group. During his master thesis he worked on the development of a sensor for monitoring cleaning processes in the pharmaceutical industry (CIP) using a broadly tunable EC-QCL as IR source. Moreover, during an internship with G. Strasser at TU Wien him worked on processing and characterization of surface emitting ring structure QCLs. At the moment, Andreas is also developing customized measurement devices for project partners in the chemical industry.

Harald Moser finished his studies on Chemical Engineering at Graz University of Technology in 2009. After a one year stay in the field of mechanics of materials and structures, he joined the Lendl research group in 2011 for his PhD thesis. His current research field includes on-line quantum cascade laser based trace gas analytics for process analytical applications.

Johannes Ofner studied chemistry at Technische Universität Wien from 2001 to 2006. He focused on physical chemistry, especially infrared spectroscopy. In spring 2008 he started his PhD studies at the Atmospheric Chemistry Research Laboratory of the University of Bayreuth (Germany) under the supervision of Prof. Dr. Cornelius Zetzsch and finished his PhD thesis with the title ‘Formation of secondary organic aerosol and its processing by atmospheric halogen species – a spectroscopic study’ in July 2011. He continued his research as a post doc in Bayreuth and joined the Lendl group in December 2012. His work is focused on development and application of spectroscopic methods (Raman and infrared spectroscopy) for atmospheric research on aerosols and trace gases as well as aerosol formation and processing and remote sensing.

Bernhard Lendl studied chemistry at Technische Universität Wien. During his PhD thesis he investigated Flow Injection Analysis coupled to Infrared Spectroscopy for process monitoring and biomedical applications. In 2001 he was appointed associate professor for Analytical Chemistry at Vienna University of Technology. From 2003 to 2004 he was guest professor at the laboratory of Prof. Miguel Valcárcel (Córdoba University, Spain). His current research focuses on the development of novel analytical techniques based on molecular spectroscopy for use in quantitative and qualitative analysis. His group concentrates on emerging new technologies such as mid-IR quantum cascade lasers, waveguide technologies, particle manipulation by ultrasound, as well as performing chemical reactions and separations in micro-fluidic systems. In 2008 he co-founded QuantaRed Technologies as a spin-off company of his research group. In 2015 he chaired the 8th international Conference on Advanced Vibrational Spectroscopy at TU Wien which was attended by 650 people. In 2016 he was appointed full professor for vibrational spectroscopy at TU Wien.

Appendix G.

Curriculum Vitae



Die approbierte gedruckte Originalversion dieser Dissertation ist an der TU Wien Bibliothek verfügbar.
The approved original version of this doctoral thesis is available in print at TU Wien Bibliothek.



Andreas Genner

Education

PhD thesis

- Title **A Quantum Cascade Laser-Based Sensor for Ambient Air Monitoring.**
2016–2020 Institute of Chemical Technologies and Analytics, TU Wien, Vienna, Austria
Supervisor Bernhard Lendl
Description A prototype for monitoring gaseous pollutants in the ambient air has been developed. It is based on the 2f-Wavelength Modulation Spectroscopy and involved the planning, assembling, programming and characterization in the lab. Moreover, its performance has been tested in field experiments (Szombathely and Vienna).

Master thesis

- Title **A New Method for Monitoring Clean-in-Place Processes by Using Quantum Cascade Lasers.**
2013–2014 Institute of Chemical Technologies and Analytics, TU Wien, Vienna, Austria
Supervisors Gottfried Strasser, Bernhard Lendl
Description Cleaning cycles of stirred-tank reactors were investigated with a custom-built infrared sensor. In addition, RingQCLs based on bifunctional QCL/QCD gain material were developed and tested at the Institute of Solid State Electronics (TU Wien).

Internship (Erasmus Programme)

- Title **Automation and Characterization of a Microfluidic Diluter.**
2010.01-07 Chalmers University of Technology, Gothenburg, Sweden

Bachelor thesis

- Title **Characterizing and Automating an External Cavity Quantum Cascade Laser.**
2009.07-12 Institute of Chemical Technologies and Analytics, TU Wien

School education

- 1997–2005 **Secondary school**, BRG Gröhrmühlgasse, Wiener Neustadt.

Work experience

PhD thesis

2016–2020 **Institute of Chemical Technologies and Analytics, TU Wien, Vienna.**

- Full-time work
- Planning and assembling the optical and mechanical layout for a multi-gas sensor,
 - Selecting the electronics (data acquisition cards, lock-in-amplifier, laser driver),
 - Programming the software to control the individual components,
 - Characterizing the diode lasers with an FTIR-spectrometer,
 - Calibration and long-term evaluation of the prototype,
 - Organizing and performing the field experiments.
 - Sideprojects:
 - Developing a sensor to monitor the side products of a formaldehyde production plant,
 - Modifying an FTIR spectrometer to quantify CO₂ in hydrofluorocarbons,
 - Programming the software for a test bench to evaluate the 3D printing properties of metal powders,
 - Teaching students the basics of laser spectroscopy (quantifying NO_x with an open-path setup and TDLAS),
 - Administrating the IT infrastructure of the work group (office and lab PC's, NAS, public website (Typo3), local MediaWiki installation).

Project staff

2009–2012 **Institute of Chemical Technologies and Analytics, TU Wien, Vienna.**

- 2014–2016
- Part-time work
- Assembling, programming and evaluating prototypes based on infrared spectroscopy,
 - Teaching students the basics of laser spectroscopy (quantifying NO_x with an open-path setup and TDLAS),
 - Administrating the IT infrastructure of the work group (office and lab PC's, NAS, public website (Typo3), local MediaWiki installation).

Project staff

2012–2014 **QuantaRed Technologies GmbH, Vienna.**

- Part-time work
- Installing an FTIR-based sensor to quantify hydrocarbons in a process stream at a refinery,
 - Learning the processing steps for QCLs at the Institute of Solid State Electronics (FKE), TU Wien, including E-beam and UV-lithography, etching techniques and deposition methods,
 - Identifying potential projects between the FKE and the CTA.

Lab assistant

2006–2008 **ESW Consulting Wruss Ziviltechnikergesellschaft mbH, Vienna.**

- Part-time work
- Different sample preparation steps for soil and water samples,
 - Basic measurements (e.g. AOX/EOX, TOC, IC, CSB, ...).

Skills and interests

Languages

German First language

English Highly proficient in both spoken and written (C1/C2)

Computer skills

Programming LabVIEW, Python, TurboPascal/Delphi, C/C++, PHP

CAD, EDA SolidWorks, Eagle

Office Microsoft Office, L^AT_EX, Adobe Illustrator, Adobe InDesign

Infrastructure Basics in Linux/Unix/macOS (Workgroup Servers), Fundamentals in Switches, Routers and VPNs

Project Redmine, Microsoft Project
Management

Other activities

Volunteer Fire

- o Platoon Commander (Zugskommandant)

Brigade

- o Certified trainer and examiner "Basisausbildung" and "Grundlagen Führen"
- o Examiner "Ausbildungsprüfung Löscheinsatz"
- o Person in charge for hazardous substances
- o Member since 2003 (Freiwillige Feuerwehr Scheiblingkirchen)

Sailing

- o Offshore license "FB 2" (since 2009)
- o GMDSS - Short Range Certificate (marine VHF radio)

Electronics Raspberry Pi, Software Defined Radio, IoT, Arduino, ESP32, 3D printing

Hobbyist

Dissemination

Papers

- [1] M. Brandstetter, A. Genner, K. Anic, and B. Lendl, "Tunable external cavity quantum cascade laser for the simultaneous determination of glucose and lactate in aqueous phase," *The Analyst*, vol. 135, no. 12, p. 3260, Dec. 2010. DOI: 10.1039/c0an00532k.
- [2] M. Brandstetter, T. Sumalowitsch, A. Genner, A. E. Posch, C. Herwig, A. Drolz, V. Fuhrmann, T. Perkmann, and B. Lendl, "Reagent-free monitoring of multiple clinically relevant parameters in human blood plasma using a mid-infrared quantum cascade laser based sensor system," *The Analyst*, vol. 138, no. 14, p. 4022, Jun. 2013. DOI: 10.1039/c3an00300k.
- [3] M. Brandstetter, L. Volgger, A. Genner, C. Jungbauer, and B. Lendl, "Direct determination of glucose, lactate and triglycerides in blood serum by a tunable quantum cascade laser-based mid-IR sensor," *Applied Physics B*, vol. 110, no. 2, pp. 233–239, Feb. 2013. DOI: 10.1007/s00340-012-5080-z.
- [4] M. R. EL-Zahry, A. Genner, I. H. Refaat, H. a. Mohamed, and B. Lendl, "Highly reproducible SERS detection in sequential injection analysis: Real time preparation and application of photo-reduced silver substrate in a moving flow-cell," *Talanta*, vol. 116, pp. 972–977, Nov. 2013. DOI: 10.1016/j.talanta.2013.07.059.
- [5] T. Siegmann-Hegerfeld, A. Genner, M. Brandstetter, B. Lendl, and M. Harasek, "Online Monitoring of TOC Contaminations in Clean- in-Place Processes for Optimized Process Control , Increased Process Efficiency and Quality," *Chemical Engineering Transactions*, vol. 35, pp. 979–984, 2013. DOI: 10.3303/CET1335163.
- [6] M. Brandstetter, A. Genner, C. Schwarzer, E. Mujagic, G. Strasser, and B. Lendl, "Time-resolved spectral characterization of ring cavity surface emitting and ridge-type distributed feedback quantum cascade lasers by step-scan FT-IR spectroscopy," *Optics Express*, vol. 22, no. 3, p. 2656, Feb. 2014. DOI: 10.1364/OE.22.002656.
- [7] H. Moser, A. Genner, J. Ofner, C. Schwarzer, G. Strasser, and B. Lendl, "Application of a ring cavity surface emitting quantum cascade laser (RCSE-QCL) on the measurement of H₂S in a CH₄ matrix for process analytics," *Optics Express*, vol. 24, no. 6, p. 6572, Mar. 2016. DOI: 10.1364/OE.24.006572.
- [8] C. Gasser, A. Genner, H. Moser, J. Ofner, and B. Lendl, "Application of a tunable Fabry-Pérot filterometer to mid-infrared gas sensing," *Sensors and Actuators B: Chemical*, vol. 242, pp. 9–14, Apr. 2017. DOI: 10.1016/j.snb.2016.11.016.
- [9] A. Genner, C. Gasser, H. Moser, J. Ofner, J. Schreiber, and B. Lendl, "On-line monitoring of methanol and methyl formate in the exhaust gas of an industrial formaldehyde production plant by a mid-IR gas sensor based on tunable Fabry-Pérot filter technology," *Analytical and Bioanalytical Chemistry*, vol. 409, no. 3, pp. 753–761, Jan. 2017. DOI: 10.1007/s00216-016-0040-9.
- [10] P. Martín-Mateos, A. Genner, H. Moser, and B. Lendl, "Implementation and characterization of a thermal infrared laser heterodyne radiometer based on a wavelength modulated local oscillator laser," *Optics Express*, vol. 27, no. 11, p. 15575, May 2019. DOI: 10.1364/OE.27.015575.
- [11] A. Genner, P. Martín-Mateos, H. Moser, and B. Lendl, "A Quantum Cascade Laser-Based Multi-Gas Sensor for Ambient Air Monitoring," *Sensors*, vol. 20, no. 7, p. 1850, Mar. 2020. DOI: 10.3390/s20071850.

Book Chapter

- [1] C. Wagner, A. Genner, G. Ramer, and B. Lendl, "Advanced Total Lab Automation System (ATLAS)," in *Modeling, Programming and Simulations Using LabVIEW®; Software*, R. De Asmundis, Ed., InTech, Jan. 2011, ch. 1, pp. 3–20. DOI: 10.5772/14110.

Proceedings

- [1] M. Brandstetter, A. Genner, K. Anic, and B. Lendl, "Tunable Mid-IR lasers: A new avenue to robust and versatile physical chemosensors," in *Procedia Engineering*, vol. 5, Elsevier, 2010, pp. 1001–1004. DOI: 10.1016/j.proeng.2010.09.278.
- [2] A. Genner, A. Ainla, and A. Jesorka, "Calibrated On-chip Dilution Module for the Multifunctional Pipette," in *Proceedings of the 3rd International Workshop on Soft Matter Physics & Complex Flows*, J. O. Fossum and E. Bouchaud, Eds., Lofoten, 2012, pp. 1–5.
- [3] M. Brandstetter, C. Koch, A. Genner, and B. Lendl, "Measures for optimizing pulsed EC-QC laser spectroscopy of liquids and application to multi-analyte blood analysis," in *Quantum Sensing and Nanophotonic Devices XI*, M. Razeghi, E. Tournié, and G. J. Brown, Eds., vol. 8993, Dec. 2013, 89931U. DOI: 10.1117/12.2038585.
- [4] M. Brandstetter, T. Sumalowitsch, A. Genner, V. Fuhrmann, and B. Lendl, "Clinical Application of a Mid-Infrared Quantum Cascade Laser Based Sensor for Multianalyte Detection in Human Blood Plasma," in *Conference on Lasers and Electro-Optics*, Washington, D.C.: OSA, 2013, AF1L.3. DOI: 10.1364/CLEO_AT.2013.AF1L.3.
- [5] C. Schwarzer, R. Szedlak, L. Burgstaller, A. Genner, T. Zederbauer, H. Detz, A. M. Andrews, W. Schrenk, and G. Strasser, "Polarization versatility of surface emitting ring cavity quantum cascade lasers," in *Conference on Lasers and Electro-Optics*, IEEE, May 2013, pp. 1–1. DOI: 10.1109/CLEOE-IQEC.2013.6800693.
- [6] H. Moser, J. P. Waclawek, A. Genner, C. Gasser, and B. Lendl, "A triple quantum cascade laser based sulfur species sensor for H₂S, CH₃SH and COS in petrochemical process streams," in *Conference on Lasers and Electro-Optics*, Washington, D.C.: OSA, 2018, AM2M.7. DOI: 10.1364/CLEO_AT.2018.AM2M.7.
- [7] A. Genner, P. Martín-Mateos, H. Moser, J. P. Waclawek, and B. Lendl, "Extending the linear concentration range of a multi-gas-analyzer," in *Quantum Sensing and Nano Electronics and Photonics XVI*, M. Razeghi, J. S. Lewis, G. A. Khodaparast, and E. Tournié, Eds., vol. 10926, SPIE, Feb. 2019, p. 95. DOI: 10.1117/12.2509331.

Posters

- [1] M. Brandstetter, A. Genner, and B. Lendl, *Nanosecond step-scan FTIR spectroscopy of a pulsed external-cavity quantum-cascade laser*, 2009.
- [2] M. Brandstetter, A. Genner, K. Anic, and B. Lendl, *Quantum Cascade Lasers: A New Avenue to Robust and Versatile Sensors for Bodily Fluids*, 2010.
- [3] M. Brandstetter, L. Volgger, E. Aguilera-herrador, A. Genner, and B. Lendl, *Demonstration of an external-cavity quantum cascade laser based blood sensor*, 2010.
- [4] A. Genner, M. Brandstetter, W. Tomischko, and B. Lendl, *Signal processing strategies for liquid phase sensors based on external cavity quantum cascade lasers*, 2010.
- [5] M. Brandstetter, G. Ramer, A. Genner, J. Kasberger, and B. Lendl, *Robust mid-IR spectroscopy using a pulsed external cavity QCL for liquid phase analysis*, 2011.
- [6] M. Brandstetter, A. Genner, L. Volgger, and B. Lendl, *Liquid phase analysis using a pulsed external cavity quantum cascade laser for mid-IR spectroscopy*, 2011.
- [7] H. Moser, M. Brandstetter, A. Genner, E. Mujagić, G. Strasser, and B. Lendl, *Time-resolved characterization of the spectral behavior of ring cavity surface emitting QCLs (RCSE-QCLs)*, 2012.
- [8] M. Brandstetter, T. Sumalowitsch, A. Genner, V. Fuhrmann, Thomas Perkmann, and B. Lendl, *Tunable Quantum Cascade Laser based Blood Sensor for Clinical Application*, 2012.

Appendix G. Curriculum Vitae

- [9] W. Tomischko, C. Reidl-Leuthner, A. Genner, and B. Lendl, *A Low Budget High Precision Driver for Pulsed Quantum Cascade Lasers*, 2012.
- [10] A. Genner, M. Brandstetter, M. Harasek, and B. Lendl, *Online Monitoring of Cleaning In Place Systems Facilitated by a Broadly Tuneable Quantum Cascade Laser*, 2012.
- [11] A. Genner, M. Brandstetter, M. Harasek, and B. Lendl, *Monitoring Industrial Processes Using a Sensor Based on an External Cavity-Quantum Cascade Laser*, 2012.
- [12] M. Brandstetter, V. Fuhrmann, A. Genner, and B. Lendl, *Blood Monitoring with an External Cavity Quantum Cascade Laser*, 2012.
- [13] H. Moser, A. Genner, J. Ofner, and B. Lendl, *Hydrogen Sulfide (H₂S) Sensing using Ring Cavity Surface Emitting QCLs (RCSE-QCLs) around 8 μ m*, 2014.
- [14] A. Genner, C. Gasser, H. Moser, T. Sumalowitsch, J. Ofner, and B. Lendl, *Online Monitoring of an Industrial Process: Application of a Fabry-Pérot Detector Based Sensor*, 2014.
- [15] C. Gasser, A. Genner, H. Moser, J. Ofner, and B. Lendl, *Tunable Fabry-Perot Detectors for Process Analytical Chemistry - Evaluation of a Prototype for Multi-Component Gas Streams*, 2015.
- [16] A. Genner, C. Gasser, H. Moser, J. Ofner, and B. Lendl, *Towards an EC-QCL based Sensor for Monitoring Side Products of Formaldehyde Production*, 2017.
- [17] H. Moser, J. P. Waclawek, A. Genner, C. Gasser, and B. Lendl, *A three-channel quantum cascade laser based sulfur species sensor for H₂S, CH₃SH and COS in petrochemical process streams Sensor setup QC Laser Sources & Spectral Windows Three-Channel QCL Sensor Architecture*, 2018.
- [18] A. Genner, P. Martin-Mateos, H. Moser, and B. Lendl, *Extending the Linear Range of a QCL Based Multi-Gas-Analyzer with Heterodyne Phase Sensitive Dispersion Spectroscopy*, 2019.
- [19] A. Genner, H. Moser, and B. Lendl, *Ambient Air Monitoring with a QCL-Based Multi-Gas-Analyzer*, 2019.